
Development of a novel wheel-rail maintenance strategy utilizing laser cladding technology

- Doctoral Thesis -

Quan Lai

B.Eng. (AeroEng)(Hons), Dec 2014

*Department of Mechanical and Aerospace Engineering
Faculty of Engineering
Monash University*

*A thesis submitted in fulfillment of the requirements for the award of the degree of
Doctor of Philosophy*

April 2018



MONASH
University



**GROUP
OF EIGHT**
AUSTRALIA

Department of Mechanical and Aerospace Engineering

The author © 2018.

All rights reserved

Under the Copyright Act 1968, this thesis may not be reproduced, stored in a retrieval system, or transmitted in any form or by any means, electronic, mechanical, photocopying, recording, or otherwise without the express permission of the author. I certify that I have made all reasonable efforts to secure copyright permissions for third-party content included in this thesis and have not knowingly added copyright content to my work without the owner's permission.

Typeset with Microsoft Word

Printed and bound in Australia by:

Monash University Print and Design Services

2 Industrial Avenue

Notting Hill, Victoria

Published by The Department of Mechanical and Aerospace Engineering

Monash University - Clayton campus

Victoria 3800

Australia

Abstract

The contact between train wheels and rail tracks is known to induce material degradation in the form of wear and rolling contact fatigue in the railhead. Current maintenance techniques such as arc welding, rail grinding, and rail replacement contribute a significant part of the cost of railway network operation. The ever-widening demand for greater axle loads and annual haulage rates, particularly in Australia – a major producer of iron ore and coal, necessitates the improvement in rail materials and maintenance strategies. Laser cladding – a state of the art surface engineering technique, is a promising resolution to alleviate the rates of degradation and extends the component longevity. The low heat input, dilution, and distortion, and high precision and surface finish integrity of laser cladding empower the technique to be a solid competitor over other surface engineering technique. Therefore, a systematic study towards a commercially viable railway maintenance technique using laser-cladding technology, whereby the undesirable by-products of wheel-rail contact, and operational cost could be diminished. Research on the optimal process parameters by inspecting the quality of the corresponding cladded specimens in terms of the clad substrate bonding strength, integrity, and the impacts of laser cladding technology on metallurgical microstructures and mechanical properties was conducted. The effects of cladding materials on microstructural and mechanical characterizations of rail steels and acquisition of temperature profiles experimentally and numerically were also investigated. The present report consists of literature review, research aims, accomplished research work, contributions of the accomplished research and future recommendations.

Declaration Statement

I hereby declare that this thesis contains no material which has been accepted for the award of any other degree or diploma at any university or equivalent institution and that, to the best of my knowledge and belief, this thesis contains no material previously published or written by another person, except where due reference is made in the text of the thesis.

Signed _____

Quan Lai

Date 27/09/2018

This thesis is lovingly dedicated to my parents for their love, encouragement and support.

Publications

Journal Papers:

Lai, Q., Abrahams, R., Yan, W., Qiu, C., Mutton, P., Paradowska, X., Soodi, M., Wu, X., 2017. Investigation of a novel functionally graded material for the repair of premium hypereutectoid rails using laser cladding technology, Composites Part B: Engineering 130, 174-191.

Lai, Q., Abrahams, R., Yan, W., Qiu, C., Mutton, P., Paradowska, A., Fang, X., Soodi, M., Wu, X., 2018. Effects of preheating and carbon dilution on material characteristics of laser-cladded hypereutectoid rail steels. Materials Science and Engineering: A 712, 548-563.

Lai, Q., Abrahams, R., Yan, W., Qiu, C., Mutton, P., Paradowska, X., Soodi, M., Wu, X., 2019. Influences of depositing materials, processing parameters and heating conditions on material characteristics of laser-cladded hypereutectoid rails, Materials Processing Technology 263, 1-20.

Roy, T., Lai, Q., Abrahams, R., Qiu, C., Mutton, P., Paradowska, X., Soodi, M., Yan, W., 2018. Effect of deposition material and heat treatment on wear and rolling contact fatigue of laser cladded rails, Wear 412-413, 69-81.

Conference papers:

Lai, Q., Abrahams, R., Yan, W., Qiu, C., Mutton, P., Paradowska, A., Fang, X., Soodi, M., Wu, X, Influence of depositing Material and heat treatment on microstructural characteristics of hypereutectoid rails repaired by laser cladding, The First International Conference on Rail Transportation, China.

Lai, Q., Abrahams, R., Yan, W., Qiu, C., Mutton, P., Paradowska, A., Fang, X., Soodi, M., Wu, X, Finite element analysis of thermal cycle in laser cladding for railway repair, 9th Australasian Congress on Applied Mechanics (ACAM9), Sydney.

Lai, Q., Abrahams, R., Yan, W., Qiu, C., Mutton, P., Paradowska, A., Fang, X., Soodi, M., Wu, X, Material characteristics of laser-cladded hypereutectoid rail steels, CORE 2018 Conference on Railway Excellence, Sydney.

Roy, T., Lai, Q., Abrahams, R., Yan, W., Qiu, C., Mutton, P., Paradowska, A., Fang, X., Soodi, M., Wu, X, Tribological behaviour of laser clad rail under rolling contact test, The First International Conference on Rail Transportation, China.

Roy, T., Lai, Q., Abrahams, R., Yan, W., Qiu, C., Mutton, P., Paradowska, A., Fang, X., Soodi, M., Wu, X, Effect of cladding direction on residual stress distribution in laser clad rails, ICRE 2017: 19th International Conference on Railway Engineering, UK.

Roy, T., Abrahams, R., Lai, Q. Yan, W., Qiu, C., Mutton, P., Paradowska, A., Fang, X., Soodi, Residual stress measurement in laser clad rail utilizing neutron diffraction technique, 9th Australasian Congress on Applied Mechanics (ACAM9), Sydney.

Acknowledgements

I would like to express my sincerest gratitude and most profound appreciation towards my esteemed supervisors, Associate Professor Ralph Abrahams and Associate Professor Wenyi Yan from Monash University, Dr Cong Qiu and Mr Peter Mutton from Institute of Railway Technology, Dr Anna Paradowska from Australian Nuclear Science and Technology Organisation and specially Dr Mehdi Soodi and Mr Andrew Dugan from Hardchrome Engineering. Their knowledge and expertise in this research field were inestimable to the accomplishment of my PhD study.

I am grateful to the ARC Linkage project [LP140100810] and many others who have kindly offered their guidance and support over the course of my PhD study. Firstly, I am thankful to Dr Iman Salehi from Institute of Railway Technology, for his advice and guidance in conducting finite element models in this study. Secondly, I would like to extend my appreciation to the staff of Mechanical Engineering workshop at Monash University for their cooperation and assistance in fabricating all the related jobs required in this research study. Thirdly, I would also like to acknowledge the Mechanical and Aerospace Engineering, Monash Center for Electron Microscopy (MCEM) and Monash X-ray Platform (MXP), for the access to all their facilities. Moreover, I would like to show courtesy to my fellow friends and colleagues without whom my PhD journey would not have been hardly as pleasant and who have contributed with their constructive suggestions and discussions to the study and. Finally, to my family, thank you for inspiring me in all of my pursuits and encouraging me to follow my studies. I am especially indebted to my parents for their care, support and guidance, which have made this thesis viable.

Contents

Abstract	iii
Declaration Statement	iv
Publications	vi
Acknowledgements	viii
Contents	ix
List of Figures	xiv
List of Tables	xxxi
Nomenclature	xxxii

Chapter 1 - Introduction	1
1.1 Research background and motivation.....	2
1.2 Research Aims and Objectives	4
1.3 Outline of Thesis.....	7
Chapter 2 - Literature Review	12
2.1 Deformation and damage of railway due to wheel passages.....	13
2.1.1 Wear in rails.....	14
2.1.2 Rolling Contact Fatigue in rails.....	22
2.2 Surface engineering techniques for enhancing the tribological and mechanical properties of rail steels.	37
2.3 Laser cladding: an interdisciplinary technology	39
2.4 Functional graded surface upon steel utilizing laser cladding	41
2.5 Laser cladding of tribological rail-steel components.....	43
2.6 Chapter summary	45
Chapter 3 – Materials and Experimental procedures	47
3.1 Description of Laser cladding rig.....	48
3.2 Selection of cladding and substrate materials.....	49
3.3 Description of rail specimens.....	51
3.4 Preheat and Post-weld heat treatment.....	52
3.5 Metallographic and mechanical characterization	52
3.5.1 Optical Microscopy (OM) and Scanning Electron Microscopy (SEM).....	52
3.5.2 X-ray diffractometric phase analysis (XRD)	54
3.5.3 Electron backscattered diffraction (EBSD) and Energy dispersive X-ray microanalysis (EDS).....	56
3.5.4 Shear Punch Testing.....	57
3.5.5 Focused Ion Beam (FIB) and Scanning Transmission Electron Microscopy (STEM)	58

Chapter 4 - Laser Cladded Premium Rails..... 60

4.1 Introduction.....	61
4.2 Experimental Setup - Optimum cladding directions.....	62
4.3 Experimental Results.....	63
4.3.1 Phase identification and distribution.....	63
4.3.2 Microstructure of the 410L cladding layers.....	75
4.3.3 Microstructure of the HAZ beneath the 410L clads.....	76
4.3.4 Microhardness tests.....	81
4.3.5 Strength of the laser deposited layers.....	85
4.4 Discussion.....	87
4.4.1 Microstructure of the laser deposited layers.....	87
4.4.2 Microstructure of the HAZs beneath the 410L deposited layer.....	91
4.4.3 Mechanical properties of the laser deposited rails.....	94
4.5 Chapter Summary.....	97

Chapter 5 - Cladding Materials and Heat Treatment..... 99

5.1 Introduction.....	100
5.2 Experimental Setup - Optimum processing parameters and heat treatments.....	101
5.3 Experimental Results.....	103
5.3.1 Comparative studies for optimum processing parameters and heat treatments.....	103
5.3.2 Microstructural characteristics of the four deposited layers.....	106
5.3.3 Influence of heat treatment and cladding materials on microstructures of the HAZs.....	129
5.3.4 Microhardness tests.....	139
5.3.5 Evaluation on the shear strength of the laser cladded rails.....	144
5.4 Discussion.....	146
5.4.1 Impacts of cladding materials and processing parameters on cladding quality.....	146
5.4.2 Assessment of structural integrity based on observed microstructural characteristics and measured mechanical properties.....	147

5.4.3 Assessment of structural integrity based on measured mechanical properties.....	152
5.5 Chapter summary	154
Chapter 6 - Elimination of HAZ's Martensitic Transformation and Observation of Carbon Dilution.....	157
6.1 Introduction.....	158
6.2 Experimental Setup.....	159
6.3 Experimental Results	160
6.3.1 Microstructural characteristics of 410L deposited layers	160
6.3.2 Microstructure of 410L deposits' HAZs.....	167
6.3.3 Microhardness tests	170
6.3.4 X-ray diffractometric phase analysis of 410L deposits.....	174
6.3.5 STEM microstructural analyses of 410L deposits.....	179
6.3.6 Shear strength of laser clad rails.....	181
6.3.7 Crystallographic texture of laser clad rails	183
6.4 Discussion	186
6.4.1 Impact of preheating condition on Microstructural characteristics of HAZs of clad rails.....	186
6.4.2 Impact of preheating condition on Microstructural characteristics of 410L laser deposits.....	192
6.4.3 Observations of carbon dilution	194
6.5 Chapter Summary.....	196
Chapter 7 - Finite Element Analysis of thermal cycle in laser cladding of rail steels	198
7.1 Introduction.....	199
7.2 Experimental procedure	202
7.3 Finite element analysis.....	203

7.3.1 Thermal model	203
7.3.2 Numerical implementation.....	204
7.4 Results and Discussion.....	206
7.5 Chapter summary	211
Chapter 8 - Conclusions & Future Work	212
8.1 Major findings and contributions	214
8.1.1 Selection of the suitable cladding direction	214
8.1.2 Correlation between elimination of martensitic formation in HAZ of hypereutectoid rails and selection of an appropriate applied heat treatment	216
8.1.3 Observations of carbon dilution from the hypereutectoid rail substrate	217
8.1.4 Selection of suitable cladding materials and processing parameters.....	218
8.1.5 Numerical study of the thermal cycle in HAZ during laser cladding and its validations	221
8.2 Recommendations for Future Work	222
References.....	224

List of Figures

Figure 1-1 Schematic of a typical laser cladding unit with a coaxial laser head.....2

Figure 2-1 Abrasive wear (scratches) on rails. [2] 15

Figure 2-2 Types of abrasive wear: A. Microploughing, B. Microcutting, C. Microcracking, D. Microfatigue. [2] 15

Figure 2-3 Mechanism of Adhesive wear. [2] 16

Figure 2-4 Delamination wear of wheels. [2] 17

Figure 2-5 Trinochemical wear mechanism. [2]..... 18

Figure 2-6 Fretting wear stages: A. Wear particles accumulated between contacting high spots, B. Growth in size of the accumulated particles, C. Transfer of the accumulated particles to the neighboring regions, D. Formation of curved zone caused by the intense wear process. [2] 19

Figure 2-7 Stages of surface fatigue mechanism. [2].....	20
Figure 2-8 Wheel with surface fatigue mechanism. [2].....	20
Figure 2-9 Train derailment in the town of Gainford, Alberta, Canada owing to surface defects.	21
Figure 2-10 Train Derailment in Ellicott city, Maryland. [1].....	22
Figure 2-11 Cracks and spalls in initial stages develop in a rail transverse section. [1]	23
Figure 2-12 Cracks and spalls in initial stages develop in a rail longitudinal section. The crack propagates into the railhead and then level out. [1].....	23
Figure 2-13 Initial stage of gauge corner checking cracks. [1]	24
Figure 2-14 Intermediate stage of gauge corner checking cracks and spalls. [1].....	24
Figure 2-15 Severe stage of gauge corner checking cracks and spalls. [1]	25
Figure 2-16 Running surface checking cracks with minor spalling. [1]	25
Figure 2-17 Initial stage of shell formation with presence of dark spots. [1].....	27
Figure 2-18 Intermediate stage of shell formation. [1].....	27
Figure 2-19 Severe stage of shell formation. [1]	28
Figure 2-20 Small transverse defect developed from shelling. [1]	28
Figure 2-21 Subsurface cracking associated with squat defects. [1]	30
Figure 2-22 Initial stage of running surface squat. [1].....	31
Figure 2-23 Intermediate stage of running surface squat. [1]	31

Figure 2-24	Severe stage of running surface squat. [1]	32
Figure 2-25	Initial stage of squats initiated by gauge corner checking. [1]	32
Figure 2-26	Intermediate stage of squats initiated by gauge corner checking. [1].....	33
Figure 2-27	Severe stage of squats initiated by gauge corner checking. [1].....	33
Figure 2-28	Surface after grinding to remove small – medium squats initiated by gauge corner checking. [1]	34
Figure 2-29	Running surface squats initiated from wheelslip. [1]	34
Figure 2-30	Squats in switches. [1]	35
Figure 2-31	Squats in turnout. [1]	35
Figure 2-32	Inspection to determine the length and depth of subsurface squat cracks using an ultrasonic depth gauge. [1]	36
Figure 3-1	Photograph of a laser-cladded hypereutectoid rail specimen with detailed dimensions prior to specimen preparation process.	51
Figure 3-2	Microstructural inspection using the JEOL 7001F scanning electron microscope with built-in features.....	53
Figure 3-3	XRD analyses using (a) Bruker D8 Advance ECO X-ray instrument. (b) X-ray diffraction chamber with rotation sample stage, energy -dispersive LYNXEYE XE-T detector and motorized anti-scatter screen.	54
Figure 3-4	(a) Oxford instrument X-Max 80 EDS detector, and (b) HKL NordlysMax electron backscattered diffraction (EBSD) camera.....	55

Figure 3-5 (a) Sample chamber in the ordinary SEM mode, and (b) Sample chamber in the EBSD mode.56

Figure 3-6 Shear strength inspection using a specially-designed shear punch testing instrument at Monash.....58

Figure 3-7 (a) Metallurgical sample preparation using FEI Quanta 3D FIB workstation. (b) Detailed microstructural investigation using the FEI Tecnai G2 F20 S-TWIN microscope.59

Figure 4-1 X-ray diffraction patterns of (a) the 410L transversely deposited layer with preheating (Group 1), (b) the 410L longitudinally deposited layer with preheating (Group 2), (c) the 410L longitudinally deposited layer with preheating, post-heating and slow cooling, and (d) the unprocessed 410L.63

Figure 4-2 Typical acquired EBSD results for the Group 1 deposits. (a1) The band contrast (BC) image for topographical information, (a2) the image of phase distribution, and the EDS images of (a3) Cr and (a4) Mn element distributions. Dendritic morphology was detected with the fine martensitic structure inside each dendritic arm (as shown in red) and retained austenite at the grain boundary (as shown in blue).....66

Figure 4-3 Typical acquired EBSD results of the Group 1 deposits at the interface. (b1) the band contrast (BC) image for topographical information, (b2) the image of phase distribution, and the EDS images of (b3) Cr and (b4) Mn element distributions. Dendritic morphology was detected with the fine martensitic structure inside each dendritic arm (as shown in red) and retained austenite at the grain boundary (as shown in blue).....67

Figure 4-4 Typical EBSD acquired results of the Group 2 deposit with (a1) the band contrast (BC) image for topographical information, (a2) the image of phase distribution, and

- the EDS images of (a3) Cr and (a4) Mn element distributions. (M=Martensite, and F=Ferrite)68
- Figure 4-5 Typical EBSD results of the 410L rail-longitudinal deposited clad (Group 2) at the interface with (b1) the band contrast (BC) image for topographical information, (b2) the image of phase distribution, and the EDS images of (b3) Cr and (b4) Mn element distributions. (M=Martensite, F=Ferrite, P= Pearlite, B=Bainite, and RA=Retained Austenite)69
- Figure 4-6 Typical EBSD acquired results of the 410L rail-longitudinal deposited clad (Group 3) in the clad with (a1) the band contrast (BC) image for topographical information, (a2) the image of phase distribution, and the EDS images of (a3) Cr and (a4) Mn element distributions. (M=Martensite, and F=Ferrite)..... 70
- Figure 4-7 Typical EBSD acquired results of the 410L rail-longitudinal deposited clad (Group 3) at the interface with (b1) the band contrast (BC) image for topographical information, (b2) the image of phase distribution, and the EDS images of (b3) Cr and (b4) Mn element distributions. (M=Martensite, F=Ferrite and RA=Retained Austenite).... 71
- Figure 4-8 Micrographs showing the fine dendritic microstructure of the cross sections of the 410L rail-transversely deposited clad (Group 1) at (a) left gauge corner (Start), (b) middle section and (c) right gauge corner. (d) Typical equiaxed dendritic grains, (e) columnar/cellular dendritic grains. (f) planar dendritic grains located from top to bottom of the Group 1 clad, respectively.72
- Figure 4-9 Micrograph showing the 410L rail-longitudinally deposited clad (Group 2) microstructure of the cross sections of the at (a) left gauge corner, (b) middle section and (c) right gauge corner. (d) Ferritic colonies in the (e) martensite matrix. (f) The Group 2 interface. (F=Ferrite, M=Martensite) 73
-

- Figure 4-10 Micrograph showing the 410L rail-longitudinally deposited clad (Group 3) microstructure of the cross sections of the at (a) left gauge corner (Start), (b) middle section and (c) right gauge corner. (d) Ferritic colonies in the (e) tempered martensite matrix. (f) Small retained austenite colonies developed near the interface, due to dilution. (F=Ferrite, TM=Tempered martensite, RA=Retained austenite) 74
- Figure 4-11 Micrograph showing the HAZ and rail substrate of the rail-cross sections at (a) left gauge corner, (b) right gauge corner, (c) middle section and (d) a representative of the longitudinal sections under the 410L rail-transversely deposited clad (Group 1). The light etching microconstituent in the HAZ of (a), (b) and (d) is martensite. (M=martensite)77
- Figure 4-12 SEM micrographs of the sub-regions in the Group 2 HAZ. (a) Partially molten zone featuring a metallurgical bond at the top. In the middle, (b) coarse-grained HAZ characterized by fully bainitic structure and (c) fine-grained HAZ characterized by a combination of pearlite and bainite, and (d) Inter-critical HAZ characterized by spheroidite at the interface under the 410L rail-transversely deposited clad (Group 2).77
- Figure 4-13 Micrograph showing the HAZ and rail substrate of the rail-cross sections at (a) left gauge corner, (b) right gauge corner, (c) middle section and (d) a representative of the longitudinal sections under the 410L rail-transversely deposited clad (Group 2). The light etching microconstituent in the HAZ of (b) and (d) is martensite. (M=martensite)78
- Figure 4-14 SEM micrographs of the sub-regions in the Group 2 HAZ. (a) Partially molten zone featuring a metallurgical bond at the top. In the middle, (b) coarse-grained HAZ characterized by fully bainitic structure and (c) fine-grained HAZ characterized by a combination of pearlite, bainite and spheroidite, and (d) Inter-critical HAZ
-

characterized by spheroidite at the interface under the 410L rail-transversely deposited clad (Group 2).78

Figure 4-15 Micrograph showing the HAZ and HE400 substrate of the rail-cross sections at (a) left gauge corner, (b) right gauge corner, (c) middle section and (d) a representative of the longitudinal sections under the 410L rail-transversely deposited clad (Group 2). Tempered martensite was found occasionally.79

Figure 4-16 SEM micrographs of the sub-regions in the Group 3 HAZ. (a) Partially molten zone featuring a metallurgical bond at the top. In the middle, (b) Coarse-grained HAZ characterized by fully pearlitic structure and (c) Fine-grained HAZ characterized by partially and fully pearlitic structure, and (d) Inter-critical HAZ characterized by spheroidite at the interface under the 410L rail-longitudinally deposited clad (Group 3).79

Figure 4-17 Vertical hardness distribution of the rail transversely deposited (Group 1) clad.... 82

Figure 4-18 Vertical hardness distribution of the rail longitudinally deposited (Group 2) clad. 82

Figure 4-19 Vertical hardness distribution of the rail longitudinally deposited (Group 3) clad. 83

Figure 4-20 Horizontal hardness distribution of (a) the rail transversely deposited clad (Group 1).84

Figure 4-21 Horizontal hardness distribution of the rail longitudinally deposited clad at rail-transverse middle sections (Group 2).84

Figure 4-22 Horizontal hardness distribution of the rail longitudinally deposited clad at rail-transverse middle sections (Group 3).85

Figure 4-23 The load-displacement curves with corresponding ultimate shear strength (USS) values acquired for the 410L deposited layers subjected to different heat treatment and processing parameters.86

Figure 4-24 Morphology of solidification cracks in the cladding layer of Group 1..... 89

Figure 5-1 Macrographs of top representative surfaces of Group 1 deposits with (1) single and (2) double layer cladding passes. Heat treatment produces involved only preheating to 350 °C (HTA). (a) 410L, (b) 420SS, (c) Stellite 6 and (d) Stellite 21. 104

Figure 5-2 Macrographs of top representative surfaces of Group 2 deposits with (1) single and (2) double layer cladding passes. Heat treatment produces involved only preheating to 350 °C (HTA). (a) 410L, (b) 420SS, (c) Stellite 6 and (d) Stellite 21. 104

Figure 5-3 Macrographs of top representative surfaces of deposits with the desired surface properties. Heat treatment produces involved preheating to 350 °C, post-heating to 350 °C and then was slow-cooled to room temperature by using a ceramic blanket (HTB). (a) 410L - Group 1, (b) 420SS - Group 2, (c) Stellite 6 - Group 2 and (d) Stellite 21 - Group 2 with (1) single and (2) double layer cladding passes..... 105

Figure 5-4 Micrographs showing typical cross sections of 410L deposits with (a) single deposition and HTA, (b) double deposition and HTA, (c) single deposition and HTB, and (d) double deposition and HTB..... 109

Figure 5-5 Micrographs showing typical cross sections of 420SS deposits with (a) single deposition and HTA, (b) double deposition and HTA, (c) single deposition and HTB, and (d) double deposition and HTB..... 110

Figure 5-6 Micrographs showing typical cross sections of Stellite 6 deposits with (a) single deposition and HTA, (b) double deposition and HTA, (c) single deposition and HTB, and (d) double deposition and HTB..... 111

Figure 5-7 Micrographs showing typical cross sections of Stellite 21 deposits with (a) single deposition and HTA, (b) double deposition and HTA, (c) single deposition and HTB, and (d) double deposition and HTB..... 112

Figure 5-8 Cross sections of 410L with single deposition and HTA, (i) top region of laser tracks, (ii) overlapping region of laser tracks, (iii) middle region of laser tracks, and (iv) interface of deposit-substrate, whose locations are shown in Figure 5-4 and discussed in Section 5.3.2..... 113

Figure 5-9 Cross sections of 410L with single deposition and HTA were discussed in Section 5.3.2, (i) top region of laser tracks, (ii) overlapping region of laser tracks, (iii) middle region of laser tracks, and (iv) interface of deposit-substrate, whose locations are shown in Figure 5-4. 114

Figure 5-10 Cross sections of 410L with single deposition and HTB were discussed in Section 5.3.2. (i) top region of laser tracks, (ii) overlapping region of laser tracks, (iii) middle region of laser tracks, and (iv) interface of deposit-substrate, whose locations are shown in Figure 5-4..... 115

Figure 5-11 Cross sections of 410L with double deposition and HTB were discussed in Section 5.3.2. (i) top region of laser tracks, (ii) overlapping region of laser tracks, (iii) middle region of laser tracks, and (iv) interface of deposit-substrate, whose locations are shown in Figure 5-4..... 116

Figure 5-12 Cross sections of 420SS with single deposition and HTA were discussed in Section 5.3.2. (i) top region of laser tracks, (ii) overlapping region of laser tracks, (iii) middle region of laser tracks, and (iv) interface of deposit-substrate, whose locations are shown in Figure 5-5..... 117

Figure 5-13 Cross sections of 420SS with double deposition and HTA were discussed in Section 5.3.2. (i) top region of laser tracks, (ii) overlapping region of laser tracks, (iii) middle region of laser tracks, and (iv) interface of deposit-substrate, whose locations are shown in Figure 5-5..... 118

Figure 5-14 Cross sections of 420SS with single deposition and HTB were discussed in Section 5.3.2. (i) top region of laser tracks, (ii) overlapping region of laser tracks, (iii) middle region of laser tracks, and (iv) interface of deposit-substrate, whose locations are shown in Figure 5-5..... 119

Figure 5-15 Cross sections of 420SS with double deposition and HTB were discussed in Section 5.3.2. (i) top region of laser tracks, (ii) overlapping region of laser tracks, (iii) middle region of laser tracks, and (iv) interface of deposit-substrate, whose locations are shown in Figure 5-5..... 120

Figure 5-16 Cross sections of Stellite 6 with single deposition and HTA were discussed in Section 5.3.2. (i) top region of laser tracks, (ii) overlapping region of laser tracks, (iii) middle region of laser tracks, and (iv) interface of deposit-substrate, whose locations are shown in Figure 5-6..... 121

Figure 5-17 Cross sections of Stellite 6 with double deposition and HTA were discussed in Section 5.3.2. (i) top region of laser tracks, (ii) overlapping region of laser tracks, (iii) middle region of laser tracks, and (iv) interface of deposit-substrate, whose locations are shown in Figure 5-6..... 122

Figure 5-18 Cross sections of Stellite 6 with single deposition and HTB were discussed in Section 5.3.2. (i) top region of laser tracks, (ii) overlapping region of laser tracks, (iii) middle region of laser tracks, and (iv) interface of deposit-substrate, whose locations are shown in Figure 5-6..... 123

Figure 5-19 Cross sections of Stellite 6 with double deposition and HTB were discussed in Section 5.3.2. (i) top region of laser tracks, (ii) overlapping region of laser tracks, (iii) middle region of laser tracks, and (iv) interface of deposit-substrate, whose locations are shown in Figure 5-6..... 124

Figure 5-20 Cross sections of Stellite 21 with single deposition and HTA were discussed in Section 5.3.2. (i) top region of laser tracks, (ii) overlapping region of laser tracks, (iii) middle region of laser tracks, and (iv) interface of deposit-substrate, whose locations are shown in Figure 5-7..... 125

Figure 5-21 Cross sections of Stellite 21 with double deposition and HTA were discussed in Section 5.3.2. (i) top region of laser tracks, (ii) overlapping region of laser tracks, (iii) middle region of laser tracks, and (iv) interface of deposit-substrate, whose locations are shown in Figure 5-7..... 126

Figure 5-22 Cross sections of Stellite 21 with single deposition and HTB were discussed in Section 5.3.2. (i) top region of laser tracks, (ii) overlapping region of laser tracks, (iii) middle region of laser tracks, and (iv) interface of deposit-substrate, whose locations are shown in Figure 5-7..... 127

Figure 5-23 Cross sections of Stellite 21 with single deposition and HTB were discussed in Section 5.3.2. (i) top region of laser tracks, (ii) overlapping region of laser tracks, (iii) middle region of laser tracks, and (iv) interface of deposit-substrate, whose locations are shown in Figure 5-7..... 128

Figure 5-24 SEM micrographs showing typical morphology of (a) bainite and pearlite and (b) spheroidite/partial spheroidite. 129

Figure 5-25 Heat affected zones and the unaffected substrate of the rail-cross sections at (a) the initial cladding runs - LHS, (b) middle cladding runs, (c) the last cladding runs - RHS

and (d) a typical longitudinal cross-section at the beginning and finishing ends of the cladding runs under (i) 410L, (ii) 420SS, (iii) Stellite 6 and (iv) Stellite 21 deposits with HTA and single deposition. (M=martensite)..... 131

Figure 5-26 Heat affected zones and the unaffected substrate of the rail-cross sections at (a) the initial cladding runs - LHS, (b) middle cladding runs, (c) the last cladding runs - RHS and (d) a typical longitudinal cross-section at the beginning and finishing ends of the cladding runs under (i) 410L, (ii) 420SS, (iii) Stellite 6 and (iv) Stellite 21 deposits with HTB and single deposition. (TM=Tempered martensite)..... 132

Figure 5-27 Heat affected zones and the unaffected substrate of the rail-cross sections at (a) the initial cladding runs - LHS , (b) middle cladding runs, (c) the last cladding runs - RHS and (d) a typical longitudinal cross-section at the beginning and finishing ends of the cladding runs under (i) 410L, (ii) 420SS, (iii) Stellite 6 and (iv) Stellite 21 deposits subjected to HTA and double deposition. 136

Figure 5-28 Heat affected zones and the unaffected substrate of the rail-cross sections at (a) the initial cladding runs - LHS, (b) middle cladding runs, (c) the last cladding runs - RHS, and (d) a typical longitudinal cross-section at the beginning and finishing ends of the cladding runs under (i) 410L, (ii) 420SS, (iii) Stellite 6 and (iv) Stellite 21 deposits subjected to HTB and double deposition. (TM=Tempered martensite) 137

Figure 5-29 The heat affected zone (HAZ)'s thickness under the 410L, 420SS, Stellite 6 and Stellite 21 deposited layers subjected to different heat treatments and a number of layers. 138

Figure 5-30 Distributions of hardness in single (1L) and double (2L) deposition of 410L under HTA and HTB..... 142

Figure 5-31 Distributions of hardness in single (1L) and double (2L) deposition of 420SS under HTA and HTB..... 142

Figure 5-32 Distributions of hardness in single (1L) and double (2L) deposition of Stellite 6 under HTA and HTB..... 143

Figure 5-33 Distributions of hardness in single (1L) and double (2L) deposition of Stellite 21 under HTA and HTB..... 143

Figure 5-34 Comparison of the load-displacement curves with corresponding ultimate shear strength (USS) values acquired for the 410L, 420SS, Stellite 6 and Stellite 21 deposited layers subjected to similar heat treatments and processing parameters. 144

Figure 5-35 Scanning electron micrographs of Stellite 6’s microstructure at (a) low magnification and (b) high magnification showing a complex combination of inter-dendritic carbides in a Co-based matrix..... 149

Figure 5-36 Scanning electron micrographs of Stellite 21’s microstructure at (a) low magnification and (b) high magnification showing Co-base matrix and inter-dendritic Mo and Cr rich carbides..... 149

Figure 5-37 Micrographs showing an interdendritic crack for Stellite 21 deposits with HTA at the starting of the second deposition. (a) Low magnification, (b) high magnification.. 150

Figure 6-1 Optical micrographs of a representative cross-section of (i) the Group 1 deposits with one layer and preheating length of 400 mm, (ii) Group 1 deposits with two layers and preheating length of 400 mm, (iii) Group 2 deposits with one layer and preheating length of 600 mm, and (iv) Group 2 deposits with two layers and preheating length of 600 mm. 162

- Figure 6-2 Optical micrographs of a representative cross-section of the Group 1-1L deposits with one layer and preheating length of 400 mm. (a) Deposit-substrate interface, (b) laser track overlapping region, (c) typical top portion of an individual track and (d) typical middle portion of an individual track. (M=Martensite, and F=Ferrite) 163
- Figure 6-3 Optical micrographs of a representative cross-section of Group 1-2L deposits with two layers and preheating length of 400 mm. For the first layer, (a) deposit-substrate interface, (b) laser track overlapping region, (c) typical top portion of an individual track and (d) typical middle portion of an individual track. (M=Martensite, and F=Ferrite) 164
- Figure 6-4 Optical micrographs of a representative cross-section of Group 2-1L deposits with two layer and preheating length of 400 mm. (a) Deposit-substrate interface, (b) laser track overlapping region, (c) typical top portion of an individual track and (d) typical middle portion of an individual track. (M=Martensite, and F=Ferrite) 165
- Figure 6-5 Optical micrographs of a representative cross-section of Group 2-2L deposits with two layer and preheating length of 400 mm. (a) Deposit-substrate interface, (b) laser track overlapping region, (c) typical top portion of an individual track and (d) typical middle portion of an individual track. (M=Martensite, and F=Ferrite) 166
- Figure 6-6 Unaffected rail substrate and corresponding HAZ of a typical rail-transverse sections at (a) left gauge corner, (b) middle section, (c) right gauge corner and (d) representative of the longitudinal sections for (i) Group 1-1L, (ii) Group 1-2L, (iii) Group 2-1L & (iv) Group 2-2L. Martensitic morphology (M=martensite) with white etching colour was detected in (c) and (d) of the (i) Group 1-1L and (ii) Group 1-2L. 168
- Figure 6-7 SEM micrographs showing typical (a) bainitic and (b) pearlitic morphologies in the sub-regions of the HAZs of Group 2-1L and Group 2-2L. 170
-

Figure 6-8 Vertical hardness distributions in the laser deposited rails (a) Group 1-1L, (b) Group 1-2L, (c) Group 2-1L and (d) Group 2-2L. 172

Figure 6-9 X-ray diffraction patterns of (a) the raw 410L powder and the 410L deposit with single layer and preheating length of 400m (Group 1-1L) at (b) the deposit-substrate interface, (c) the deposit halfway surface and (d) deposit top surface, respectively. 176

Figure 6-10 X-ray diffraction patterns of (a) the raw 410L powder and the 410L deposit with double layer and preheating length of 400m (Group 1-2L) at (b) the deposit-substrate interface, (c) the deposit halfway surface and (d) deposit top surface, respectively. 176

Figure 6-11 X-ray diffraction patterns of (a) the raw 410L powder and the 410L deposit with a single layer and preheating length of 600m (Group 2-1L) at (b) the deposit-substrate interface, (c) the deposit halfway surface and (d) deposit top surface, respectively. 177

Figure 6-12 X-ray diffraction patterns of (a) the raw 410L powder and the 410L deposit with double layer and preheating length of 600m (Group 2-2L) at (b) the deposit-substrate interface, (c) the deposit halfway surface and (d) deposit top surface, respectively. 177

Figure 6-13 (a) Bright field TEM and (b) Dark-field TEM images of a representative ferritic grain in the vicinity of the deposit's top surface, showing no precipitation on the grain boundary. (c) High magnification TEM image of the EDS scan line (1) with the length of 1.4 nm and its resulting EDS profiles. (d) The range from 0 to 60 counts of the EDS profiles. 180

Figure 6-14	Shear-punch test curves with the corresponding USS procured for the virgin rail, Group 1-1L, Group 1-2L, Group 2-1L and Group 2-2L.	182
Figure 6-15	Results of EBSD large area mapping of Group 1-1L. (a) Orientation map being used in conjunction with (b) Inverse Pole Figure (IPF) legends. (c) (100), (110) and (111) pole figures attached with an intensity legend. (d) Distribution of grain size. (e) Distribution of misorientation angle.	187
Figure 6-16	Results of EBSD large area mapping of Group 2-1L. (a) Orientation map being used in conjunction with (b) Inverse Pole Figure (IPF) legends. (c) (100), (110) and (111) pole figures attached with an intensity legend. (d) Distribution of grain size. (e) Distribution of misorientation angle.	188
Figure 6-17	Results of EBSD large area mapping of Group 1-2L. (a) Orientation map being used in conjunction with (b) Inverse Pole Figure (IPF) legends. (c) (100), (110) and (111) pole figures from the second cladding layer. (d.1) Distribution of grain size. (d.2) The detailed distribution of grain size less than 100 μm . (e) Distribution of misorientation angle.	189
Figure 6-18	Results of EBSD large area mapping of Group 2-2L. (a) Orientation map being used in conjunction with (b) Inverse Pole Figure (IPF) legends. (c) (100), (110) and (111) pole figures from the second cladding layer. (d.1) Distribution of grain size. (d.2) The detailed distribution of grain size less than 100 μm . (e) Distribution of misorientation angle.	190
Figure 7-1	Schematic of the laser cladded rail sample with detailed dimensions used for the preliminary study.	205
Figure 7-2	Schematic of finite element mesh model of the 68kg hypereutectoid rail substrate.	206

Figure 7-3 Micrograph showing the HAZ and rail substrate of the rail-cross sections at (a) left gauge corner, (b) right gauge corner, (c) middle section and (d) a representative of the longitudinal sections under the 410L rail-transversely deposited cladding layer (Group 1). The light etching microconstituent in the HAZ of (a), (b) and (d) is martensite. (M=martensite)..... 206

Figure 7-4 Micrograph showing the HAZ and rail substrate of the rail-cross sections at (a) left gauge corner, (b) right gauge corner, (c) middle section and (d) a representative of the longitudinal sections under the 410L rail-transversely deposited cladding layer (Group 2). The light etching microconstituent in the HAZ of (b) and (d) is martensite. (M=martensite) 207

Figure 7-5 Numerical simulations of the thermal profile during laser deposition of Group 1 specimens..... 209

Figure 7-6 Numerical simulations of the thermal profile during laser deposition of Group 2 specimens..... 209

List of Tables

Table 2-1 Comparison of numerous surface engineering techniques.....	37
Table 3-1 Chemical compositions of the depositing materials.....	50
Table 3-2 Chemical compositions of the substrate material (N.S = Not significant).	50
Table 4-1 Three different repair process procedures.....	62
Table 5-1 Heat treatment procedures applied for the comparative study of heating conditions.	101
Table 5-2 Parameter sets and deposited layer number applied for the comparative study.....	102
Table 6-1 Parameter sets applied for the comparative study of pre-heating length and deposited layer number.....	160
Table 7-1 Parameter sets applied for the comparative study of heat treatment.....	203

Nomenclature

Abbreviation	Definition
Ac3	The temperature at which transformation of ferrite to austenite
BC	Band Contrast
BCC	Body-Centred Cubic
EBSD	Electron Backscattered Diffraction
EDS	Energy Dispersive X-ray Microanalysis
F	Ferrite
FCC	Face-Centred Cubic
FEG	Field Emission Gun
FIB	Focused Ion Beam
G	Temperature Gradient
HAADF	High-Angle Annular Dark-Field
HAZ	Heat Affected Zone
HPDL	High Power Diode Laser
HTA	Heat treatment involving preheating Only
HTB	A combined heat treatment including preheating and PWHT

HV	Vickers pyramid number
HVOF	High-Velocity Oxy-Fuel
kgf	Kilogram-Force
LAM	Large Area Mapping
LD	Longitudinal Direction
M	Martensite
MGT	Million Gross Tonnes
MIG	Metal Inert Gas
N.S	Not Significant
ND	Normal Direction
OM	Optical Microscopy
OM	Optical Microscopy
PWHT	Post Weld heat treatment
R	Solid-liquid Interface growth rate
RA	Retained Austenite
RBED	Retractable solid-state Backscattered Electron Detector
RCF	Rolling Contact Fatigue
SA	Submerged Arc
SEM	Scanning Electron Microscopy
SMA	Shield Metal Arc
STEM	Scanning Transmission Electron Microscopy
TD	Transverse Direction
TIG	Tungsten Inert Gas
TM	Tempered Martensite
USS	Ultimate Shear Strength
UTS	Ultimate Tensile Strength
XRD	X-ray Diffractometric Phase Analysis
YS	Yield Strength

Symbols	Description
W_{ad}	Wear Rate
V	Volume
L	Sliding Distance
K	Coefficient of Wear
F_N	Normal Load
H	Hardness of Softer Material
ρ	Density
γ	Austenite
β	Stefan-Boltzman constant
α	Ferrite/Martensite
q	Heat Flux Vector
ε	Emissivity of Material
wt. %	Weight Percentage
t	Time
T	Temperature
r	Radial Distance
Q	Heat Source
k	Thermal Conductivity
h	Coefficient of Convection
h_{rough}	Coefficient of Convection for Rough Surfaces
q_{rad}	Radiation Heat Transfer
q_{conv}	Convection Heat Transfer
C_p	Specific Heat
T_s	Surface Temperature
T_∞	Measured Ambient Temperature

1

Introduction

This thesis is to present the doctoral research study on developing a novel railway maintenance technology in Australian heavy haul railway using laser cladding. In this chapter, an introduction of the conducted research is provided, which consists of the background knowledge and research incentives. The main objectives of this research study are underlined and elaborated by the specific aims.

1.1 Research background and motivation

Material degradation caused by wear at the interface of mechanical components is problematic for a number of engineering industries. The degradation deteriorates the components' effectiveness and performance, which leads to the requirement of regular maintenance or even replacement of the components. Employment of surface coating techniques seems to be a solution so that special metallic coatings can be applied on either new or used engineering components to gain superior surface properties (wear, corrosion and erosion resistance, etc.). Various surface coating techniques (Shielded metal arc, high-velocity oxy-fuel, tungsten inert gas, metal inert gas, etc.) have evolved to develop and manufacture functionally graded materials. Nevertheless, each technique presents its drawbacks such as low level of precision for discrete regions; high distortion, porosity, and dilution; post-treatment reworking required, etc. Therefore, the demand for a single surface engineering and remanufacturing technique capable of delivering high quality of surface finish and deposit and high satisfactory of repair parts has experienced a significant boost.

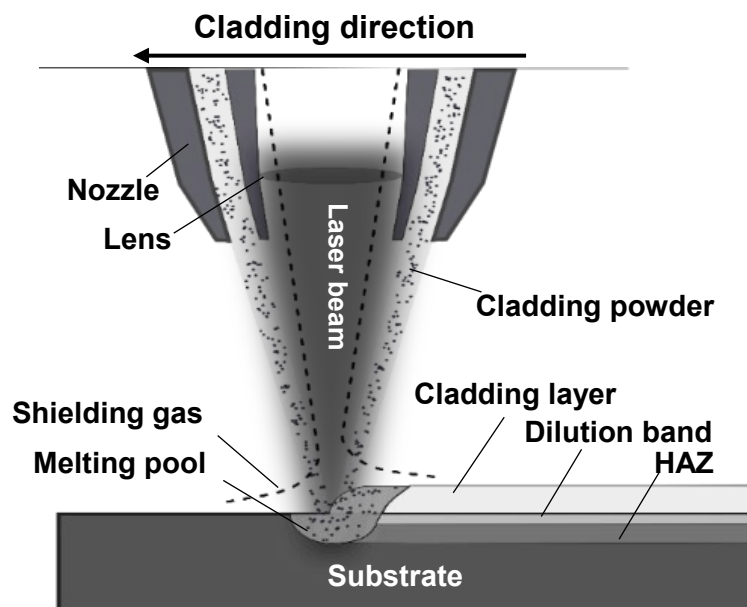


Figure 1-1 Schematic of a typical laser cladding unit with a coaxial laser head.

Laser cladding technique has recently attracted escalating interests from both academic research and engineering industries. Technically, laser cladding is a melting process in which laser beam is used to fuse a material addition onto a substrate, as shown in Figure 1-1. Despite exhibiting moderate deposit rates, laser cladding technique is considered as a promising, reliable alternative due to its ability to demonstrate distinct advantages over the conventional coating techniques:

- Laser cladding offers enhanced thermal control, which results in minimal dilution zone and heat affected zone (HAZ).
 - Its low heat input produces minimal thermal distortion, which minimises the number of post-treatment processes required.
 - The great ability to adapt to automation systems supplies laser cladding with close control of the shape of the clad and surface roughness.
 - True metallurgical bond is generated by laser cladding between the clad layer and the substrate. Thus, the issues of chipping and peeling due to mechanical bond that frequently arises in numerous conventional coating techniques, especially those involving thermal spraying, are removed.
 - High solidification and cooling rates are attained by the substrate acting as an active heat sink. This leads to fine solidification clad microstructures, which enable the cheaper substrate with a coarse microstructure to possess superior wear and corrosion resistance.
 - Furthermore, laser process is safe, economical and environmentally friendly. Laser power is clean optical energy, and it uses few contaminating materials. For optical energy, only
-

little environmental disturbance (noise, external electrical and magnetic fields) is generated, which allows processing to be conducted in local, ergonomic surroundings.

- The absence of tool wear and less scrap during laser cladding process reduce equipment maintenance costs.

Due to the aforementioned advantages, extensive research has been conducted on laser cladding and supports unprecedented growth of laser cladding applications. Its numerous applications in automotive, aerospace, machinery, nuclear, petrochemical, power generation, shipbuilding and recently medical industries illustrated the novelty and effectiveness of the technique. Therefore, the breadth of application motivates the utility of laser cladding technique for development of functionally graded materials at one of both wheel-rail contacting surfaces, which are subjected to a combination of wear and rolling contact fatigue.

Nevertheless, information on the suitable materials addition for rail steels using laser cladding; and the wear and fatigue performance of the laser-cladded rail specimens is sparse in the open literature. Comprehensive studies on the relationship between microstructure and mechanical properties of high strength cladded materials for rail steels are deficient.

1.2 Research Aims and Objectives

The project aims to establish commercially profitable laser cladding technologies for the fabrication of functionally graded materials for wheels and rails. Such materials can be utilized to prolong service lives of components via diminishing surface deterioration. Alternatively, the technologies can be applied as novel repair/ refurbish technologies or to dealing with side effects

of wheel-rail contact, for instance, wheel squeal and flanging noise. The research achievements will be employed directly by rail steel manufacturers of special track components to fabricate novel cladding alloys for applications of rail transportation industry and by rail infrastructure owners to improve their maintenance strategies and schedules. In order to accomplish the aforementioned aim, the following tasks are tailored and targeted.

Task 1: Determine the most suitable cladding materials for rail steel deposition under the different processing condition

- *Determine the most suitable cladding materials for prior-service rail cladding, and innovative repair and maintenance.*

This current research will attempt a range of high strength powdered materials used as hard-surfacing alloy additions in cladding process. The material additions are selected based on their potential hardness and work hardening behaviour, which is potentially beneficial to the final cladded rail steels.

- *Determine the optimum processing condition to be used during the cladding deposition on rail steel*

The cladding experiments will be conducted under a variety of processing conditions. The impact of conditions will be investigated and analysed as detailed in Task 2 in order to conclude the optimal deposition conditions and its corresponding processing parameters. Thanks to

Hardchrome Engineering, systematic approach will be executed for all materials. Furthermore, the approach is designed in such a way that it mimics the industrial deposition methodology. Single-track depositions will be first examined to obtain the optimal processing parameters, which will then apply for overlap depositions to prevent inter-run voids. In other words, single tracks, overlapping tracks, and multi-layer tracks will be deposited onto rail steels in turn. Processing parameters consisting of laser power (4-10 kW), transverse speed (400-800 mm/min) and powder flow rate (15-30 g/min) will be adjusted. Specimens obtained will be prepared for examination under an optical microscope and scanning electron microscope (SEM) along with electron dispersion X-ray spectroscopy (EDS).

Task 2: Determine the effects of processing parameters on the microhardness, metallurgical microstructure of the steel and the mechanical properties of the rail steels introduced by the laser cladding process.

- *Microstructural characterization*

Depending on the function of rail components, their microstructure can be varied across different microstructural types such as pearlite, austenite, and bainite (lesser extent). Hence, their mechanical properties are also varied accordingly due to the close relationship between mechanical property and microstructure. For instance, rails commonly contain pearlitic microstructure since this microstructural type provides the excellent combination of toughness and resistance to wear and rolling fatigue damage, whereas austenitic manganese rail steels are preferred in switches and crossings as these components are subjected to increased impact (dynamic) loading and toughness required. Bainitic microstructural steels can be utilized for both applications owing to the lower carbon content, more readily weldable comparing to the other microstructural types. Therefore, it is crucial to detect any alterations in the microstructure of the steel components after cladded,

since laser cladding process forms a metallurgical bond between the clad and steel substrate, which facilitates the rapid transfer of energy into the substrate. The substrate acts as an active heat sink and thus creating a HAZ beneath the clad. Besides, if there are significant differences in thermal coefficient between the clad and substrate, cracks can be introduced at the interface. By utilising the techniques of optical microscopy and SEM, the metallurgical microstructures of the clad steel components will be characterised to verify the cladding conditions, which optimise the joint with a smaller HAZ, crack-free cladding, and a refined structure.

- *Evaluate the mechanical properties of the cladding material*

Shear punch testing will be used to investigate the correlation of the metallurgical microstructure and the macroscopic mechanical of the clad steel. Shear-punch test curves with the corresponding USS over a transverse cross-section of the clad material will be analysed, so that values of the shear yield strength, ultimate shear strength, corresponding tensile yield strength and ultimate tensile strength will be obtained. Comparisons of shear punch test data would provide a beneficial indication for the strength of laser clad rails. Furthermore, five kgf Vickers indentation will be performed on the rail cross sections, i.e. middle, right and left gauge corner sections, of the clad specimens to acquire estimations of the tribological performance of the deposits in wheel-rail contact.

1.3 Outline of Thesis

A comprehensive outline of the research work accomplished to acquire the aims above is reported in this thesis. The thesis is written in the following chapters:

- **Chapter one**

At first, the chapter introduced the significance of development novel, improved rail materials to reduce the rates of material degradation at wheel rail contacting surfaces and extend maintenance intervals. Due to the inappropriateness of current techniques, and the effectiveness of laser cladding technique in fabricating the applicable functionally graded materials under wheel-rail contact conditions, the need for the establishment of an advanced surface engineering technique for the new functionally graded rail materials was also outlined. Aims of the entire project needed to be achieved have been specified in this chapter; hence, minor tasks will be created accordingly and accomplished to obtain the aims specified.

- **Chapter two**

Chapter 2 is a review of the literature. This chapter reviews in details previously published work on the damage mechanisms in wheel-rail contact, and the ever-increasing demands in rail transportation industry for greater axle loads, durability, lifetime and frequency of train operation. The chapter summarizes the commonly used surface engineering techniques, which have been evolved to develop and manufacture functionally graded materials. The advantages and disadvantages of the laser cladding over conventional surface engineering techniques are also discussed simply and intuitively. Moreover, applications of laser cladding in a multitude of industry fields were covered to validate the efficiency and effectiveness of the technique. In this chapter, a literature review for the applications of laser cladding upon ferrous components was conducted to unveil the capability of laser cladding for advancing railway infrastructure productivity. Finally, published studies related to laser cladding of tribological rail-steel components were discussed, and knowledge gaps were highlighted in this area of research.

- **Chapter Three**

General description of the experimental procedures employed is detailed. The focus of this chapter is on:

- Description of laser cladding rig
- Selection and specifications of cladding and rail substrate materials
- Experimental set-up of the applied heat treatment
- Details on the procedures for the preparation of metallurgical specimens and metallographic characterization
- Specifications of the apparatus used for mechanical characterization.

- **Chapter Four**

In this chapter, the effects of cladding direction, preheating and post heating (PWHT) heat treatment on microstructural and mechanical properties of functionally graded rail materials and their corresponding heat affected zones (HAZ) are presented. Laser cladding of a premium hypereutectoid rail grade with 410L stainless steel powder was conducted using a fibre laser gun with a powder feeder. Two different cladding directions and different heat treatments were investigated.

- **Chapter Five**

The effects of utilizing different cladding materials and heating conditions on the microstructural and mechanical characteristics of laser-cladded hypereutectoid rails which are extensively used in heavy-haul rail systems were investigated in this chapter. Laser cladding of premium hypereutectoid rails with 410L, 420SS, Stellite 6 and Stellite 21 for both single and double deposition was studied under two heating conditions, i.e. preheating only (HTA) and a combination (HTB) of preheating and post weld heat treatment (PWHT). The most suitable cladding material for wheel-rail contact among the considered materials was established by assessing all crucial aspects, i.e. surface quality, hardness, material strength.

- **Chapter Six**

The impacts of preheating conditions and carbon dilution on the microstructural and mechanical properties of laser cladded rails using single and double cladding layers have been investigated for a hypereutectoid steel grade typically used under heavy haul conditions. Dilution of carbon from the hypereutectoid substrate was observed, and its effect on the microstructures of the 410L ferritic stainless-steel deposits was investigated.

- **Chapter Seven**

This chapter reports the influence of laser cladding directions on thermal cycle and the corresponding microstructures and service performance of laser cladded premium hypereutectoid rails. For two separate cladding directions, thermal information of pre-, during and post-laser treatment on three-dimensional 68 kg rail models was simulated via ANSYS platform. Furthermore, microstructural characteristics of the actual rails under the analogous processing conditions were assessed via optical microscopy. Potential mechanical and tribological properties were characterized by Vickers indentation. The unified correlations between the measured

properties and observed microstructural features were acquired. The reasons for the formation of martensite renowned for great cracking tendency at certain regions in HAZ were unveiled. Thus future prevention of forming martensite can be achieved.

- **Chapter Eight**

A summary of all the research outcomes is made. These include remarks recapitulated from the published research and their contributions to the railway industry. Furthermore, recommendations for future work are presented in this chapter.

2

Literature Review

This chapter reviews in details previously published work on the damage mechanisms in wheel-rail contact, and the ever-increasing demands in rail transportation industry for greater axle loads, durability, lifetime and frequency of train operation. The chapter summarizes the commonly used surface engineering techniques, which have been evolved to develop and manufacture functionally graded materials. The advantages and disadvantages of the laser cladding over conventional surface engineering techniques are also discussed simply and intuitively. Moreover, applications of laser cladding in a multitude of industry fields were covered to validate the efficiency and effectiveness of the technique. In this chapter, a literature review for the applications of laser cladding upon ferrous components was conducted to unveil the capability of laser cladding for advancing railway infrastructure productivity. Finally, published studies related to laser cladding

of tribological rail-steel components were discussed, and knowledge gaps were highlighted in this area of research.

2.1 Deformation and damage of railway due to wheel passages

Australia is one of the most substantial exporters of iron ore and coal to many countries throughout the world. Approximately 360 million tons of iron ore and 135 million tons each of metallurgical and thermal coal were exported according to Australian Bureau of Agricultural and Resource Economics in 2010 [3]. The majority of these minerals is transported long distances from mines to ports, principally by railway systems. Generally, the average annual axle loads for iron ore and coal haulage is in the range of 35-40 tonnes and 28-30 tonnes respectively [4]. These axle loads are significantly greater than typical passenger and freight transportation, whose axle loads are 20-28 tonnes and 25 tonnes respectively. Moreover, the increase of annual mineral haulage rates is rapid in recent years due to the quick development of mines and ports. It is planned to rise from 200 million gross tonnes (MGT) per annum to 300 MGT per annum by 2020 [5]. In order to accommodate the combination of the high axle loads and haulage rates, methods such as utilization of high strength rail materials (rail steel manufacturer's responsibility) and rail maintenance strategies (rail infrastructure operator's responsibility) are currently employed.

Typically, there are two common forms of material degradation in wheel-rail contact, which are wear and rolling contact fatigue occurring in the railhead. The most susceptible rail components under a combination of these degradation modes are switches, crossings and insulated rail joints. If left untreated, harmful plastic deformation and even functional failures of rail materials would take place rapidly. Head checks, spalling, squat defects, etc. are the typical damage mechanisms involved in the functional failures. The rail components, therefore, incur greater financial burden due to their higher maintenance costs associated with repairing or replacing, rebuilding tracks and

train service interruptions [6, 7]. Surface engineering techniques, particularly laser cladding, offer a promising solution to cut down the costs by providing the necessary material characteristics to resist these damage mechanisms.

2.1.1 Wear in rails

Wear is the resulting phenomena of the interaction of rail and wheel, which is commonly classified in seven categories, i.e. adhesive wear, abrasive wear, delamination wear, tribochemical wear, fretting wear, surface fatigue wear, and impact wear [2].

Abrasive wear is generated when a hard surface slide and roll under pressure on a soft surface causing loss of material by penetration, as shown in Figure 2-1. The unique characteristic of this wear type is that there is no tiny debris that may cause more severe damages [2, 8]. This type of wear is divided into four different mechanisms, i.e. microplowing, microcuttings, microcracks and microfatigue, as shown in Figure 2-2. The microplowing mechanism occurs primarily on the soft surfaces and causes strains around the wear tracks. In this mechanism, wear tracks without the loss of materials are found and extruded materials are regularly left on the both sides of the created wear tracks. The microcutting mechanism occurs when there is an increase in the hardness of the material. A greater increase in hardness will transfer fine cutting mechanism to fine crack mechanism. In the microcrack mechanism, cracks are formed in the wear tracks and some particles are removed. The particles gathered in the constantly moving contact surface would induce a microfatigue mechanism. The critical factors in the abrasive wear are instability of mechanical properties, hardening rate, ductility and strain distribution [9-12].



Figure 2-1 Abrasive wear (scratches) on rails. [2]

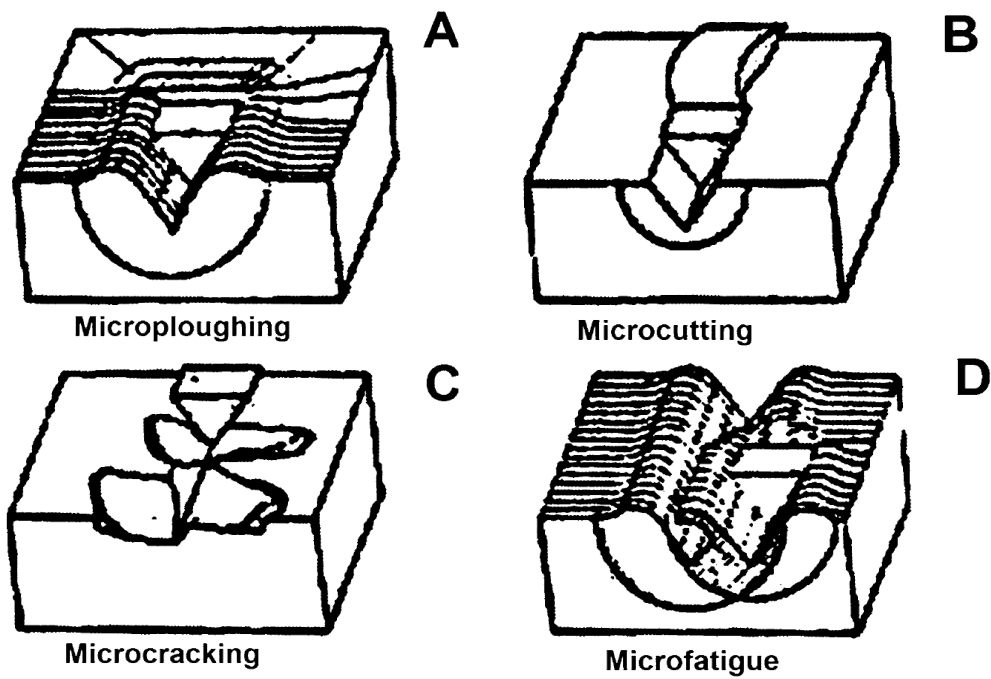


Figure 2-2 Types of abrasive wear: A. Microploughing, B. Microcutting, C. Microcracking, D. Microfatigue. [2]

Adhesive wear occurs when the two contacting surfaces have a local slip that causes a material transfer from one surface to the other, as shown in Figure 2-3 [2]. In other words, the non-homogeneous surfaces of engineering parts produced by the error tolerance in manufacturing processes create scattered points with high stress concentration. As a result, plastic deformation was occurred in the scattered points on the surface. Depending on the wear rate and the resulting wear particle size, adhesive wear mechanism is classified into two types, i.e. moderate and severe. The moderate form is commonly found in straight lines and gentle arches and the severe form is found in dry flanges. [33,34] The propensity of forming material adhesion is dependent on the material properties of the contacting components, loading conditions, and contacting surface characteristics, i.e. pollution and roughness [2]. The wear rate due to adhesive phenomenon can be calculated as follows:

$$W_{ad} = \frac{V}{L} = K \frac{F_N}{H} \quad (2.1)$$

Where W_{ad} is wear rate, K is coefficient of wear. V is worn volume, L is sliding distance, F_N is normal load and H is the hardness of the softer material.

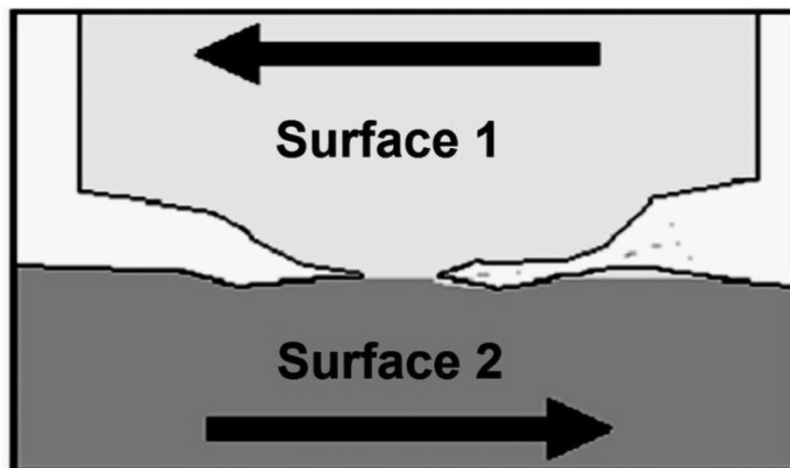


Figure 2-3 Mechanism of Adhesive wear. [2]

Delamination wear occurs when there is material separation in the contacting surfaces. Delamination wear is also reported to cause wear in microscopic level, as shown in Figure 2-4. By preventing the plastic deformed layer, the wear rate can be decreased significantly. It is reported that there are three stages in the mechanism of delamination wear, i.e. plastic deformation, formation of cracks, and crack propagation. As the contacting surfaces are sliding against each other due to periodic loading, plastic shear deformation is accumulated causing cracks at the surface and subsurface. Due to the continuous influence of the applied cyclic loadings, the resulting cracks expand and connect to neighboring cracks and voids. For surfaces with low strength, these cracks penetrate the surface from subsurface levels and the resulting wear particles appear in the form of thin and long sheets. In the contact between a hard-metallic material with high Young's modulus and a softer metallic material with lower Young's modulus, the deformation from the softer surface is drawn towards the interior of the contacting surfaces. As a result, work hardening phenomenon occurred under the layer of softer material. [2, 10, 11, 13]



Figure 2-4 Delamination wear of wheels. [2]

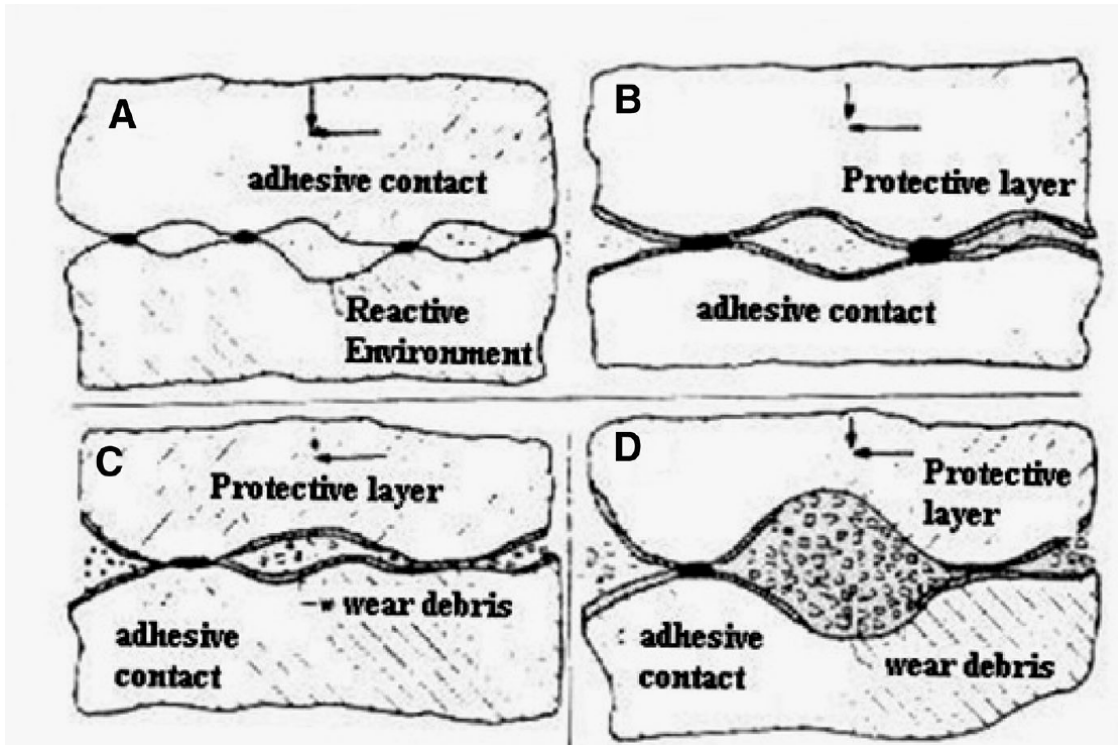


Figure 2-5 Tribochemical wear mechanism. [2]

Tribochemical wear occurs when the abrasive process happens simultaneously with formation and separation of the environmental reactions, i.e. oxide film, at the interface, as shown in Figure 2-5. The action of the stresses in the wear mechanism would remove the oxide film and clean the contact surface. This contact surface will be oxidized in the next half loading cycle. The tribochemical wear mechanism is a continuous separation process which is greatly influenced by the surface properties of the contacting surfaces, i.e. flexibility, material strength and adhesion. Tribochemical reactions producing harder protective layers can lower adhesive wear, however they can increase abrasive wear. Greater chemical activity of the involving materials would promote the development of thicker and harder protective layers. As a result, lower adhesive wear is achieved. The degree of adhesive wear reduction depends on the slip severity, contact pressure, temperature and surface quality. The use of lubricants and additives can reduce the friction coefficients between contacting surfaces and thus mitigate adhesive wear. However, the presence of lubricants and additives can create several surface layers and promote a sudden material deterioration owing to the increasing risk of adhesion.

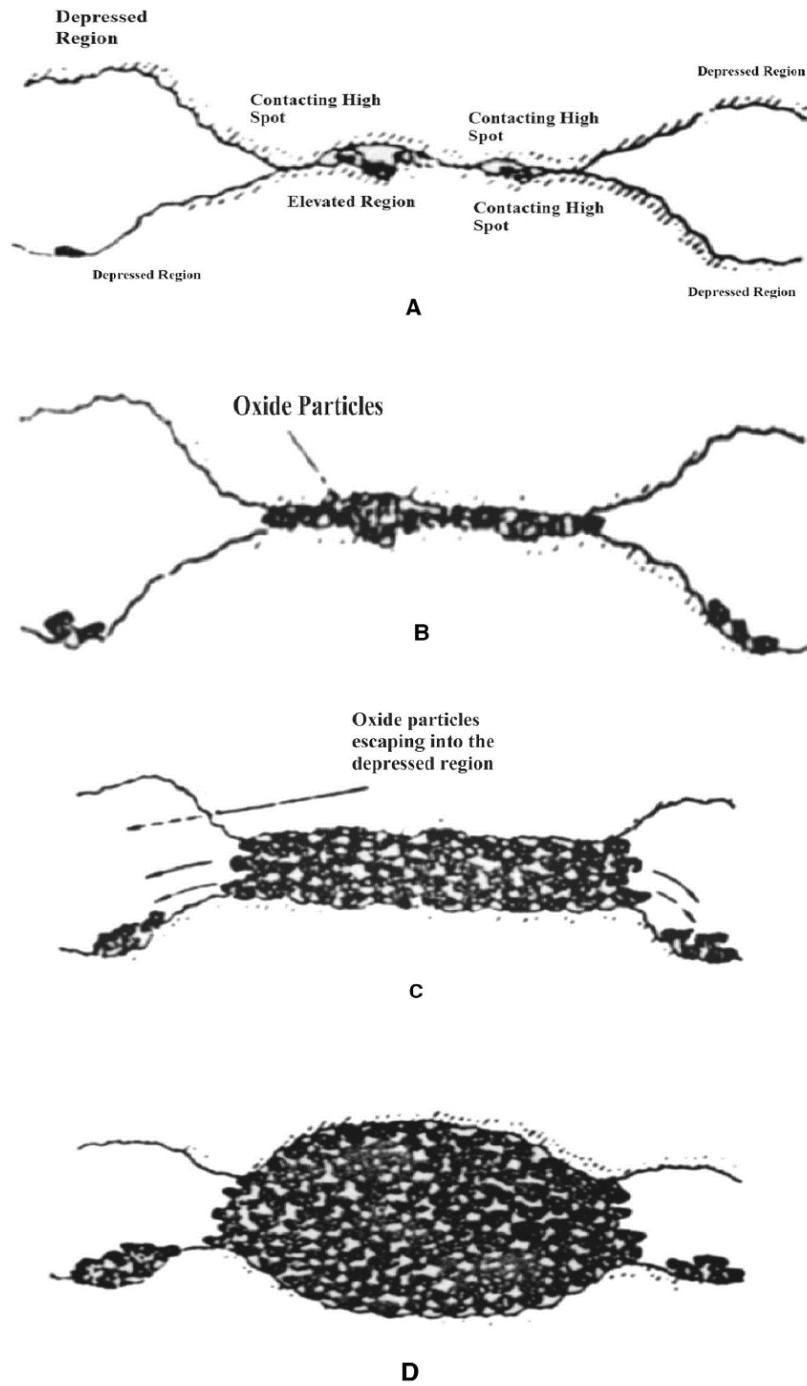


Figure 2-6 Fretting wear stages: A. Wear particles accumulated between contacting high spots, B. Growth in size of the accumulated particles, C. Transfer of the accumulated particles to the neighboring regions, D. Formation of curved zone caused by the intense wear process. [2]

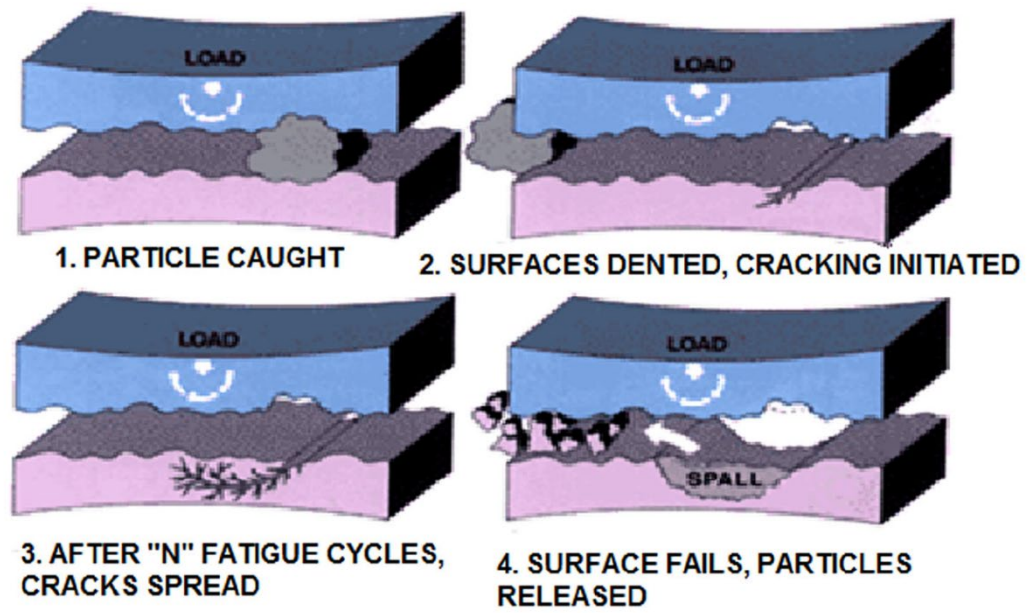


Figure 2-7 Stages of surface fatigue mechanism. [2]

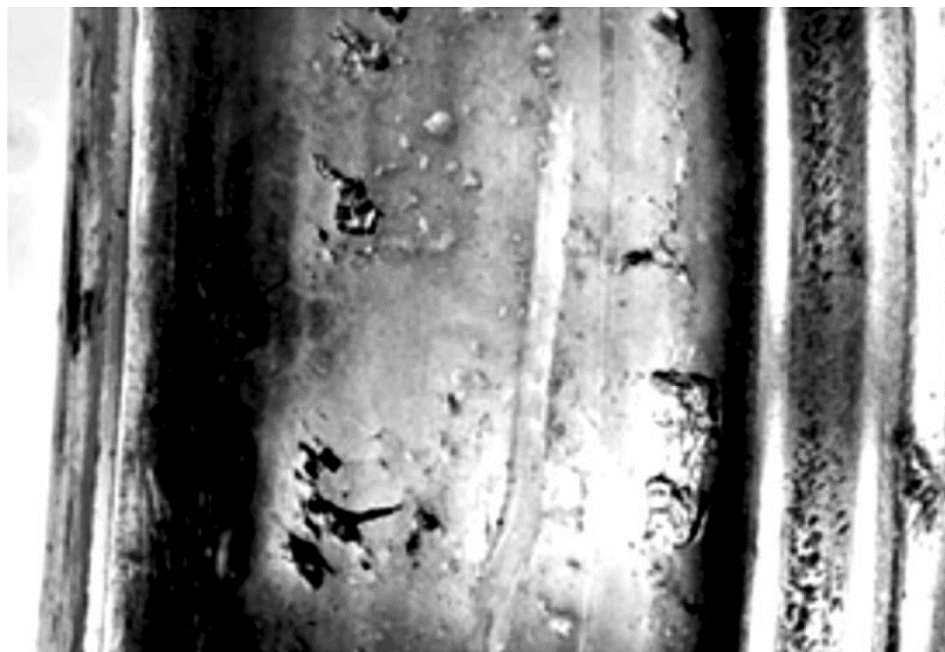


Figure 2-8 Wheel with surface fatigue mechanism. [2]

Fretting wear occurs when two contacting surfaces are subjected to tangential and oscillating movements under the applied stresses, as shown in Figure 2-6. Corrosion and oxidation are commonly detected with this wear type. There are four stages in the fretting wear mechanism, i.e. adhesive wear, tribochemical wear, fatigue surface wear, abrasive wear. Factors affecting the fretting wear are the cyclic number, the motion range, force, frequency, temperature, hardness, lubrication and atmospheric environment. [14, 15]

Surface fatigue wear occurs when the contacting surfaces are in sliding contact and under fluctuating stresses, as shown in Figure 2-7. In this wear mechanism, cyclic loadings cause the formation of cracks and material separation from the contacting surfaces, as shown in Figure 2-8. Smooth lines and arches are common indications of this type of wear, even with lubrication. [14, 15]

Impact wear occurs when the contacting surfaces are under high stress concentration during a short period of time. Main factors influencing this type of wear are materials, contact stress range, impact speed and type of loadings. [10]



Figure 2-9 Train derailment in the town of Gainford, Alberta, Canada owing to surface defects.

In the railway industry, wear is the most critical issues. If remained untreated, catastrophic failures would happen rapidly. On October 19th, 2013, in the town of Gainford, Alberta, Canada, a freight train derailed and caused chaos, as shown in Figure 2-9. As this train had thirteen of its carriages containing crude oil and LPG (liquid petroleum gas), 106 homes were evacuated with one home damaged. A large section of the track, approximately 185m, was destroyed and upon investigation it was found that the high rail of this curve (approximately 550m radius) broke into several pieces as the rail was near its wear limits, displayed heavy surface fatigue and contained many transverse defects.

2.1.2 Rolling Contact Fatigue in rails

Development of rolling contact fatigue (RCF) is commonly seen in most railway systems. It refers to a number of rail defects due to the impacts of excessive shear stresses at the wheel-rail interface. If not inspected and treated properly, catastrophic failures will occur, e.g. The derailment in Maryland as shown in Figure 2-10. [1]

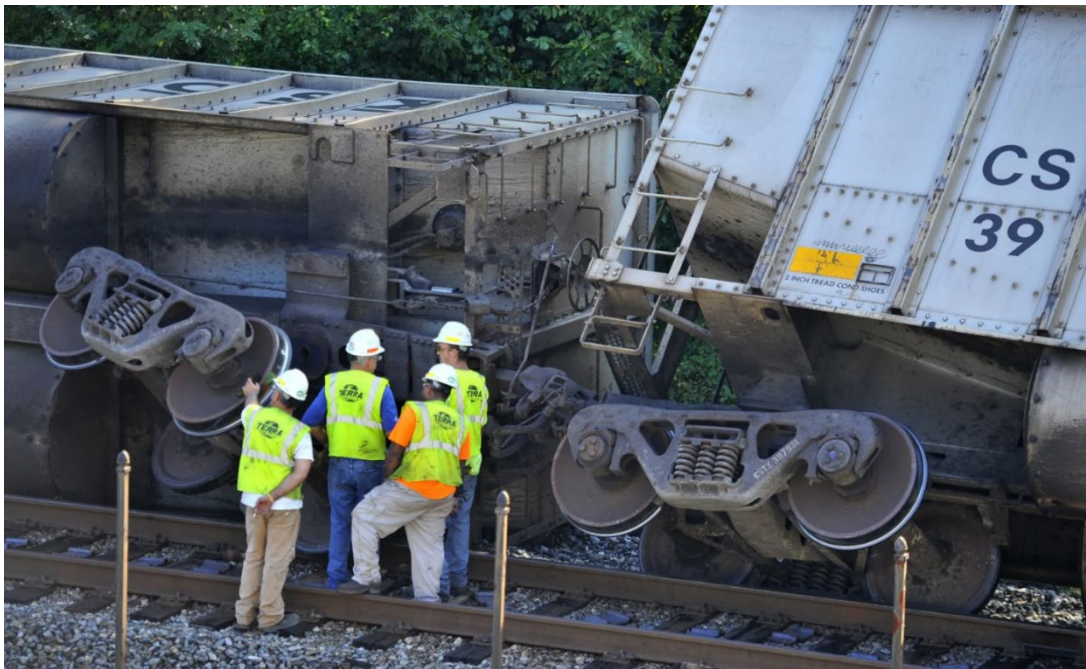


Figure 2-10 Train Derailment in Ellicott city, Maryland. [1]

Depending on the crack initiation location, RCF defects can be classified into two types, i.e. surface and subsurface, which are detailed as follows:

2.1.2.1 Surface Defects

i. Gauge Corner Checking

Gauge corner checking is a decaying condition of rail surfaces in the sharp curves of the high rails, shallower curves and tangent track. This type of defect contains cracks that can be diagnosed with “fish scales” appearance on the rail surfaces. The cracks are found to spread evenly across the rail head and initiate at or in the vicinity of rail surface at intervals of 2 - 5 mm along the rail track. Depth of the cracks are typically about 2 – 5 mm and the downward penetration angle is approximately $10^\circ - 30^\circ$ to the rail surface, as shown in Figures 2-11 and 2-12. At the final stage of this defect type, the cracks break into small “wedges or spalls”. Figures 2-13, 2-14 and 2-15 show respectively initial, intermediate and severe stages of gauge corner checking.

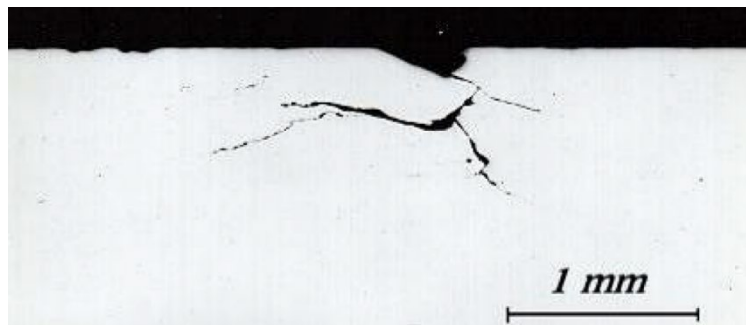


Figure 2-11 Cracks and spalls in initial stages develop in a rail transverse section. [1]

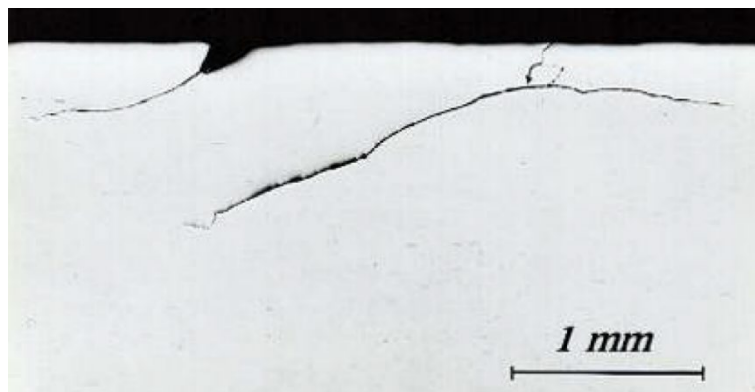


Figure 2-12 Cracks and spalls in initial stages develop in a rail longitudinal section. The crack propagates into the railhead and then level out. [1]

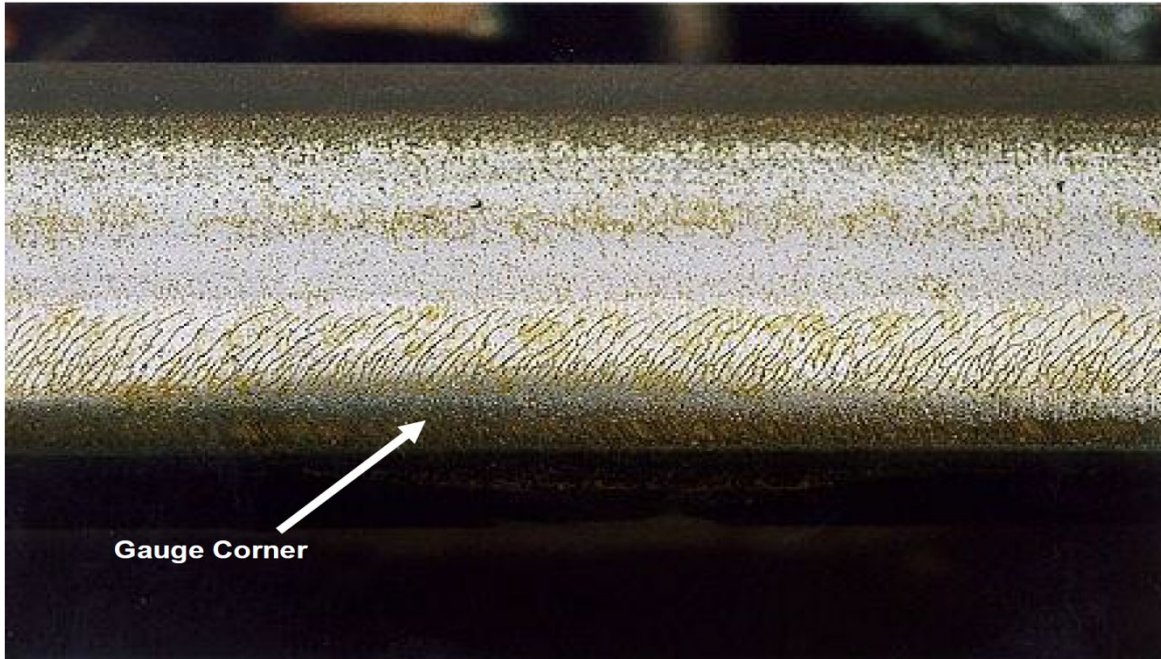


Figure 2-13 Initial stage of gauge corner checking cracks. [1]

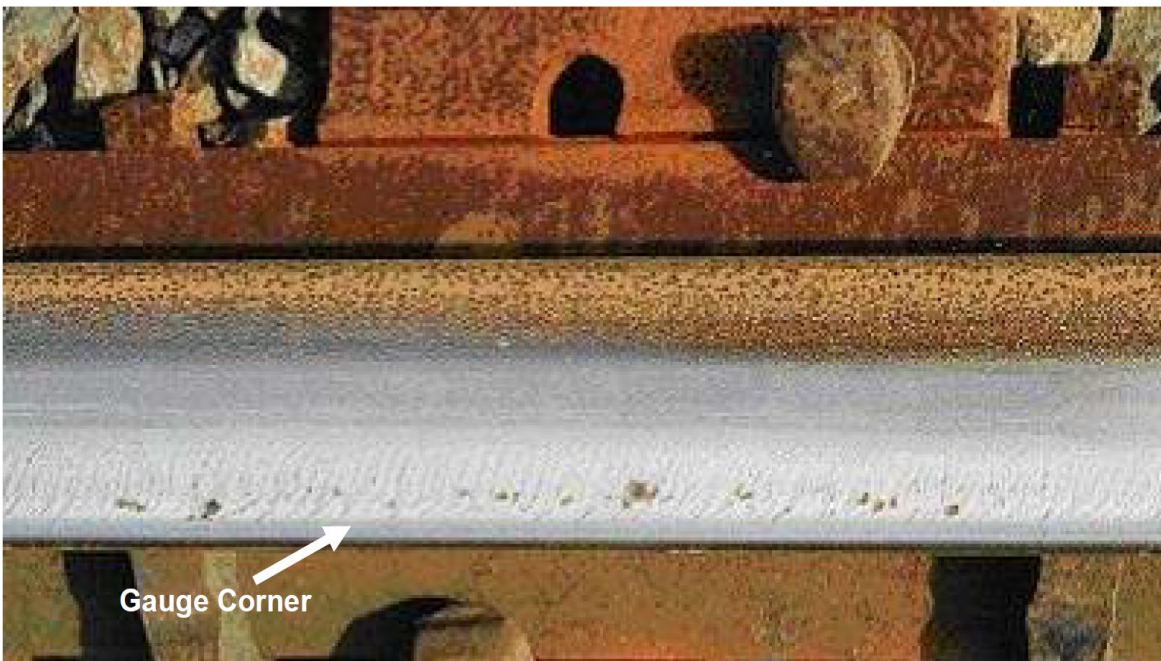


Figure 2-14 Intermediate stage of gauge corner checking cracks and spalls. [1]

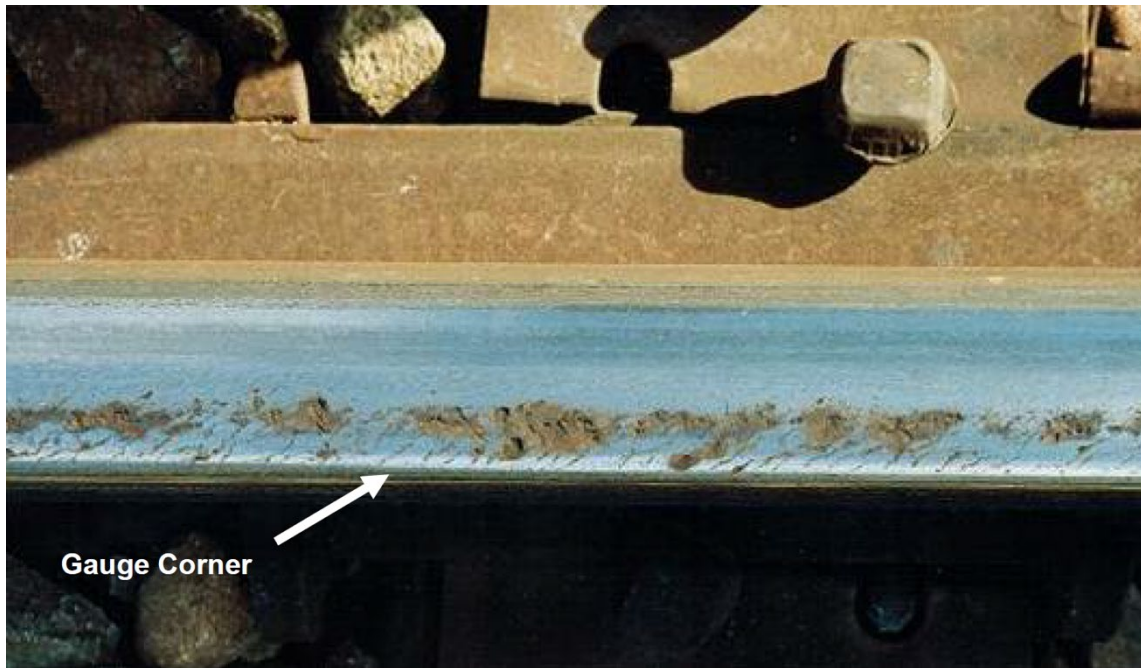


Figure 2-15 Severe stage of gauge corner checking cracks and spalls. [1]

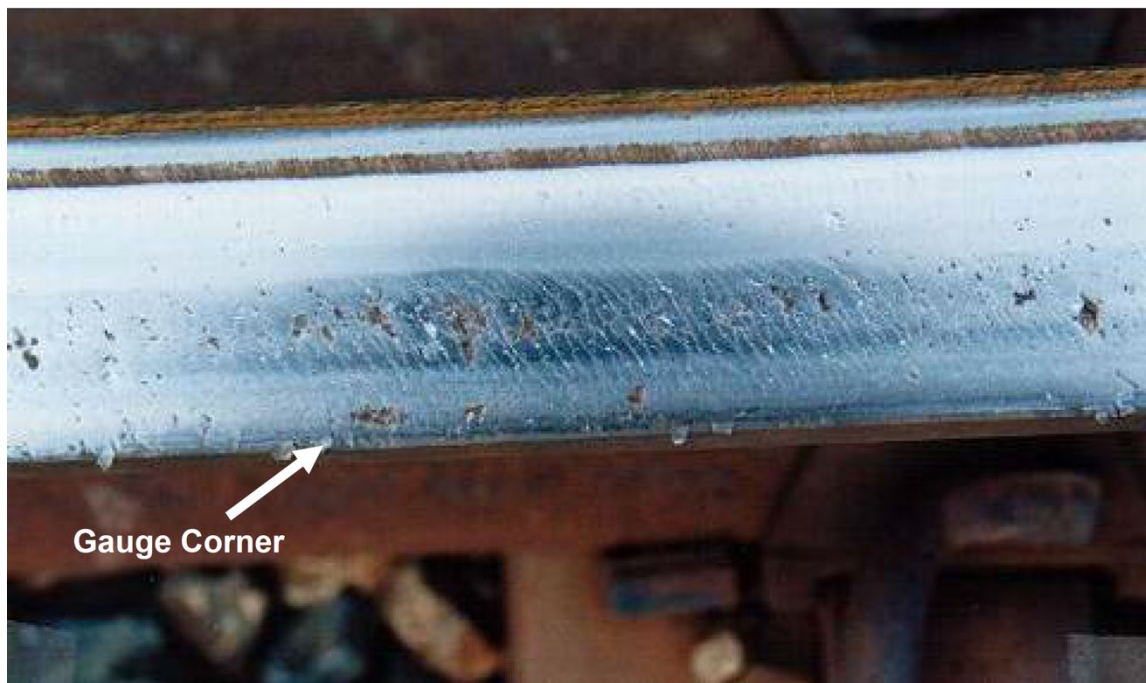


Figure 2-16 Running surface checking cracks with minor spalling. [1]

ii. Running Surface Checking

Running surface checking is another type of RCF defect, which is also known as flaking. This surface decaying condition occurs on the running surface of the low and high rails. During the first stage, the rail surface is observed to have cracks with a “mosaic/snakeskin” pattern. Similar to the gauge corner checking, “spalls” are produced when the cracks develop to the latter stages, as shown in Figure 2-16. It is reported that the “spalls” can be measured up to 10 - 15 mm in width and 3 mm in depth.

2.1.2.2 Subsurface Defects

i. Shelling

Shelling refers to defects below the rail surface which occur typically at 2 - 8 mm below the gauge corner of high rails in curved tracks. Similar to the defects of gauge corner checking and running surface checking, this type of subsurface defects is also caused by excessive shear stresses at the contacting regions, however, shelling is less frequently occurring compared to them. Initially, shelling defects can be noticed as dark spots in the gauge corners. Figures 2-17, 2-18 and 2-19 show respectively initial, intermediate and severe stages of shelling.

In the latter stages, shelling cracks grow based on the rail shape on the gauge corner with a propagation angle of 10° - 30° to the rail surface. The cracks can either develop into shells or transverse defects. If remained undetected, these defects can result in a derailment. It is worth noting that not all transverse defects are directly initiated from an existing shelling defect, but from inclusions in the rail materials. Due to the internal characteristics of the transverse defects, as shown in Figure 2-20, only ultrasonic rail inspection should be used to detect the transverse defects, rather than normal visual inspection, and the inspection should be done on a regular basis to avoid catastrophic failures.



Figure 2-17 Initial stage of shell formation with presence of dark spots. [1]

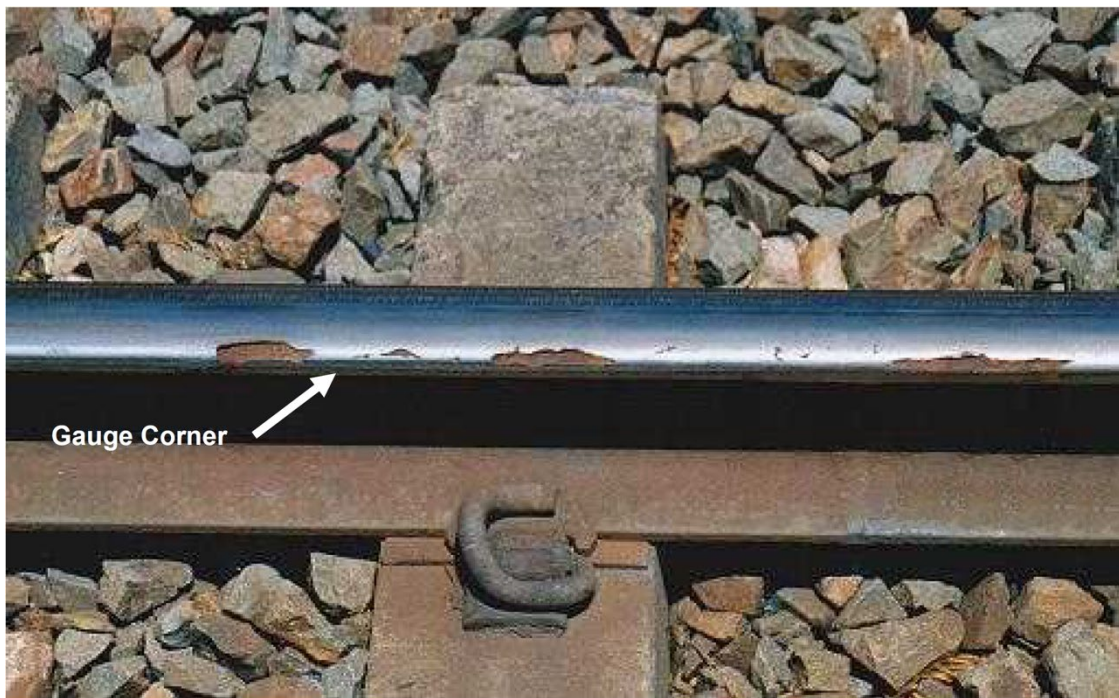


Figure 2-18 Intermediate stage of shell formation. [1]

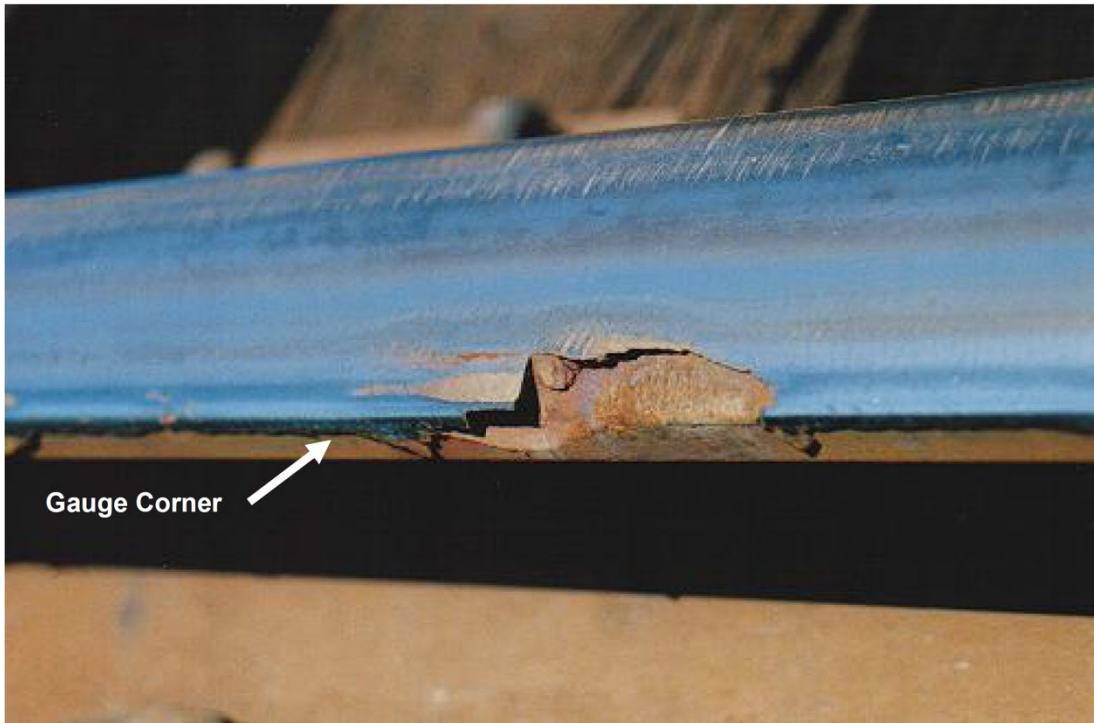


Figure 2-19 Severe stage of shell formation. [1]

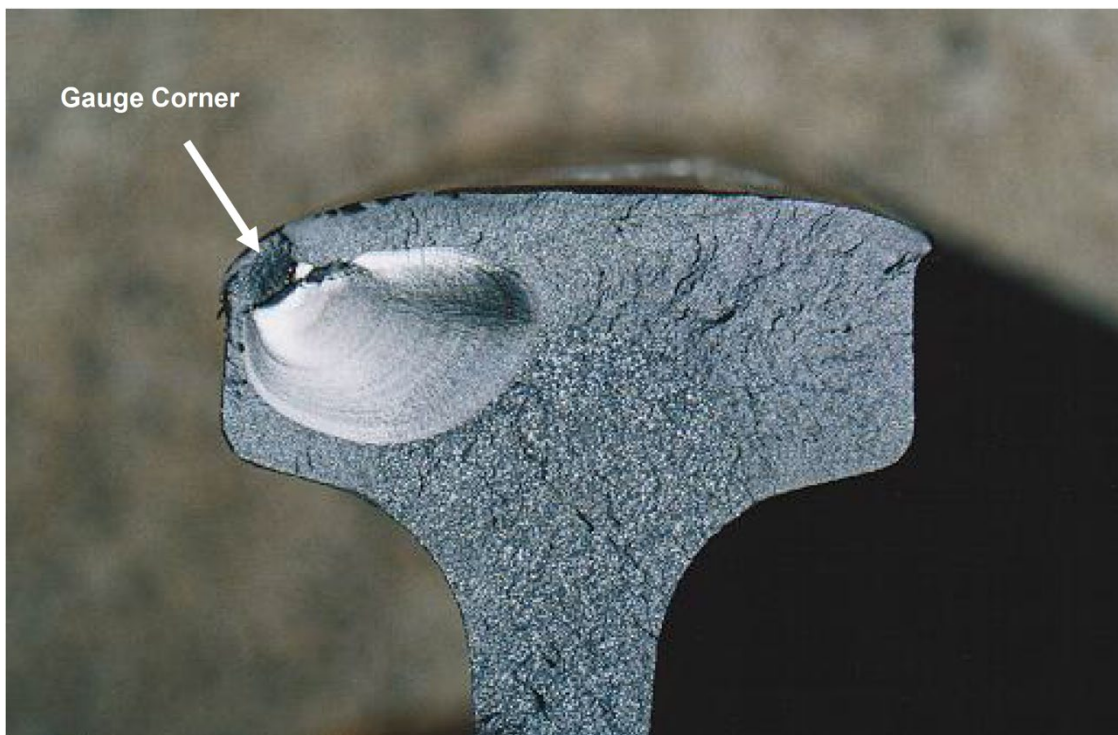


Figure 2-20 Small transverse defect developed from shelling. [1]

ii. Squat Defects

Squats are another common form of subsurface defects. Squat defects are subsurface laminations initiated from small surface cracks which can grow downwards to the rail feet at an angle of 20° - 30° to the rail surface. As approaching the depth of 4 - 6 mm, the cracks change its major propagation plane from rail-vertical to rail-horizontal plane, as shown in Figure 2-21. Two main types of squats are running surface squats and gauge corner squats. Running surface squats are generated by combined effects of thermal traction and wheel slip, as a result, this squat type can occur any place in the contact patch. Gauge corner squats are initiated by previously-formed cracks, particularly cracks formed by surface RCF defects, thus the squats are often found near the gauge corner, on the curves of high rails and in turnouts. Figures 2-22, 2-23 and 2-24 show respectively initial, intermediate and severe stages of running surface squats. Figures 2-25, 2-26 and 2-27 show respectively initial, intermediate and severe stages of gauge corner squats.

Squats can be spotted by a darkened area on the rail surface, which is attributed to surface depression and reduction in polishing by train wheels. In running surface squats, shape of a double-sided kidney is commonly detected. However, some irregular shapes can also be found. Some triangular surface cracks may be found in both gauge corner and running surface squats. Shape of gauge corner squats will be changed after a rail-grinding, as shown in Figure 2-28.

Confusions between squats and wheelburn defects can be avoided by recognizing the primary different features. Squats are established via several stages over a long period of time, whereas wheelburns is an instant and sudden defect after an incident of wheel slip. Moreover, wheelburns do leave matching defects on the opposite rail, whereas squats do not. Figure 2-29 shows an image of typical running surface squats initiated from wheelburn.

Squats occur likely in curved track with radius of 800-1600m, specifically in the transitions of sharp curves and on the high rail in the curved track. Squats may also appear in unacted rails in turnouts, both passenger and/or freight lines, all types of sleepers and rail and both Standard Carbon (SC) and Head Hardened (HH) rails, as shown in Figures 2-30 and 2-31. Squats are not found in tunnels unless there is water present. The actual length and depth of the subsurface squats can be easily determined using an ultrasonic depth gauge, as shown in Figure 2-32.

Generally, current repairing methods for rail defects are: 1. Rail replacement, 2. Rail-grinding, 3. Arc welding. The rail replacement is one of the most expensive repairing methods which involves removing the damaged rail sections. The rail-grinding removes a large amount of rail materials which is approximately 6 mm in thickness. During rail-grinding operation, all defect traces ought to be removed, or else residual stress will be increased. Arc welding is a sophisticated repairing process. Therefore, if not executed correctly, this can induce harmful transverse defects and derailments.



Figure 2-21 Subsurface cracking associated with squat defects. [1]



Figure 2-22 Initial stage of running surface squat. [1]



Figure 2-23 Intermediate stage of running surface squat. [1]



Figure 2-24 Severe stage of running surface squat. [1]

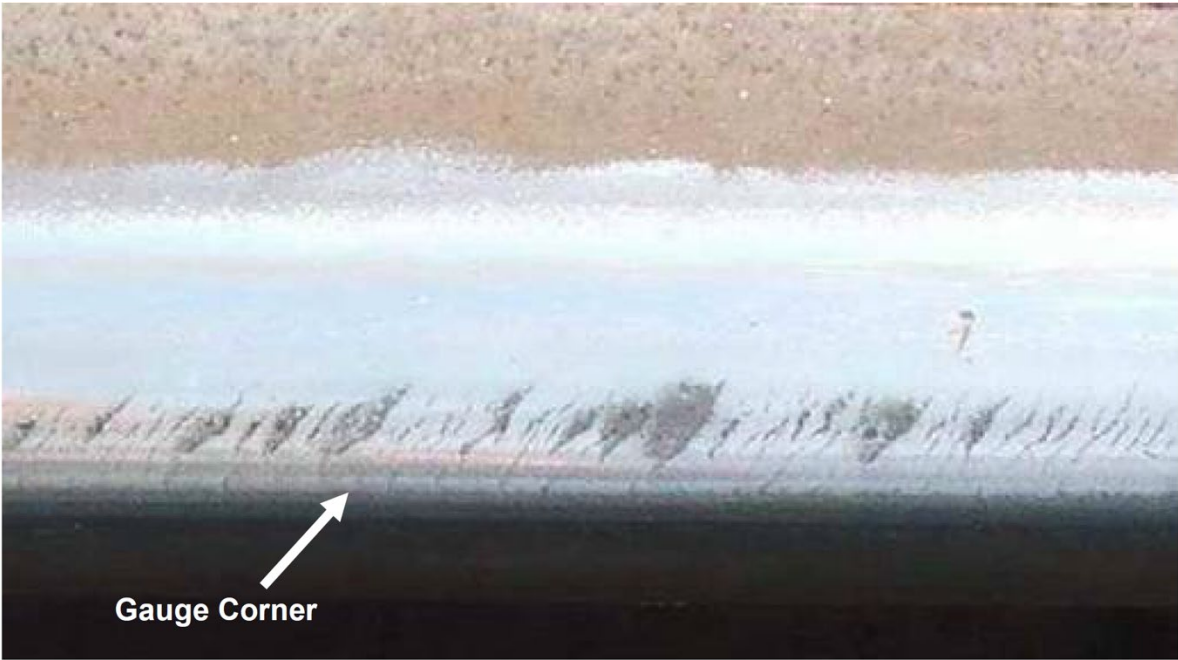


Figure 2-25 Initial stage of squats initiated by gauge corner checking. [1]



Figure 2-26 Intermediate stage of squats initiated by gauge corner checking. [1]



Figure 2-27 Severe stage of squats initiated by gauge corner checking. [1]

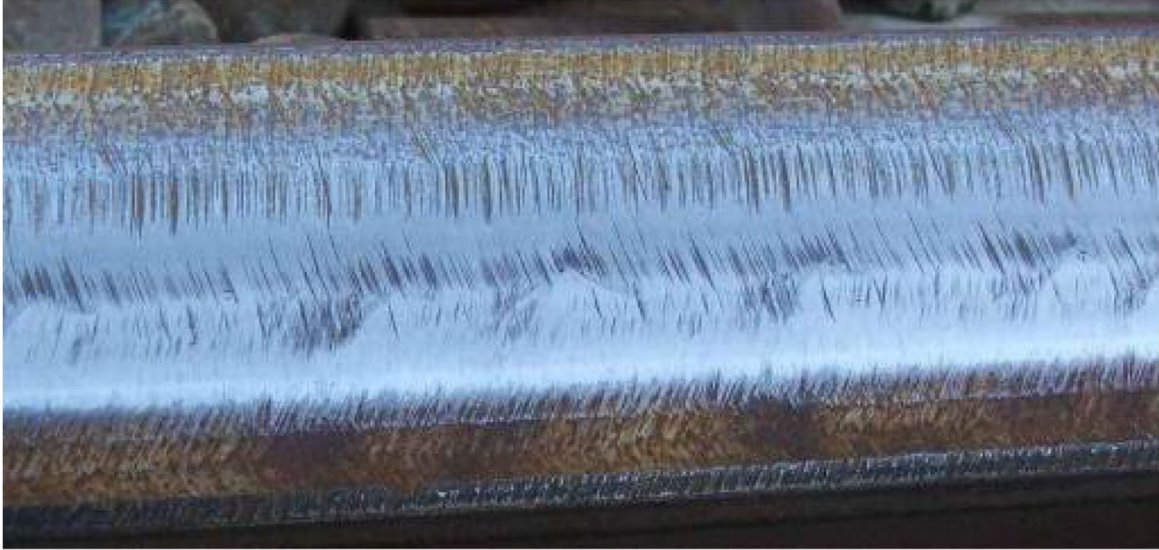


Figure 2-28 Surface after grinding to remove small – medium squats initiated by gauge corner checking. [1]



Figure 2-29 Running surface squats initiated from wheelslip. [1]



Figure 2-30 Squats in switches. [1]



Figure 2-31 Squats in turnout. [1]



Figure 2-32 Inspection to determine the length and depth of subsurface squat cracks using an ultrasonic depth gauge. [1]

Besides using the aforementioned maintenance methods to accommodate the need for elevated axle loads and annual haulage rates, application of surface engineering techniques is also considered at the special trackwork in order to alleviate the workload of ensuring the safety of rail network of both the rail steel manufacturer and rail infrastructure operator. The primary functions of surface engineering are to either coat or repair, refurbish the valuable components. The coating is essential to deposit a thin layer of material addition onto the surface of a chosen substrate. The surface properties of the substrate thereby become those of the material addition. Formation of a functionally graded material with properties commonly unachievable by employing the substrate only is established. The deposited layer can offer superior wear and corrosion resistance and other desired surface properties depending on the selected chemical composition whereas the substrate material withstands all primary forces. For repair/refurbishment, surface engineering techniques can retrieve valuable components with damages during operation or errors in design or machining process.

2.2 Surface engineering techniques for enhancing the tribological and mechanical properties of rail steels.

Common surface engineering techniques are shielded metal arc (SMA) welding, submerged arc (SA) welding, and metal inert gas (MIG) welding, which have been widely used to repair and recondition the damaged regions or components [16-18]. Other current techniques, such as tungsten inert gas (TIG) welding, plasma spraying welding, high-velocity oxy-fuel (HVOF) welding, plasma transferred arc welding, and laser cladding, have also been considered as alternatives recently. However, each the technique possesses its limitation. For the sake of comparison, a table simplifying the advantages and disadvantages of the aforementioned techniques has been constructed in Table 1.

Table 2-1 Comparison of numerous surface engineering techniques.

	Laser Cladding	Shield Metal Arc	Metal Inert Gas	Submerged Arc	Tungsten Inert Gas	Plasma Spraying	Flame	High Vel Oxy-Fuel	Plasma Transferred Arc
Thickness (mm)	0.2 - 2	1.6 - 10	1 - 6	2 - 10	0.5 - 3	0.1 - 2	0.8 - 2	0.3 - 1.5	1 - 5
Deposition rate (kg/h)	0.2 - 7	0.5 - 2.5	2.3 - 11	5 - 25	0.5 - 3.5	0.5 - 7	0.45 - 2.7	1 - 5	2.5 - 6.5
Distortion	Low	Medium	Medium	High	High	Low	High	Low	Medium
Precision	High	Low	Low	Low	Medium	Medium	Low	Low	Medium
Dilution (%)	1 - 5	15 - 25	15 - 20	10 - 50	10 - 20	5 - 30	1 - 10	Low	Medium
Integrity	High	High	High	High	Medium	Low	Medium	Medium	Medium

After analyzing the table thoroughly, only four techniques are considered dominant to the rest by achieving concurrently multiple desired comparative aspects, such as low/medium distortion, high/medium precision, high/medium surface integrity, high/medium deposition rate and low/medium dilution. They are Laser cladding, Plasma spraying, HVOF and Plasma transferred arc. Further comparison among the best four techniques shows that laser cladding is the most competitive.

HVOF is mainly applicable to coat a broad area with a maximal feasible thickness of 1.5mm. Low cost compared to the conventional arc weld, low porosity (<1%), and excellent adhesion are major benefits for applying such technique. However, HVOF can be extremely complicated, because many processing variables affect the properties and microstructure of HVOF coatings. The process of HVOF must be performed in a specialized spraying precinct equipped with suitable sound attenuation and dust extraction facilities, thus application of HVOF on field is virtually infeasible. Laser cladding is preferred as small, discrete regions need to be cladded since the laser beam can be manipulated easily, lower heat input produces less distortion and post-treatment required, and good surface integrity can be obtained.

Plasma spraying is primarily employed to gain wear and corrosion protection layers on top of the metal substrates. Great flexibility, low distortion of substrates, excellent suitability for low melting temperature substrates like Zinc and quick coating for wide areas with minimal dilution from the substrate are the technique's advantages. The problems being that plasma spraying presents high porosity of 1% or above, chemical heterogeneity and weak adhesion to substrate if the difference in thermal expansion coefficients between material addition and substrate are significant. Laser cladding is competitive as free porosity, fine surface integrity and homogeneous coating layers are needed.

Plasma transferred arc offers high clad thickness and large coverage area with a single pass and produces a sound, homogeneous bond with the substrate. However, the technique suffers from large heat affected zones (HAZ), greater distortion and dilution due to its high heat input, especially for application of small components.

Owing to the special characteristics of the laser, laser cladding is capable of delivering sound metallurgical bonds with the highest precision (provided suitable processing parameters are used), minimal dilution and distortion of the treated components. Technically, laser cladding is a melting process in which the laser beam is used to fuse an alloy addition onto a substrate. In contrast to other surface engineering techniques, the aim of laser cladding is to melt merely a thin layer of the substrate together with as much of the alloy addition as possible. Surface properties can be tailored to a given application by selecting an alloy with excellent wear, erosion, oxidation or corrosion properties [19].

2.3 Laser cladding: an interdisciplinary technology

Laser cladding has gained an increasing reputation in recent years due to its peculiar features. A multitude of industrial fields such as aerospace, automotive, marine, defence, etc. have widely applied the technology for their material processing like metallic coating, valuable parts repair/refurbishment, prototyping and even low volume manufacturing. Companies within these fields conducted research projects on their own budgets, which were even prior to academic research [20].

After the invention of the laser in the 1960s [21], various material processing techniques were established including laser cladding. The development of high power gas lasers enhanced the technical potentiality of laser cladding, so that, in late 1970s, Rockwell International

Corporation[22] utilized a pre-placed laser cladding technique to examine its appropriateness in coating dense ceramic layers to metallic substrates. Meanwhile, various research groups attempted to improve efficiency and effectiveness of the technique by developing devices and systems. The research conducted by William M. Steen and Vijitha Weerasinghe made a great stride in the improvement of laser cladding technology[23, 24]. They presented a novel system of cladding material delivery using powder injection and demonstrated the viability of the developed system via many publications [25-27]. In the 1980s, the research group of Jyoti Mazumber at the University of Illinois also contributed crucial elemental principles to the field. They established different mathematical models and experimental work to study the mechanism of the technique, and the cladability between ceramic cladding materials and metallic substrates. The improvement in tribological and physical properties of the substrates were also their interests [28-32]. Furthermore, the 1980s was the decade of rapid development of laser cladding technology. Innovative methods for handling substrate and depositing material addition, and improved devices such as dynamic powder feeders, hemispherical reflecting devices, etc. facilitated the growth of laser cladding's applications in various industries. Particularly, those are the applications for extra wear and corrosion resistance of substrate components [33-35]. In 1981, Rolls Royce executed the first industrial application to laser-clad engine components of the RB-211 jet, which was the Nimonic turbine blade interlock shrouds. Then, Pratt and Whitney hard-faced their nickel-base alloy turbines of JT engines in 1983[36]. By realizing the benefits of the technique, many other manufacturers in the aerospace industry such as Allison, General Electric, etc. followed and started to adopt the technique into their manufacturing process. Few companies such as Avco Everett Metalworking Lasers Inc and United Technologies Industrial Laser Inc were established in the 1980s to specialize only in metallic coating and repair using laser cladding technique. This emphasized the demands of industry for the technique [20]. Automotive industry began employing the technique in the 1990s by Fiat, Toyota, Mercedes Benz, etc. to develop the engine valve seats and cylinder bores using laser cladding process [37, 38]. Meanwhile, published papers and reports relating to the employment of laser cladding to investigate a wide range of substrates and cladding materials were boosted and continued to increase in quantity until now. Almost all core materials

in aerospace, automotive, marine, defence, medical and many other industries were clad with different crucial alloys and composites to prolong their service lives. The cladding materials are commonly nickel based, cobalt based, chromium based, aluminium based, magnesium based, copper based, bronze, niobium-based, iron-based amorphous alloys, and ceramic-metal composites. Recently, bioactive bioceramic materials were used for medical applications instead of the above alloys. The substrate materials are diverse and heavily rely on specific criteria of each application. Titanium alloys, Brass, Nickel, Magnesium alloys, Aluminium alloys, etc. were typical substrate materials found in the literature. Particularly, steel was the most common substrate owing to its popularity across numerous industrial sectors.

2.4 Functional graded surface upon steel utilizing laser cladding

Steel is the most widely used engineering material in marine, nuclear power and fossil power plants, transportation, chemical processing, petroleum production and refining, pipelines, mining, construction and metal-processing equipment. The primary reasons for the large demands for steels are due to its low costs of manufacturing and processing, its abundant raw materials in nature and its unique range of mechanical properties. Nevertheless, the corrosion costs are multi-billion dollars on an annual basis. Components made of steel are also susceptible to wear and fatigue. By introducing the technique of laser cladding, Conde et al. [39] described the process of acquiring a Nickel-based hard facing alloy, which consists of a clad layer of Ni-Cr-B-Si and a substrate of carbon steel (C-Mn steel) with a high power diode laser (HPDL). The surface hardness of the clad layers (500-700 HV) was significantly higher than that of the base steel (150 HV). The surface hardness increased if hard phases such as Ni_3B and $Cr_{23}C_6$ were present. The microstructure of the coatings is complicated and varied accordingly to the selected composition of the power fed. Toshiyuki et al. [40] conducted a research on fatigue performance of laser-clad alloy steel and reported 2-5 times improvement compared to the un-clad specimens. Dahotre et al. [41] explored deposition of Fe-based amorphous/glassy layer on a plain carbon (AISI 1010).

A significant enhancement to corrosion resistance was revealed via applying potentiodynamic polarization to a 3.56 wt.% NaCl solution.

Expansive range of cladding materials has been attempted on steel substrates by many research groups in the search for excellent combinations. For Cobalt, alloy addition, Stellites are prevalent owing to attractive mechanical, thermal and chemical properties at elevated temperature. As laser clad, Stellites exhibited dendritic microstructure growing in a relatively perpendicular plane to the surface. Within the perpendicular plane, dendrites may develop in various directions and sizes, which primarily depend on the heat input and corresponding solidification rate. Thus, the less heat input is, the finer the microstructure of clad layer becomes and the smaller volume fraction of tiny interdendritic carbides generates. Advances in the performance of the clad samples were reported and attributed to improvements in microstructure comparing to traditional techniques. Moreover, the performance could be further enhanced by including Nitrates, Borides, and Carbides into Stellites since they formed particulate-reinforced metal matrix composite at the cladding surface. The linear correlation between hardness and carbides' volume fraction were achieved. [19, 42-53]

For Nickel based alloy addition, Tuominen et al. [54] demonstrated the possibility of laser cladding of a preplaced high-velocity oxyfuel sprayed (HVOF) layer with high Nickel-Chromium content (53.3% Cr, 42.5% Ni, 2.5% Mo, 0.5% B) onto mild steel substrate (Fe37) using Nd:YAG laser. At the appropriate processing parameters, sound, nonporous, crack-free bonding was achieved with minimal dilution between the cladding layer and the substrate. Formation of a dense oxide layer on top of the homogeneous clad was reported as well. Likewise, many other research groups such as Singh et al. [55], Wetzig et al. [56], Pilloz et al. [57], etc. have applied nickel-based alloys as the material added to steel substrates in their laser cladding process. The reasons being is that Nickel based alloys apply to components operating in extreme environments, particularly at elevated

temperature (i.e. Nuclear reactor). These alloys are preferred to those made of Cobalt since Nickel alloys are more cost-effective and operational. Most articles on the aforementioned research groups have specified the microstructure of the Nickel base clads by fine dendrites in a particulate-reinforced metal matrix. The interdendritic reinforcing particles such as Ni_3Fe , Ni_3Si , B_4C , CrB and Cr_3Si are commonly detected, which vary accordingly to the chemical composition of the raw cladding alloys.

For Iron based alloy addition, the primary purpose of its employment is to reinforce the corrosion resistance of C-Mn steel substrates. Eiholzer et al. [58] and Singh et al. [59] have attempted laser cladding of Fe-Cr-Mn-C on steel and demonstrated ultrafine microstructure with a uniform distribution of complex carbides in a ferrite matrix owing to an increase in solid solubility of alloying elements. In the ferrite matrix, carbides such as M_6C were detected, which improve wear resistance compared to those of Stellite alloy addition associated with lower hardness carbides M_7C_3 . Other chemical compositions of clads such as Fe-Cr-W-C [60], Fe-Cr-C-W [61], etc. were also conducted onto steel substrates. The increases in hardness of the clad samples compared to those of bare substrates were reported. Resultantly, the aforementioned research validating the feasibility of laser cladding for steel substrates has generated fundamental knowledge to unveil the capability of this innovative surface engineering process for advancing railway infrastructure productivity.

2.5 Laser cladding of tribological rail-steel components

With the rapidly increasing trend of axle loads and rail traffic, the presence of rolling contact fatigue and wear damages at contact surfaces of tribological applications, particularly train wheels and rails, is problematic in modern railway infrastructure. In order to satisfy the demand on today's rail transportation industry and the encouraging achievements from the research on laser

cladding for steel, laser cladding technique has been employed by numerous research groups to modify the surface properties based on the component's design criteria, while the steel substrate's properties are almost unchanged [62]. Niederhauser et al. [63] studied the fatigue behaviour of B82 steels (0.51 wt% C, 0.32 wt% Si, 0.006 wt% S and 0.72 wt% Mn) cladded with Co-Cr alloys (5.6 wt% Mo, 2.15 wt% Ni, 0.125 wt% C). This steel is widely used for railway wheels in Sweden. The laser cladding in two successive layers with parallel runs to cover an entire specimen gave rise to tempered martensite HAZ below the clad. The results presented a consistent and favourable fatigue behaviour of the cladded specimens.

Ringsberg et al. [64] investigated the rolling contact fatigue resistance of the pearlitic UIC 900A (R260) steel cladded with a Co-Cr alloy using finite element numerical simulation. Franklin et al. [65] worked on laboratory tests also investigated rolling contact fatigue and wear behavior of laser cladded specimens made of rail steel UIC (260 grade) 900A. The laser cladded specimens endured with no cracks after 200,000 cycles of water-lubricated twin disc testing, whereas the substrate material alone formed clear cracking after 4000 cycles. Chosen coatings showed great Rolling Contact Fatigue damage resistance compared to the substrate material alone. Excellent bonding quality was detected for all coatings. Sequentially, Jonas et al. [64] also compared his three-dimensional finite element calculations based on Shakedown theory to the twin-disc laboratory tests. The results shown in shakedown diagrams for numerous wheel-rail contact situations were consistent with the experimental results. Ultimately, Heinsch and colleagues [66] conducted actual field tests regarding rolling contact fatigue and squeal noise behaviour of laser-cladded prototype UIC 900A (260-grade) rails. The 6-meter rail prototypes exhibited no rolling contact fatigue damage after a period of one year, where the non-treated rail displayed pronounced rolling contact fatigue damage. Excellent metallurgical bonding between coatings and rail materials was proven. Nevertheless, the selected coatings did not reduce or prevent noise occurrence.

In summary, the literature review suggests that the ever-increasing demands in rail transportation industry for greater axle loads, durability, lifetime and frequency of train operation necessitate the fabrication of rails possessing superior surface properties to diminish wear and rolling contact fatigue damages. In order to acquire such surface properties, utilization of surface engineering techniques, particularly laser cladding technique, is considered, since the laser technique is a non-equilibrium synthesis and presents dominant advantages over the others. Moreover, an array of academic research and studies on laser cladding of broad range of material additions on steel substrates, in conjunction with their industrial applications across many fields generate solid basis. Such basis strongly encourages the employment of laser cladding technique onto tribological steel components in the railway industry, whose information on cyclic fatigue behaviour is sparse in the literature.

In conclusion, the attention to the use of laser cladding technique has only experienced a substantial boost in recent years, absence or deficiency of knowledge occurs in its applications to rail transportation industry. Therefore, a detailed investigation of (i) the influence of laser cladding parameters on microstructure, mechanical property development in the clad region and HAZ of rail steels; (ii) their correlation to fatigue behaviour, and (iii) the establishment of reliable process models demonstrating microstructural resolution associated with cladding thermo-mechanics, is proposed.

2.6 Chapter summary

A review of literature had disclosed the importance and significance of utilising laser cladding in improving the current railway maintenance strategies and developing the innovative rail-wheel maintenance technology. Consequentially, accurate prediction and comprehension of the mechanical performance and metallurgical characteristics of laser clad rails are crucial. However, previous studies have been targeted merely either hypereutectoid or eutectoid rail

grades. Applications of laser cladding to premium hypereutectoid rail grade, commonly used in heavy-haul rail systems, remained limited in the open literature.

The Australasian Railway Association (2009) predicted that 95% of bulk commodities by land and gross tonne kilometres would be transported by rail by 2017. From the current annual haulage rates of 200 million gross tonnes (MGT) per annum for individual iron ore or coal haulage systems, the projected annual haulage rates in mineral haulage systems will be ~300 MGT per annum.

To expand the national economy, development of railway infrastructure has been considered as a national priority for investment owing to the increase in demand for freight transportation. Novelty in technology must be developed and implemented in railway industry to cope and withstand such high demand. This study falls directly within the crucial segment of the national development.

To meet the ever-growing demands for the increased axle loads, which lead to increasing rates of rail degradation, and high frequency of train operations, which limit the extent to which rail track is available for maintenance activities such as rail replacement, the development of effective and time-efficient strategies for rail-wheel maintenance and implementation of high strength rail grade, i.e. hypereutectoid rails, are necessitated to ensure the structural integrity of rail infrastructure. An investigation into examining the feasibility and employability of laser cladding to the premium rails was an integral part of this current research.

3

Materials and Experimental procedures

This chapter's objective is to detail the typical procedures concerning the preparation of the sample and experimental testing undertaken in the research. The laser cladding rig used for the experimental work is described in the following section. The justification for selection of cladding and substrate materials is discussed in Section 3.2. The experimental methodology is outlined in Section 3.3. Specifications of the apparatus used for preheating and post-weld heat treatment (PWHT) are described in Section 3.4. Procedures for the preparation of metallurgical specimens and metallographic inspections are listed in Section 3.5.

3.1 Description of Laser cladding rig

The laser deposition process was carried by simultaneously melting the cladding powder and substrate materials using a laser coaxial head. This laser head was manipulated by a Motoman XRC SK 16X 6-axis CNC unit. The 4 kW IPG fibre laser gun is used, which is produced in an active medium generated by an optical fibre doped with Ytterbium. Melting efficiency, which is the percentage of ejected powder that forms the cladding layer, was maximized by adjusting the focus point of the powder stream exactly to the location of melting pool. However, the wearing of laser and powder nozzles gradually causes the misalignment of the laser ray and powder focus and decreases the efficiency. Realignment was done before each attempt to remain the optimum efficiency.

Cladding powder was delivered to the melting pool via the laser head using a Sultzer-Metco twin-10 powder feeder. The powder flow rate was controlled by the feeder. To ensure the optimum melting efficiency and constant flow rate, the feeder was operated for a known period, then the ejected powder was weighted, and the flow rate can be determined. Based on the determined flow rate, further adjustment and alignment will be taken. The constant tilted angle of the laser head was used to avoid the reflection of the laser beam from melting the nozzle. The angle of 10° was selected for all the trials.

The melting pool is prone to oxidation with oxygen in the atmosphere. To prevent the oxidation process, Argon and Helium are used as shielding gases. Helium is not cost-effective but provides better shielding against oxidation in the melting pool. In the current study, a shielding gas consisting of 50% Argon and 50% Helium was used at the flow rate of 30 L/min. The flow rate of the carrier gas was measured to be 20 L/min.

3.2 Selection of cladding and substrate materials

Steels are extensively utilized in numerous engineering applications, e.g. automotive components, shafting and surgical tools, chemical mixers, etc. [67], which require high strength and high resistance to wear and corrosion [67, 68]. Nevertheless, owing to the concurrent presence of damage mechanisms, i.e. wear and corrosion, the behavior and performance of the steel components might be negatively affected, and their service life would be significantly shortened [69]. Consequentially, improvement of surface properties is necessitated, and application of various surface engineering techniques offers a promising solution to prolong the service life of engineering parts. Stainless steels and Co-based hard facing alloys are commonly used in engineering applications and industrial fields which require excellent strength and superior resistance to wear and corrosion [67, 68].

Co-based alloys are appropriate for the protective coating used in many industries demanding excellent surface properties, i.e. wear, corrosion and heat resistance [70-73]. Stellite alloys are the most renowned cladding material group. Various grades and modifications of the alloys are commercially available which would allow excellent compatibility for applications with specific requirements. Carbon content is the critical factor to classify the Stellite alloys. The higher carbon content, the higher risk of cracking during deposition. The 410L grade martensitic stainless-steel powder supplied by Hoganas Belgium Pty Ltd. was selected as the clad material owing to its high ductility and excellent corrosion resistance and hardness.

Therefore, for cladding materials, four different depositing materials, namely 410L stainless steel (~150 μm), 420 stainless steel (~150 μm), Stellite 6 (45-106 μm) and Stellite 21 (45-125 μm), were selected to centrally clad onto the hypereutectoid rail head. Chemical compositions of the

depositing materials are shown in Table 3-1. The clad material was in powder form and deposited during processing (co-deposition) via a coaxial laser head.

Table 3-1 Chemical compositions of the depositing materials.

Elements in weight percent (wt.%)																
Materials	Fe	C	Mn	Si	S	P	Ni	Cr	Mo	Cu	V	Nb	Ti	Al	W	Co
410L	Bal	0.01	0.51	0.47	0.01	0.01	0.08	12.7	0.01	0.05	0.01	0.02	<0.01	0.01		
420SS	Bal	0.24	1.17	0.63	0.01	0.01	0.22	12.6	0.03	0.03	0.02	0.01	<0.01	0.02		
Stellite 6	0.09	0.99	0.02	1.58	<0.01	0.03	0.72	28.3	0.01	0.01	<0.01	<0.01	0.01	<0.01	4.10	Bal
Stellite 21	0.16	0.23	0.59	0.86	0.01	0.01	2.28	27.0	5.20	<0.01	<0.01	<0.01	<0.01	<0.01	0.05	Bal

Table 3-2 Chemical compositions of the substrate material (N.S = Not significant).

Elements in weight percent (wt.%)											
Identification	C	Si	Mn	P	S	Cr	Ni	Mo	V	Nb	Al
Rail substrate	0.93	0.28	0.95	0.018	0.014	0.20	<0.01	<0.01	<0.01	<0.01	<0.005
R400HT (*)	0.88- 1.07	0.18- 0.62	0.95- 1.35	0.025 (max)	0.025 (max)	<0.30	N.S	N.S	0.030 (max)	N.S	0.004

(*) European Committee for Standardization (CEN), EN13674-1:2011 Railway Applications-Track-Rail-Part 1: Vignole railway rails 46kg/m and above.

3.3 Description of rail specimens

As per the experience with in situ rail repairs being 200-800 mm long to mimic the rail repair with full constraint and a representative heat sink during a laser cladding deposition, 400-mm repair length and 70-mm width of cladding dimensions on a 600-mm long rail were selected. Such dimensions would allow an extensive investigation at the vital locations of a rail repair, i.e. the start and end of the cladding layer (transient state condition), and the middle of laser tracks (steady-state condition). Figure 3-1 shows the generic sizes of the laser deposits and substrates of rail steel along with a defined coordinate system.

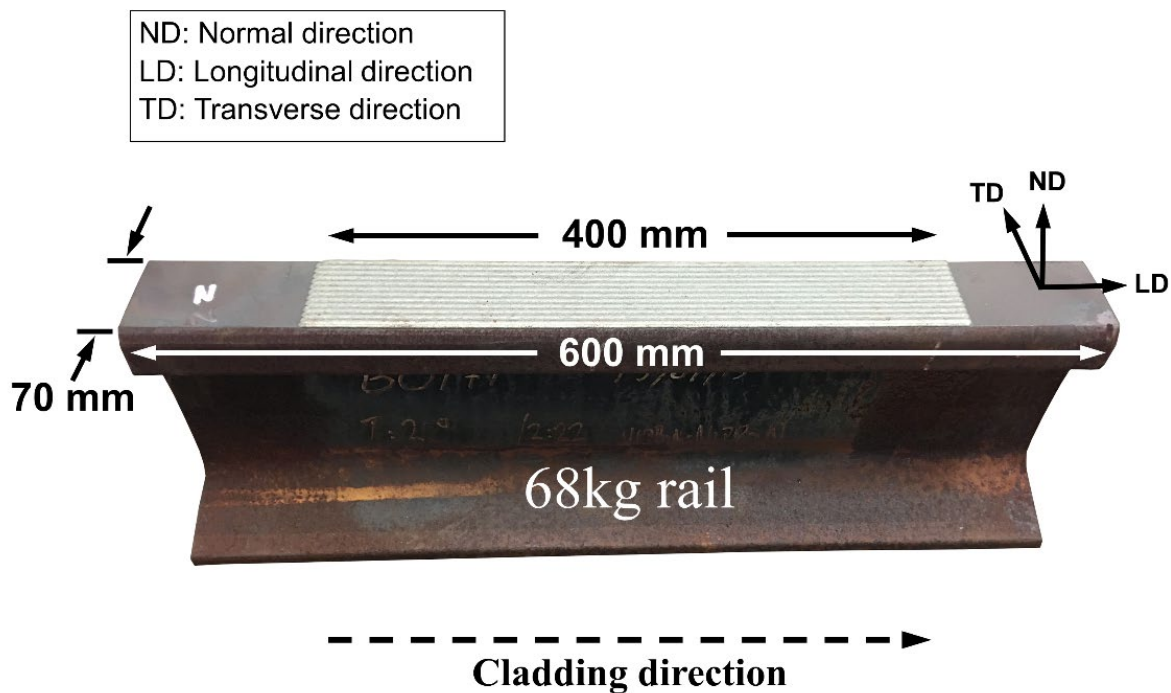


Figure 3-1 Photograph of a laser-cladded hypereutectoid rail specimen with detailed dimensions prior to specimen preparation process.

3.4 Preheat and Post-weld heat treatment

Evaporation of the moisture on the laser treated specimens can induce porosity in the cladding layer. The oxygen and hydrogen gases engendered by the moisture are encapsulated in the claddings. To eliminate this issue, in conjunction with prolonging the cooling rate, the heating condition of preheating to 350 °C was conducted by using a conventional manual oxy torch. To monitor the homogeneity of preheating temperature, three thermocouples were attached and measured at the start, middle and end of the cladded region during the preheating application to the full railhead. Immediately upon the achievement of the preheating temperature of 350 °C across the specimen, the laser deposition was initiated. Thereafter, PWHT was carried out to tailor the cooling rate, hence acquiring the desired properties, i.e. microstructure and hardness, for the designed functionally graded material. Besides PWHT, ceramic heating blankets were also located across the repaired rail to ensure that the temperature of 350 °C across the cross-section of the specimen was obtained.

3.5 Metallographic and mechanical characterization

3.5.1 Optical Microscopy (OM) and Scanning Electron Microscopy (SEM)

The metallurgical specimens were sectioned in the transverse direction (Y), then mounted, ground, polished to reveal the microstructure of each of the three groups (Table 2). A two-stage etching procedure was applied. A 2% Nital etching solution was used to visualize rail steel substrate microstructure. A Kalling's no. 2 (5g CuCl₂, 100 ml HCl and 100ml ethanol) was used to reveal the microstructure of the laser deposited layer.

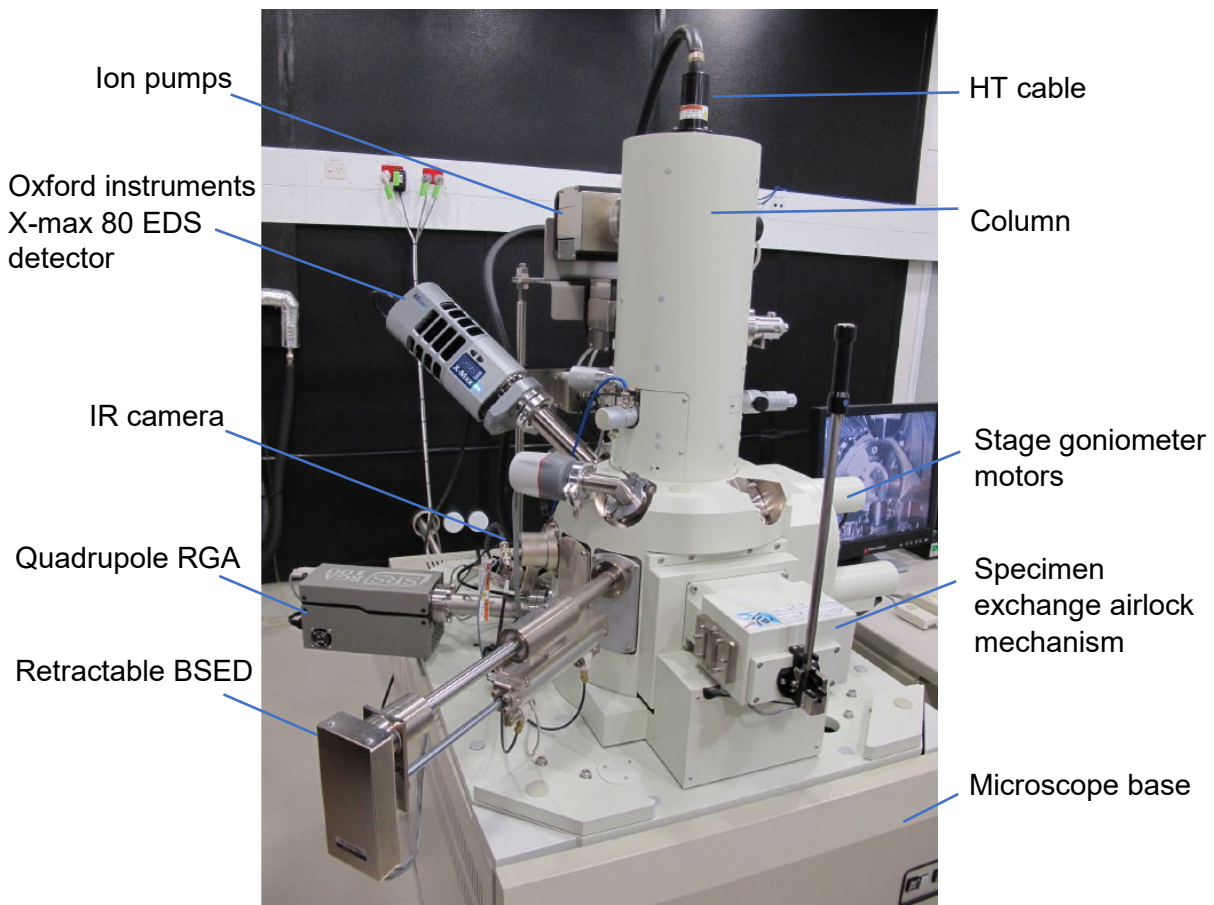


Figure 3-2 Microstructural inspection using the JEOL 7001F scanning electron microscope with built-in features.

The metallographic specimens were then analyzed using Nikon Eclipse optical microscope to provide overviews of sample microstructures and JEOL 7001F FEG scanning electron microscope (SEM) to detail the microstructural characteristics further. The JEOL 7001F is an advanced scanning electron microscope equipped with a Schottky-type field emission gun (FEG), as shown in Figure 3-2. Due to the available maximum electron probe current above 200nA, the microscope is capable of both moderately high-resolution imaging and high throughput analytical work. The accelerating voltage ranging from 30kV down to 0.1kV can be used in a “gentle beam” mode, and a voltage is applied to the sample stage, which is to alleviate the problem of sample charging. A

conventional secondary electron detector (E-T type) and a retractable solid-state backscattered electron detector (RBED) are equipped in the microscope, which allows high-resolution images to be acquired. The Oxford instruments X-Max 80 Silicon Drift type EDS detector is also equipped to take rapid point and area (mapped) X-ray composition measurements including “quantitative” mapping, at high count rates and resolution. High-speed phase mapping and crystallographic studies, and EDS compositional analysis were conducted by means of an HKL Nordlys S electron backscattered diffraction (EBSD) camera and Oxford Instruments Aztec software system.

3.5.2 X-ray diffractometric phase analysis (XRD)

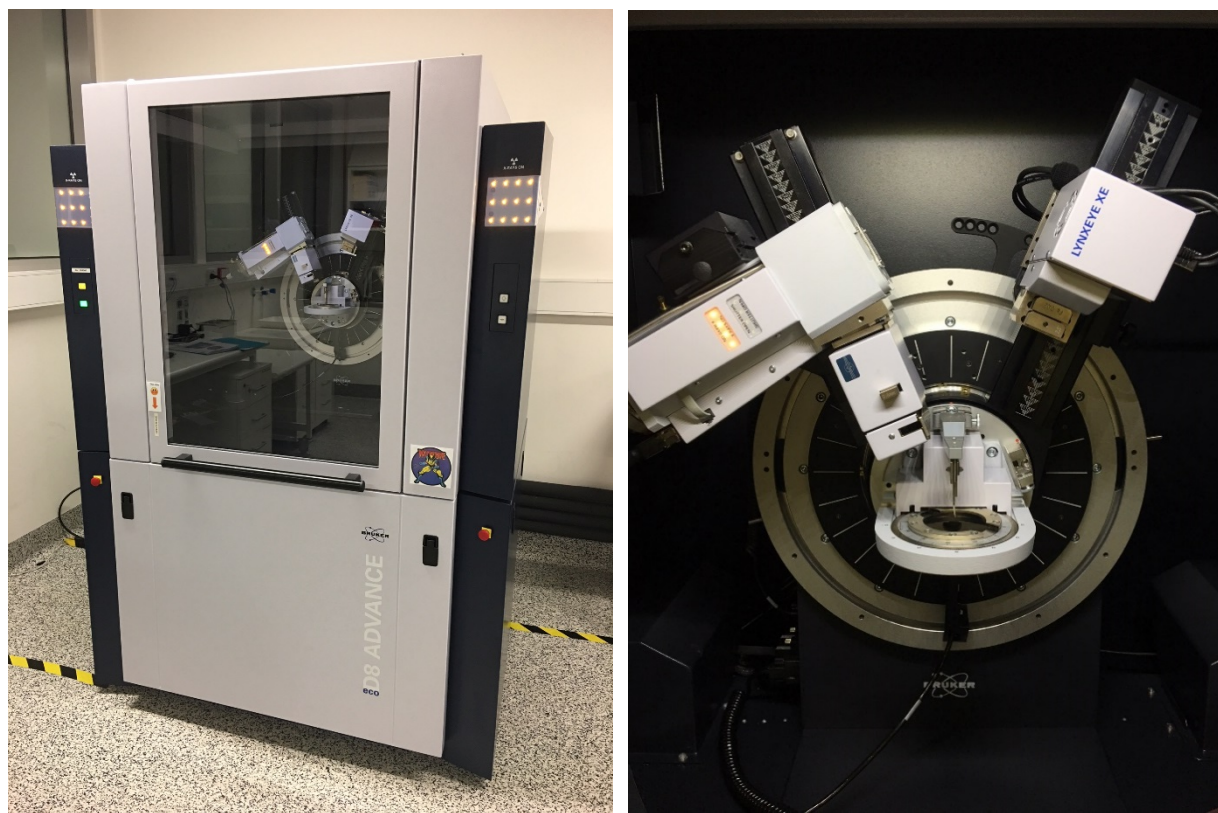


Figure 3-3 XRD analyses using (a) Bruker D8 Advance ECO X-ray instrument. (b) X-ray diffraction chamber with rotation sample stage, energy -dispersive LYNXEYE XE-T detector and motorized anti-scatter screen.

By means of XRD, crystalline phases are able to be easily identified and quantified. Information on the arrangement of atoms over a short distance and crystal structure can also be revealed. Features of diffractogram obtained from XRD measurement, i.e. peak positions, intensities, oscillations and other shapes, can be used to characterize laser cladded samples fully.

Phase identification and crystallographic studies were undertaken using Bruker D8 Advance ECO X-ray diffractometer with Co K_{α} radiation, as shown in Figure 3-3. A Co X-ray source was selected instead of Cu to avoid strong fluorescence of ferrous materials and the resulting polychromatic radiation. Furthermore, background intensities of ferrous specimens are consistently lower in diffractograms using the Co X-ray source. A dedicated post-analysis software package, DIFFRAC.SUITE, was used to retrieve information on phases and crystallography. To ensure that the laser deposits are fully characterized, X-ray diffraction profiles were taken at various discrete depths of the deposits.

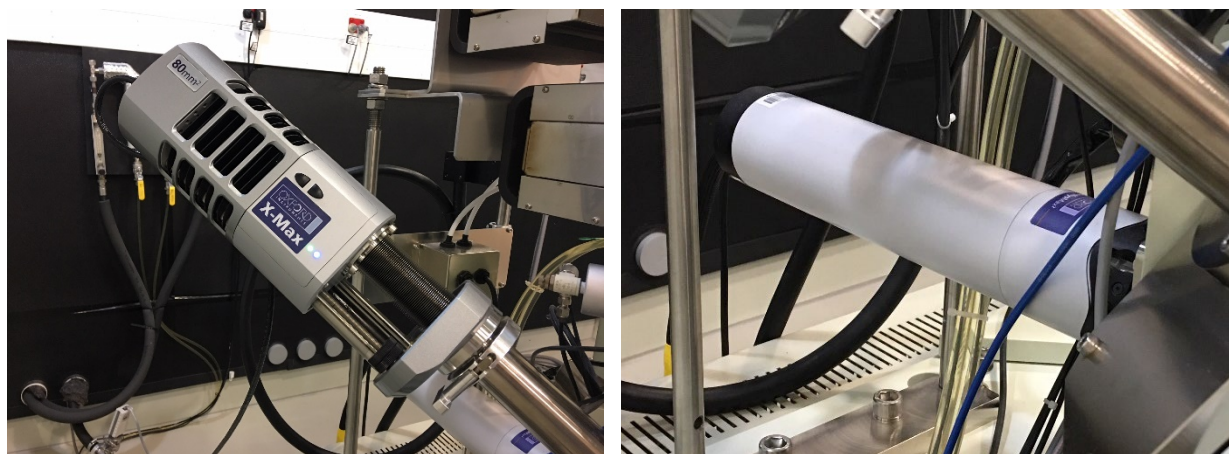


Figure 3-4 (a) Oxford instrument X-Max 80 EDS detector, and (b) HKL NordlysMax electron backscattered diffraction (EBSD) camera.

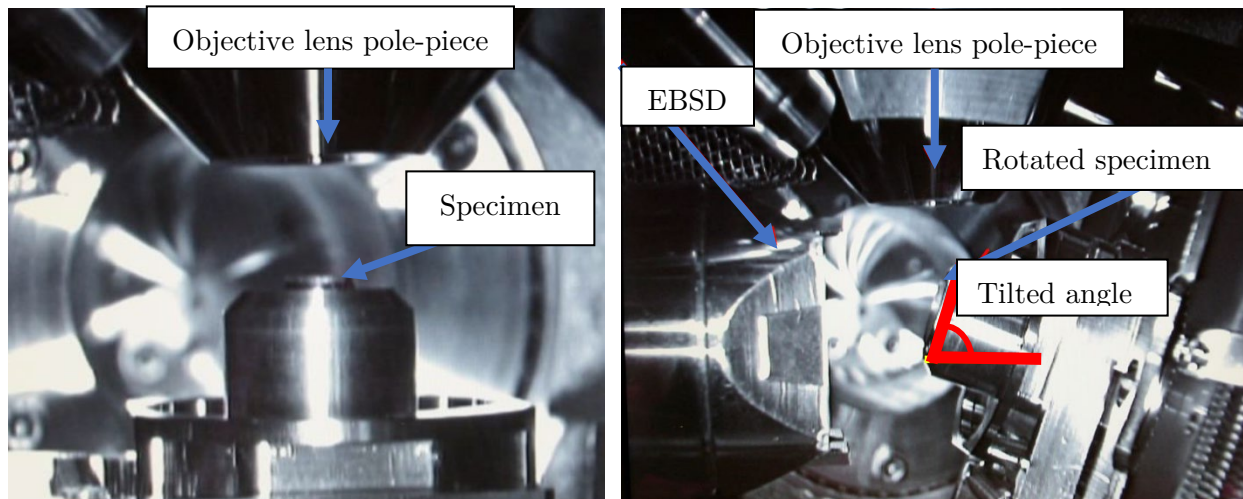


Figure 3-5 (a) Sample chamber in the ordinary SEM mode, and (b) Sample chamber in the EBSD mode.

3.5.3 Electron backscattered diffraction (EBSD) and Energy dispersive X-ray microanalysis (EDS)

As shown in Figure 3-4, an HKL NordlysMax electron backscattered diffraction (EBSD) camera and Oxford instrument Aztec software system permit high-speed phase mapping and crystallographic studies of suitable samples, in conjunction with EDS compositional analysis if required.

The EBSD detector is retractable and fitted with quad diode detectors for backscattered/forescattered imaging. In general, the good standard operating condition of 20 kV, with a working distance of 15 mm for EBSD and an angle of 70° towards the Nordlys detector was required for EBSD, as shown in Figure 3-5. In this work, large EBSD area mapping (LAM) was undertaken one night long at a binning factor of 4×4 , a probe current of 16 mA and a step size of $0.25 \mu\text{m}$ to ensure vital characteristics being captured. A montage of EBSD was, therefore, obtained from a set of acquired fields. Individual field was able to be interrogated as an area of

interest to extract local information on crystal orientation, grain size, texture, phase identification, distribution and transformations. EDS data could be also simultaneously acquired and analysed with the obtained EBSD data using LAM.

3.5.4 Shear Punch Testing

One of the main stress modes developed under wheel-rail contact is shear which acts at an angle to the loading direction [74]. Depending on the magnitude of traction/creepage forces, the maximum shear stress can be either located at rail surface or subsurface, where rolling contact fatigue (RCF) damage is commonly detected. Conditions with low creepage are established with $T/N < 0.3$ at the contact patch, where T and N are respectively the tangential and normal forces, and consequently the maximum shear stress occurs at subsurface levels. On the other hand, $T/N > 0.3$ is associated with the high creepage conditions, where the maximum shear stress occurs at the surface. Material behaviour, i.e. RCF damage and cumulative wear, is found to be governed by the magnitude and the locations of the stresses [75]. Therefore, it is crucial to evaluate shear strength of the laser treated rails by means of shear punch testing and compare to that of virgin rails. Furthermore, shear punch testing is also an effective method to assess other material properties, namely yield strength (YS), ultimate tensile strength (UTS), etc., when the material availability is limited [76-78].

The shear strength of a specimen is calculated using shear punch testing results. Material shear strength equation:

$$\tau = \frac{F}{\pi dt} \quad (3.1)$$

The division of the shear force F by the area of shear results in shear stress τ . The punch diameter and sample thickness are d and t , respectively.

The shear punch testing rig is designed according to the principle of blanking to determine shear strength of a specimen, as shown in Figure 3-6. The testing specimens are placed between a die and a matrix to alleviate the bending effects during the test. The shear punch was guided using a punch guide, traversing linearly along a built-in linear bearing. A grinding step was also involved to ensure the similar thickness between the top and bottom surfaces by removing merely a small amount of material at a time. This ensures even forces being applied to the specimens and an adequate tightness between the die, matrix and punch guide.

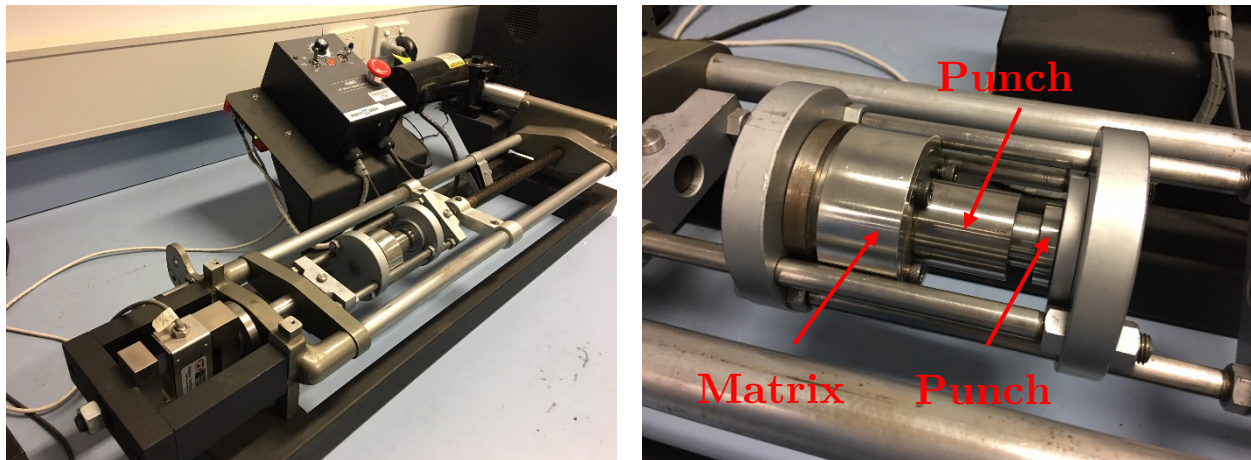


Figure 3-6 Shear strength inspection using a specially-designed shear punch testing instrument at Monash

3.5.5 Focused Ion Beam (FIB) and Scanning Transmission Electron Microscopy (STEM)

To investigate the diffusion behaviour of carbon in laser clad rail steels, a focused ion beam (FIB) milling method was employed using the FEI Quanta 3D FIB workstation. FIB samples were sectioned using a Buehler IsoMet low speed saw machine equipped with a diamond blade to

minimize the preparation artefacts. Site-specific in-situ lamellae were extracted from the obtained FIB samples in a virtually stress-free manner.

The following main steps were applied to fabricate exquisitely the thin foils for STEM analyses: 1) Depositing platinum (Pt) to cover and protect the area of interest, 2) Rough ion milling, 3) Performing J-cut, 4) Lifting out the lamella, 5) Mounting the lamella on a copper grid, 6) Thinning the lamella and 7) Finally polishing procedures were conducted on the foil. STEM images were taken in high-angle annular dark-field (HAADF) mode using an FEI Tecnai G2 F20 S-TWIN microscope operating at an accelerating voltage of 200 kV.



Figure 3-7 (a) Metallurgical sample preparation using FEI Quanta 3D FIB workstation. (b) Detailed microstructural investigation using the FEI Tecnai G2 F20 S-TWIN microscope.

4

Laser-cladded Premium Rails

In this chapter, the effects of cladding direction, preheating and post heating (PWHT) heat treatment on microstructural and mechanical properties of functionally graded rail materials and their corresponding heat affected zones (HAZ) are presented. Laser cladding of a premium hypereutectoid rail grade with 410L stainless steel powder was conducted using a fibre laser gun with a powder feeder. Two different cladding directions and different heat treatments were investigated.

4.1 Introduction

The aim of this chapter is to determine the optimum cladding directions and suitable heat treatment to opt for laser cladding deposition on rail steels and to investigate the effects of cladding directions and heat treatment on the microhardness, metallurgical microstructure of the cladded rail steels and the mechanical properties of these microstructure introduced by the cladding process. The preferable cladding material and heat treatment for a wheel-rail contact using 410L stainless steel were optimized and established by evaluating all crucial aspects, i.e. microstructural and mechanical features.

The number of research papers has validated the importance and significance of utilizing laser cladding in the future rail maintenance strategies. Consequentially, understanding and predicting the mechanical performance and metallurgical characteristics of rail steels after cladding are crucial. Nevertheless, many previous studies [16, 63-65, 79-81] focused on eutectoid rail grades and applications of laser cladding to premium hypereutectoid rail grade, commonly used in heavy-haul rail systems, are limited in the open literature. This rail grade is renowned for its superior load bearing capacity, better service durability, smaller crack propagation rate and longer maintenance intervals compared to conventional rail grades [65].

Furthermore, most of the previous work have investigated the processing parameters, structure and characteristics for other cladding materials, and the main focus was on other industrial fields rather than railway area, particularly in heavy haul industry.

Concerning this, the current chapter focuses on the selection of a preferable cladding direction for wheel-rail conditions by investigating microstructural and mechanical characteristics of the

cladded rails. Laser cladding of 410L stainless steel was performed on a premium hypereutectoid rail grade using a 4 kW IPG fibre laser. Microstructural evolutions of the 410L depositing layer and the heat affected zone (HAZ) of the rail substrate were analysed via optical microscopy (OM) and Scanning Electron Microscopy (SEM). Electron dispersive X-ray spectroscopy (EDS) was also utilised for compositional analyses at the deposited layer and the clad-substrate interface. Phases of the 410L deposited layer were analysed using X-ray diffractometer (XRD) and Electron Backscattered Diffraction (EBSD). Indications of the tribological and mechanical performance of laser deposited layers were obtained via Vickers indentation and shear punch tests, respectively. Finally, the correlation between the microstructural characteristics and mechanical properties were discussed.

4.2 Experimental Setup - Optimum cladding directions

The specimens of cladded rails were processed according to the method described in Chapter 3. Three groups of specimens were produced to determine the optimum cladding direction, defined in Table 4-1.

Table 4-1 Three different repair process procedures.

Specimens	Process parameter sets	Heat treatment procedure	Cladding direction
Group 1	3.2 kW, 1000 mm/s and 26.4 g/min	Preheating at 350 °C (HTA)	Transverse
Group 2	3.2 kW, 1000 mm/s and 26.4 g/min	Preheating at 350 °C (HTA)	Longitudinal
Group 3	3.2 kW, 1000 mm/s and 26.4 g/min	Preheating at 350 °C, Post-heating at 350 °C, Slow-cool to room temperature (HTB)	Longitudinal

Two cladding directions, i.e. rail-longitudinal direction and rail-transverse direction, were conducted, as shown in Figure 3-1, whereas all other factors remained constant. 410L was selected as the only cladding material. The chemical composition of the 410L powder is listed in Table 3-

1. Preparation of the metallographic specimens and the applied heat treatments were conducted according to the method described in Chapter 3.

4.3 Experimental Results

4.3.1 Phase identification and distribution

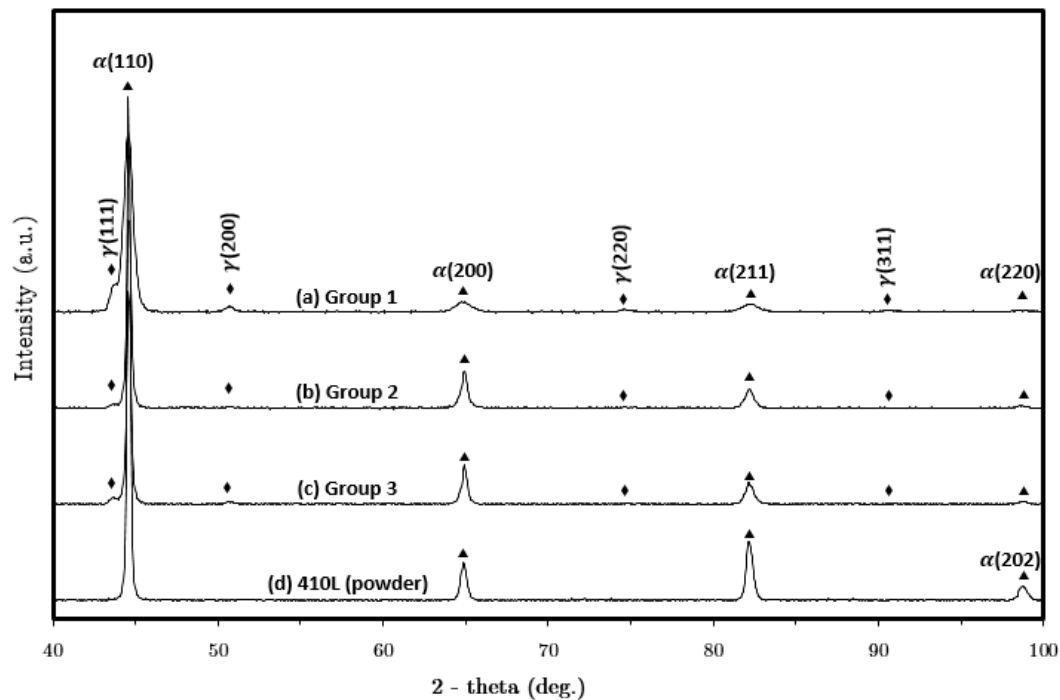


Figure 4-1 X-ray diffraction patterns of (a) the 410L transversely deposited layer with preheating (Group 1), (b) the 410L longitudinally deposited layer with preheating (Group 2), (c) the 410L longitudinally deposited layer with preheating, post-heating and slow cooling, and (d) the unprocessed 410L.

Results of the XRD qualitative phase analysis, as depicted in Figure 4-1 shows the main phases of the 410L transversely deposited layer with HTA (Group 1), the 410L longitudinally deposited layer with HTA (Group 2), the 410L longitudinally deposited layer with HTB (Group 3) and the 410L unprocessed powder. Peaks and corresponding Miller indices associated with ferrite/martensite - α (BCC) and austenite - γ (FCC) iron phases were detected for the three

layers. Compared to the laser treated specimens, the spectra of the 410L powder was only found with α (BCC) iron, since the powder is made of the unprocessed 410L stainless steel powder with low carbon content. This might imply that the exposure to laser irradiation facilitates the increase in C concentration in the layers due to dilution from the substrate. The small right shifts of α peaks suggest a certain degree of distortion in the crystal structure of α iron. The Group 1 specimens with the broadest α peaks indicating the finest grain size of ferrite/martensite phases, and the greatest intensity of γ peaks suggesting the highest volume fraction of austenite in the deposited layer's microstructure are observed in Figure 4-1. Differences in characteristics of the peaks in Group 2 and 3 are non-prominent. However, the intensity of the Group 3's γ peaks are detected to be slightly greater than that of Group 2, therefore, the volume fraction of austenite in Group 3 could be marginally greater to some extent. The absence of carbide peaks in the obtained X-ray patterns may be attributed to the detection limitation of XRD [82].

In order to justify the X-ray diffractometric phase analysis, the technique of EBSD has been performed to confirm the phases further and determine the distribution of each phase within the deposited layers. Figure 4-2 and Figure 4-3 show the acquired EBSD and EDS results of the Group 1 specimens in the middle of the layer and at the interface, respectively. Dendritic morphology was detected with the fine martensitic structure inside each dendritic arm as evident in Figure 4-2 (a1) and Figure 4-3 (b1). By using EBSD, the phases in the deposited layer and interface were respectively shown in Figure 4-2 (a2) and Figure 4-3 (b2). Body-centred cubic (BCC) crystal structure was detected in the dendritic arms, whereas face-centred cubic (FCC) crystal structure was detected both between the dendritic arms (or the dendritic grain boundaries) and near the clad-substrate interface.

EDS was conducted for the chemical composition of the deposited layer and in the vicinity of the interface. The resulting post-cladded distribution of Chromium (Cr) and Manganese (Mn) alloying elements in the layer were respectively shown in Figure 4-2 (a3) and (a4), and likewise at the interface, shown in Figure 4-3 (b3) and (b4) respectively. Compared to other alloying elements

detected, only Chromium (Cr) and Manganese (Mn) alloying elements demonstrated stronger tendency to segregate into the dendritic grain boundaries upon rapid solidification.

The EBSD and EDS results of the Group 2 specimens shown in Figure 4-4 and Figure 4-5 are respectively taken at the middle and at the interface of the Group 2 deposited layer. Colonies of ferrite with light grey colour are observed to form trails inside a dark grey coloured martensitic matrix as shown in Figure 4-4 (a1). Pronounced colour contrast is detected along the interface, which indicates that a dilution band forms in the metallurgical bonding established by laser cladding as evident in Figure 4-5 (b1). In the current EBSD technique, both the colonies and the matrix possess BCC crystal structure, excepting the small regions in the interface with FCC crystal structure as evident in Figure 4-4 (a2) and Figure 4-5 (b2). For the EDS analysis, most of the alloying elements demonstrated homogeneous distribution over the entire layer, but small spots with a greater concentration of Cr and Mn elements were detected near the interface, where the FCC crystal structure was as shown in Figure 4-4 (a3) - (a4) and Figure 4-5 (b3) - (b4). For the EDS analysis, most of the alloying elements demonstrated a homogeneous distribution over the entire layer, however small spots with a greater concentration of Cr and Mn elements were detected near the interface, where the FCC crystal structure was, as shown in Figure 4-4 (a3) - (a4) and Figure 4-5 (b3) - (b4).

Similarly, Figure 4-6 (a) and Figure 4-7 (b) show the acquired EBSD and EDS results of the Group 3 specimens in the middle and at the interface, respectively. Inside a tempered martensitic matrix, larger colonies of ferrite formed more pronounced ferritic trails compared to those of the Group 2 deposited layer as shown in Figure 4-6 (a1). By means of EBSD technique, BCC crystal structure was also detected to be associated with the colonies and the matrix, and FCC crystal structure was associated with the small dilution regions located at the interface as evident in Figure 4-6 (a2) and Figure 4-7 (b2). In common with the Group 2 deposited layer, EDS analysis shows the homogeneous distribution of all alloying elements excepting for Cr and Mn elements,

particularly at the interface. The regions with a higher concentration of Cr and Mn are found to coincide with the location of FCC crystal structure as shown in Figure 4-6 (a3) - (a4) and Figure 4-7 (b3) - (b4).

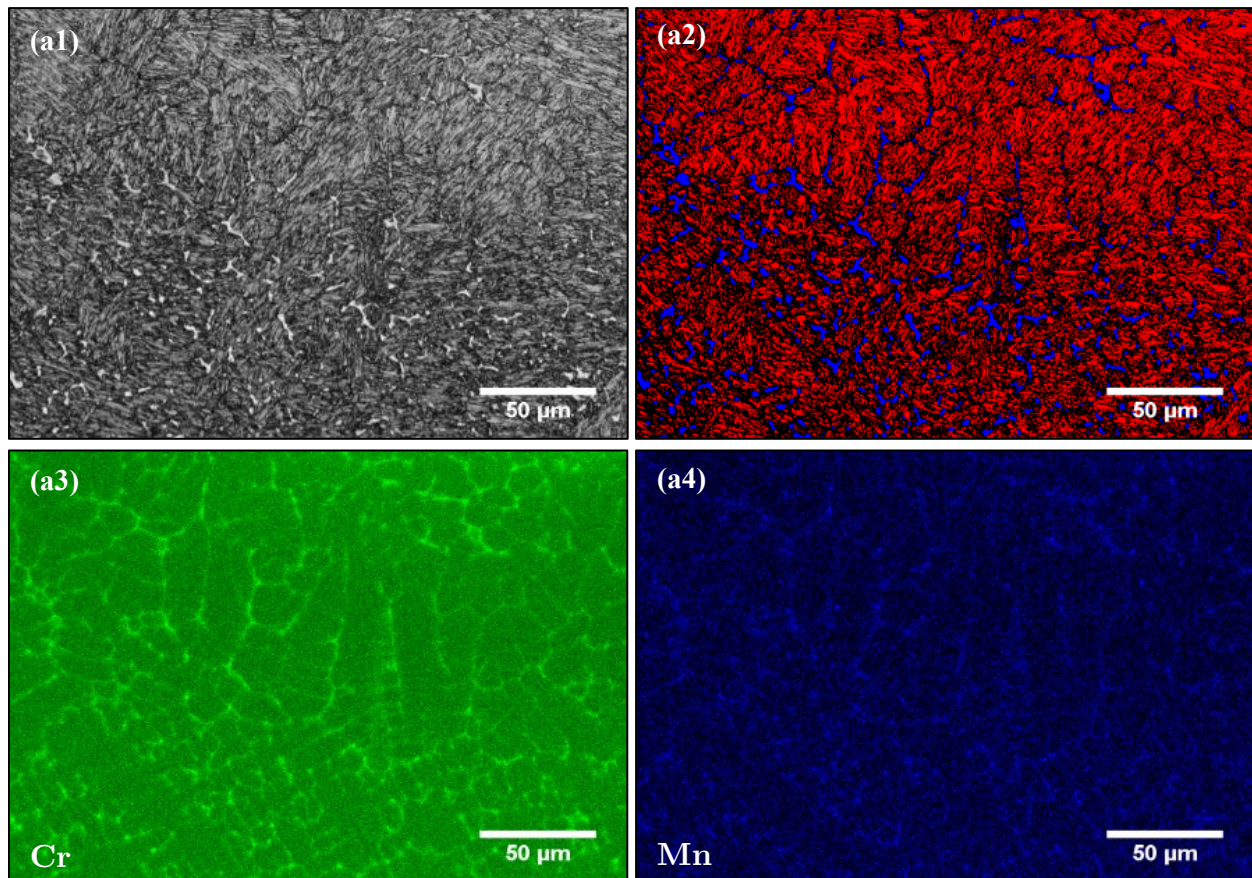


Figure 4-2 Typical acquired EBSD results for the Group 1 deposits. (a1) The band contrast (BC) image for topographical information, (a2) the image of phase distribution, and the EDS images of (a3) Cr and (a4) Mn element distributions. Dendritic morphology was detected with the fine martensitic structure inside each dendritic arm (as shown in red) and retained austenite at the grain boundary (as shown in blue).

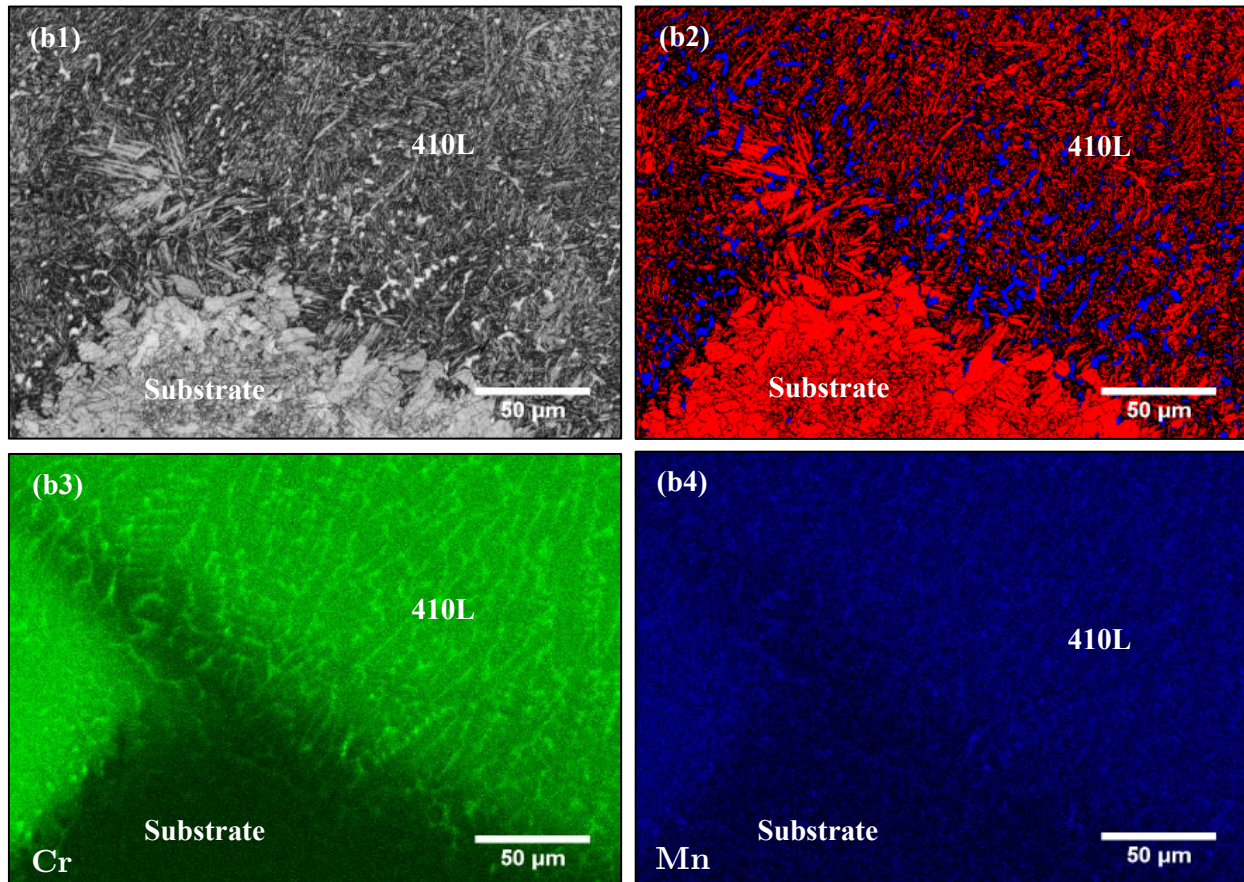


Figure 4-3 Typical acquired EBSD results of the Group 1 deposits at the interface. (b1) the band contrast (BC) image for topographical information, (b2) the image of phase distribution, and the EDS images of (b3) Cr and (b4) Mn element distributions. Dendritic morphology was detected with the fine martensitic structure inside each dendritic arm (as shown in red) and retained austenite at the grain boundary (as shown in blue).

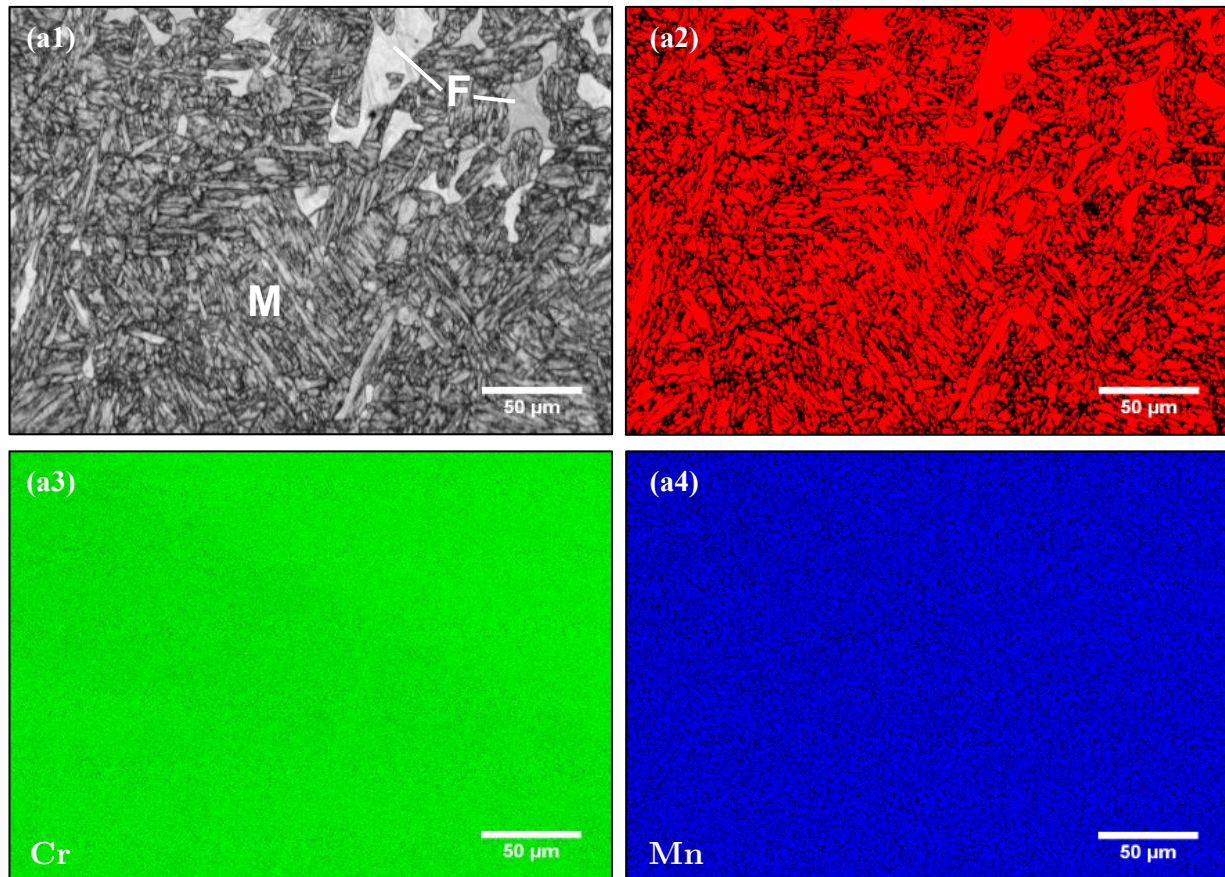


Figure 4-4 Typical EBSD acquired results of the Group 2 deposit with (a1) the band contrast (BC) image for topographical information, (a2) the image of phase distribution, and the EDS images of (a3) Cr and (a4) Mn element distributions. (M=Martensite, and F=Ferrite)

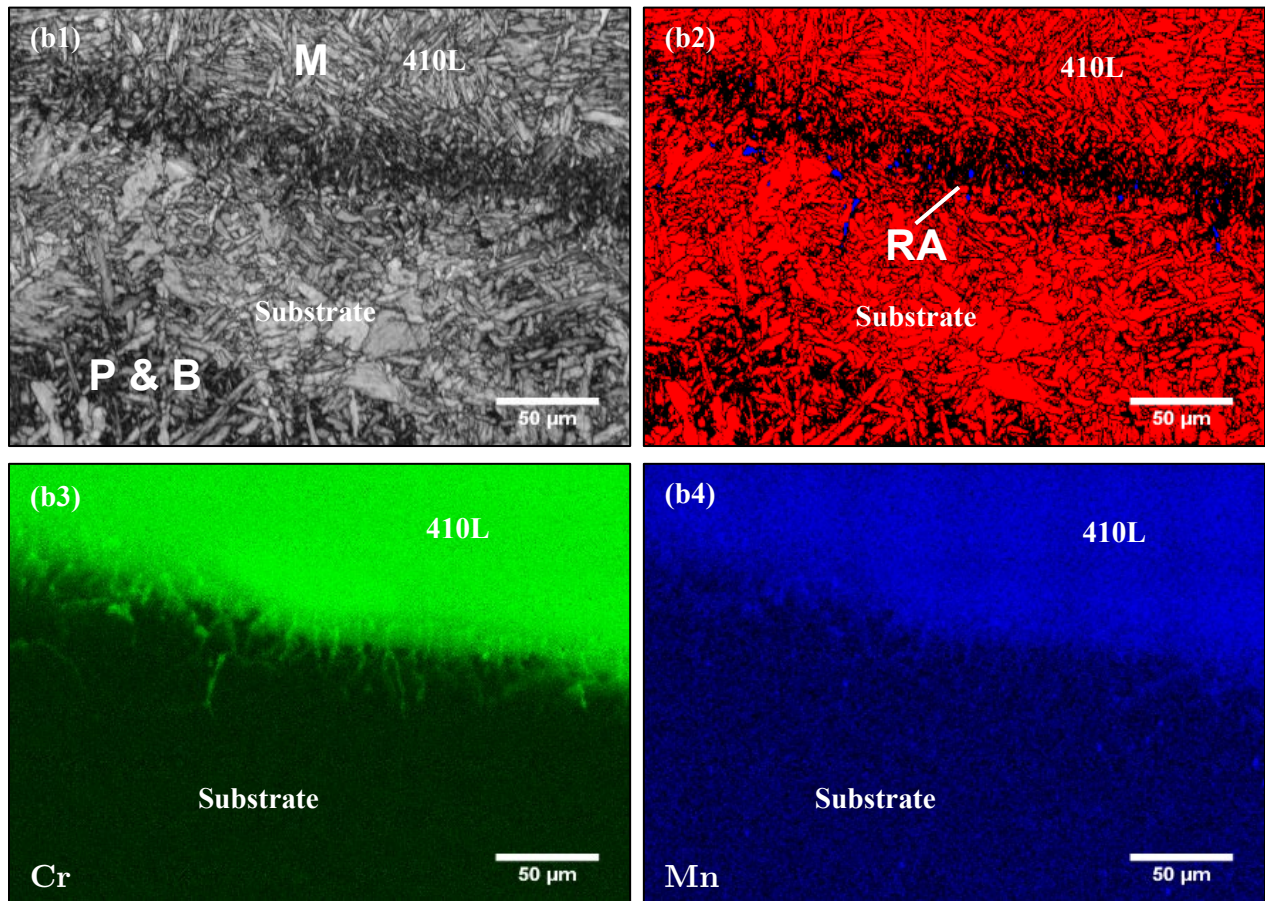


Figure 4-5 Typical EBSD results of the 410L rail-longitudinal deposited clad (Group 2) at the interface with (b1) the band contrast (BC) image for topographical information, (b2) the image of phase distribution, and the EDS images of (b3) Cr and (b4) Mn element distributions.

(M=Martensite, F=Ferrite, P= Pearlite, B=Bainite, and RA=Retained Austenite)

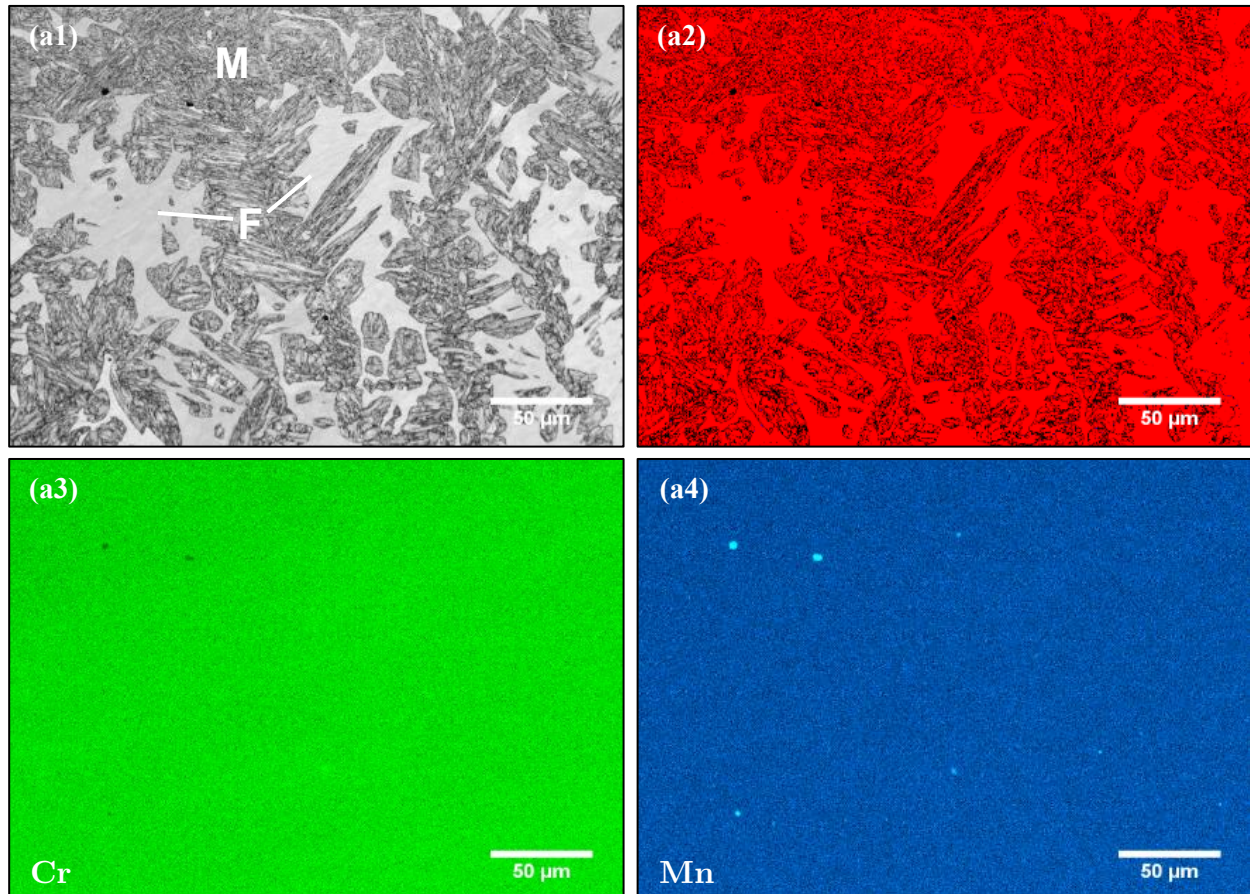


Figure 4-6 Typical EBSD acquired results of the 410L rail-longitudinal deposited clad (Group 3) in the clad with (a1) the band contrast (BC) image for topographical information, (a2) the image of phase distribution, and the EDS images of (a3) Cr and (a4) Mn element distributions.

(M=Martensite, and F=Ferrite)

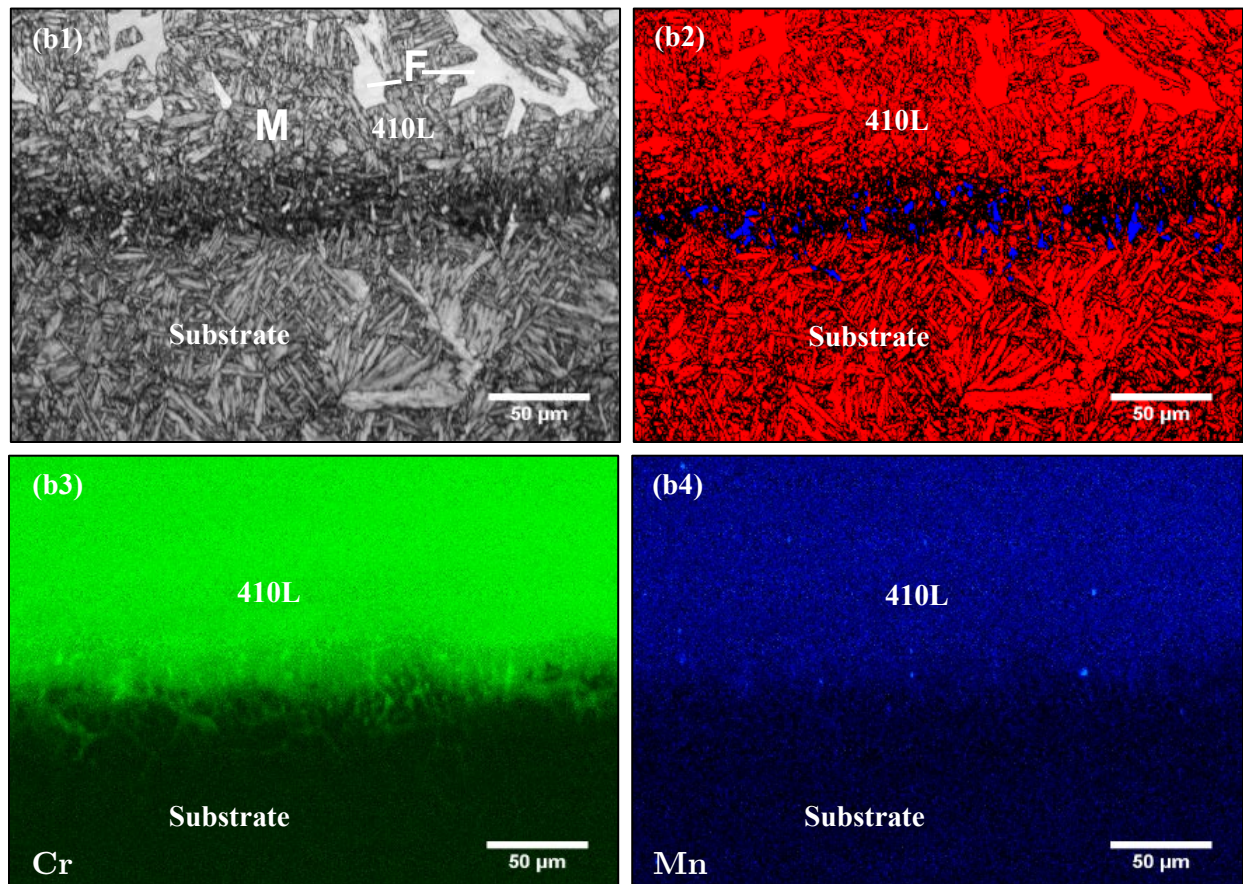


Figure 4-7 Typical EBSD acquired results of the 410L rail-longitudinal deposited clad (Group 3) at the interface with (b1) the band contrast (BC) image for topographical information, (b2) the image of phase distribution, and the EDS images of (b3) Cr and (b4) Mn element distributions.

(M=Martensite, F=Ferrite and RA=Retained Austenite)

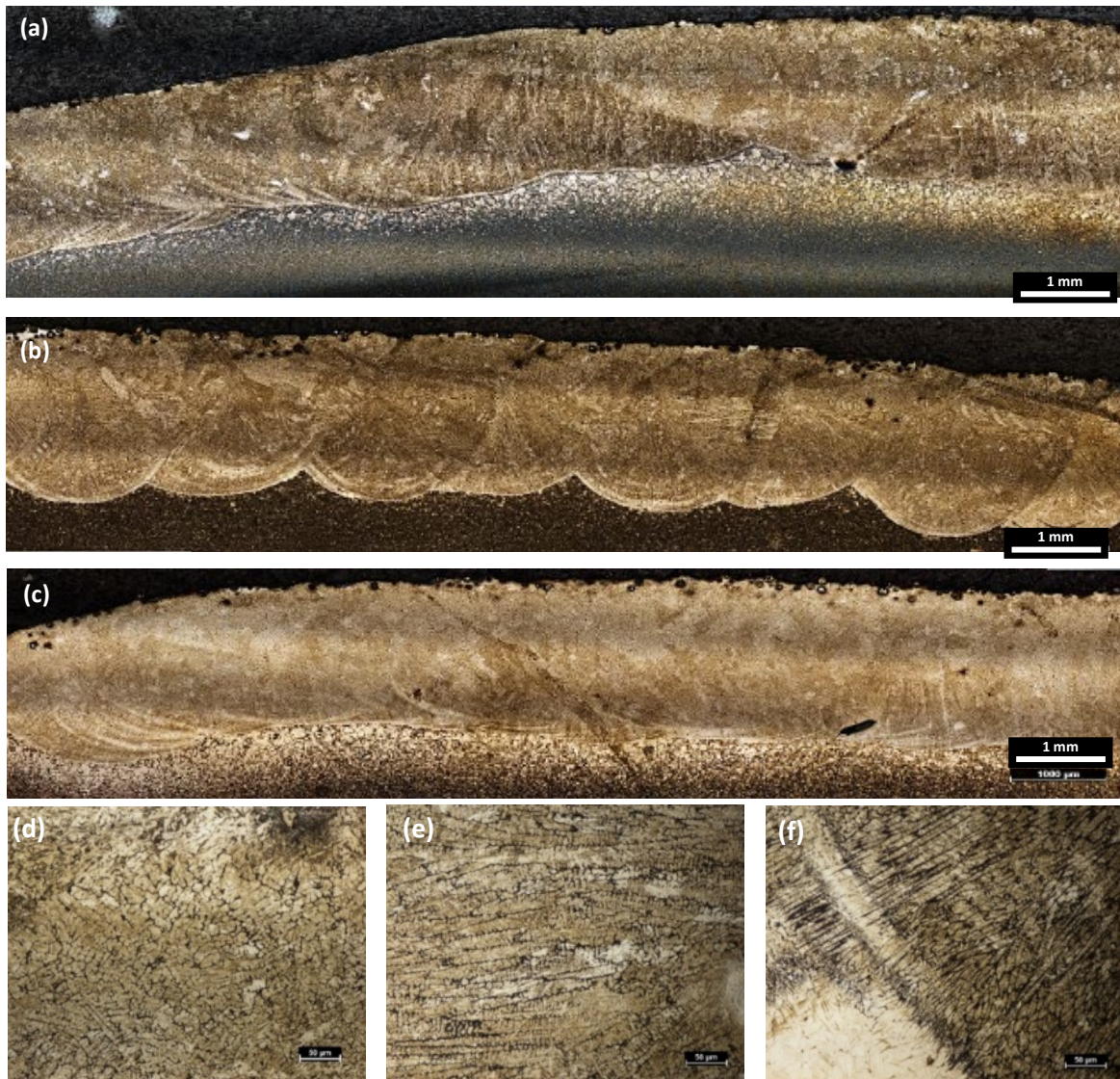


Figure 4-8 Micrographs showing the fine dendritic microstructure of the cross sections of the 410L rail-transversely deposited clad (Group 1) at (a) left gauge corner (Start), (b) middle section and (c) right gauge corner. (d) Typical equiaxed dendritic grains, (e) columnar/cellular dendritic grains. (f) planar dendritic grains located from top to bottom of the Group 1 clad, respectively.

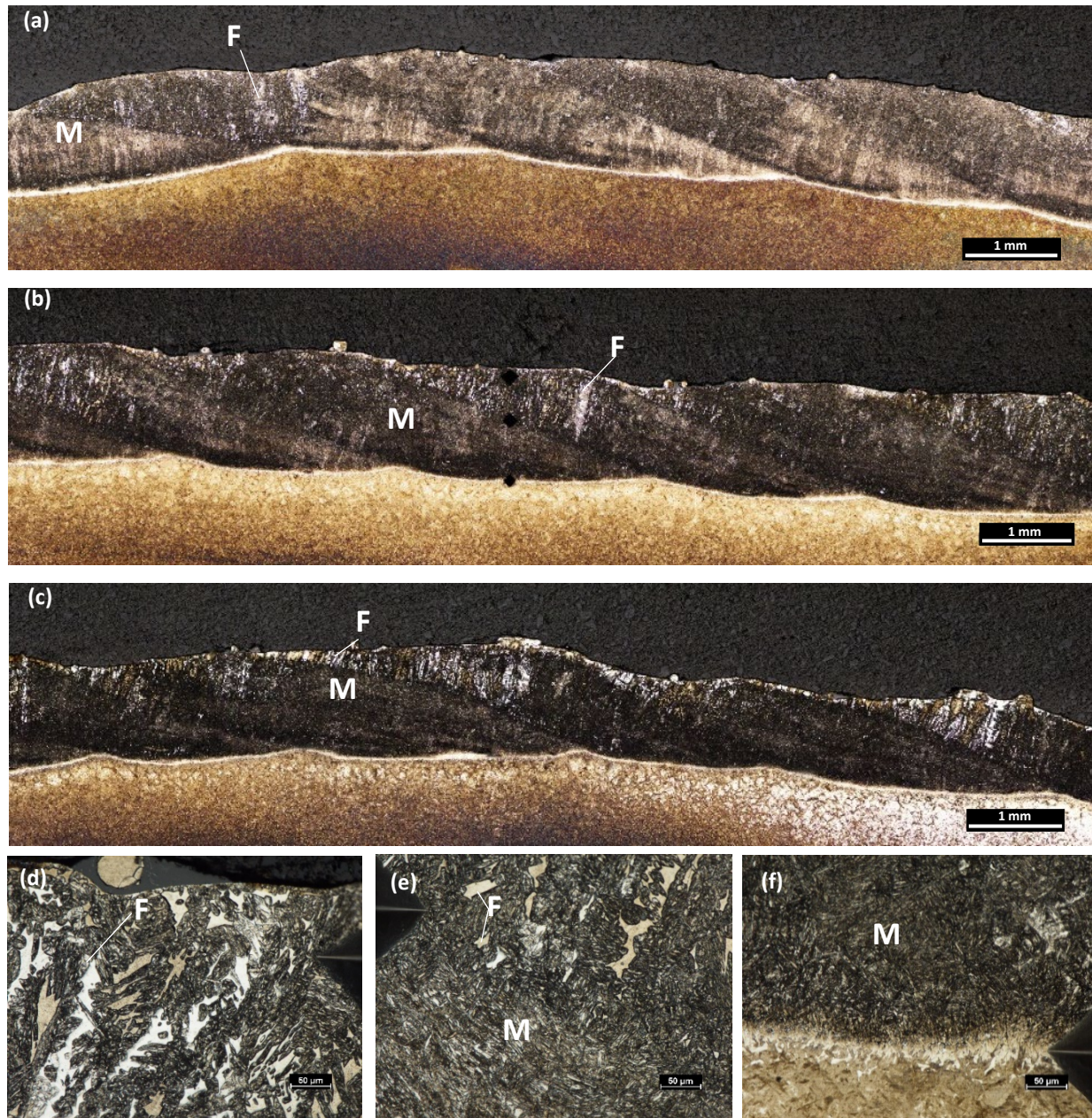


Figure 4-9 Micrograph showing the 410L rail-longitudinally deposited clad (Group 2) microstructure of the cross sections of the at (a) left gauge corner, (b) middle section and (c) right gauge corner. (d) Ferritic colonies in the (e) martensite matrix. (f) The Group 2 interface. (F=Ferrite, M=Martensite)

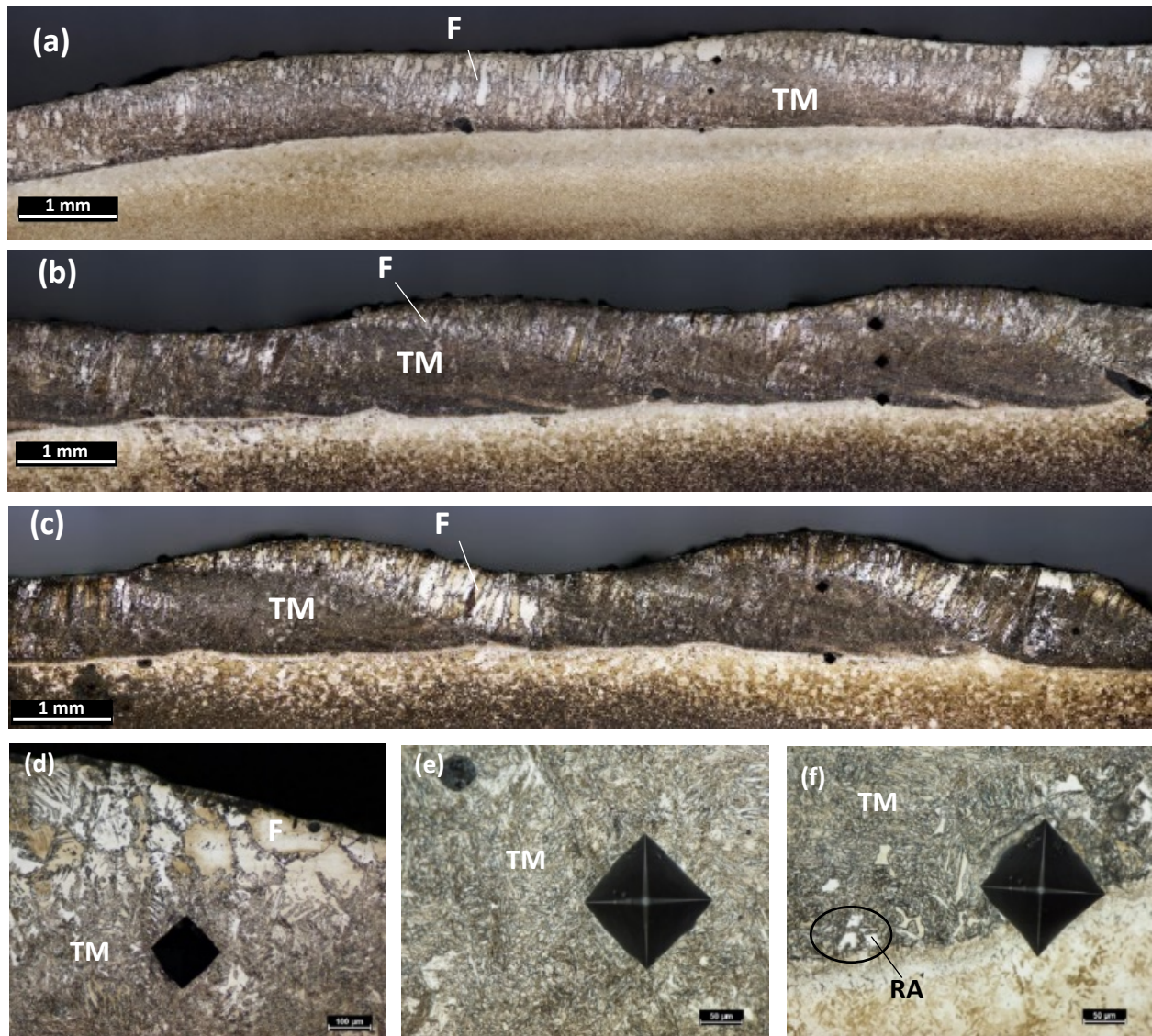


Figure 4-10 Micrograph showing the 410L rail-longitudinally deposited clad (Group 3) microstructure of the cross sections of the at (a) left gauge corner (Start), (b) middle section and (c) right gauge corner. (d) Ferritic colonies in the (e) tempered martensite matrix. (f) Small retained austenite colonies developed near the interface, due to dilution. (F=Ferrite, TM=Tempered martensite, RA=Retained austenite)

4.3.2 Microstructure of the 410L cladding layers

Figure 4-8 (a)-(c) show optical images of the rail cross-sections at left gauge corner (Start), middle section, and right gauge corner of the 410L rail-transversely deposited layer (Group 1), respectively.

The 410L transversely deposited layer contains a large portion of the fine dendritic. Three dendritic morphologies were discernible (i) Equiaxed dendritic zone shown in Figure 4-8 (d), (ii) Columnar/cellular dendritic zone shown in Figure 4-8 (e), and (iii) Planar dendritic zone shown in Figure 4-8 (f) located from the top to bottom of the layer respectively. These dendritic morphologies were consistently detected across the entire thickness; this is consistent with findings in the literature [83, 84].

The micrographs of the rail cross-sections at left gauge corner (Start), middle section, and right gauge corner of the Group 2 deposited layer were shown in Figure 4-9 (a)-(s), respectively. Compared to the Group 1 specimens, in addition to the martensite, ferritic colonies are observed on the surface of the deposited layer as evident in Figure 4-9 (a)-(f) as bright colours etching band. It is noted that ferritic colonies observed periodically throughout the deposited layer on the surface and overlap region of laser traverses.

Similarly, Figure 4-10 (a)-(c) show the rail cross-sections at left gauge corner (Start), middle section, and right gauge corner of the 410L rail-longitudinally deposited layer (Group 3) respectively. Compared to the Group 2 specimens increases in size and density of ferritic colonies are observed in the deposited layer as evident in Figure 4-10 (a)-(e). The periodic occurrence of the ferritic bands is more pronouncedly observed throughout the deposited layer.

4.3.3 Microstructure of the HAZ beneath the 410L clads

The optical images of the rail transverse sections depicting the heat affected zone (HAZ) and the unaffected rail substrate under the 410L rail-transversely deposited layer (Group 1) at left gauge corner, middle section and right gauge corner are shown in Figure 4-11 (a)-(c) respectively. Likewise, Figure 4-11 (d) shows the microstructure of a representation of the rail longitudinal sections.

Four sub-regions were detected inside the Group 1 HAZ. (i) Partially molten zone featured by a metallurgical bond between the deposited layer and substrate shown in Figure 4-12 (a). (ii) Coarse-grained HAZ, in rail-transverse sections, characterised by full pearlite at the middle section as shown in Figure 4-12 (b), and martensite was observed in this zone at the gauge corners shown in Figure 4-11 (a) and (b). In contrast, in the rail-longitudinal sections, martensite was discerned in all sections of this zone as shown in Figure 4-11 (d). (iii) Fine-grained HAZ with partially and fully pearlitic structure in finer nodules are shown in Figure 4-12 (c). (iv) Spheroidised and partial spheroidised microstructure were located adjacently to the unaffected substrate and at the furthest regions from the interface shown in Figure 4-12 (d).

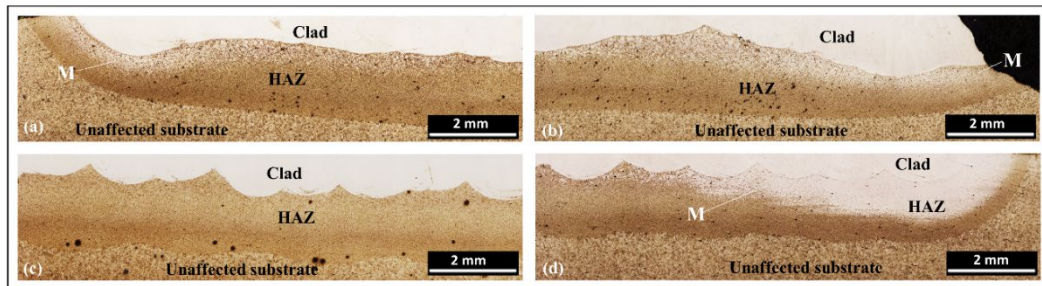


Figure 4-11 Micrograph showing the HAZ and rail substrate of the rail-cross sections at (a) left gauge corner, (b) right gauge corner, (c) middle section and (d) a representative of the longitudinal sections under the 410L rail-transversely deposited clad (Group 1). The light etching microconstituent in the HAZ of (a), (b) and (d) is martensite. (M=martensite)

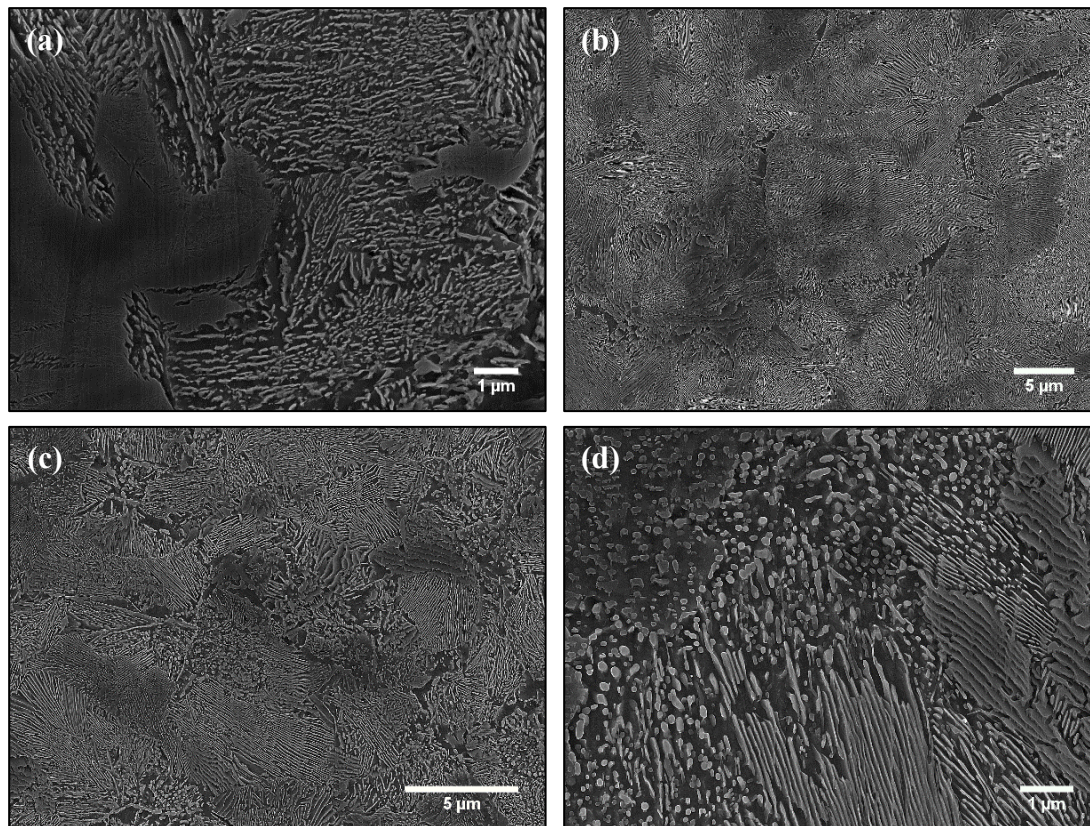


Figure 4-12 SEM micrographs of the sub-regions in the Group 2 HAZ. (a) Partially molten zone featuring a metallurgical bond at the top. In the middle, (b) coarse-grained HAZ characterized by fully bainitic structure and (c) fine-grained HAZ characterized by a combination of pearlite and bainite, and (d) Inter-critical HAZ characterized by spheroidite at the interface under the 410L rail-transversely deposited clad (Group 2).

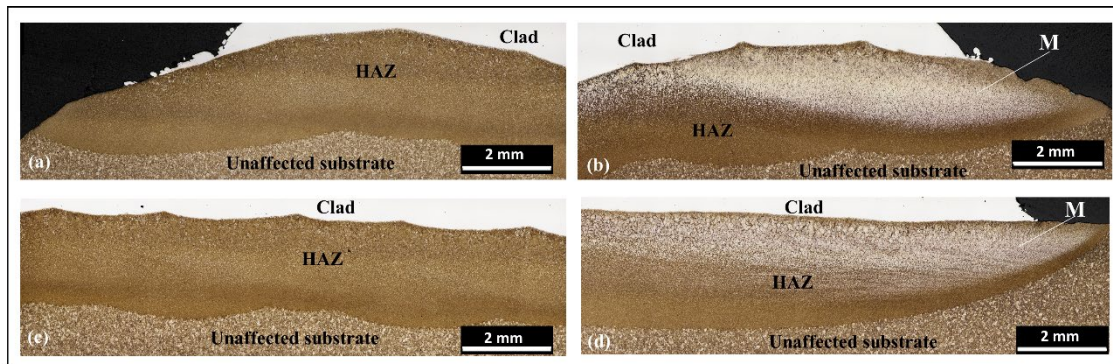


Figure 4-13 Micrograph showing the HAZ and rail substrate of the rail-cross sections at (a) left gauge corner, (b) right gauge corner, (c) middle section and (d) a representative of the longitudinal sections under the 410L rail-transversely deposited clad (Group 2). The light etching microconstituent in the HAZ of (b) and (d) is martensite. (M=martensite)

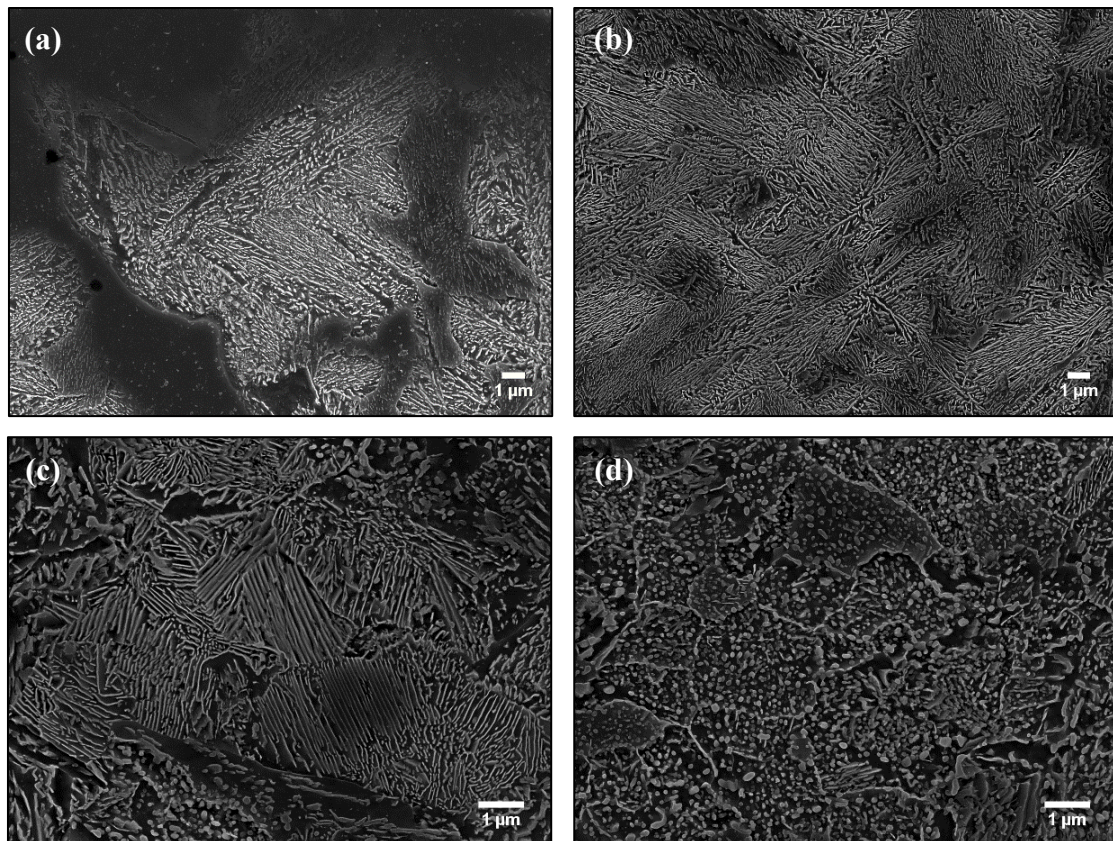


Figure 4-14 SEM micrographs of the sub-regions in the Group 2 HAZ. (a) Partially molten zone featuring a metallurgical bond at the top. In the middle, (b) coarse-grained HAZ characterized by fully bainitic structure and (c) fine-grained HAZ characterized by a combination of pearlite, bainite and spheroidite, and (d) Inter-critical HAZ characterized by spheroidite at the interface under the 410L rail-transversely deposited clad (Group 2).

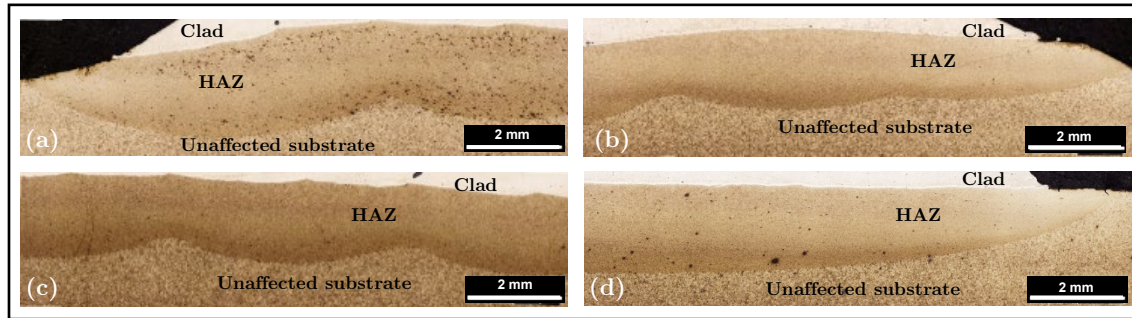


Figure 4-15 Micrograph showing the HAZ and HE400 substrate of the rail-cross sections at (a) left gauge corner, (b) right gauge corner, (c) middle section and (d) a representative of the longitudinal sections under the 410L rail-transversely deposited clad (Group 2). Tempered martensite was found occasionally.

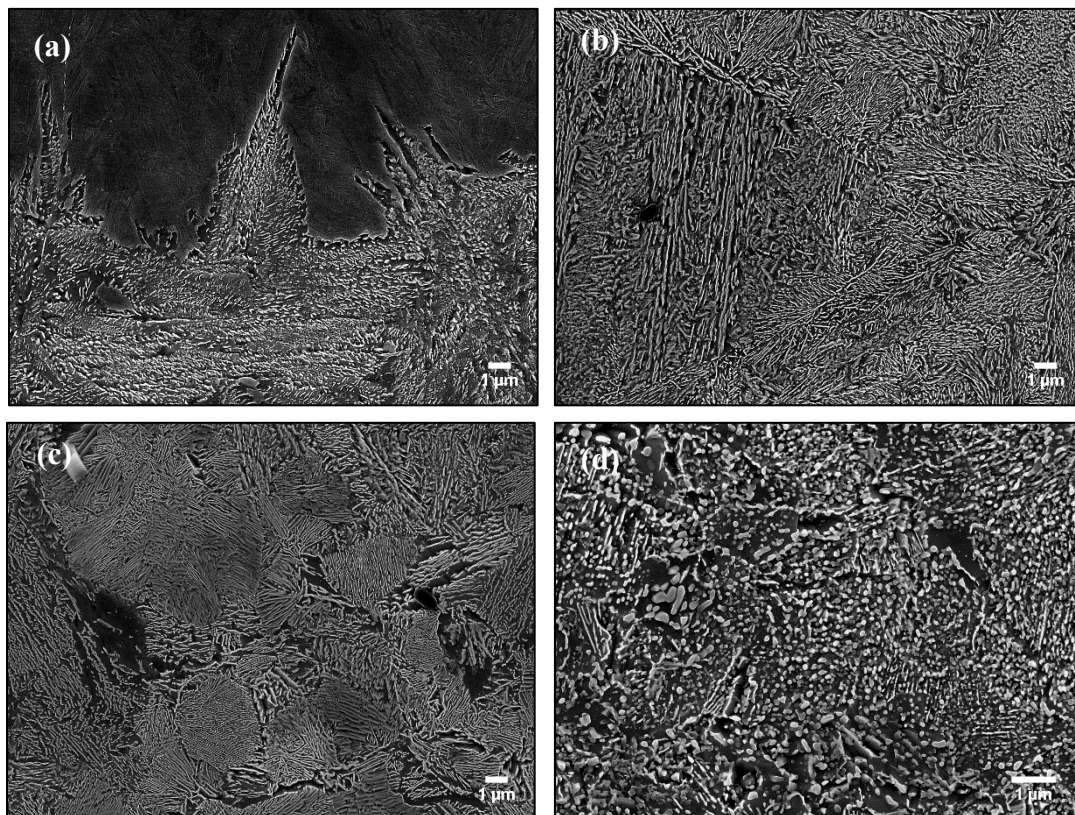


Figure 4-16 SEM micrographs of the sub-regions in the Group 3 HAZ. (a) Partially molten zone featuring a metallurgical bond at the top. In the middle, (b) Coarse-grained HAZ characterized by fully pearlitic structure and (c) Fine-grained HAZ characterized by partially and fully pearlitic structure, and (d) Inter-critical HAZ characterized by spheroidite at the interface under the 410L rail-longitudinally deposited clad (Group 3).

Micrographs of the rail transverse sections depicting the HAZ and substrate under the Group 2 deposited layer at left gauge corner, middle section and right gauge corner are shown in Figure 13 (a)-(c), respectively. A representative microstructure of the rail longitudinal sections of the Group 2 specimens is shown in Figure 13 (d). Similar to the Group 1 specimens, the aforementioned four sub-regions were also discerned in the HAZ of the Group 2 specimens. However, for the Group 2 specimens, the microstructures in (ii) the aforementioned coarse-grained HAZ and (iii) fine-grained HAZ were replaced respectively with bainitic morphology as shown in Figure 4-14 (b) and a combination of pearlite and bainite as shown in Figure 4-14 (c). It is noted that these morphologies are observed in all specimens of the rail transverse and longitudinal sections. (i) The partially molten zone featuring a metallurgical bond and (iv) Inter-critical HAZ with spheroidite were analogous to those of the Group 1 specimens as shown respectively in Figure 4-14 (a) and (b).

Figure 4-15 (a)-(c) show the micrographs of the rail transverse sections depicting the HAZ and base material under the 410L rail-longitudinally deposited layer (Group 3) at left gauge corner, middle section and right gauge corner, respectively. A representative microstructure of the rail longitudinal sections of the Group 3 specimens is shown in Figure 4-15 (d).

For the Group 3 specimens, the four sub-regions were also found with the analogous microstructural characteristics to those in the HAZ of the Group 2 specimens. (i) The partially molten zone featuring a metallurgical bond is discerned in Figure 4-16 (a). The microstructures in (ii) the coarse-grained HAZ with bainitic morphology, (iii) fine-grained HAZ with a combination of pearlite and bainite, and (iv) Spheroidised or partial spheroidised microstructure are shown in Figure 4-16 (b)-(d), respectively.

4.3.4 Microhardness tests

Measurements of microhardness were performed on rail-transverse sections of the three deposited layers to investigate the effect of the applied laser heat source and heat treatments on surface hardness of the deposited layer, HAZ and substrate. In this study, indentations of 5 kgf were conducted vertically from the top surface of the deposited layer to the unaffected base material in the middle and at the gauge corners.

For the rail-transversely deposited layer (Group 1), the vertical microhardness distribution of its rail-transverse sections as shown in Figure 4-17 showed the clad's average hardness values of 678 HV, 720 HV, and 687 HV for the middle section, left gauge corner, and right gauge corner respectively. The average hardness at gauge corners is greater than that of the middle section. Likewise, for the HAZ, the variation in average hardness is analogous to that of the clad. The average hardness of 388 HV, 455 HV and 437 HV was measured for the middle section, left gauge corner, and right gauge corner respectively. These average hardness values are comparable to the value of the unaffected base material, which is deduced to be approximately 400 HV.

The vertical microhardness distribution at rail-transverse sections of the Group 2 deposited layer is shown in Figure 4-18. The deposited layer's average hardness values of 373 HV, 403 HV, and 388 HV were measured for the middle section, left gauge corner, and right gauge corner respectively. Moreover, the average hardness values in the Group 2 HAZ were determined to be 403 HV, 399 HV, and 635 HV at the middle section, left gauge corner, and right gauge corner respectively.

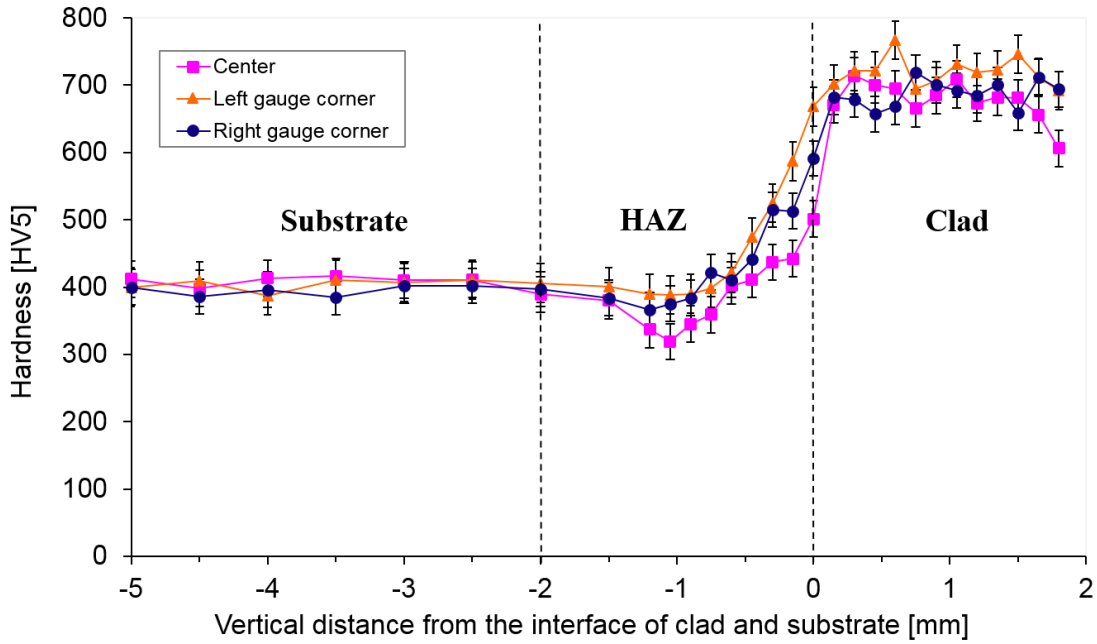


Figure 4-17 Vertical hardness distribution of the rail transversely deposited (Group 1) clad.

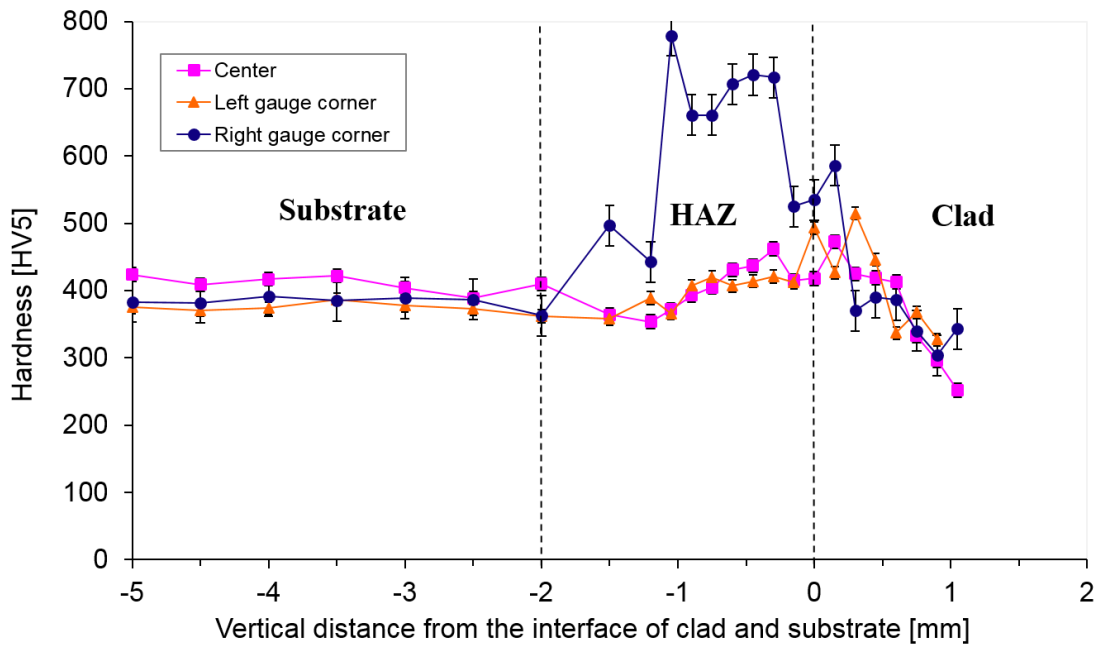


Figure 4-18 Vertical hardness distribution of the rail longitudinally deposited (Group 2) clad.

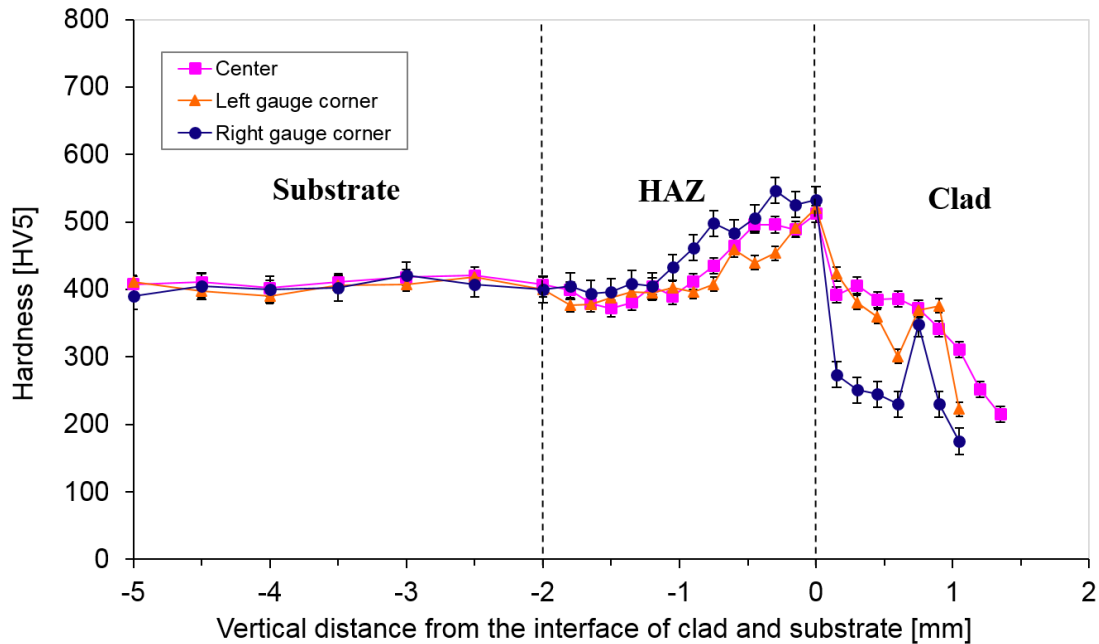


Figure 4-19 Vertical hardness distribution of the rail longitudinally deposited (Group 3) clad.

Figure 4-19 illustrates the vertical microhardness distribution of the rail longitudinally deposited layer (Group 3). Comparing to the Group 2 specimens, the deposited layer's average hardness decreases to 340 HV, 348 HV and 251 HV for the middle section, left gauge corner, and right gauge corner respectively. Comparing to those of the Group 1 and Group 2 deposited layers, the average hardness of HAZ in Group 3 remains fairly stable across the railhead. The hardness of HAZ for the middle section left gauge corner and right gauge corner was averaged to be 429 HV, 419 HV, and 460 HV, respectively.

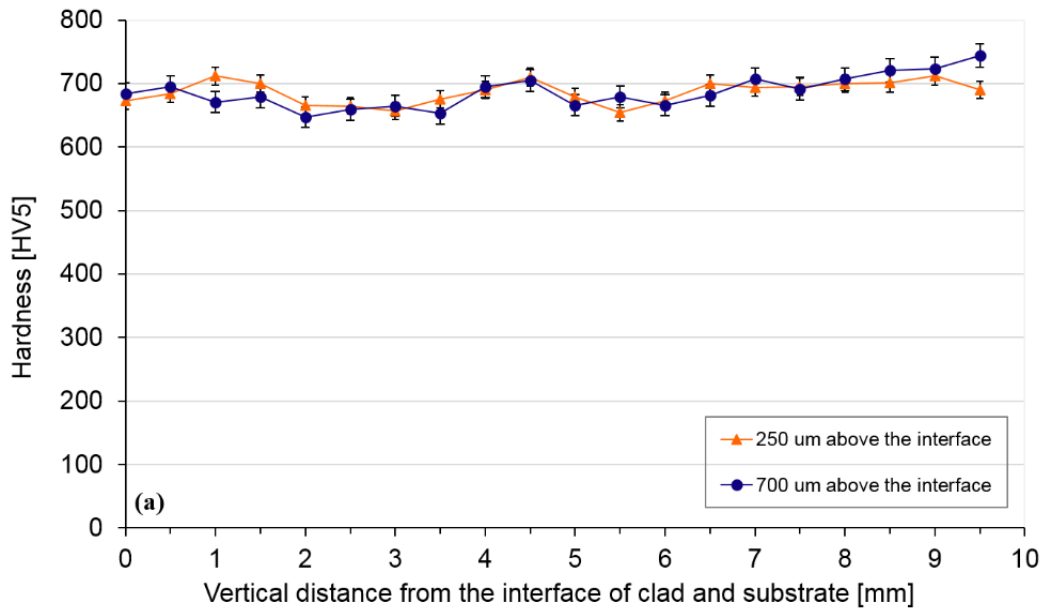


Figure 4-20 Horizontal hardness distribution of (a) the rail transversely deposited clad (Group 1).

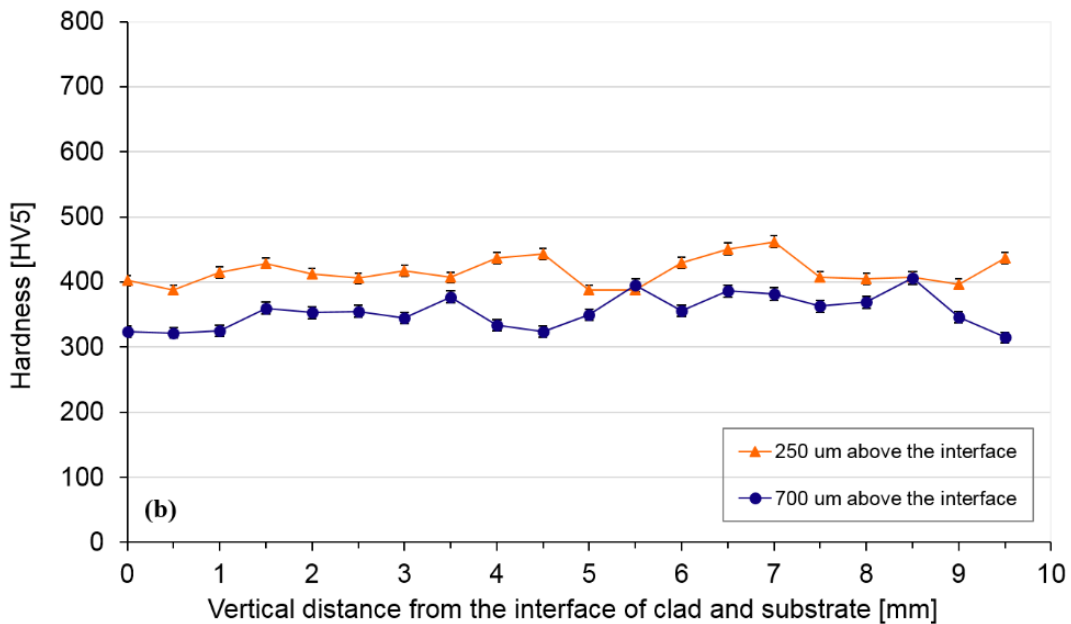


Figure 4-21 Horizontal hardness distribution of the rail longitudinally deposited clad at rail-transverse middle sections (Group 2).

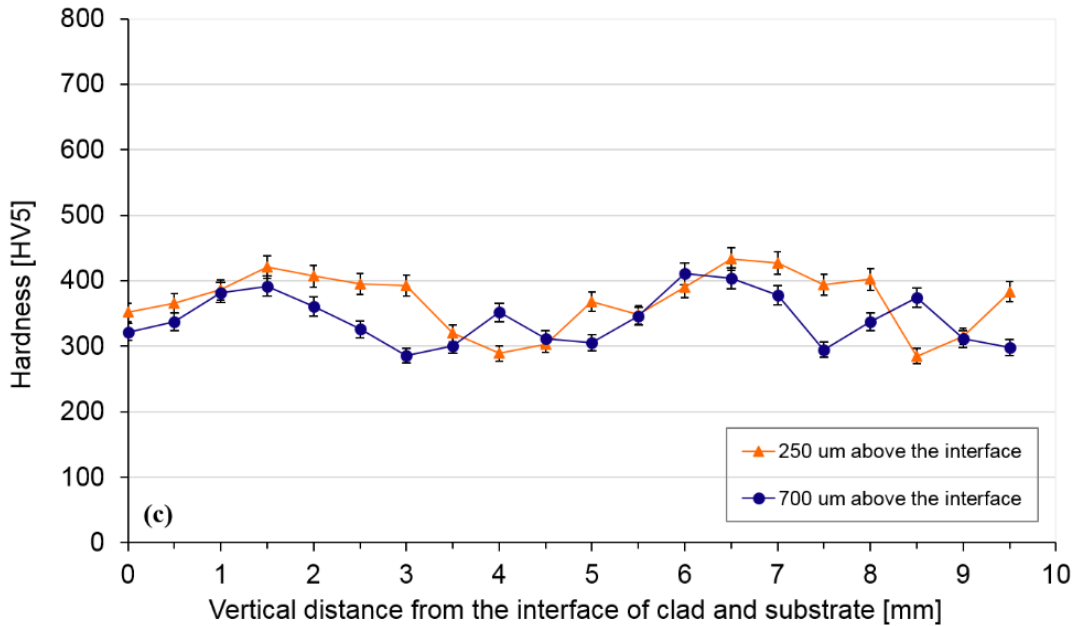


Figure 4-22 Horizontal hardness distribution of the rail longitudinally deposited clad at rail-transverse middle sections (Group 3).

To study the influence of the remelted regions between laser tracks on surface hardness of the laser cladded rails, measurements of hardness distribution were conducted horizontally on the deposited layers of Group 1, Group 2 and Group 3 as shown in Figure 4-20, Figure 4-21 and Figure 4-22, respectively. Overall, the hardness values vary in a sinusoidal fashion with horizontal distance across the deposited layers, which is attributed to the presence of the remelted regions. The sinusoidal variation in hardness of the Group 1 and Group 3 are respectively the smallest and greatest in magnitude amongst the three deposited layers as shown in Figure 4-20, Figure 4-21 and Figure 4-22.

4.3.5 Strength of the laser deposited layers

One of the main stress modes developed under wheel-rail contact is shear which acts at an angle to the loading direction [5]. Depending on the friction coefficient or creepage, the maximum shear can be either located at rail surface or subsurface, where rolling contact fatigue (RCF) damage is

commonly detected. RCF damage is found to increase with greater shear stress [85]. Therefore, it is crucial to evaluate shear strength of the laser treated rails by means of shear punch testing. Shear punch testing is also an effective method to assess other material properties, namely yield strength (YS), ultimate tensile strength (UTS), etc., when the material availability is limited [76-78]. Figure 4-23 shows the average load-displacement curves of five measurements for the three specimen groups.

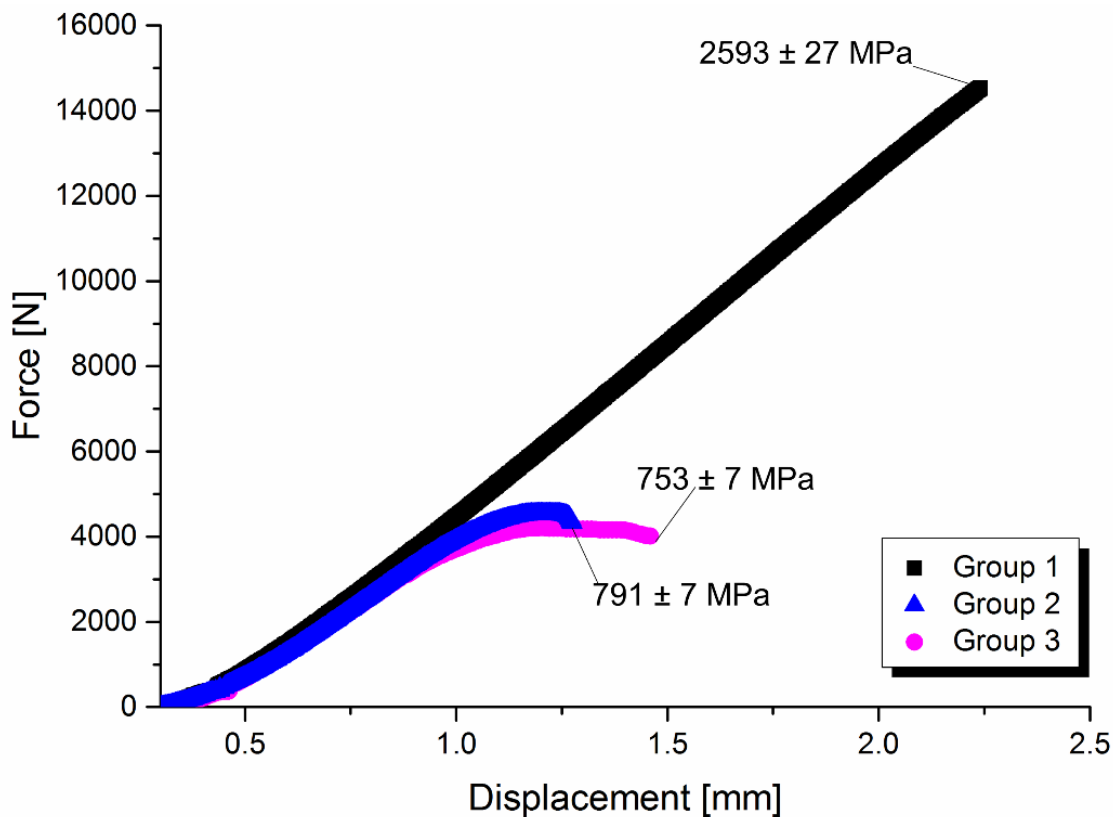


Figure 4-23 The load-displacement curves with corresponding ultimate shear strength (USS) values acquired for the 410L deposited layers subjected to different heat treatment and processing parameters.

The solid Group 1 specimens required an average shearing force of 14.45 kN and corresponding ultimate shear strength (USS) of 2593 ± 27 MPa to fail with a fast brittle fracture. However, similar measurements for the Group 2 and Group 3 revealed typical elastic-plastic behaviour upon fracture with average failure loads of 4.5 kN and 4.2 kN and their corresponding USS of 791 ± 7 MPa and 753 ± 7 MPa. Correlation between ultimate shear and tensile data has been well-established from previous studies [86]. Thus, estimations of the ultimate tensile strength (UTS) of 4667 ± 49 MPa, 1423 ± 14 MPa, and 1355 ± 14 MPa can be safely made of the deposited layers of Group 1, Group 2, and Group 3 respectively. Pun et al. [87] reported that the ultimate tensile strengths (UTS) of two comparable premium rail grades were 1384 MPa and 1429 MPa, which suggests the UTS of 410L depositing layers are comparable to the virgin rails in term of strength.

4.4 Discussion

At similar cladding process parameters, using different cladding directions and heat treatment regimes, during the laser deposition, on the railheads generated variation in the microstructure of the deposited layers and HAZ.

4.4.1 Microstructure of the laser deposited layers

4.4.1.1 The rail transversely deposited layer with preheating only (Group 1)

Previous works [83, 84] reported the influence of local G/R ratio, where G is temperature gradient, and R is solid-liquid interface growth rate, on solidification modes over the thickness of deposited layers. In this current work, the fine dendritic structure, in the rail-transversely deposited layer (Group 1), was formed by the rapid heat transfer facilitated by the substrate acting as an effective heat sink during the cladding process. It also causes variation in G and R across the thickness of the deposited layer. Planar dendrites developed in highly localised regions with significant G/R

ratio near the interface, since the local temperature gradient (G), was virtually infinite. The ratio significantly was reduced as approaching the middle section of the deposited layer, which resulted in the gradual formation of cellular and columnar dendrites. Likewise, the G/R ratio was approximately lowest in the vicinity of the top surface giving mostly equiaxed dendritic grain. Consequentially, from the top to the bottom of the deposited layer, the three typical grain morphologies of the dendritic structure in Group 1 deposited layer were equiaxed grains, cellular grains, columnar grains and planar crystals as observed in Figure 4-8. [83]

The X-ray diffraction patterns of the laser treated 410L stainless steels were demonstrated to contain alpha (α) and gamma (γ) irons. The martensite (α) and retained austenite (γ) were reported to locate in dendrites and dendritic grain boundaries, respectively [88, 89]. Similarly, the XRD and EBSD results in the current investigation show the presence of martensite with BCC within the dendrites and retained austenite with FCC between the dendrites (or at dendritic grain boundaries) and at the interface. According to [89], segregation of Carbon (C) promoted the growth of retained austenite phase. However, in the current work micro-segregation of Chromium (Cr) and Manganese (Mn) to the dendritic grain boundaries was also noted in the specimens of Group 1. During the rapid solidification, the distributions of Chromium (Cr), as shown in Figure 4-2 (c) and Figure 4-3 (c), and Manganese (Mn), as shown in Figure 4-2 (d) and Figure 4-3 (d), alloying elements were greatly influenced by large cooling rate respectively. In other words, the Cr and Mn elements showed high tendency to segregate to the last areas to solidify, which are the locations between the dendritic arms/at grain boundaries in this case [90].

The amount of retained austenite in the steel was greatly influenced by the alloying elements [91]. The Mn and Cr segregated to the dendritic grain boundaries as shown in Figure 4-2 (a3, a4) and Figure 4-3 (b3, b4). The combined effects of alloying elements led to the formation of retained austenite at the dendritic grain boundaries in the Group 1 specimens.

The other elements were distributed homogeneously throughout the deposited layer. The retained austenite at the interface is probably coming from an origin that is different to the one discussed above and could be attributed to the substrate dilution, so that the carbon (C), acting as an austenitic stabilizer, of the 0.84–0.95 wt.% C rail substrate melted participates in the constitution of the 0.01 wt.% C deposited layer. Solidification cracks were detected in the transversely deposited layer (Group 1) as shown in Figure 4-24, which have been reported to be caused by rapid cooling rate, which induced substantial residual stress in the deposited layer [92].

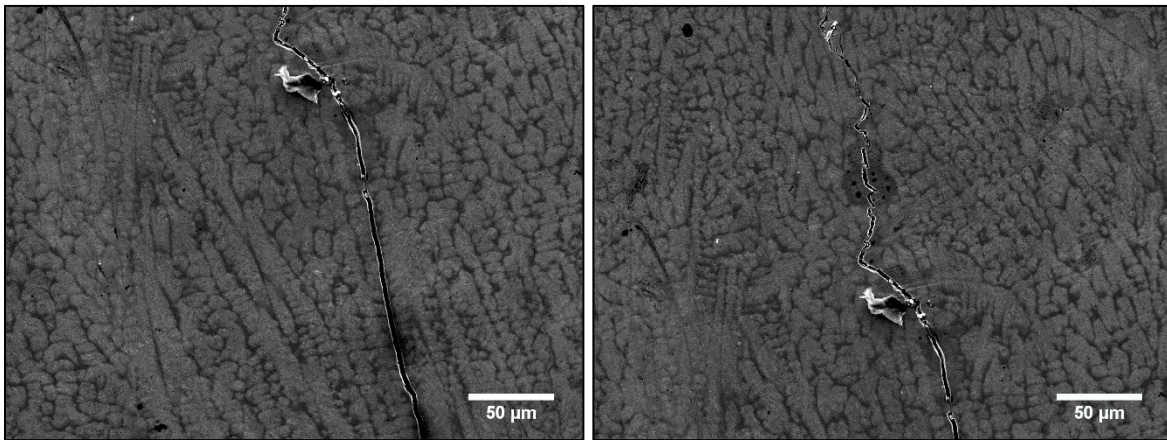


Figure 4-24 Morphology of solidification cracks in the cladding layer of Group 1.

4.4.1.2 The rail-longitudinally deposited layer with preheating only (Group 2)

As being subjected to a modification in cladding direction, there are corresponding changes in morphology and microstructural characteristics of the rail-longitudinally deposited layer (Group 2). Phases, such as retained austenite, ferrite and martensite were identified by the outcomes of the XRD and EBSD analyses. Small occasional retained austenite colonies near the 410L - rail interface and bands of elongated ferritic colonies, located near the top surface and in the laser overlapping regions as evident in Figure 4-1 and Figure 4-4. Both the bands and the matrix possess BCC, whereas the small retained austenite colonies in the vicinity of the interface with FCC owing to the aforementioned substrate dilution.

The employment of rail-longitudinal cladding direction in Group 2 specimens removed the prevalent dendritic characteristics in the deposited layer's microstructure of the regular laser treated specimens reported by previous studies [70, 83, 93, 94], or the Group 1 specimens in particular. It may be attributed to a decrease in the total accumulated heat used to penetrate the substrate, correspondingly lowering the total amount of dilution and the thermal gradient during the clad solidification. The longer length of each laser run will result in less heat accumulated for subsequent runs owing to heat conduction via substrate and air convection. Furthermore, the repeated occurrence of martensite in the vicinity of the interface, and ferrite colonies near the top surface might indicate the variation in dilution level, particular carbon with high diffusivity in steel [95, 96]. The further away from the interface, the lower dilution level will be. The greater dilution level near the interface might facilitate the phase transformation of martensite. In contrast, ferrite colonies, densely occupy the nearby top surface where the dilution level might be lower. In addition, ferrite was found to nucleate from the interface between two separate laser runs. This can be caused by the insufficient concentration of local alloying elements to dilute to the new deposited layer.

4.4.1.3 The rail-longitudinally deposited layer with preheating, post-heating and slow cooling (Group 3)

The rail-longitudinal cladding direction applied in the Group 3 specimens induced the deposited layer's microstructural characteristics, which is relatively analogous to those of the Group 2 deposited layer. Retained austenite, ferrite and martensite were still recognised by the results of the XRD and EBSD analyses. However, the application of PWHT and slow cooling has tempered the martensite formed and facilitated the increases in grain size and volume fraction of ferrite as discussed in Section 4.3.2.

4.4.2 Microstructure of the HAZs beneath the 410L deposited layer

Under the 410L deposited layers, multiple sub-regions in the HAZs were developed as a result of the substrate microstructure subjected to the effects of heating and cooling during the laser cladding process. For hypereutectoid rail steel, four main sub-regions are pronouncedly identifiable from the interface to the unaffected substrate, (i) Partially molten zone, (ii) Coarse-grained HAZ, (iii) Fine-grained HAZ, and (iv) Inter-critical HAZ respectively. Each of these sub-regions is completely influenced by their local thermal history. All sub-regions were discerned in the three deposited layers as evident from Figure 4-11 to Figure 4-16.

4.4.2.1 The rail transversely deposited layer with preheating only (Group 1)

For the rail-transversely deposited layer (Group 1), in the spheroidised or partial spheroidised zone shown in Figure 4-12 (c) and (d), the local peak temperature is always below the critical temperature when austenite begins to form, which implies that the majority of the heat supplied in this zone is to temper the pearlitic microstructure of the substrate [97, 98].

Fine-grained HAZ with the fully pearlitic morphology within fine nodules in the region located directly above the transition region, as shown in Figure 4-12 (c). The local peak temperature was determined to be greater than the critical temperature A_{c3} , which is the temperature at which austenitic transformation was completed. However, the rapid cooling rate induced a fine grain structure within the sub-region.

Adjoining to the interface, thereby, the coarse-grained HAZ is subjected to the high peak temperature beyond A_{c3} . The higher temperature facilitates the significant grain growth. During the cooling stage, depending on the cooling rate, the austenitic grains undergo different solid-state

transformations. The resulting phases might be pearlite, bainite, martensite or tempered martensite. For rail-transverse sections, coarse-grained HAZ characterised by full pearlite at the middle section shown in Figure 4-11 (c) and Figure 4-12 (b), and martensite at the gauge corners shown in Figure 4-11 (a) and (c). Similarly, in the rail longitudinal sections, the larger extent of the martensitic was detected at all sections near the interface, especially where the starting and ending of the laser tracks are, see in Figure 4-11 (d). It is attributed to the pre-heating temperature applied was not sufficient to prevent the martensitic transformation. In other words, the resulting temperature of the preheated substrate was under the martensitic transformation temperature, which led to a similar effect to quenching. Therefore, the larger surrounding surface area, the larger extent of martensite formed. As the process proceeding, the heat was accumulated above the martensitic transformation temperature and induced the pearlitic coarse-grained HAZ at the middle section of the laser cladding pad, as shown in Figure 4-12 (b). Nevertheless, the accumulated heat was dissipated more rapidly at the gauge corners due to the large neighbouring surface area of the substrate. Thus, martensite was formed. At the starting and ending of the laser tracks, the neighbouring substrate's surface area was even larger, correspondingly larger extent of martensite was found.

The partially molten zone was at the exact interface of the Group 1 clad and rail substrate, shown in Figure 4-12 (a). It implies that a metallurgical bond has been established, which possesses better sustainability for high impact loads, heavy loaded and stresses situations comparing to mechanical bond.

4.4.2.2 The rail-longitudinally deposited layer with preheating only (Group 2)

Heat affected zones which are generated by laser cladding in the parent material of the Group 2 specimens are also composed of the aforementioned four sub-regions. In the coarse-grained HAZ, for the rail transverse sections, the pre-heating temperature applied was capable of avoiding the

martensitic transformation at the left gauge corner sections where the starting laser runs are and also the middle section as shown respectively in Figure 4-13 (a) & (c), but not at the right gauge corner where the ending laser runs are as shown in Figure 4-13 (b). This phenomenon is related to the heat dissipation of the applied preheating temperature, as the laser source is travelling from the left gauge corner to the right gauge corner. The microstructural features of the left gauge corner and middle sections were more clearly revealed by the means of SEM and was seen to consist of bainite as shown in Figure 4-14 (b). For longitudinal sections, the resulted HAZ's microstructure is martensite, which agrees with that of the Group 1 specimens and suggests that the preheating temperature of 350 °C at length equal to the cladding length is insufficient to hinder the formation of martensite in the HAZ. The Fine-grained HAZ with pearlite inside fine nodules is shown in Figure 4-14 (c) at all rail transverse and longitudinal sections. Similar to the Group 1 specimens, the spheroidised pearlite was present next to the unaffected base rail, as its local peak temperature was only to temper the microstructure.

4.4.3 The rail-longitudinally deposited layer with preheating, post-heating and slow cooling (Group 3)

For the rail-longitudinally deposited layer (Group 3), the four sub-regions were also discerned. Under the influence of the Group 3 heat treatment regime, the microstructural features in the HAZ are relatively analogous to those of the group 2. At almost all rail transverse and longitudinal sections, the solid phase in the coarse-grained HAZ was transformed to bainitic morphology as shown in Figure 4-16 (b), the Fine-grained HAZ with pearlite inside fine nodules is shown in Figure 4-16 (c), and spheroidised pearlite as shown in Figure 4-16 (d). The involvement of post weld heat treatment (PWHT) in the Group 3 heat treatment regime is to mitigate the residual stresses, as a hardness control method and enhance material strength for the deposited layers; and eliminate martensitic formation in the HAZ or, at least, reduce the cracking tendency of the martensite formed in the HAZ by its tempering effects. Tempered martensite was observed instead, particularly at the starting and ending of the laser tracks. This implies PWHT has limited

effect to avoid martensite formation in the HAZ, but it was able to lower cracking tendency in the HAZ, as there were not many pronounced cracks detected.

4.4.3 Mechanical properties of the laser deposited rails

4.4.3.1 The rail transversely deposited layer with preheating only (Group 1)

The inverse correlation between hardness and wear rate was well established in the literature, which is the higher the hardness, the lower the wear rate [50, 99, 100]. Therefore, indications of the laser deposited layers' tribological performance in wheel-rail contact can be obtained by means of Vickers indentation. Krishna et al. [101] have reported that the highest average hardness of the laser surface melted AISI 410 stainless steel sheets is 350 HV. However, in the current study, the highest average hardness of 720 HV was acquired for the rail-transversely deposited layer (Group 1), which is corresponding to the aforementioned martensitic dendrites. It implies that the only application of pre-heating to 350 C at the heating length of 400 mm in Group 1 specimens was insufficient to lessen the rapid cooling rate conditioned by the substrate and prevent the formation of martensite. Lewis et al. [102, 103] have reported that martensitic stainless steels with an average hardness of approximately 650 HV showed superior wear and rolling contact fatigue (RCF) resistance compared to the R260 reference rail. However, the martensitic microstructure of the deposited layer is known for greater brittleness and cracking tendency compared to other microconstituents for a given C content. The average hardness at gauge corners of both the deposited layer and HAZ was greater than that of the middle section, which may be attributed to the accumulation of heat at the middle tracks. The Group 1 HAZ's average hardness of approximately 400 HV, is comparable to the value of the unaffected base material. The local hardness variation in the HAZ is significant, particularly at gauge corners, owing to the proximity of martensite and spheroidite in the HAZ with approximately 700 HV and 300 HV, respectively. Even though the Group 1 deposited layer's UTS is approximately three times than that of virgin

rails, its fast-brittle fracture behaviour and solidification cracks suggest a poor performance in wheel-rail contact.

4.4.3.2 The rail longitudinally deposited layer with preheating only (Group 2)

Along with the preheating temperature of 350 °C at the heating length of 400m, the utilization of the rail-longitudinal cladding direction has lowered the deposited layer's average hardness values approximately to the average hardness of the laser surface melted AISI 410 stainless steel sheets of 350 HV [101]. There were no significant changes in the trends from the left gauge corner to the right gauge corner. The hardness was found to be the lowest in the vicinity of the deposited layer's top surface owing to the presence of ferrite, and steadily increasing as martensite was predominant towards the clad-substrate interface. With the above preheating conditions, the change in the cladding direction was incapable of removing martensite or reducing the peak hardness values significantly in the HAZ. Indeed, the peak average hardness values recorded in the HAZ and associated with martensite were 635 HV at the right gauge corner where the last laser tracks are. This further consolidates the discussion of the infeasibility in applying the preheating temperature of 350 °C at the heating length equal to cladding length in avoiding martensitic formation in the HAZ. With comparable strength to that of virgin rails and acceptable average hardness, sufficiently good performance in wheel-rail contact can be expected for the Group 2 deposited layer.

4.4.3.2 The rail longitudinally deposited layer with preheating, post-heating and slow cooling (Group 3)

On the other hand, for rail-longitudinally deposited layer (Group 3), the addition of post-heating to 350 °C and slow cooling accompanied by the change in cladding direction over-tempered the deposited layer's microstructure. Accordingly, the deposited layer's average hardness was

decreased substantially. Comparing to the substrate's average hardness of 400 HV, the lowest deposited layer's hardness of 251 HV was considered to be soft, which might cause detrimental effects towards the wear resistant characteristics of the cladded rail. The relatively homogeneous microstructure with mostly bainite in the Group 3 HAZ produced hardness values ranging from 370 - 550 HV across the entire railhead, which is adequate for the rail-wheel applications in term of wear resistance. No crack was detected in the Group 3 HAZ. The deposited layer's average hardness decreases to 340.11 HV, 347.57 HV and 250.57 HV for the middle section, left gauge corner, and right gauge corner respectively as shown in Figure 4-19. It was noted that the variation in hardness between the gauge corners was significant. The reason being is that the laser tracks were cladded from right corner to left corner. Thus the local temperature of the left gauge corner is more likely to be lower than that of the right as the rail preheating temperature is cooling down over time. Based on the results of this study, it is suggested to shorten the cladding length or/and use solid-solution strengthening, such as Lanthanum oxide, to increase the hardness of the 410L material.[104, 105]

An investigation by Hang et al. [106] established the existence of remelted regions in multiple overlapping clad-tracks. In agreement with that, the horizontal microhardness distribution of the three deposited layers in the current investigation indicates hardness values varied in a sinusoidal fashion with horizontal distance across the deposited layers, as evident from Figure 4-20 to Figure 4-22. The troughs of the hardness profiles fell into the remelted regions of the deposited layers, where the microstructure is likely tempered or even recrystallized by the heat of the later tracks and the heat treatments applied. In the case of the rail longitudinally deposited layer (Group 3), the microstructure of aforementioned deposited layer at the remelted regions consists of the largest extent of ferrite amongst the three deposited layers. This ferritic microstructure is known to be associated with low hardness, which results in the pronounced troughs in the hardness profile of the Group 3 layer as shown in Figure 4-20. Also, the sinusoidal hardness variation was found in the horizontal hardness profile of the Group 2 layer, but to a lesser extent in amplitude, due to the corresponding smaller amount of ferrite in the remelted regions, as evident in Figure 4-4 and

Figure 4-9. Lastly, the sinusoidal variation in hardness distribution of the Group 1 layer was the least pronounced as fine dendritic martensite was predominant in its resulted deposited layer's microstructure. The observed microstructural characteristics of the remelted regions for the three deposited layers were well correlated with their hardness variations. Despite the fairly good UTS with typical elastic-plastic behaviour, the hardness variation in Group 3 is not favourable for rail-wheel contact, since softened zones on the rail surface are prone to corrugation and may trigger deep rolling contact fatigue (RCF) cracks.

4.5 Chapter Summary

The conclusions made from the investigation of the influence of altering cladding directions and heat treatments applied to the potential performance of the laser-cladded rail steels in wheel-rail contact are summarised as follows:

- For HAZ, the application of preheating to 350 °C at the heating length equal to the cladding length was concluded to be insufficient to prevent the formation of martensite for both cladding directions, the rail-transverse (Group 1) and rail-longitudinal directions (Group 2). Thus, cracking in the HAZ would be likely unavoidable. Nevertheless, the combination of pre-heating, post-heating and slow cooling was proven to provide beneficial tempering to the HAZ microstructure, particularly in those with martensite, and excellent microstructural consistency across the entire rail-longitudinally deposited railhead (Group 3).
 - For the 410L deposited layers, cladding direction has a significant impact on the microstructural characteristics of the deposited layers. Fine dendritic martensite with cracks in the Group 1 was replaced with the resulted microstructure consisting of martensite matrix and occasional ferritic colonies in the Group 2 by being subjected only
-

to a change in cladding direction. It is attributed to the combined effects of cooling rate and dilution conditioned by the substrate. Employment of post-heating and slow cooling leads to a detrimental softening effect on the 410L rail-longitudinally deposited layer (Group 3) with relatively low hardness. It is recommended to shorten the cladding length or/and use solid-solution strengthening to increase the hardness of the 410L material.

- The strength and fracture mechanism of the 410L laser deposited layers are considerably dependent on cladding directions. Rail-longitudinal cladding direction resulted in more favourable mechanical properties in the laser deposited layers
- Distribution of the microconstituents in the deposited layers, particularly retained austenite and ferrite, was strongly influenced by the micro-segregation of alloying elements within the deposited layers during solidification and at the interface owing to dilution from the parent material.
- Microstructural characteristics of the deposited layer's remelted regions was dependent on the cladding directions and heat treatments; and showed a similar correlation with hardness distribution.

The presented findings established the influence of laser depositing directions and heat treatments on the microstructure of the 410L deposited layer and the HAZ of the rail substrate, and the corresponding strength and hardness distribution in the laser deposited layers, which are the key indications of wear and mechanical performance of the cladded rail in wheel-rail contact.

5

Cladding materials and Heat treatments

The effects of utilizing different cladding materials and heating conditions on the microstructural and mechanical characteristics of laser-cladded hypereutectoid rails which are extensively used in heavy-haul rail systems were investigated in this chapter. Laser cladding of premium hypereutectoid rails with 410L, 420SS, Stellite 6 and Stellite 21 for both single and double deposition was studied under two heating conditions, i.e. preheating only (HTA) and a combination (HTB) of preheating and post weld heat treatment (PWHT). The most suitable cladding material for wheel-rail contact among the considered materials was established by assessing all crucial aspects, i.e. surface quality, hardness, material strength.

5.1 Introduction

This chapter explores the influence of cladding materials, processing parameters and heating conditions on the underlying microstructural features and mechanical properties of laser-cladded premium rails. Cladding materials of 410L, 420SS, Stellite 6 and Stellite 21 with single and double depositions are considered for the comparative study of processing parameters. Chemical compositions of the depositing materials are shown in Table 3-1. To maintain the thickness of the laser deposits for comparison, transverse speed and powder feed rate were modified concurrently in the ranges of 1000 - 1200 mm/min and 3 - 4 RPM, respectively. Two heating conditions, i.e. preheating only (HTA) and a combination (HTB) of preheating and post weld heat treatment (PWHT) are applied after the optimum parameters for each cladding material was obtained. The most suitable cladding material for rail-wheel contact was established by assessing all crucial aspects, i.e. surface defects, hardness, microstructural and mechanical properties. Process parameters for each considered material were optimized to achieve no surface defects.

To establish functionally graded rails, in this chapter, laser cladding of the cladding materials was applied to 600-mm premium hypereutectoid rail pieces, as shown in Table 3-2, using a coaxial fibre laser nozzle. Interpretation of microstructures of both the cladding layers and the heat affected zone (HAZ) in the rail substrate was achieved based on images of optical microscopy (OM) and Scanning Electron Microscopy (SEM). To investigate and compare mechanical properties between different depositing materials, shear punch and tensile testing were performed. Indications of wear resistance of cladding layer were obtained via Vickers indentation, thereby, the correlation between the microstructural characteristics and the wear performance was also established.

5.2 Experimental Setup - Optimum processing parameters and heat treatments

In the current work, comparative studies of the deposition of the four cladding materials on rail substrate were conducted by changing the heating conditions, process parameters and number of deposited layers. The heating condition of preheating to 350 °C was conducted by using a conventional manual oxy torch. To monitor the homogeneity of preheating temperature, three thermocouples were attached and measured at the start, middle and end of the cladded region during the preheating application to the full rail head. Immediately upon the achievement of the preheating temperature of 350 °C across the specimen, laser deposition was initiated. Thereafter, PWHT was carried out to tailor the cooling rate, hence acquiring the desired properties, i.e. microstructure and hardness, for the designed functionally graded material. Besides PWHT, ceramic heating blankets were also located across the repaired rail to ensure that the temperature of 350 °C across the cross-section of the specimen was obtained. Descriptions of the distinct heating conditions used are listed in Table 5-1.

Table 5-1 Heat treatment procedures applied for the comparative study of heating conditions.

Label	Heat treatment procedures
HTA	Preheating to 350 °C
HTB	Preheating to 350 °C, post-heating to 350 °C and then was slow-cooled to room temperature by using a ceramic blanket.

Table 5-2 Parameter sets and deposited layer number applied for the comparative study.

Specimen Groups	Process parameter sets	No. of deposited layers
G1-1L	1000 mm/min; 3 RPM powder; 3200W	1
G1-2L	1000 mm/min; 3 RPM powder; 3200W	2
G2-1L	1200 mm/min; 4 RPM powder; 3200W	1
G2-2L	1200 mm/min; 4 RPM powder; 3200W	2

To maintain the thickness of the laser deposits for comparison, transverse speed and powder feed rate were modified concurrently and accordingly, while laser power was kept as constant. Transverse speed and powder feed rate were varied in the ranges of 1000 - 1200 mm/min and 3 - 4 RPM, respectively. The ranges were selected to give no detected surface defects for the cladding materials. The used process parameter sets were detailed in Table 5-2. Cladding direction was in the rail-longitudinal direction for all the depositions.

Representative metallographic specimens were prepared by sectioning the cladded rails in both rail-transverse and longitudinal directions. The obtained specimens were undergone the basic steps for standard metallographic specimen preparation, i.e. grinding, mounting, polishing and etching. For etching, a two-stage etching procedure was implemented to provide a comprehensive microstructural characterization; in the first stage, Kalling's no. 2 (5g CuCl₂, 100 ml HCl and 100 ml ethanol) and CoM1 (50 ml Distilled water and 50 ml HCl) solution were used to unveil the microstructure of the stainless steel and Co-base deposits, respectively and a 2% Nital etchant was used in the second stage to study the rail steel substrate's microstructure. A Nikon Eclipse optical microscope and a JEOL 7001F FEG scanning electron microscope were utilized to perform

the microstructural characterization on the obtained specimens. Evaluation of the mechanical properties of the cladded layers was achieved via the Struers A300 Duramin hardness tester and shear punch tests.

5.3 Experimental Results

5.3.1 Comparative studies for optimum processing parameters and heat treatments

To obtain defect-free surfaces and identify the appropriate process parameters and heat treatments, an investigation of surface defects and structural integrity of the cladded rails using the studied cladding materials was conducted. High-quality close-up images of the top surfaces for each of the specimen groups are shown in the following figures. For Group 1 with only preheating (HTA), except for Stellite 6 deposits, all other single deposition showed intact cladding surfaces with no visible surface cracks, as shown in Figure 5-1 (a.1) - (d.1). Stellite 6 deposits were found to have surface bubbles, as shown in Figure 5-1 (c.1). The molten pool evaporated and voids formed towards the last laser tracks. For double deposition, similar characteristics were found, as shown in Figure 5-1 (a.2) - (d.2), but the surface bubbles were more severe for Stellite 6, as shown in Figure 5-1 (c.2).

With an increase in the transverse speed and powder feed rate yet constant cladding thickness, cladding surfaces subjected to HTA for Group 2 single and double depositions were found to be free of surface defects as shown in Figure 5-2 (a.1) - (d.1) and Figure 5-2 (a.2) - (d.2), respectively. However, for 410L stainless steel, the second deposition with the traverse speed of 1200 mm/min and 4 RPM was found to cause the molten stainless steel to evaporate, as shown in Figure 5-2 (a.2).

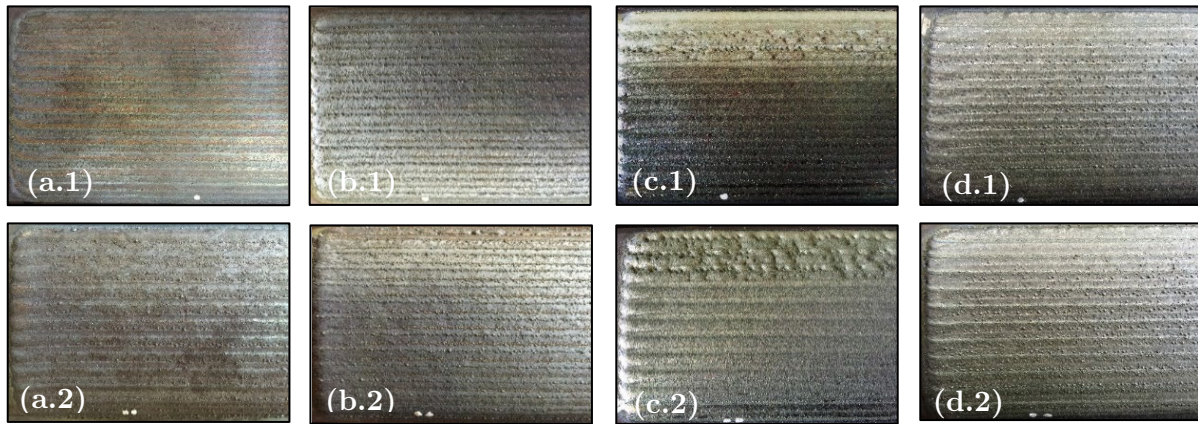


Figure 5-1 Macrographs of top representative surfaces of Group 1 deposits with (1) single and (2) double layer cladding passes. Heat treatment produces involved only preheating to 350 °C (HTA).

(a) 410L, (b) 420SS, (c) Stellite 6 and (d) Stellite 21.

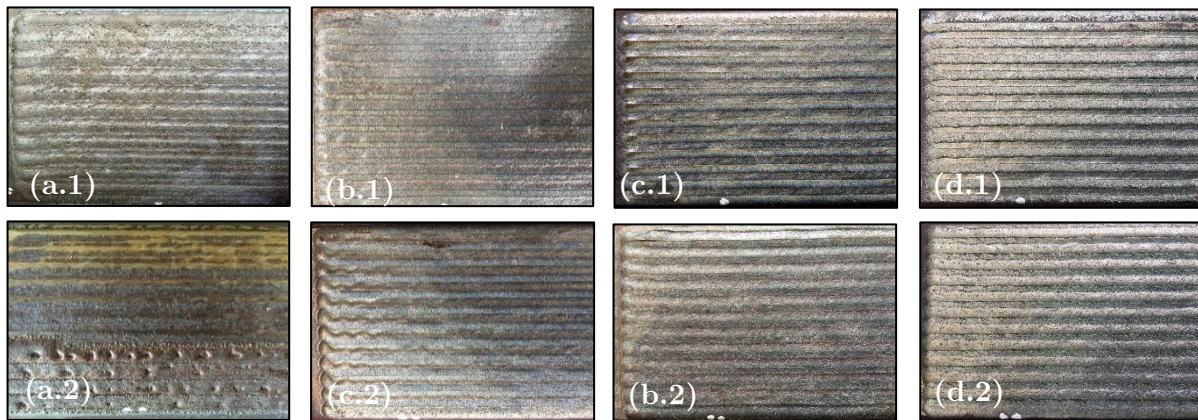


Figure 5-2 Macrographs of top representative surfaces of Group 2 deposits with (1) single and (2) double layer cladding passes. Heat treatment produces involved only preheating to 350 °C (HTA).

(a) 410L, (b) 420SS, (c) Stellite 6 and (d) Stellite 21.

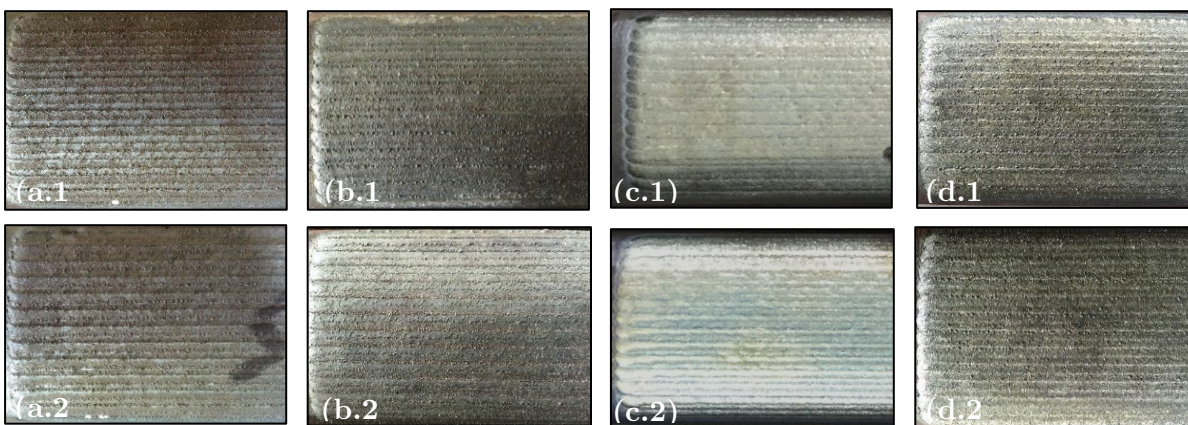


Figure 5-3 Macrographs of top representative surfaces of deposits with the desired surface properties. Heat treatment process involved preheating to 350 °C, post-heating to 350 °C and then was slow-cooled to room temperature by using a ceramic blanket (HTB). (a) 410L - Group 1, (b) 420SS - Group 2, (c) Stellite 6 - Group 2 and (d) Stellite 21 - Group 2 with (1) single and (2) double layer cladding passes.

In summary, regardless of the number of clad layers, a defect-free surface of the 410L clads was achieved by using Group 1 processing parameters, as shown in Figure 5-1 – 5-3 (a.1) and Figure 5-1 – 5-3 (a.2). It implies that the upper limit of laser traverse speed for the 410L cladding materials is 1200 mm/min (Group 2). Otherwise, heating problems associated with the evaporation of the cladding materials will occur. The surface integrity of Stellite 6 cladding is affected by the traverse speed of the laser source. At 1000 mm/min (Group 1) of traverse speed, both Stellite 6 clads with one and two layers exhibited heating bubbles at the last laser tracks as shown in Figure 5-1 (c.1) and Figure 5-1 (c.2). Whereas for the cladding processed at 1200 mm/min (Group 2) with no heating problems were observed, as shown in Figure 5-2 (c.1) and Figure 5-2 (c.2). It suggests that the lower limit of traverse speed for Stellite 6 is 1000 mm/min. Finally, for 420SS and Stellite 21, surfaces of the claddings processed at 1000 mm/min and 1200 mm/min were free of bubbling problems.

To control the hardness of the claddings and their corresponding HAZs, HTB was employed for the specimen groups observed with no defects and good surface integrity. Group 1 (1000 mm/min;

3 RPM powder and 3200 W) was chosen to apply HTB for 410L stainless steel as shown in Figure 5-3 (a.1) - (a.2), whereas Group 2 (1200 mm/min; 4 RPM powder; 3200 W) was selected to apply HTB for 420SS, Stellite 6 and Stellite 21 as shown in Figure 5-3 (b.1) - (b.2), Figure 5-3 (c.1) - (c.2) and Figure 5-3 (d.1) - (d.2). By repeating these parameters, the specimens obtained showed similar morphologies, i.e. no voids nor bubbling problems, compared with those subjected to HTA as shown in Figure 5-3.

5.3.2 Microstructural characteristics of the four deposited layers

Based on the above results, the cladded rails with defect-free surfaces were subjected to further microstructural analyses. Typical cross sections for the four comparative specimen groups of 410L, 420SS, Stellite 6 and Stellite 21 are shown in Figure 5-4 – Figure 5-7, respectively. Each of these figures shows four separate micrographs which refer to a different number of cladding layers and the applied heat treatments.

The 410L single-layer deposits subjected to HTA and HTB were observed with similar microstructural characteristics regarding metallurgical phases, as shown in Figure 5-4 (a) and Figure 5-4 (c), respectively. Lai et al. [107] investigated the effects of altering cladding directions on the microstructural and mechanical characteristics of rails cladded with 410L and reported colonies of ferrite inside a martensitic matrix. In the current investigation, comparable microstructural characteristics were found in the 410L deposits. Regardless of the heat treatments applied, ferritic grains dominate the regions near the top surface of the claddings and the overlapping regions of one track and the subsequent track, as shown in Figure 5-8 (i)-(ii) and Figure 5-10 (i)-(ii). For double layers, the ferritic grains formed in the first deposition were joint with those of the latter deposition, as shown in Figure 5-9 and Figure 5-11. Hence, the nucleation site of ferritic grains was close to the fusion line between the two layers. Large grains of ferrite

were observed to elongate through the thickness of the second layer due to the absence of preheating temperature. The main microstructures of the second layer consist of large ferritic dendrites and a small portion of martensite as shown in Figure 5-4 (c) and Figure 5-4 (d). Whereas martensite was the main microstructure of the first layer, regardless of the heat treatments applied, as shown in Figure 5-9 and Figure 5-11.

The overview micrographs of 420SS deposits with single deposition showed a significant portion of fine martensitic dendrites, as shown in Figure 5-5 (a) and Figure 5-5 (c). Previous works by Hemmati et al. [83] and Kou [108] collectively showed the influences of two factors, i.e. the temperature gradient and the growth rate of solid-liquid interface, on the microstructural characteristics of the cladding deposits. The factors varied inversely from each other as moving through the cladding's thickness, and hence, three resulting dendritic morphologies were detected, i.e. Equiaxed, Columnar/cellular and Planar dendrites, irrespective of the heat treatments applied. Similar microstructural characteristics were observed in the 420SS deposits with double deposition, as shown in Figure 5-5 (b) and Figure 5-5 (d). Figure 5-12 – Figure 5-15 show micrographs of typical microstructural characteristics of the 420SS deposits at higher magnifications.

Figure 5-6 (a) and Figure 5-6 (b) showed micrographs of single and double layer Stellite 6 deposits which was subjected to HTA, respectively. An investigation by Farnia et al. [109] reported that Co-rich dendrites enclosed by regions of interdendritic lamellar with W, Cr and Co carbides were observed for the microstructures of Stellite 6. In the current work, microstructural characteristics of the Stellite 6 deposits were observed to be consistent with those of the previous work through the thickness of the deposits. Typical dendritic morphologies were observed and shown in Figure 5-16 and Figure 5-17, and no significant variations in microstructural characteristics were detected between the laser track's overlap, and other cladding regions were detected.

For the Stellite 6 deposits subjected to HTB, microstructures with similar characteristics to those of HTA were observed. Nevertheless, cracks were observed to occur in subsurface regions of the deposits for both single and double layers, particularly at the overlapping or remelted regions of the cladding tracks, as shown in Figure 5-6 (c) and Figure 5-6 (d). The carbide grain boundaries where ductility was reduced by the formation of the hard and brittle carbides were observed to be sites for crack propagation, as shown in Figure 5-18 and Figure 5-19. Brandt et al. [110] reported that the presence of intergranular cracks might be attributed to the combined effects of several factors, i.e. dilution from the hypereutectoid rail substrate, excessive cladding temperature, creep deformation required for relaxation of the residual stresses owing to the application of PWHT, etc. Cracking of the Stellite 6 deposits as subjected to HTB was observed with similar characteristics to the PWHT cracking phenomenon, commonly occurred in the low alloy steels containing additions of Cr, Mo and Co, and subjected to PWHT, which might adversely influence the application of the deposits.

For Stellite 21, optical micrographs of the cross sections of single and double layer specimens subjected to HTA, as shown in Figure 5-7 (a) and Figure 5-7 (b) respectively, showed microstructures including Co-rich primary dendrites and interdendritic regions with hard carbides, as shown in Figure 5-20 and Figure 5-21. Investigation of Rajeev et al. [71] reported that, due to the nature of Stellite 21's elements, microstructures of Stellite 21 contained a complex set of carbides in a Cr-Co-Mo matrix. Nevertheless, cracks occurred periodically in the remelted/overlapping regions of the Stellite 6 deposits subjected to HTB, and the cladding-substrate interface was the preferred site for crack initiation, as shown in Figure 5-7 (c) and Figure 5-7 (d). Magnified micrographs of cracking of Stellite 21 deposits subjected to HTB are shown in Figure 5-22 and Figure 5-23. Addition of a second cladding layer was observed to increase the crack length. It might be attributed to the alloying elements of W, Cr and Mo in Stellite 21, and reheating/remelting during multi-track cladding. In other words, the remelted/overlapping regions of one laser track would be considered as the heat affected zones of the subsequent laser tracks.

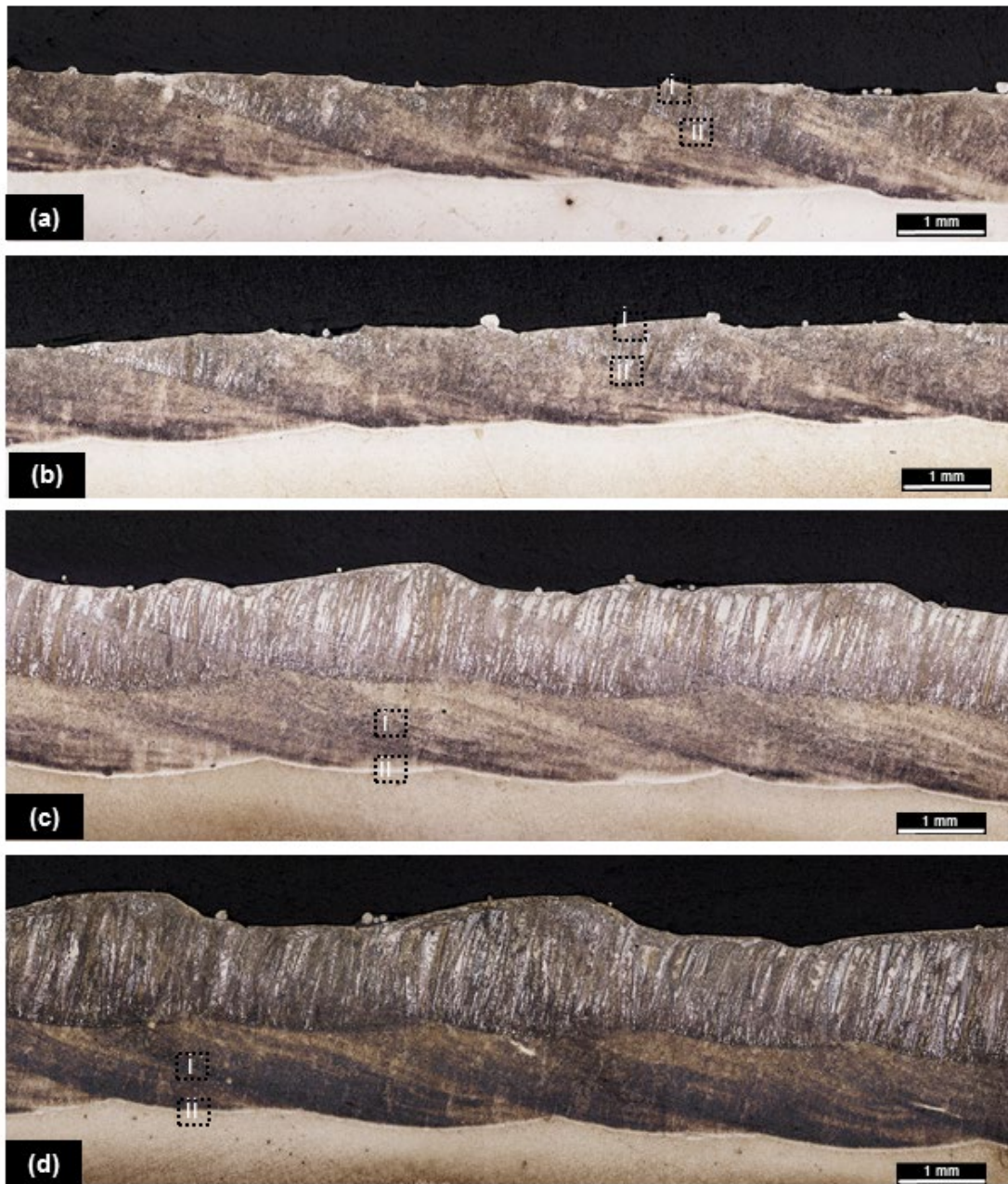


Figure 5-4 Micrographs showing typical cross sections of 410L deposits with (a) single deposition and HTA, (b) double deposition and HTA, (c) single deposition and HTB, and (d) double deposition and HTB.

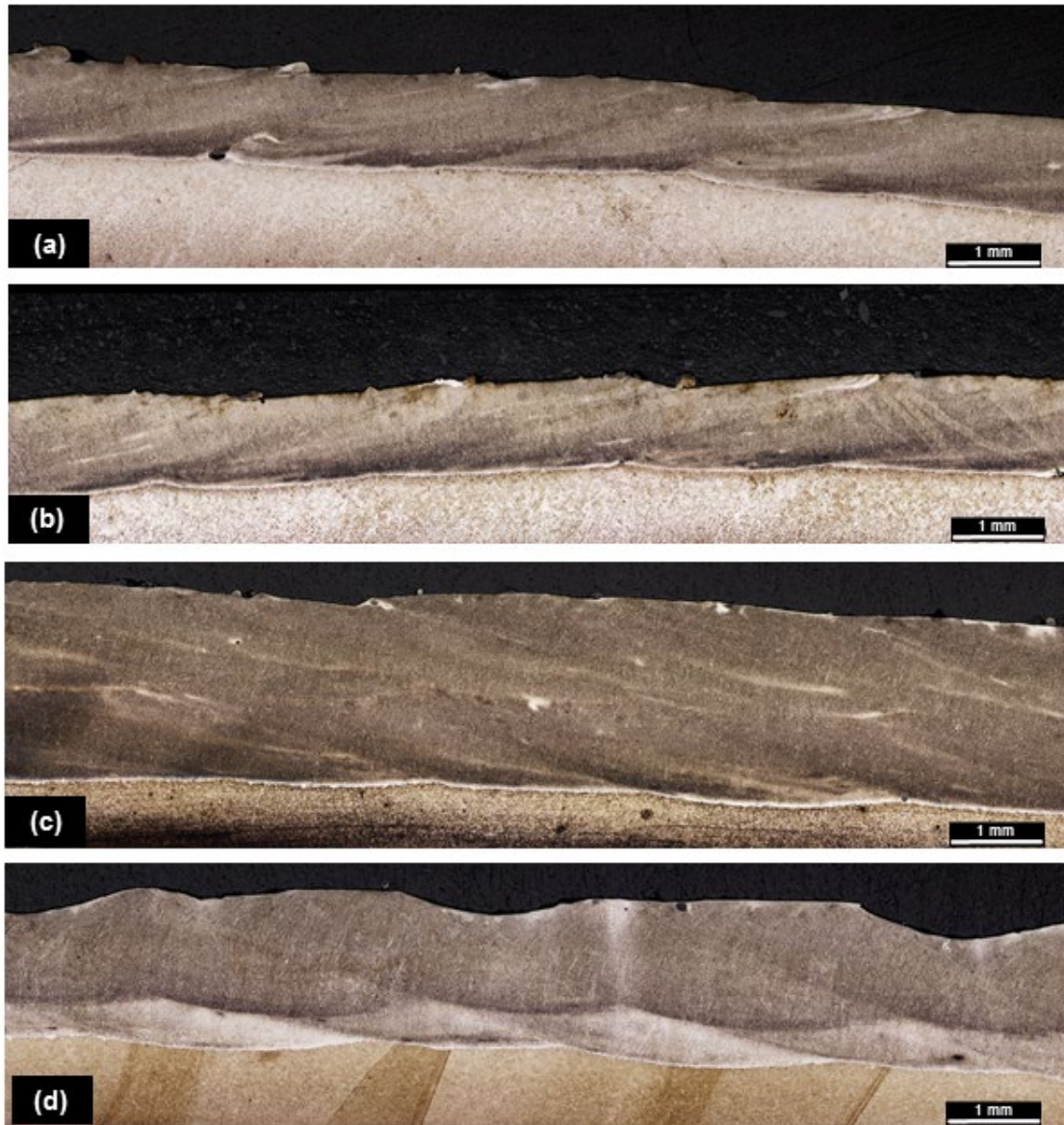


Figure 5-5 Micrographs showing typical cross sections of 420SS deposits with (a) single deposition and HTA, (b) double deposition and HTA, (c) single deposition and HTB, and (d) double deposition and HTB.

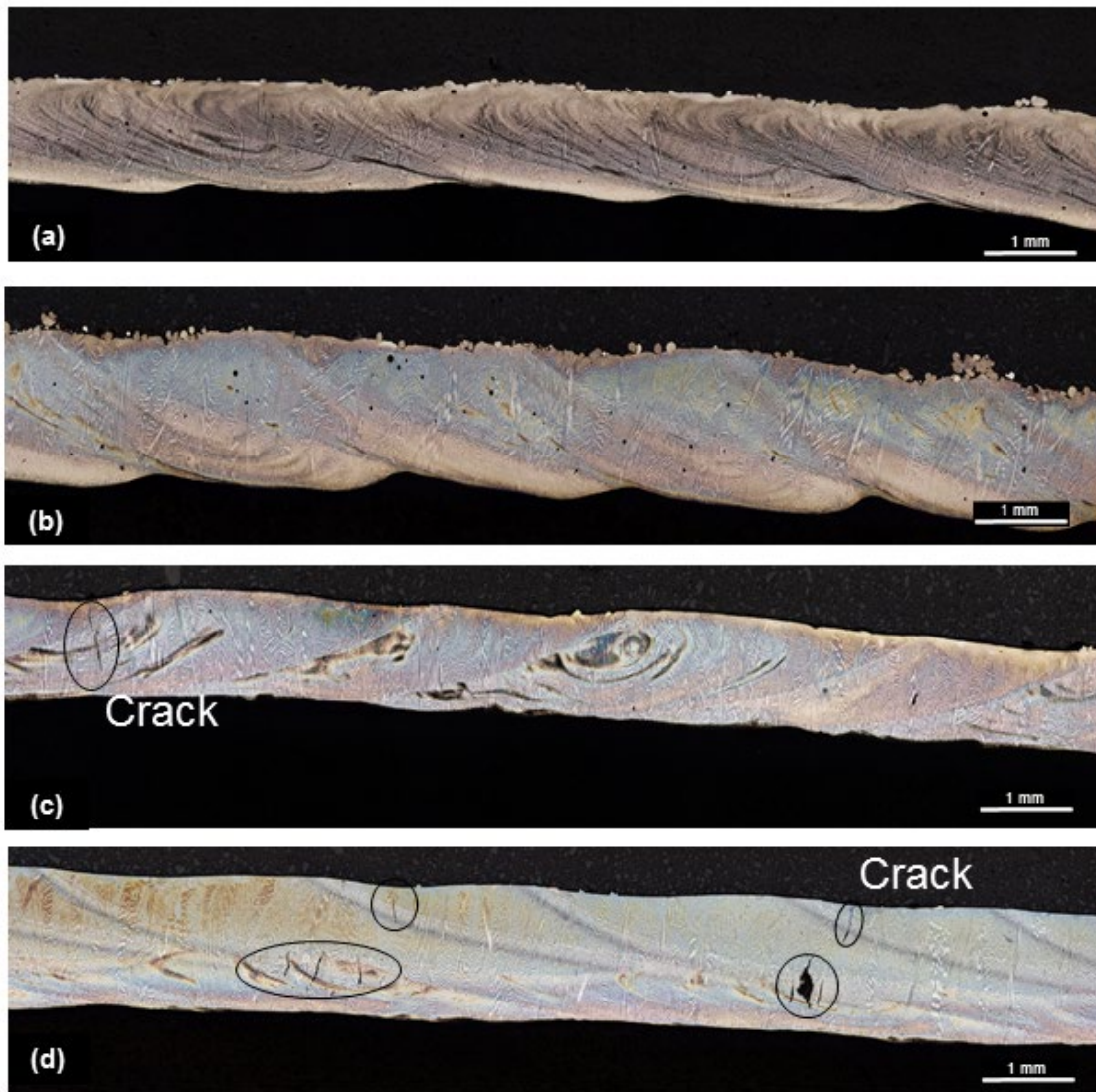


Figure 5-6 Micrographs showing typical cross sections of Stellite 6 deposits with (a) single deposition and HTA, (b) double deposition and HTA, (c) single deposition and HTB, and (d) double deposition and HTB.

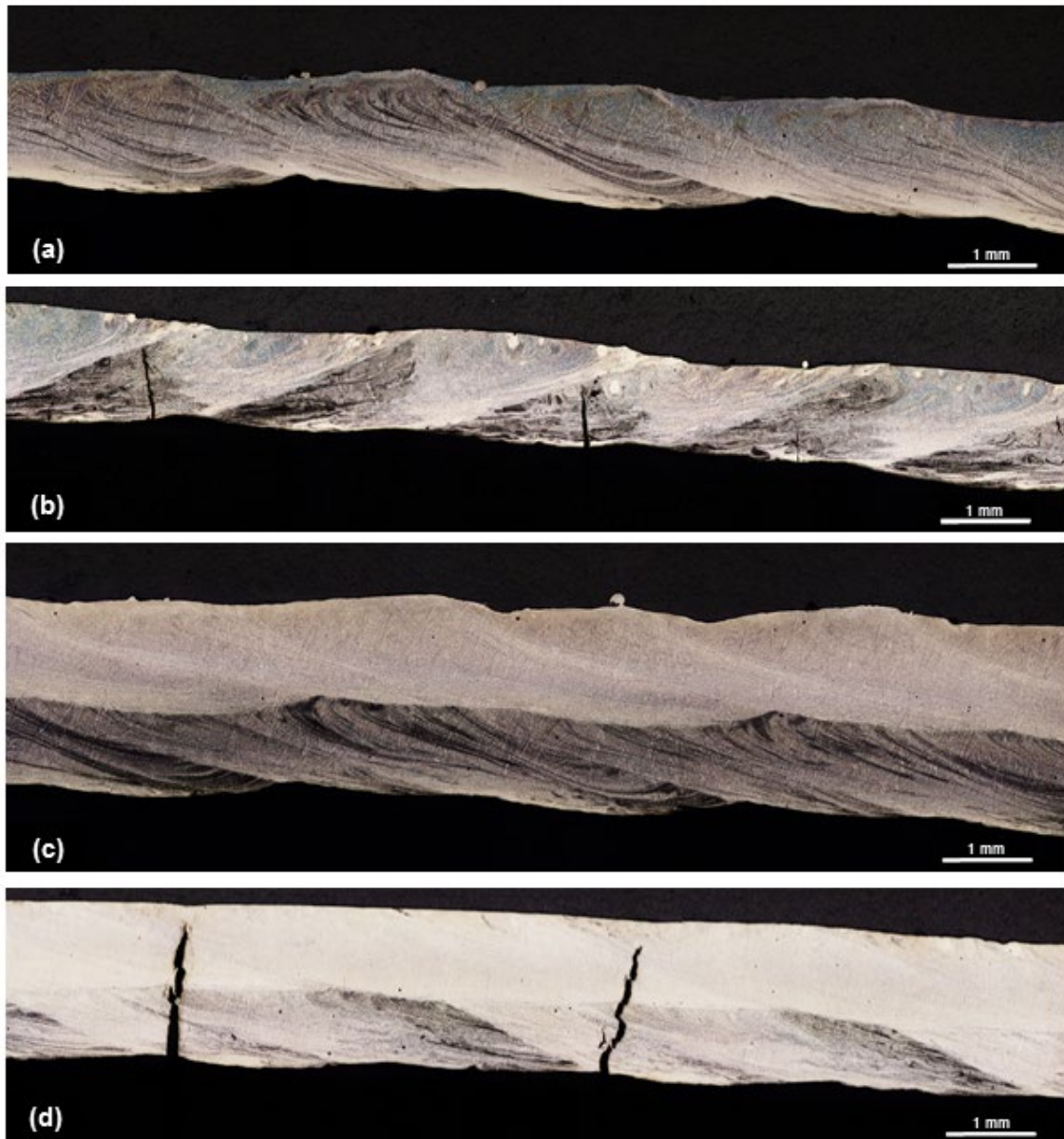


Figure 5-7 Micrographs showing typical cross sections of Stellite 21 deposits with (a) single deposition and HTA, (b) double deposition and HTA, (c) single deposition and HTB, and (d) double deposition and HTB.

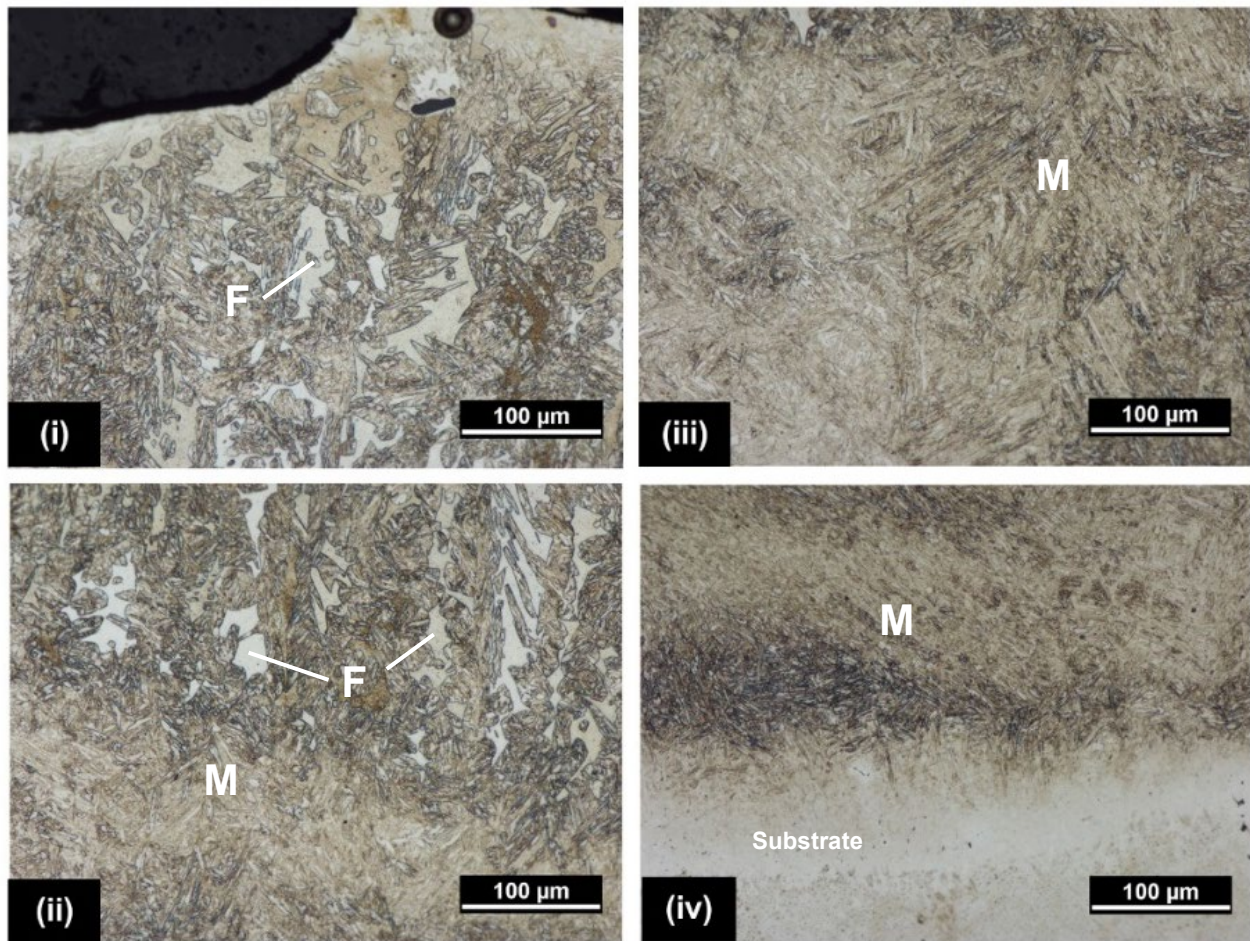


Figure 5-8 Cross sections of 410L with single deposition and HTA, (i) top region of laser tracks, (ii) overlapping region of laser tracks, (iii) middle region of laser tracks, and (iv) interface of deposit-substrate, whose locations are shown in Figure 5-4 and discussed in Section 5.3.2.

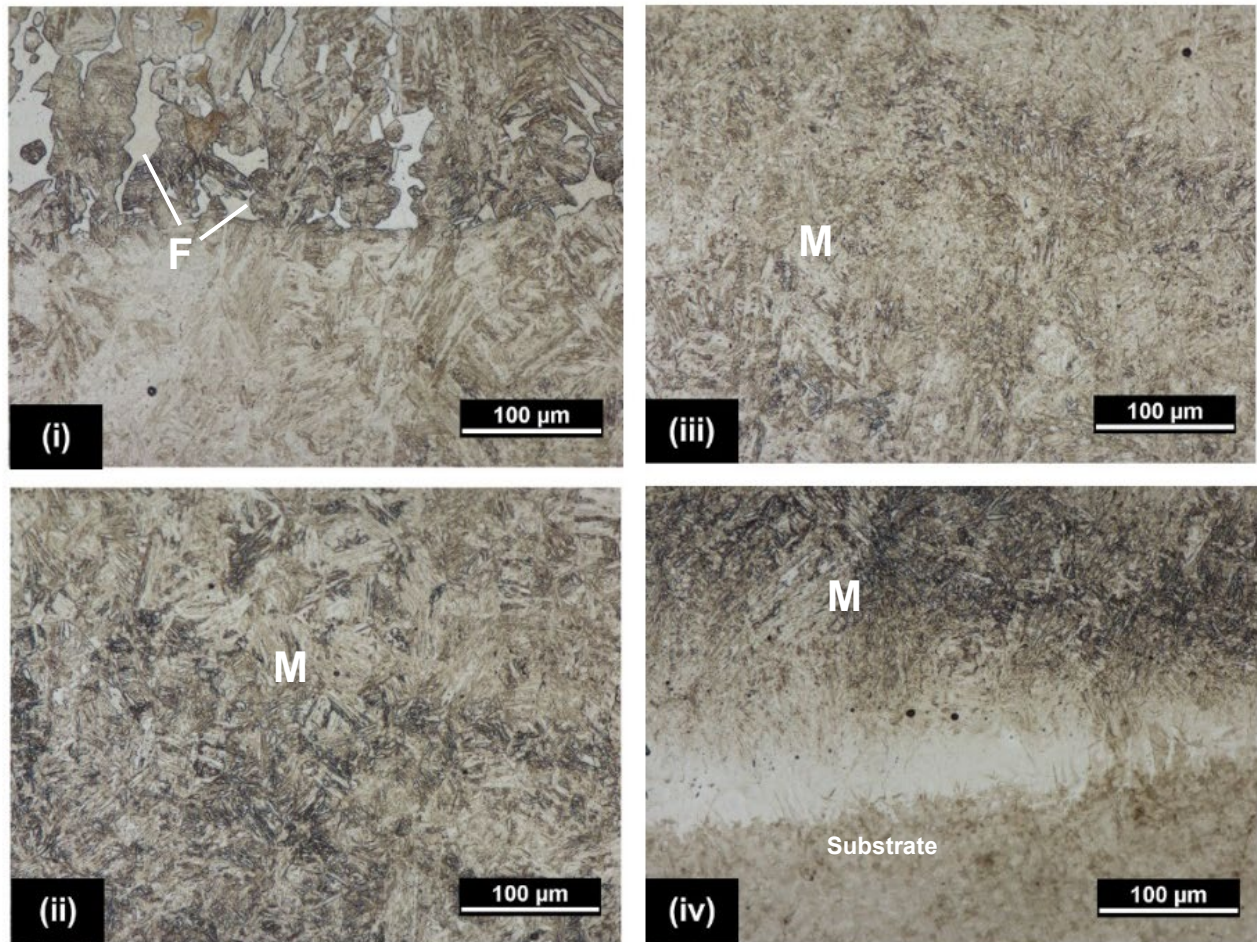


Figure 5-9 Cross sections of 410L with single deposition and HTA were discussed in Section 5.3.2, (i) top region of laser tracks, (ii) overlapping region of laser tracks, (iii) middle region of laser tracks, and (iv) interface of deposit-substrate, whose locations are shown in Figure 5-4.

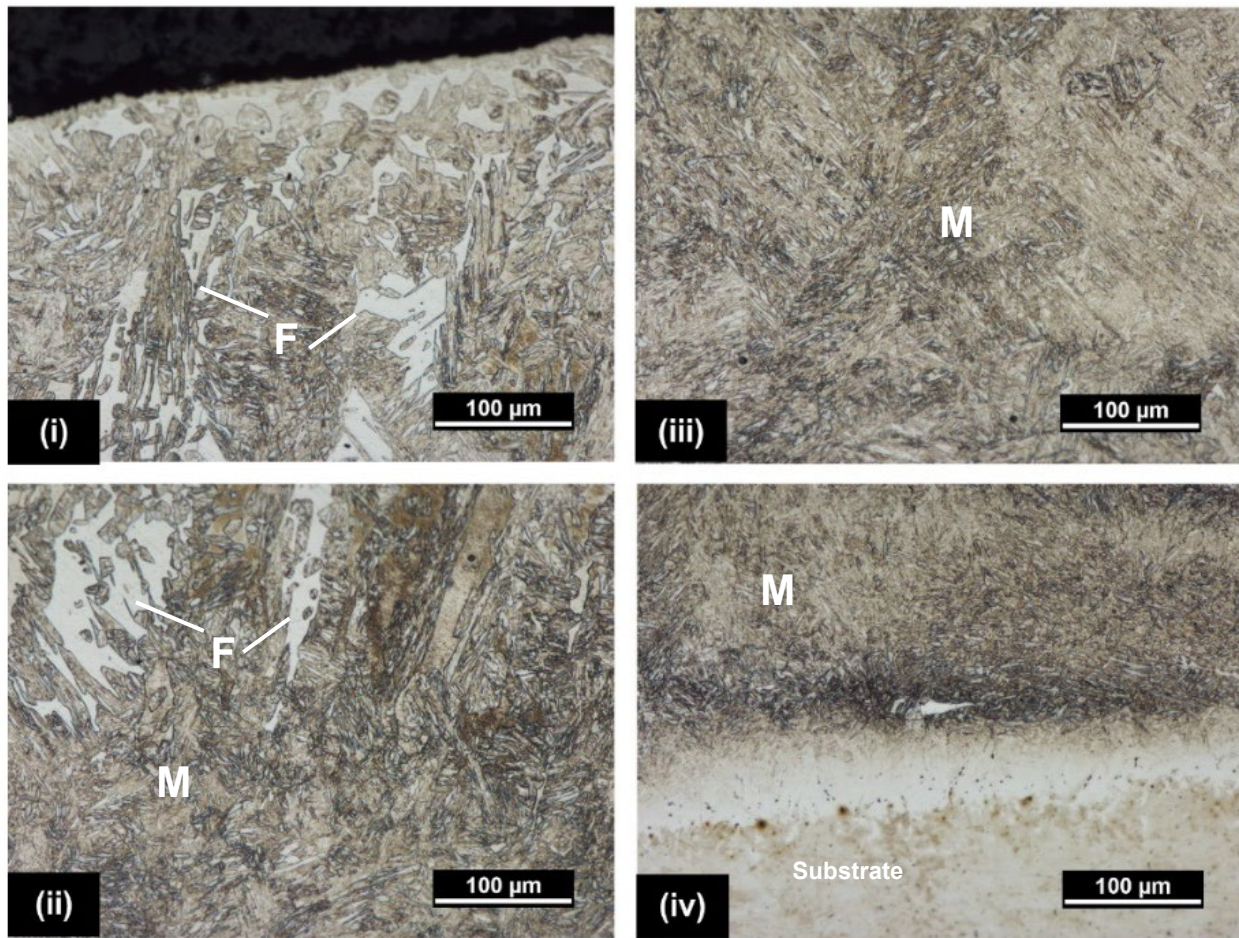


Figure 5-10 Cross sections of 410L with single deposition and HTB were discussed in Section 5.3.2. (i) top region of laser tracks, (ii) overlapping region of laser tracks, (iii) middle region of laser tracks, and (iv) interface of deposit-substrate, whose locations are shown in Figure 5-4.

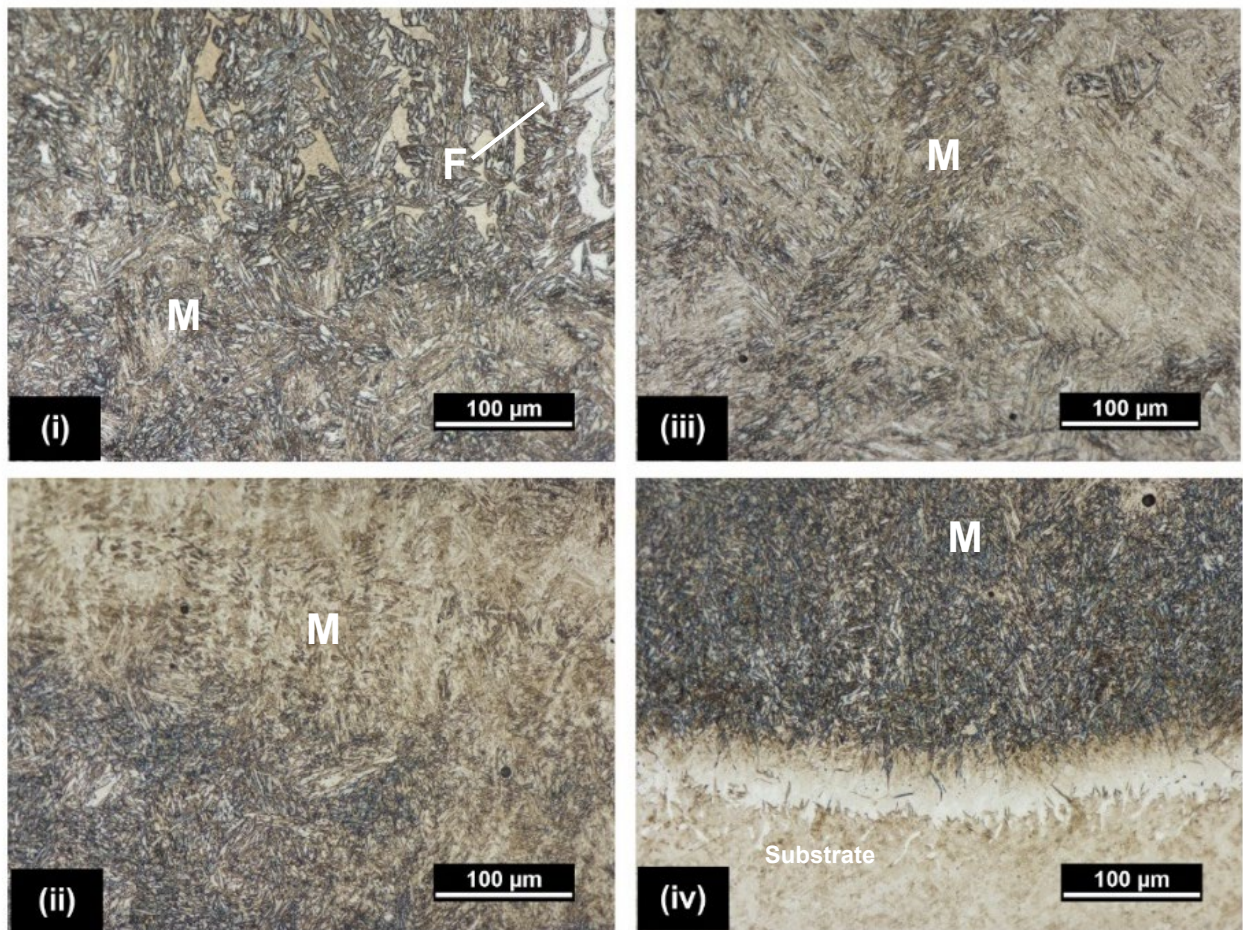


Figure 5-11 Cross sections of 410L with double deposition and HTB were discussed in Section 5.3.2. (i) top region of laser tracks, (ii) overlapping region of laser tracks, (iii) middle region of laser tracks, and (iv) interface of deposit-substrate, whose locations are shown in Figure 5-4.

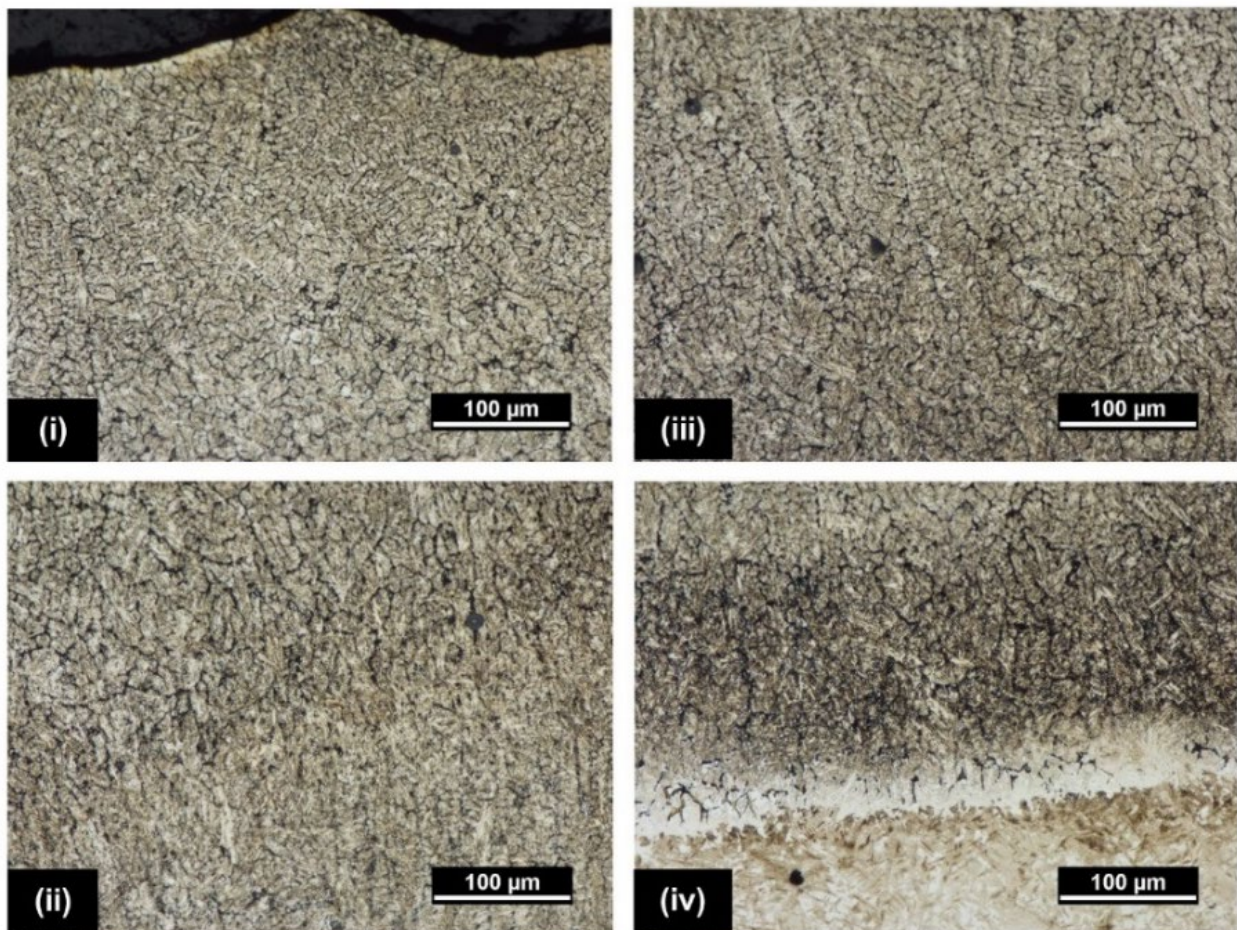


Figure 5-12 Cross sections of 420SS with single deposition and HTA were discussed in Section 5.3.2. (i) top region of laser tracks, (ii) overlapping region of laser tracks, (iii) middle region of laser tracks, and (iv) interface of deposit-substrate, whose locations are shown in Figure 5-5.

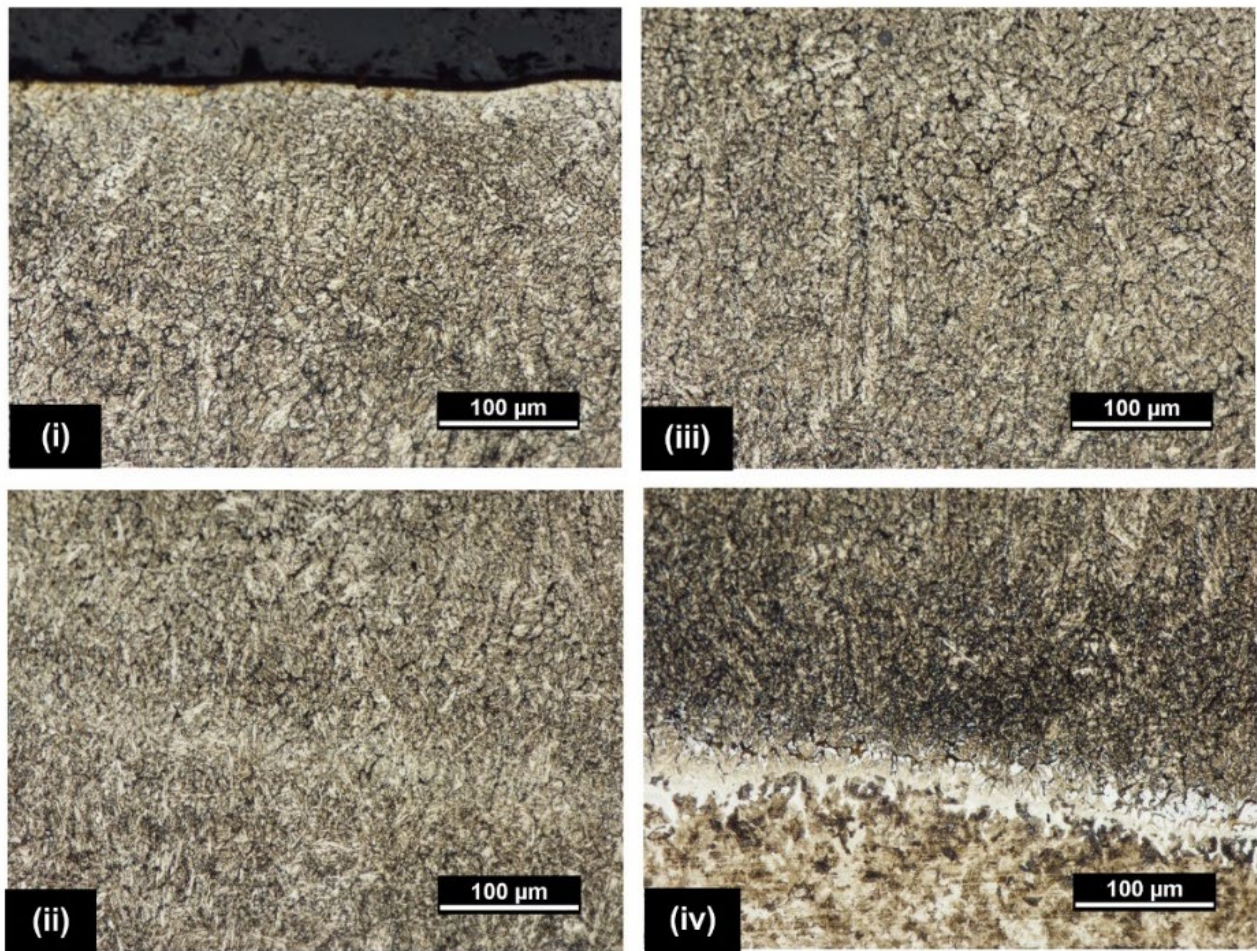


Figure 5-13 Cross sections of 420SS with double deposition and HTA were discussed in Section 5.3.2. (i) top region of laser tracks, (ii) overlapping region of laser tracks, (iii) middle region of laser tracks, and (iv) interface of deposit-substrate, whose locations are shown in Figure 5-5.

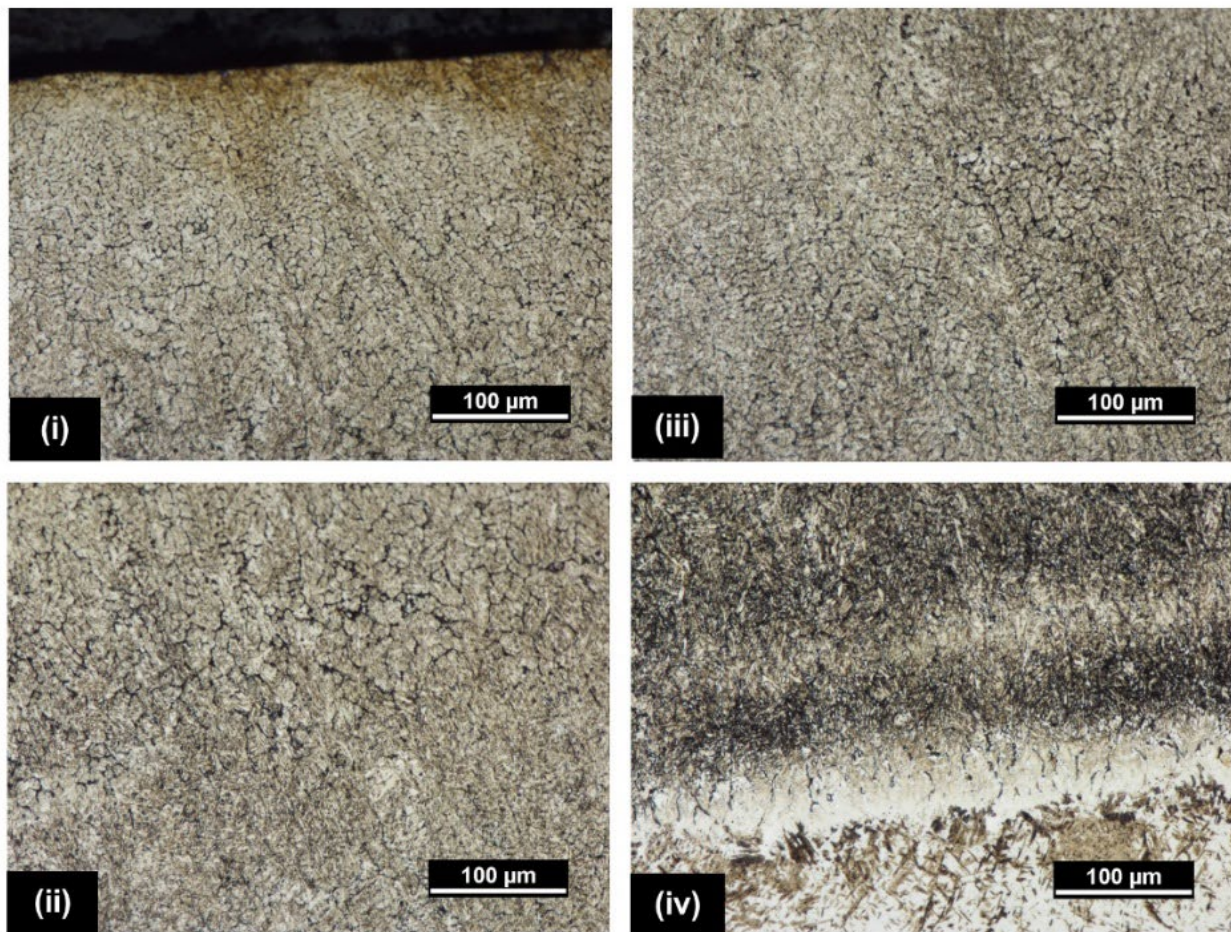


Figure 5-14 Cross sections of 420SS with single deposition and HTB were discussed in Section 5.3.2. (i) top region of laser tracks, (ii) overlapping region of laser tracks, (iii) middle region of laser tracks, and (iv) interface of deposit-substrate, whose locations are shown in Figure 5-5.

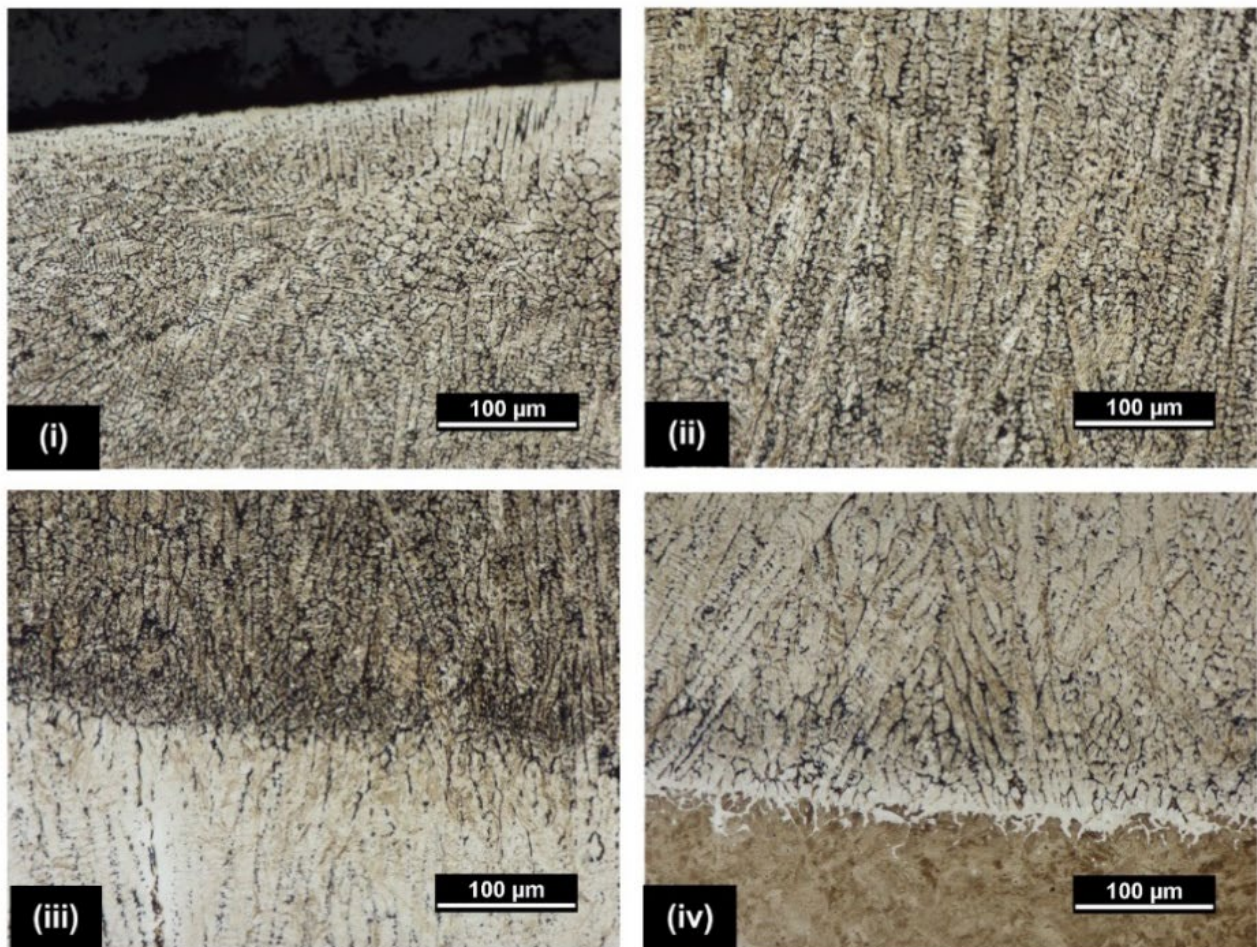


Figure 5-15 Cross sections of 420SS with double deposition and HTB were discussed in Section 5.3.2. (i) top region of laser tracks, (ii) overlapping region of laser tracks, (iii) middle region of laser tracks, and (iv) interface of deposit-substrate, whose locations are shown in Figure 5-5.

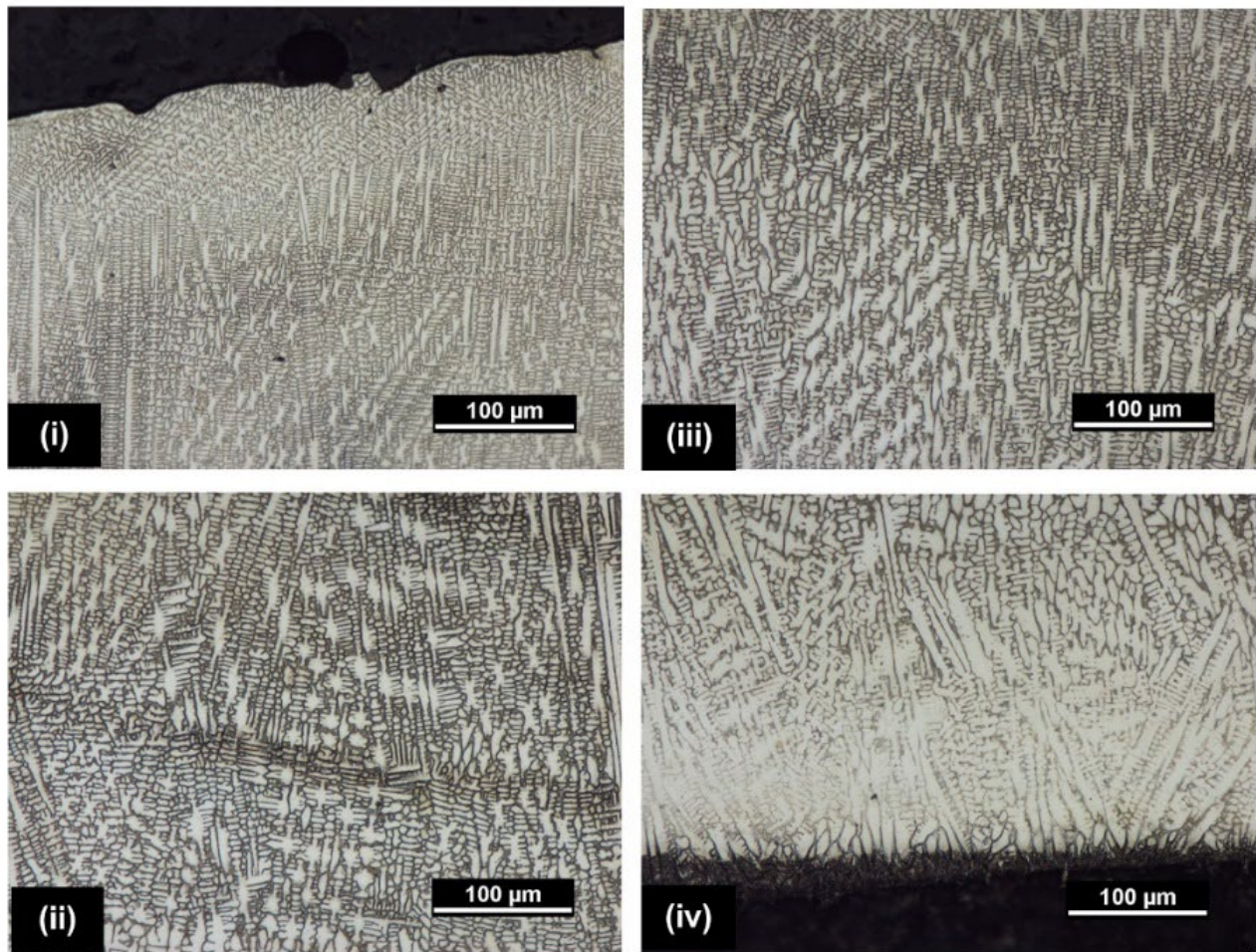


Figure 5-16 Cross sections of Stellite 6 with single deposition and HTA were discussed in Section 5.3.2. (i) top region of laser tracks, (ii) overlapping region of laser tracks, (iii) middle region of laser tracks, and (iv) interface of deposit-substrate, whose locations are shown in Figure 5-6.

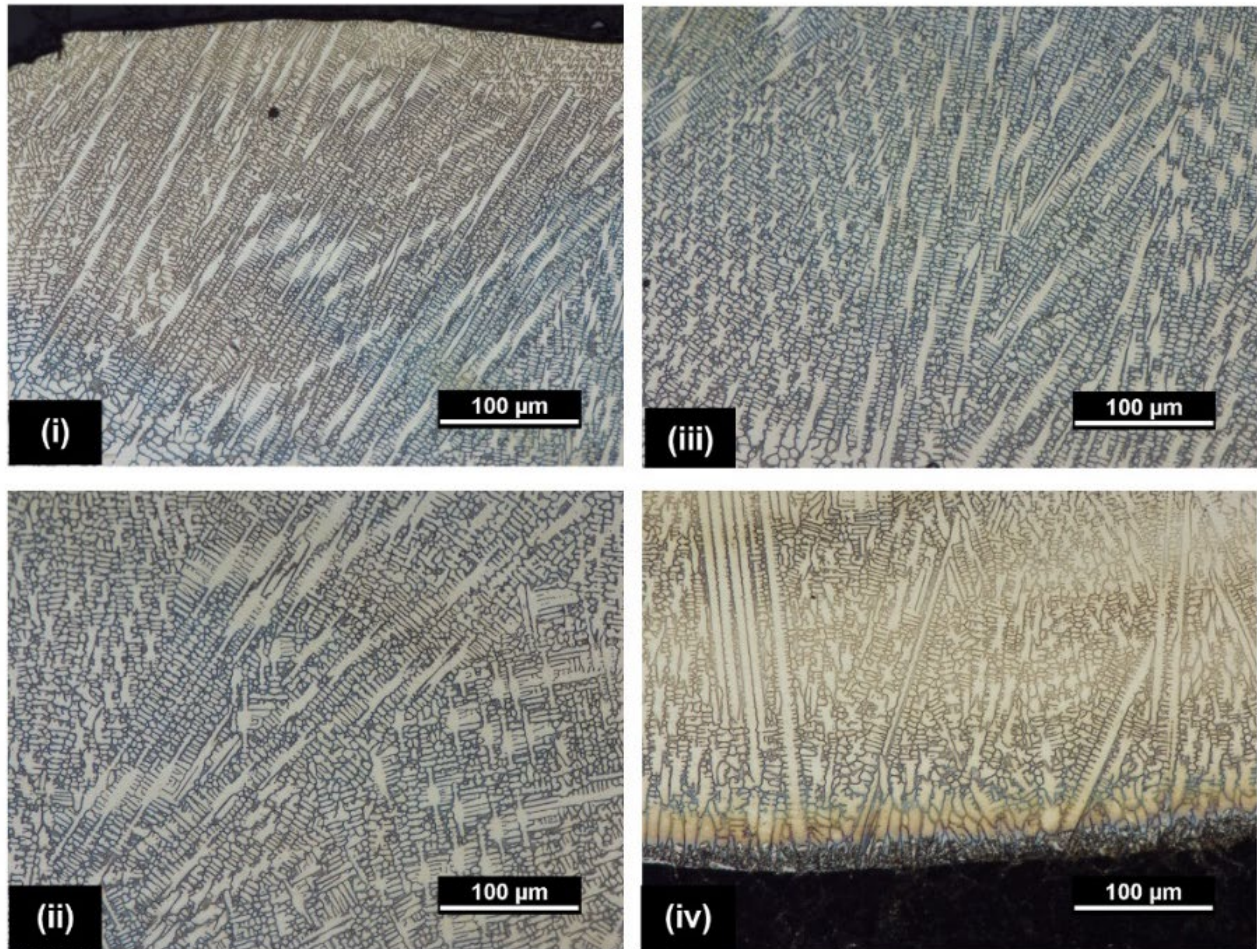


Figure 5-17 Cross sections of Stellite 6 with double deposition and HTA were discussed in Section 5.3.2. (i) top region of laser tracks, (ii) overlapping region of laser tracks, (iii) middle region of laser tracks, and (iv) interface of deposit-substrate, whose locations are shown in Figure 5-6.

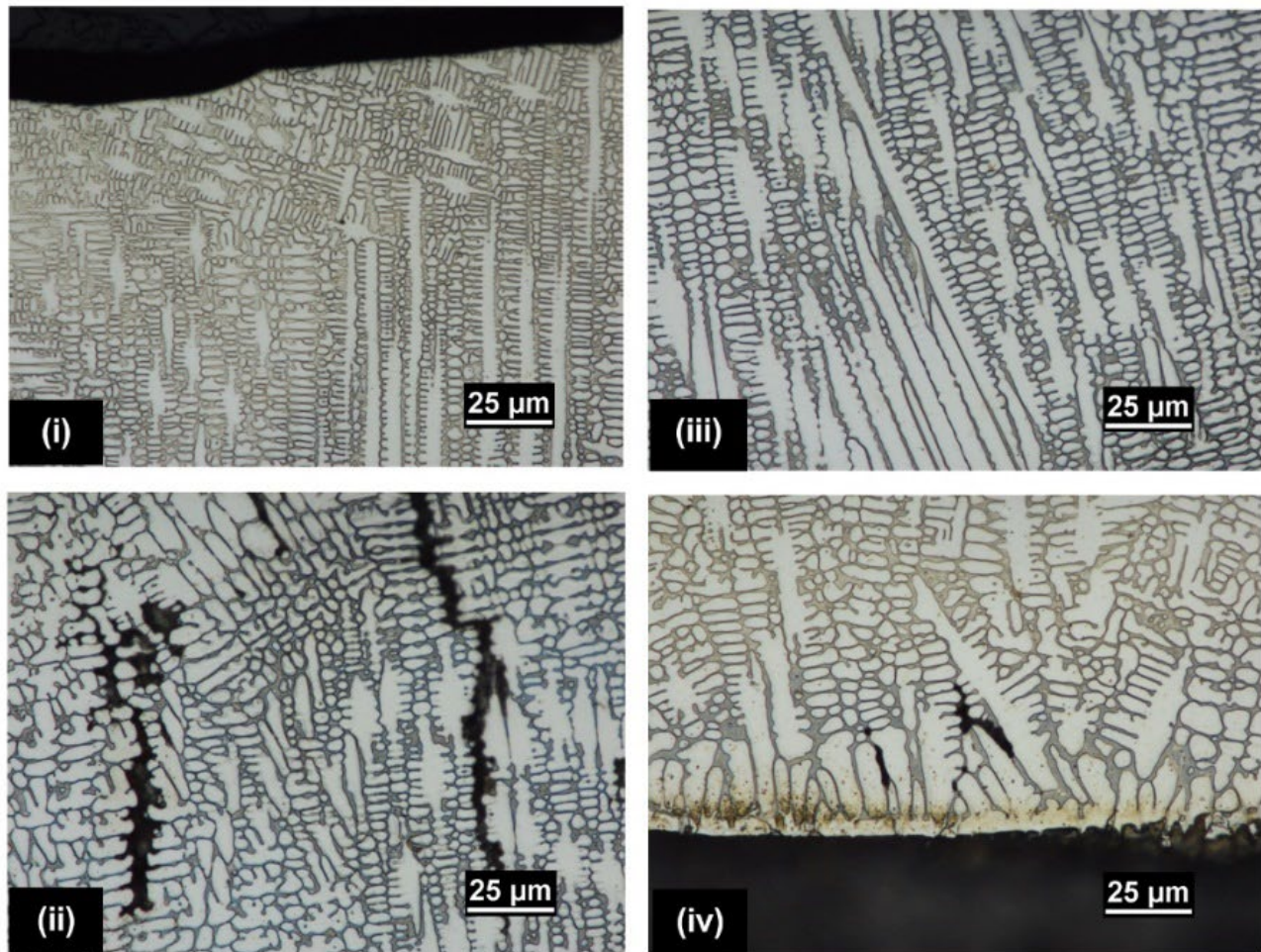


Figure 5-18 Cross sections of Stellite 6 with single deposition and HTB were discussed in Section 5.3.2. (i) top region of laser tracks, (ii) overlapping region of laser tracks, (iii) middle region of laser tracks, and (iv) interface of deposit-substrate, whose locations are shown in Figure 5-6.

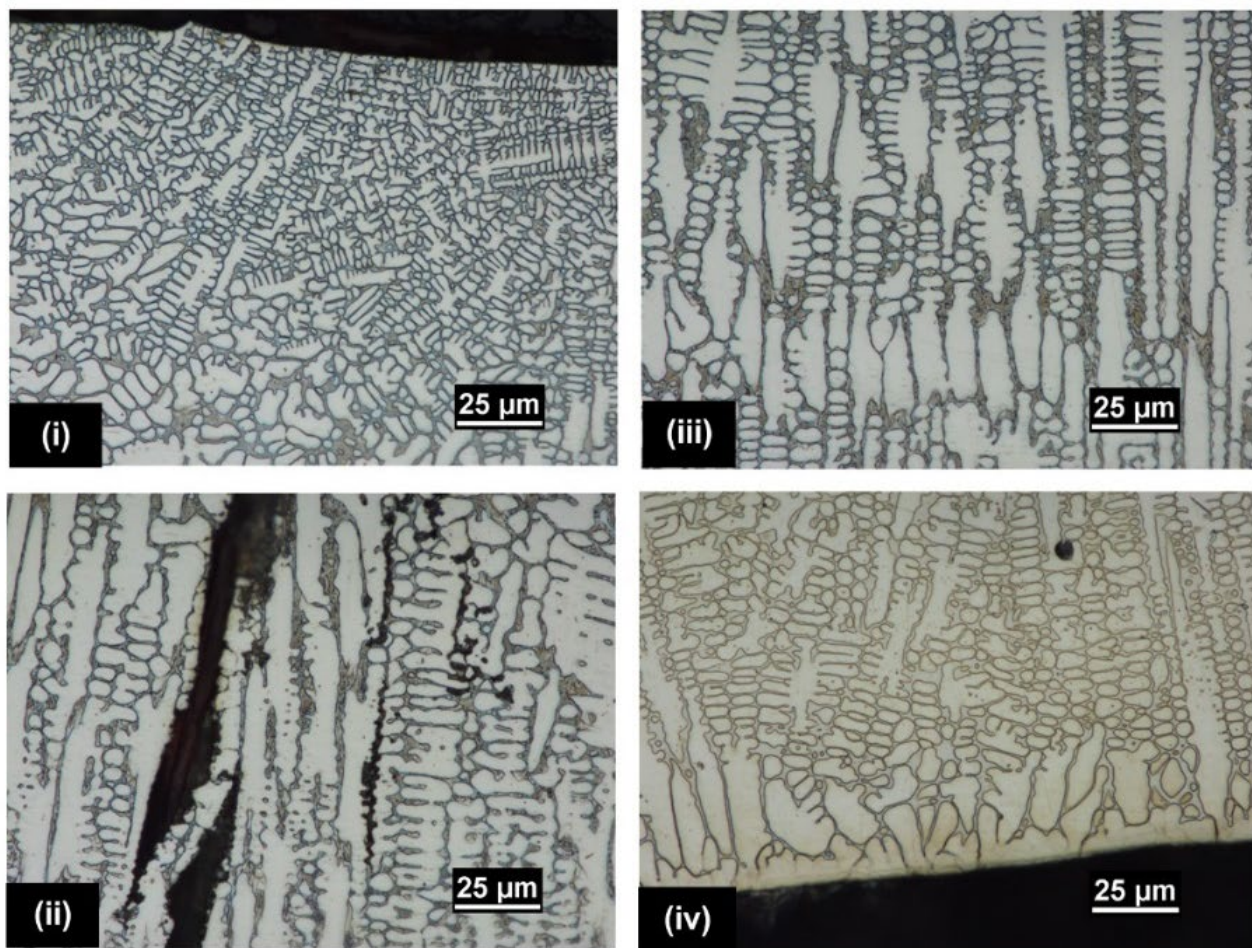


Figure 5-19 Cross sections of Stellite 6 with double deposition and HTB were discussed in Section 5.3.2. (i) top region of laser tracks, (ii) overlapping region of laser tracks, (iii) middle region of laser tracks, and (iv) interface of deposit-substrate, whose locations are shown in Figure 5-6.

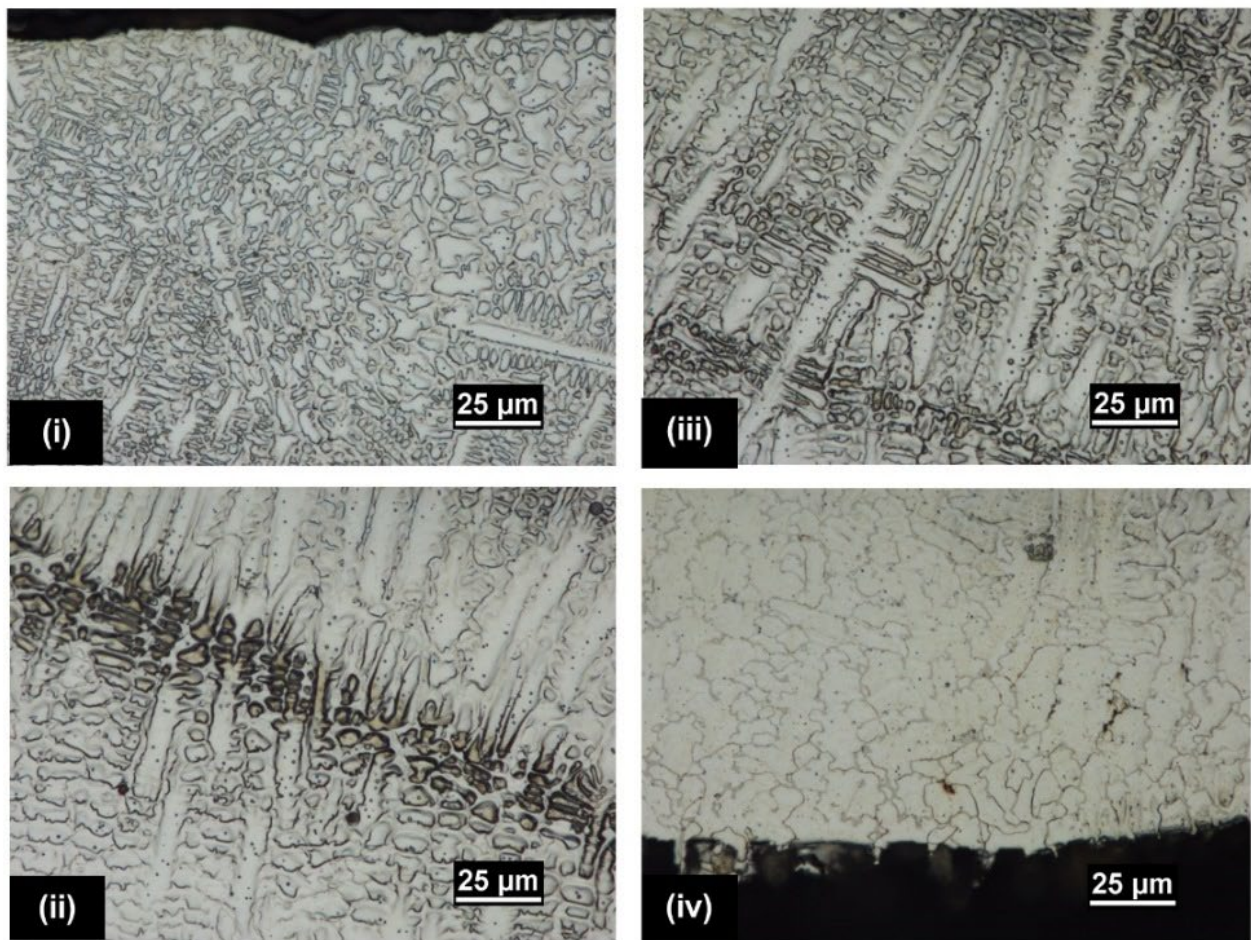


Figure 5-20 Cross sections of Stellite 21 with single deposition and HTA were discussed in Section 5.3.2. (i) top region of laser tracks, (ii) overlapping region of laser tracks, (iii) middle region of laser tracks, and (iv) interface of deposit-substrate, whose locations are shown in Figure 5-7.

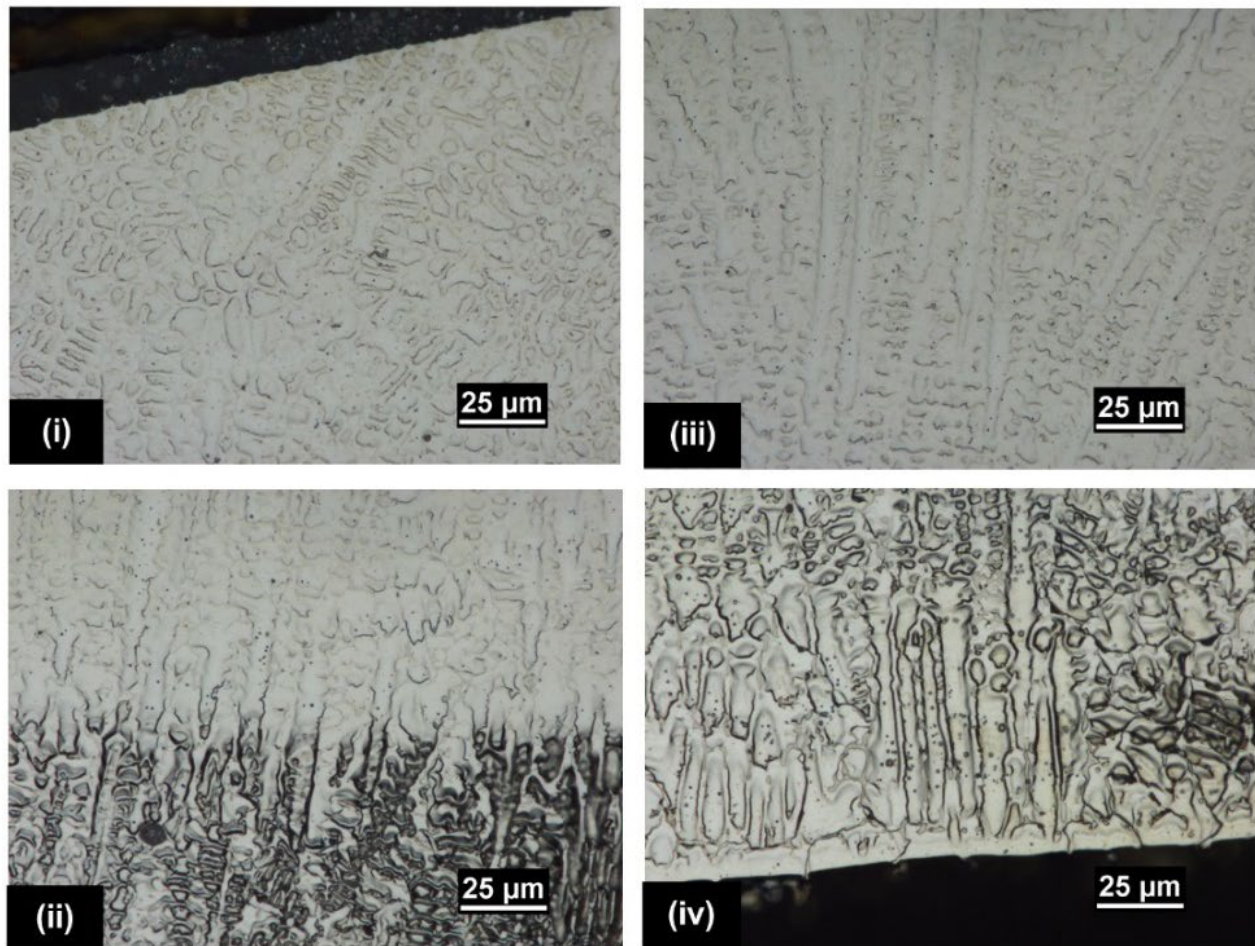


Figure 5-21 Cross sections of Stellite 21 with double deposition and HTA were discussed in Section 5.3.2. (i) top region of laser tracks, (ii) overlapping region of laser tracks, (iii) middle region of laser tracks, and (iv) interface of deposit-substrate, whose locations are shown in Figure 5-7.

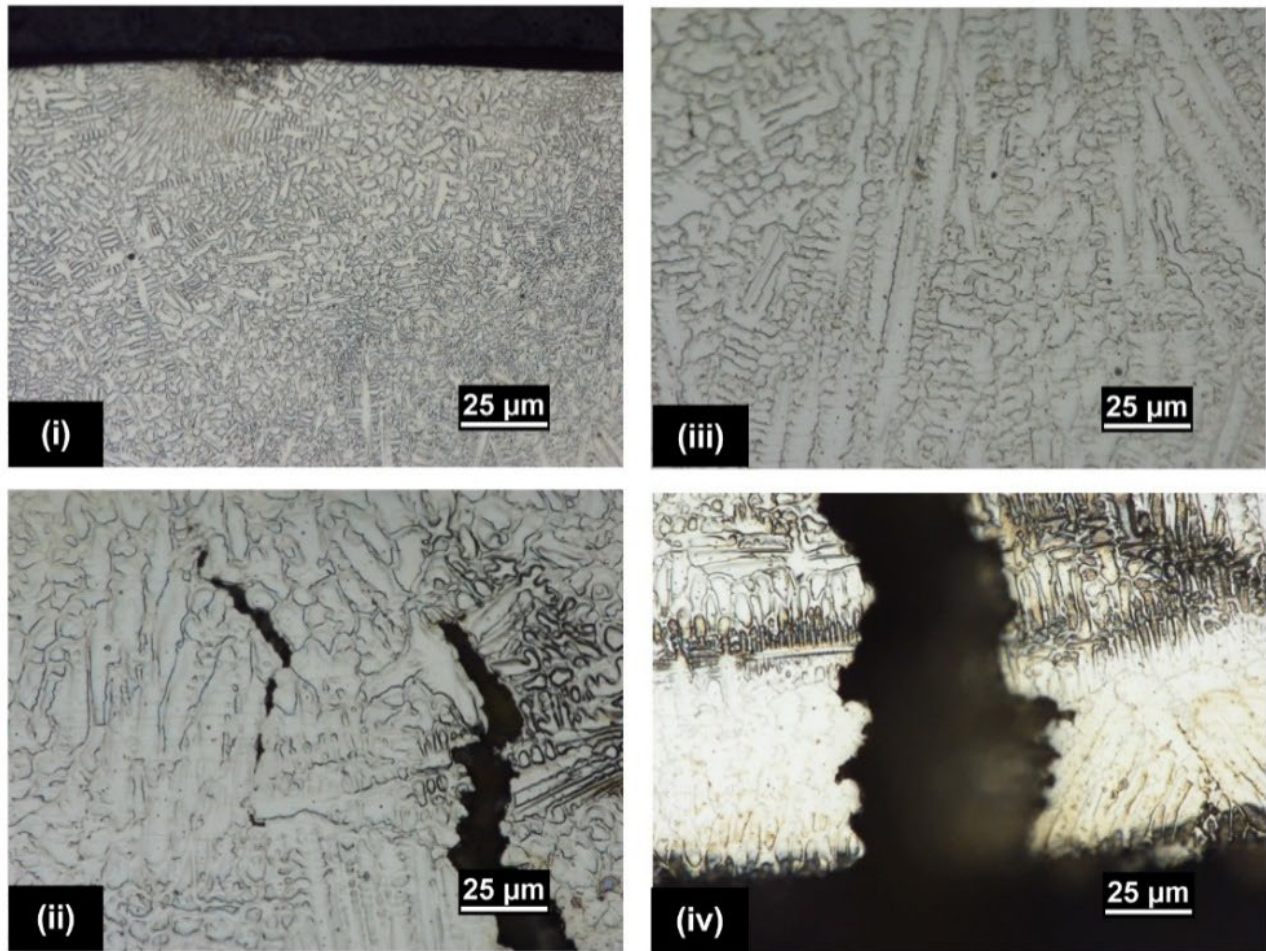


Figure 5-22 Cross sections of Stellite 21 with single deposition and HTB were discussed in Section 5.3.2. (i) top region of laser tracks, (ii) overlapping region of laser tracks, (iii) middle region of laser tracks, and (iv) interface of deposit-substrate, whose locations are shown in Figure 5-7.

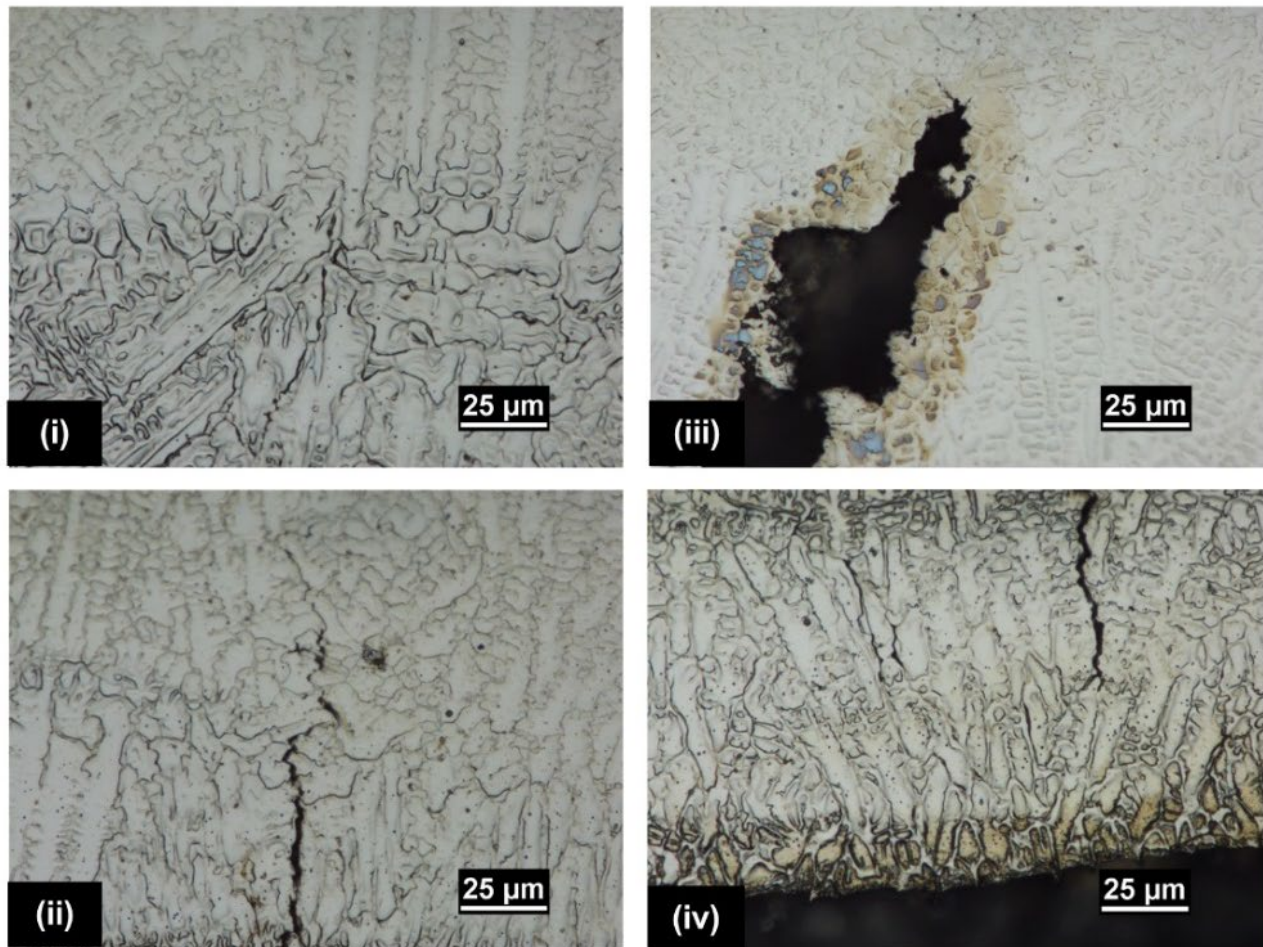


Figure 5-23 Cross sections of Stellite 21 with single deposition and HTB were discussed in Section 5.3.2. (i) top region of laser tracks, (ii) overlapping region of laser tracks, (iii) middle region of laser tracks, and (iv) interface of deposit-substrate, whose locations are shown in Figure 5-7.

5.3.3 Influence of heat treatment and cladding materials on microstructures of the HAZs

Optical micrographs of cladded rails in the transverse direction were obtained to investigate and compare the microstructural characteristics of the HAZs of the four studied cladding materials. Similar to a previous investigation performed by Lai et al. [107], the establishment of numerous HAZ sub-regions was detected as a result of the rail's microstructure subjected to the thermal impacts of the laser cladding treatment. Irrespective of the depositing materials, four typical sub-regions, i.e. i) Partially molten, ii) Coarse-grained, iii) Fine-grained, iv) Spheroidised/partial spheroidised HAZ, were detected.

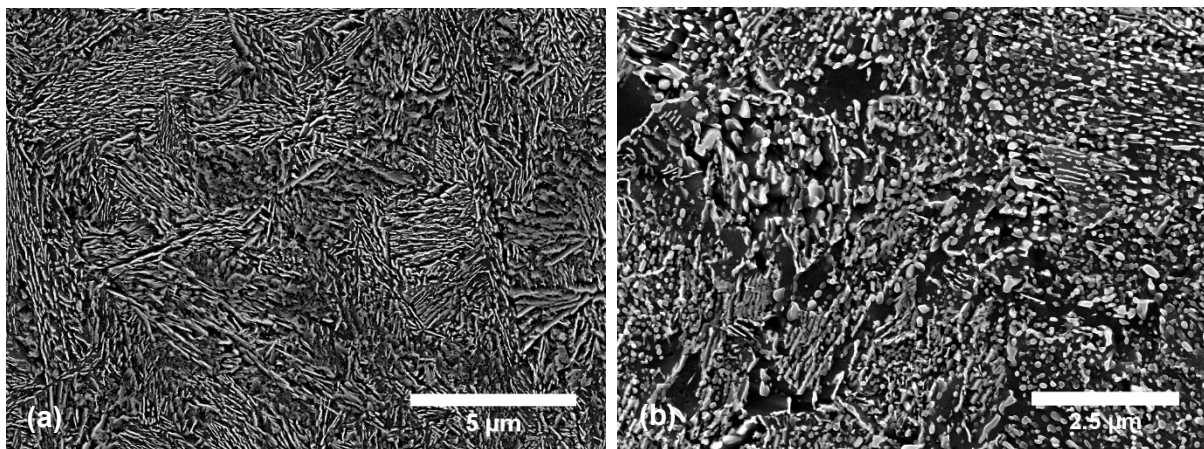


Figure 5-24 SEM micrographs showing typical morphology of (a) bainite and pearlite and (b) spheroidite/partial spheroidite.

For single deposition treated with HTA, the microstructure of the coarse-grained regions was characterized by bainitic morphology, whereas the fine-grained regions were characterized with bainitic and pearlitic morphology. Spheroidised/partial spheroidised microstructure was found to locate contiguous to the unaffected substrate, as shown in Figure 5-24. These microstructural characteristics were observed in the optical micrographs of the four materials, i.e. (i) 410L, (ii) 420SS, (iii) Stellite 6 and (iv) Stellite 21 undergone HTA and subjected to single deposition as shown in Figure 5-25. For each material, the four individual micrographs correspond to (a) the initial cladding runs, (b) the middle cladding runs, (c) the last cladding runs, and (d) typical longitudinal sections at the beginning and finishing ends of the cladding runs. Likewise, specimens subjected to HTB with single deposition were also found with the preceding microstructural characteristics in the HAZs, as shown in Figure 5-26.

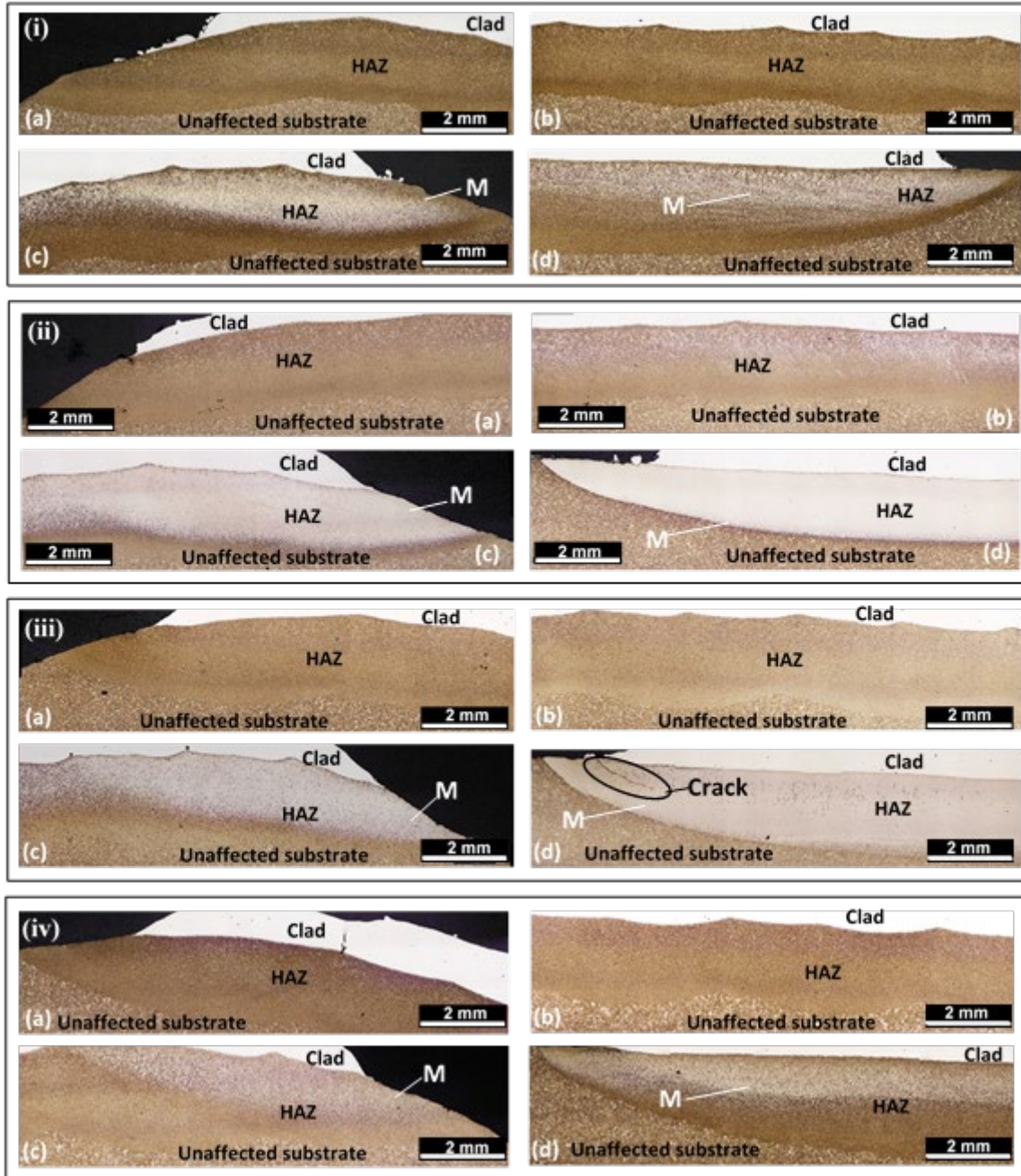


Figure 5-25 Heat affected zones and the unaffected substrate of the rail-cross sections at (a) the initial cladding runs - LHS, (b) middle cladding runs, (c) the last cladding runs - RHS and (d) a typical longitudinal cross-section at the beginning and finishing ends of the cladding runs under (i) 410L, (ii) 420SS, (iii) Stellite 6 and (iv) Stellite 21 deposits with HTA and single deposition. (M=martensite)

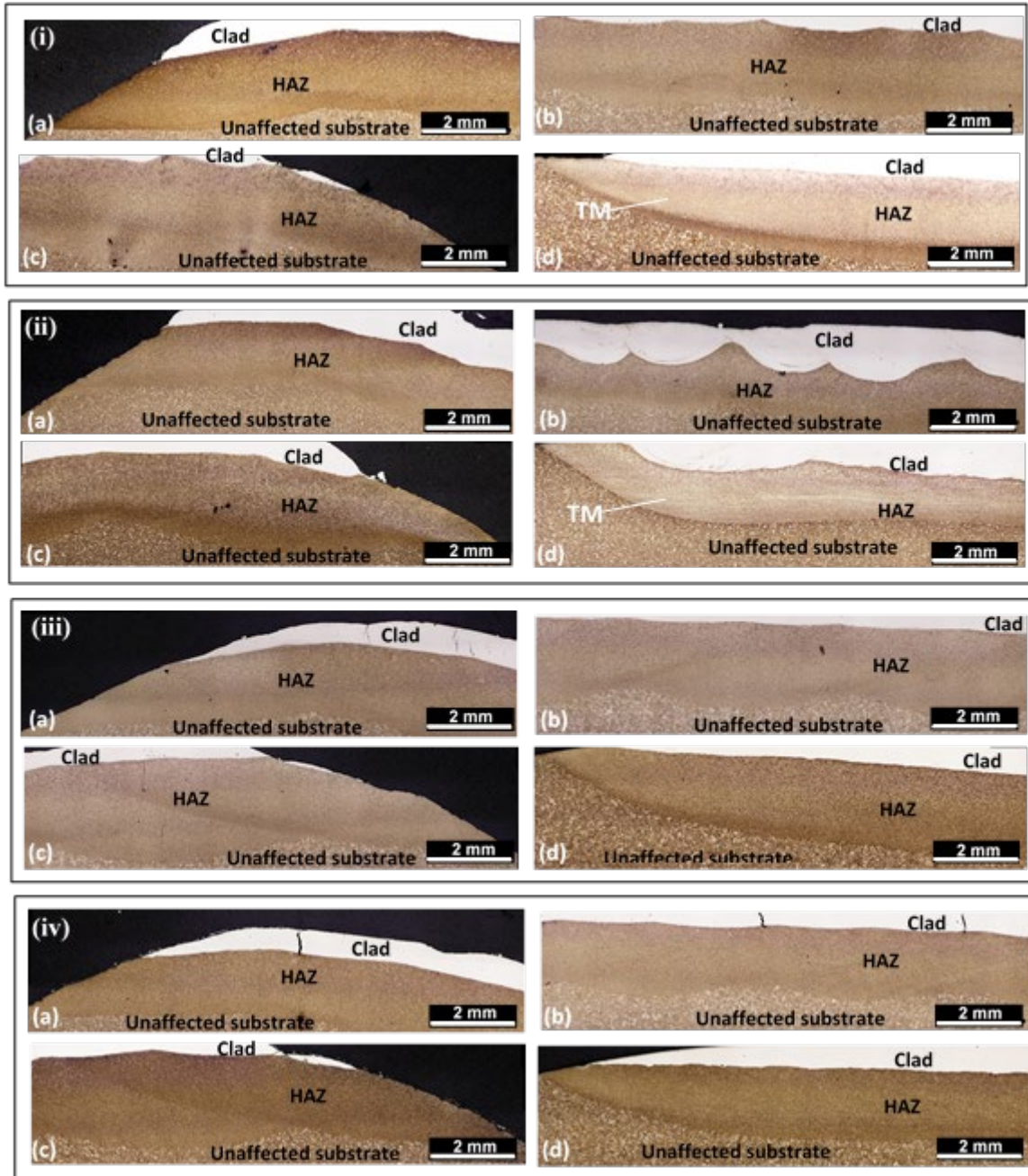


Figure 5-26 Heat affected zones and the unaffected substrate of the rail-cross sections at (a) the initial cladding runs - LHS, (b) middle cladding runs, (c) the last cladding runs - RHS and (d) a typical longitudinal cross-section at the beginning and finishing ends of the cladding runs under (i) 410L, (ii) 420SS, (iii) Stellite 6 and (iv) Stellite 21 deposits with HTB and single deposition.
(TM=Tempered martensite)

However, owing to the difference in the melting point of the cladding powders, effects of the preheating conditions on the microstructural characteristics of the HAZ of the cladded rails is dependent on the cladding materials. As a result, a martensitic morphology dominated the coarse-grained HAZ at (c) the last cladding runs, and (d) the starting and finishing cladding ends, as shown in Figure 5-26. For 420SS and Stellite 6, martensite was observed even in the fine-grained HAZ and spheroidised/partial spheroidised zone as shown in Figure 5-25 (ii)(d) and Figure 5-25 (iii)(d). Due to the brittle nature of martensitic phase, cracking was found in the HAZ as evident in Figure 5-25 (iii)(d).

In single layer deposition subjected to HTB, the addition of PHWT and slow cooling altered the characteristics of microstructure and morphology of the HAZs. Martensite was mitigated in volumetric extent and tempered by reducing the cooling rate and maintaining the heating temperature below the eutectoid temperature for a long period, respectively. The dominance of martensitic phase at (c) the last cladding runs, and (d) the starting and finishing cladding ends was eliminated and replaced with tempered martensite as shown in Figure 5-26 (i)(d) and Figure 5-26 (ii)(d), or even bainitic morphology as shown in Figure 5-26 (iii)(d) and Figure 5-26 (iv)(d). No cracking was discerned in Figure 5-26.

The achieved results collectively suggested that the application of HTA was, by itself, incapable of preventing the martensitic transformation in the HAZ for all cladding materials listed in Table 1a, particularly at the RHS sections, as shown in Figure 5-25 (c). No martensitic transformation was found at the LHS sections and the middle sections, as shown in Figure 5-25 (a) and Figure 5-25 (b) respectively. It may be attributed to the reduction in the temperature of preheating over time at the RHS sections, as a result of the moving pattern of the heat source between gauge corners. Therefore, the effectiveness of the applied preheating on preventing the occurrence of quenching phenomenon at the RHS sections was adversely affected. Using SEM, the other typical

features of the microstructure of the LHS sections were observed to be bainitic and pearlitic morphology. The microstructure of HAZs in the longitudinal section was found with martensite, which was consistent with those in the transverse sections. It can be inferred that the preheating temperature of 350 °C at 400-mm length of depositing was inadequate to prevent martensite from forming in the HAZ. Martensitic microstructures are known to result in lower toughness and greater cracking potential. Cracking was, therefore, detected in the HAZ, where martensite as evident in Figure 5-25 (iii)(d).

The functions of PWHT in Group 2 specimens were to mitigate the residual stresses introduced by the cladding process, tailor the hardness values of the claddings, and improve the material properties of the claddings. Substitution of tempered martensitic morphology was achieved, particularly at the ends of the laser runs, hence cracking was able to be controlled by the tempering effects of PWHT. It also indicates the minimal effects of using PWHT on avoiding martensitic formation in the HAZ. However, this is based on the observation of one sample; assessment of more samples is required to fully establish the effect of PWHT on the reduction of residual stress levels and the tendency to avoid crack formation.

Similar microstructural characteristics to the single deposition were observed in the HAZ of the laser clad rails with double deposition. The microstructure in the four sub-regions of the HAZ was consistent for all cladding materials and shown in Figure 5-27 and Figure 5-28. Martensite was discernible for the groups of specimens subjected to HTA, particularly at (c) the last laser tracks, and (d) the starting and finishing track ends, as shown in Figure 5-27, due to the rapid heat dissipation caused by the thermal sinking effect of bulk rail substrate. Due to the application of PWHT in HTB, tempered martensite developed in the HAZs of the clad rails, as shown in Figure 5-28. Additionally, the sub-regions, i.e. fine-grained and spheroidised/partial spheroidised

regions, were found to develop twice in two separate regions across the HAZ's thickness. It was attributed to the overlapping of HAZs in the multiple layer deposition.

By depositing layer by layer to build-up thickness of the deposits, the heat absorbed in melting the previous deposit caused less heat penetration into the substrate. Therefore, HAZs of the second layers appeared thinner and in the middle of the previous HAZ. The heat produced by the second deposition did not avoid the formation of martensite in the HAZs by being distant from the HAZ, thus not prolonging the cooling rate of the HAZ, and in fact, may increase the probability of it occurring. The resulting peak temperature of the HAZ in the second deposition may be lower than that of the first deposition due to the long distance between the heat source and the HAZs of the second layers. Additionally, the thermal gradient was more significant in the second deposition because of the drop in the effective temperature of preheating over time via thermal convection and conduction. Thus, quenching phenomenon was more likely to occur. As a result, martensite was found almost across the entire HAZ of second layers as evident in Figure 5-27 and Figure 5-28.

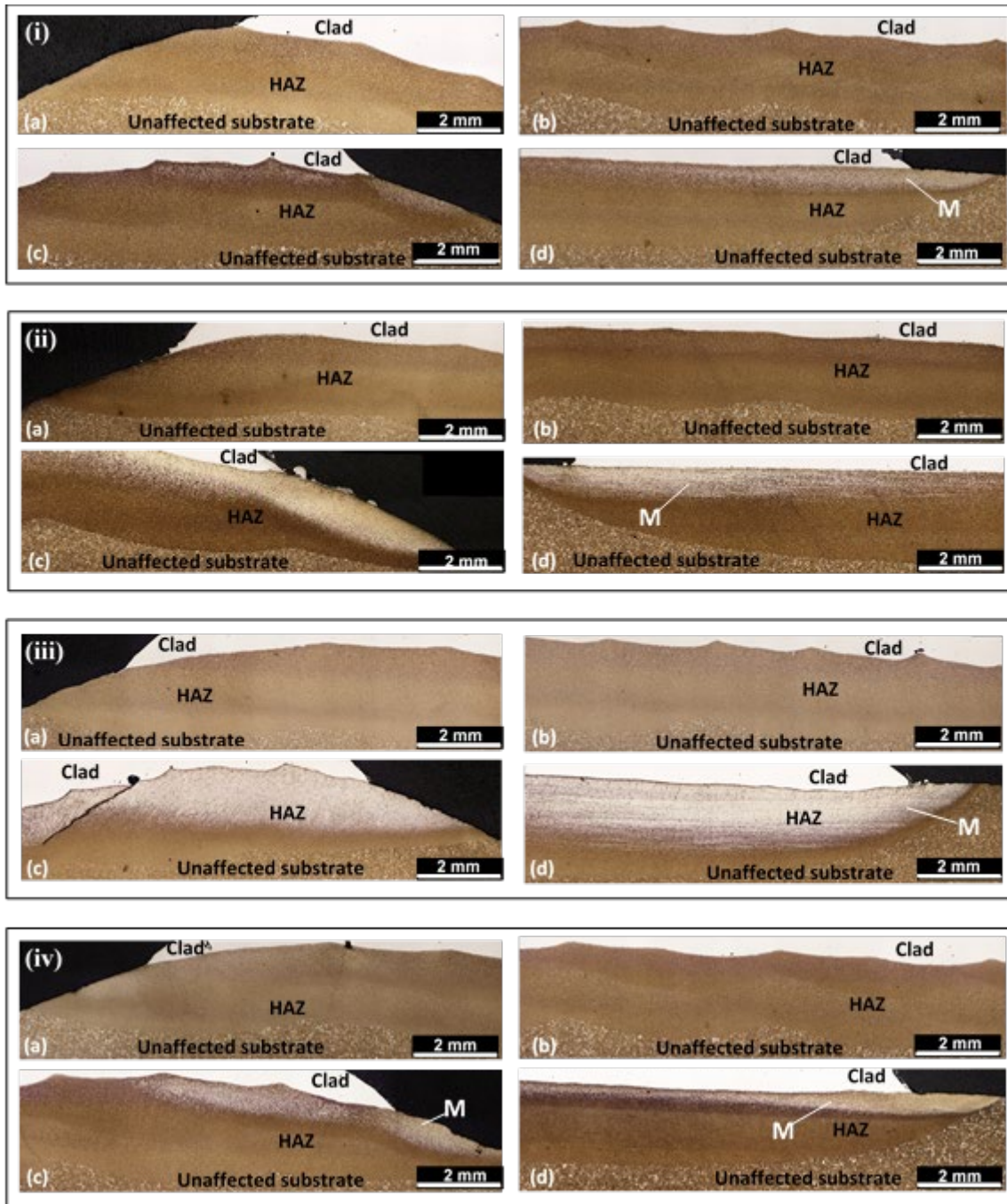


Figure 5-27 Heat affected zones and the unaffected substrate of the rail-cross sections at (a) the initial cladding runs - LHS , (b) middle cladding runs, (c) the last cladding runs - RHS and (d) a typical longitudinal cross-section at the beginning and finishing ends of the cladding runs under (i) 410L, (ii) 420SS, (iii) Stellite 6 and (iv) Stellite 21 deposits subjected to HTA and double deposition.



Figure 5-28 Heat affected zones and the unaffected substrate of the rail-cross sections at (a) the initial cladding runs - LHS, (b) middle cladding runs, (c) the last cladding runs - RHS, and (d) a typical longitudinal cross-section at the beginning and finishing ends of the cladding runs under (i) 410L, (ii) 420SS, (iii) Stellite 6 and (iv) Stellite 21 deposits subjected to HTB and double deposition. (TM=Tempered martensite)

With the aid of an image analysing software, namely ImageJ, thickness measurements of HAZs of the four depositing materials subjected to HTA (preheating only) and HTB (preheating, PWHT and slow cooling) were determined and correlated to the aforementioned microstructural characteristics, as shown in Figure 5-29.

For most of the depositing materials, the variation in HAZ's thicknesses between single and double deposition was not significant. It may suggest that the thickness of HAZs is likely to be independent on the number of deposited layers but strongly depends on the first deposition.

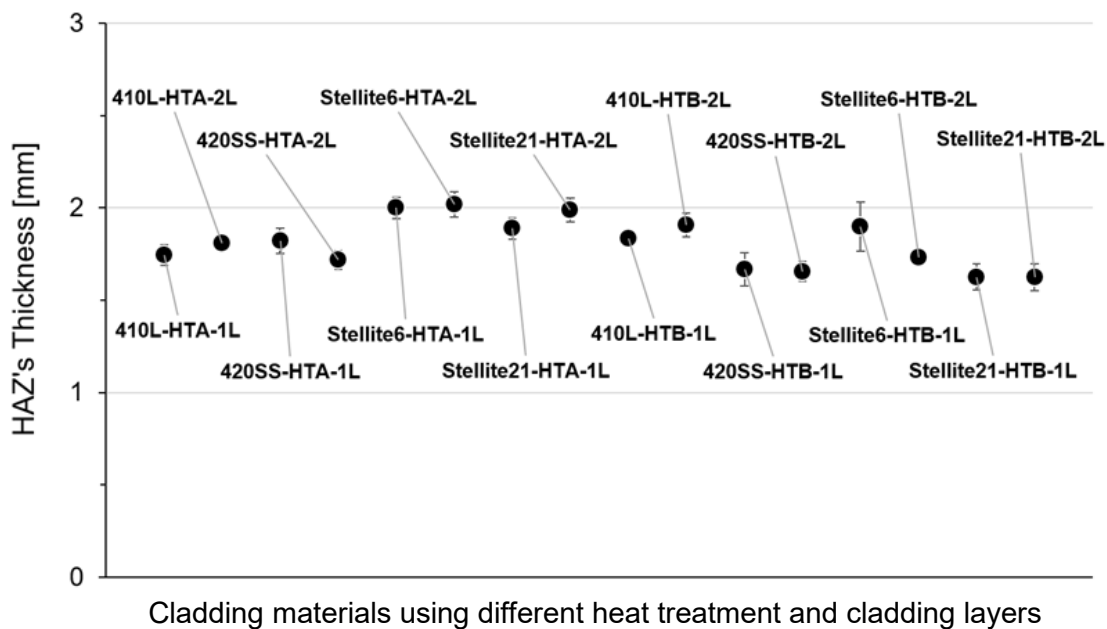


Figure 5-29 The heat affected zone (HAZ)'s thickness under the 410L, 420SS, Stellite 6 and Stellite 21 deposited layers subjected to different heat treatments and a number of layers.

PWHT did not determine the size and volume of the HAZs obtained due to the fact that laser cladding involves a rapid solidification process. However, variations of few hundred micrometres in thickness between HAZs undergone HTA and HTB were detected. It is possible that there may be some processing discrepancies such as the misalignment of the laser beam and powder focus and wearing the powder nozzle which led to the loss of depositing materials.

5.3.4 Microhardness tests

Utilization of 5 kgf Vickers indentation was considered to investigate the influences of changing depositing materials and applied heat treatments on the hardness of the laser clad hypereutectoid rails. Measurements were performed on the rail-transverse sections, i.e. middle, right and left gauge corner sections, of the four depositing materials subjected to two different heat treatment regimes.

The vertical microhardness distribution of 410L is shown in Figure 5-30. The 410L cladding layers, subjected to HTA, were determined with average hardness values of 372 HV and 375 HV for single and double deposition, respectively. As subjected to HTB, the average hardness values of cladding were 356 HV and 362 HV for single and double deposition, respectively. For the HAZs, the average hardness values were determined to be 457 HV and 490 HV respectively for single and double deposition undergone HTA, whereas, specimens which were subjected to HTB, the average hardness values of HAZ were measured to be 385 HV and 356 HV respectively for single and double deposition.

For 420SS, the vertical microhardness variation of the cross sections subjected to HTA is shown in Figure 5-31. Average hardness values of 649 HV and 629 HV were obtained respectively for the claddings with single and double deposition. The average hardness values of the corresponding

HAZs were 457 HV and 490 HV. Under HTB, average hardness values of the claddings for single and double deposition were determined respectively to be 572 HV and 531 HV, while their corresponding average hardness values of HAZ were 417 HV and 347 HV, respectively.

Average hardness values were 441 HV and 501 HV for the cross sections under HTA of Stellite 6 deposits with single and double layers respectively, as shown in Figure 5-32. The corresponding average hardness values of the HAZ were found to be 368 HV and 334 HV. For the single and double layer specimens treated with HTB, the average hardness values of the deposits were 452 HV and 441 HV, and the average hardness values of the HAZ were 395 HV and 359 HV, respectively.

Vertical microhardness distribution of the Stellite 21 cladded rails is shown in Figure 5-33. Average hardness values of 390 HV and 420 HV were achieved for the single and double layer deposits subjected to HTA. Whereas, the corresponding HAZ's average hardness values were 379 HV and 339 HV. For the single and double layer, specimens underwent HTB, the average hardness values were decreased to 362 HV and 337 HV respectively for the deposits with single and double deposition, 361 HV and 336 HV for the corresponding HAZs of the single and double deposition.

Regardless of the cladding materials and the number of layers, minor decreases in the average hardness were observed in the cladding layers and the corresponding HAZs treated with HTB compared to those subjected to HTA. It might be attributed to the application of PWHT, which tempered the microstructures. The reduction in hardness was necessary to comply with the hardness requirements of between 400 and 500 HV and to temper any martensite formed in the HAZ, hence reducing the tendency of cracking. Investigations by Harati et al. [111], Xu et al. [112] and Ganesh et al. [113] reported that, during the process of double deposition of Co-base alloys,

remelting or reheating occurred and affected the microstructure of the first layer. Hardness values of the first layers were, therefore, lower than those of the second layers.

In the current work, effects of depositing multi-layers on hardness distribution were also observed in the deposits of Co-base alloys, i.e. Stellite 6 and Stellite 21, but not obvious in the stainless-steel deposits, i.e. 410L and 420SS, as shown in Figure 5-30 – Figure 5-33. Similar to the previous investigations by [107], the hardness distribution of the 410L deposits showed high hardness values from the cladding-substrate interface to the fusion line between the two deposits, as shown in Figure 5-30, due to the carbon dilution from the substrate of hypereutectoid rail to the deposits. As a result of the high carbon content in the composition of 420SS martensitic stainless steel, high hardness values associated with the martensitic microstructure were detected. Depending on the heat input into the 420SS workpieces, reduction in hardness of the 420SS deposits might be varied owing to the tempering effect on the martensitic microstructure. The single deposition treated with HTA had the least amount of heat input, as shown in Figure 5-31. Hence the corresponding average hardness reached the highest value of 649 HV. As adding more cladding layers and heat treatment, the average hardness values of cladding were reduced, i.e. double deposition with HTA - 629 HV, single deposition undergone HTB - 572 HV and double deposition treated with HTB - 531 HV.

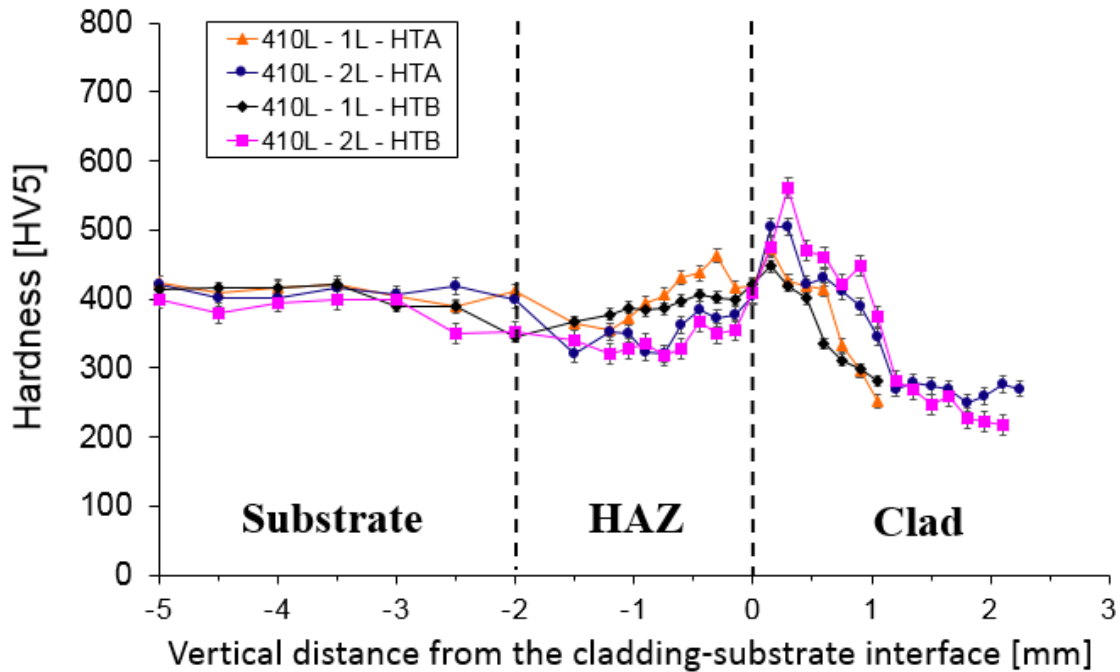


Figure 5-30 Distributions of hardness in single (1L) and double (2L) deposition of 410L under HTA and HTB.

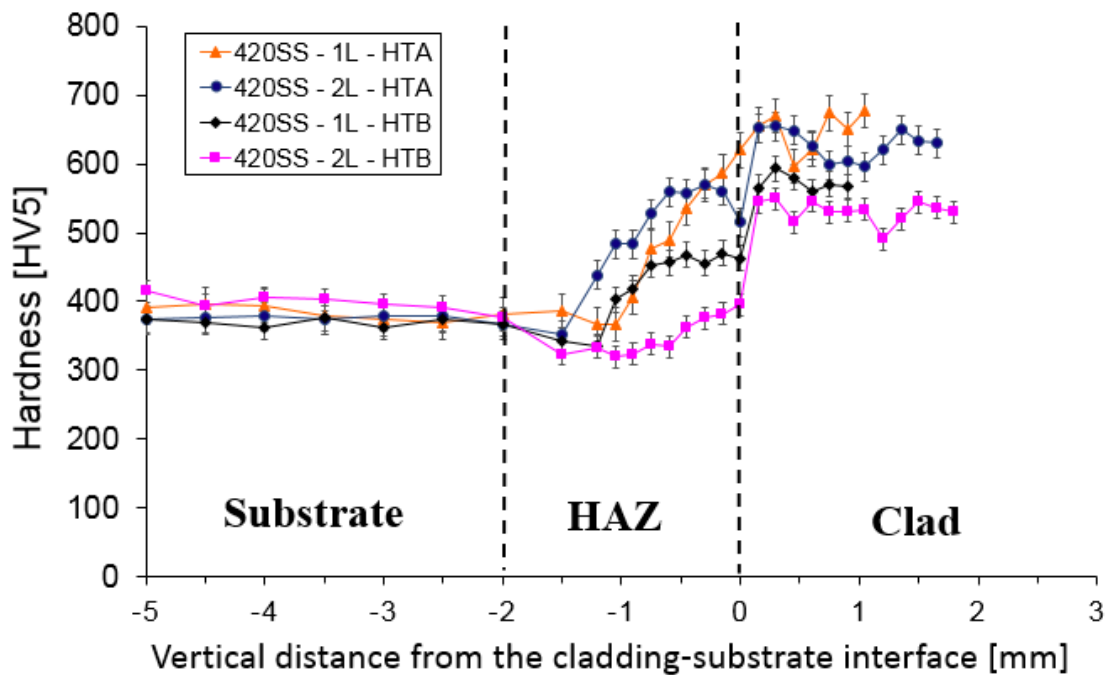


Figure 5-31 Distributions of hardness in single (1L) and double (2L) deposition of 420SS under HTA and HTB.

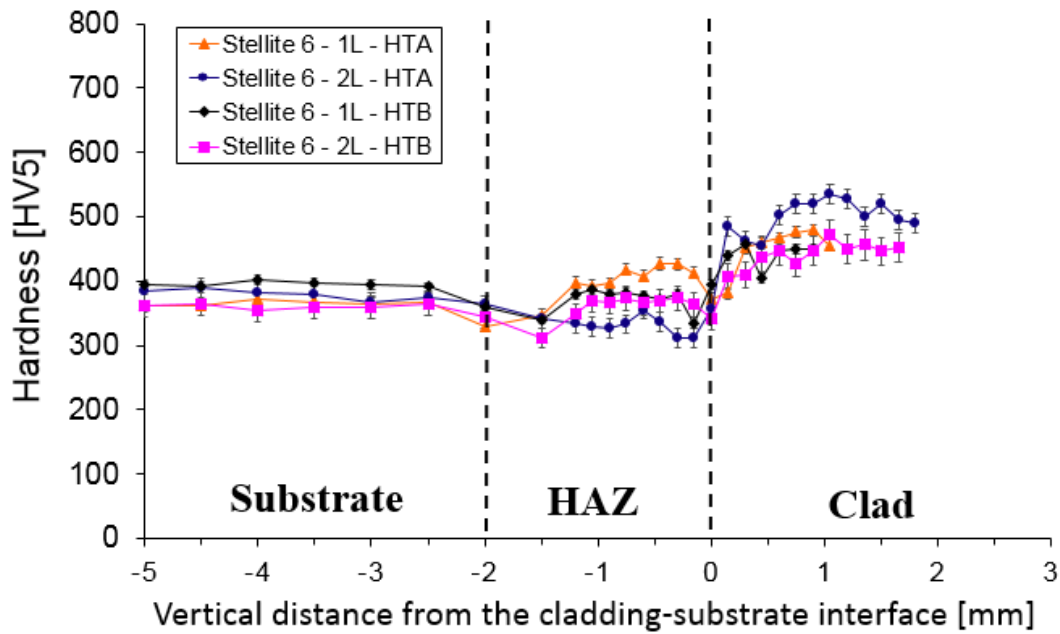


Figure 5-32 Distributions of hardness in single (1L) and double (2L) deposition of Stellite 6 under HTA and HTB.

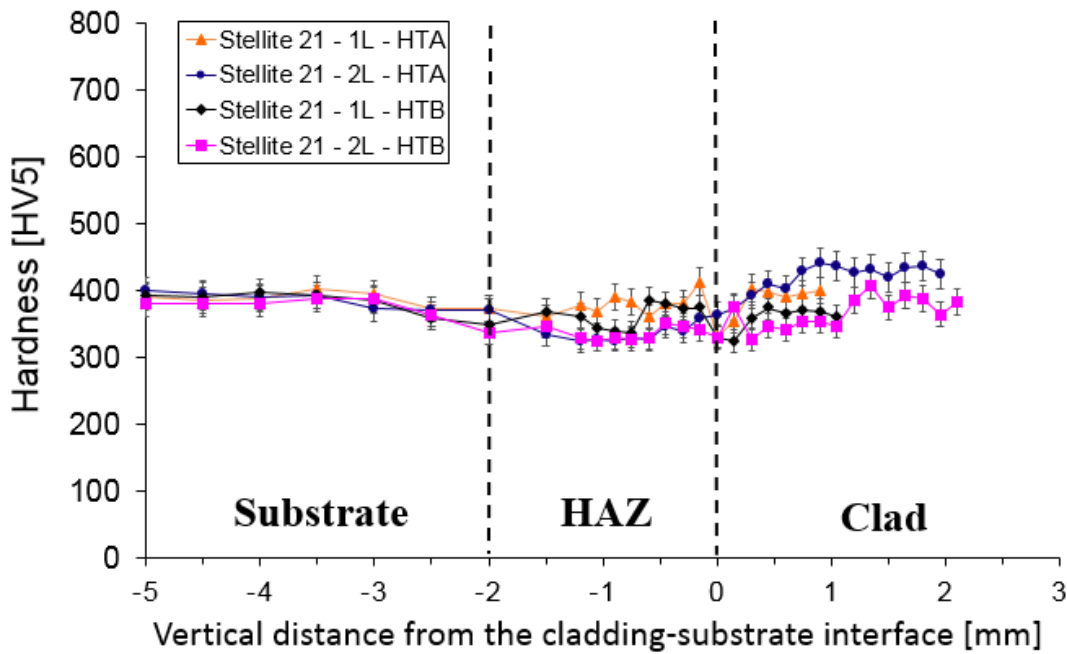


Figure 5-33 Distributions of hardness in single (1L) and double (2L) deposition of Stellite 21 under HTA and HTB.

5.3.5 Evaluation on the shear strength of the laser cladded rails

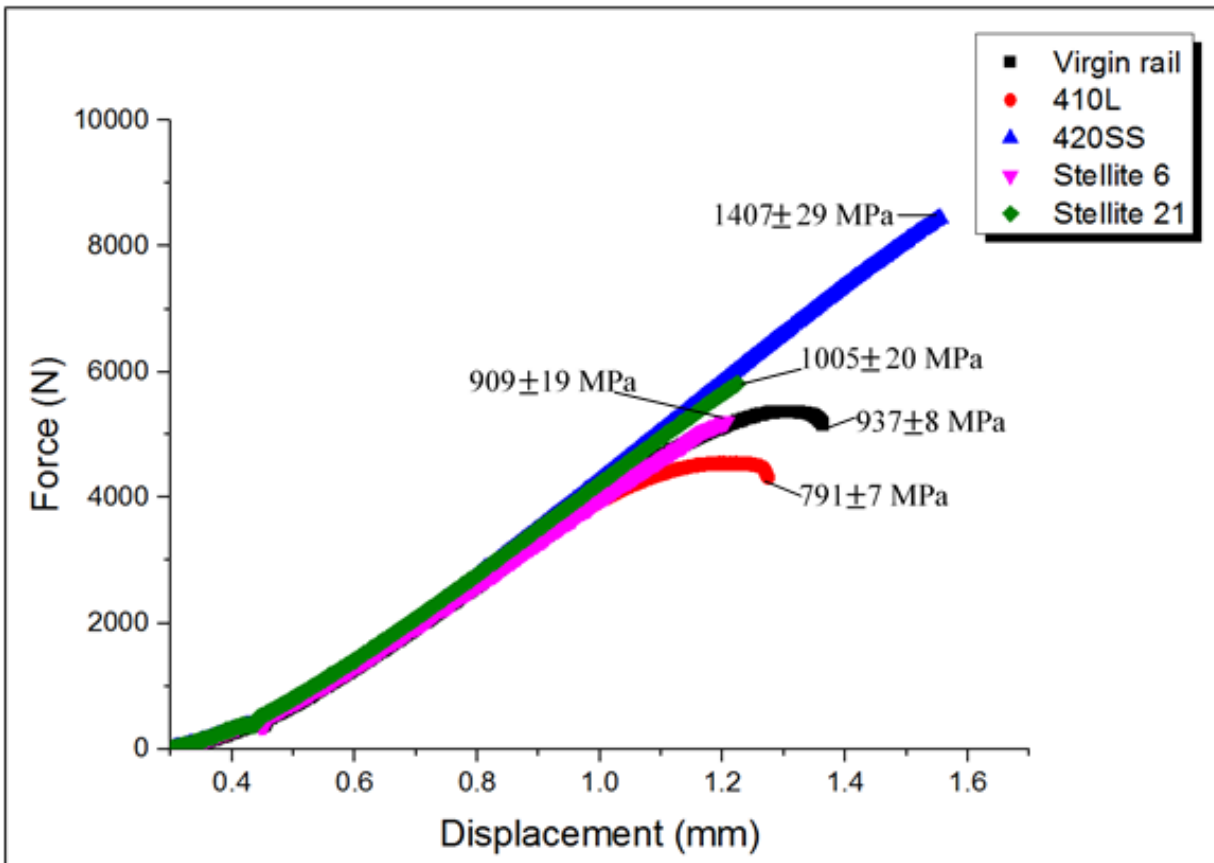


Figure 5-34 Comparison of the load-displacement curves with corresponding ultimate shear strength (USS) values acquired for the 410L, 420SS, Stellite 6 and Stellite 21 deposited layers subjected to similar heat treatments and processing parameters.

Johnson [74] reported the development of shear stress under wheel-rail contact, which is one of the vital causes of railway damage. Locations with high shear stresses are commonly observed with rolling contact fatigue (RCF) defects. Traction/adhesion and creepage are influencing parameters which decide such locations. Conditions with low creepage are established with T/N

<0.3 at the contact patch, where T and N are respectively the tangential and normal forces, and consequently the maximum shear stress occurs at subsurface levels. On the other hand, $T/N >0.3$ is associated with high creepage conditions, where shear stress is detected to be maximum at the surface. Furthermore, Magel [75] reported that material behaviour, i.e. RCF damage and cumulative wear, was found to be governed by the magnitude and the locations of the local stresses. Therefore, the shear strength of the cladded rails ought to be determined and compared to that of virgin rails. By successfully obtaining the mechanical properties, i.e. shear strength, ultimate shear strength, tensile yield strength, ultimate tensile strength, etc. from shear punch tests, Guduru et al. [76] and Hankin et al. [77] have established a useful tool to evaluate the material behaviour of small-sized specimens. In the current investigation, shear punch testing was selected to perform on the cladded rail, given that the cladding thickness was thin.

To establish a reference stiffness curve, a sample of 0.6 mm thickness was prepared from the parent rail material which complied with the specified the requirements outlined in EN 13674-1 (2011) [114] for the R400HT grade. Figure 5-34 shows the average plots of five results for every tested specimen. The pearlitic rail steel sample failed at a shearing force of 5380 N and the corresponding ultimate shear strength of 937 ± 8 MPa with typical elastic-plastic behaviour as shown in Figure 5-34. Similar measurements for the four depositing materials, also with a 0.6 mm sample thickness, revealed different mechanical behaviour from that of the rail. It can be observed in Figure 5-34 that the 420SS, Stellite 6 and Stellite 21 depositing materials exhibited fast brittle fracture, which means minimal plastic deformation was experienced. Fracture forces of 8445 N, 5198 N and 5815 N and their corresponding ultimate shear strength of 1407 ± 29 MPa, 909 ± 19 MPa and 1005 ± 20 MPa were recorded for 420SS, Stellite 6 and Stellite 21, respectively. On the other hand, similar to the rail, elastic-plastic deformation was observed for the 410L samples, and its failure load and ultimate shear strength were 4550 N and 791 ± 7 MPa, which are 84% of those of the rail.

Investigations of Guduru et al. [76] and Sellamuthu et al. [115] showed a direct relationship between ultimate shear and tensile strength. Thus, a proven estimation of the ultimate tensile strength of 1423 ± 12 MPa can be made for the 410L deposited layer. Pun et al. [116] have reported values of ultimate tensile strength being 1384 MPa and 1429 MPa for the nearest equivalent rail grades. It indicates that the 410L claddings are still within the acceptable range of ultimate tensile strength. All the other depositing materials predicted ultimate tensile strengths values are also well beyond the upper limit of the range.

5.4 Discussion

5.4.1 Impacts of cladding materials and processing parameters on cladding quality

A strong metallurgical bond is established between the substrate and the cladding material using laser cladding. As a result, a specific part of the substrate is covered with the superior material. However, it is of great importance to find the appropriate process parameters to achieve required hardness and strength particularly for rail-wheel contact, to reduce the size of the HAZ carbon dilution and to mitigate the tendency to crack.

Owing to the variations in melting points of the cladding materials, evaporation of the molten pool was observed to occur differently between the cladding materials. At a transverse speed of 1000 mm/s and 3 RPM (Group 1), Stellite 6 was susceptible to the heating issue for both single and double deposition, as shown in Figure 5-1 (c.1) and Figure 5-1 (c.2). At the transverse speed of 1200 mm/s and 4 RPM (Group 2), 410L was observed to develop bubbling for the double deposition, as shown in Figure 5-2 (a.2). The surface of the other cladding materials was observed to be free of defects for the selected ranges of processing parameters. It indicates that each of the cladding materials has its own corresponding optimum processing parameters, which would define the surface quality of the cladding. Therefore, the transverse speed of each cladding material was selected to be the maxima under a condition that resulted in a defect-free surface to minimize the

network downtime when conducting the laser treatment. Utilization of Group 1 (1000 mm/min; 3 RPM powder and 3200 W) for 410L and Group 2 (1200 mm/min; 4 RPM powder and 3200 W) for 420SS, Stellite 6 and Stellite 21 was able to establish deposits with no surface defect.

5.4.2 Assessment of structural integrity based on observed microstructural characteristics and measured mechanical properties

Metallurgical analyses were conducted on each of the cladding materials, which were carried out under the obtained optimum sets of processing parameters, to further assess their potential structural integrity. Furthermore, to achieve the hardness within specifications for rail-wheel contact and to prevent/temper any possibly formed martensite, two specimen groups were investigated; one undergone HTA (preheating only) and other undergone HTB (preheating, PWHT and slow cooling).

For specimen groups subjected to HTA, the deposits were observed to be defect-free. Depending on the chemical composition of the cladding materials, the microstructure of each cladding material was distinctive from one another.

The 410L deposits were observed with microstructures containing colonies of ferrite and a martensitic matrix, as shown in Figure 5-4. Lai et al. [117] reported that effects of carbon dilution from the hypereutectoid substrate to the 410L claddings were severe. In the current work, ferritic microstructure has been noted to occupy the regions near the top surface of claddings for single deposition, and virtually the entire microstructure of the second layers of the double deposition, whereas the remaining portion of the microstructure was the martensite matrix. It was attributed to the fact that ferrite contains approximately zero carbon and the carbon dilution from the hypereutectoid substrate was not able to reach such regions with far distances from the cladding-

substrate interface. The fast solidification during the cladding process, which provided insufficient time for the alloying elements to homogenize, was also a vital factor in the formation of the ferritic microstructure.

High carbon content in the chemical composition allowed microstructure of 420SS deposits to consist of mainly martensitic dendrites. In the current investigation, not only single deposition of 420SS on the rail substrate was conducted but also double deposition. Microstructural characteristics of (i)-(iii) were found respectively across the thickness of claddings starting from the cladding-substrate interface for single deposition, as shown in Figure 5-5. For double deposition, a similar arrangement of microstructural characteristics was detected in the first layer and the second layer starting from the interface between the two claddings, as shown in Figure 5-5 and Figure 5-9. This investigation suggests that the microstructural characteristics of the 420SS claddings formed after a rapid solidification were independent on the application of HTA. The absence of HTA in the second deposition, owing to the heat dissipation, did not cause noticeable changes in the microstructural characteristics, which further confirmed the ineffectiveness of HTA to eliminate martensitic formation from the HAZ.

Consistent with the chemical composition of the Stellite 6, in particular, a high content of Co, a complex combination of interdendritic carbides in a Co-based matrix was observed for the microstructure subjected to HTA, as shown in Figure 5-35. Dendritic structure of Stellite 6 was fine and homogeneous throughout the deposits. Similar yet finer dendritic morphologies to those of 420SS deposits were also observed, as shown in Figure 5-6, which might suggest the occurrence of rapid solidification during the laser deposition. The application of HTA has not modified the microstructural characteristics of the deposits since differences in microstructural characteristics between single and double deposition were minor. The microstructural observations were consistent with the investigation by Gholipour et al. [72] on laser cladding of 17-4 PH stainless

steel with Stellite 6. Moreover, a relatively similar correlation in microstructures between laser treated and other welded processes was revealed, which might be inferred that the laser cladding process has not significantly altered the primary microstructural properties of Stellite 6 alloys while having smaller microstructures.

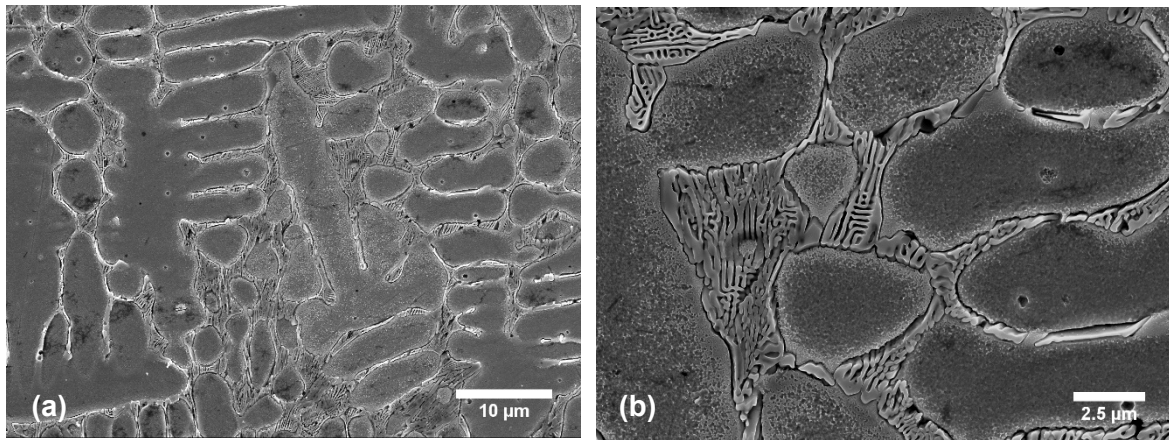


Figure 5-35 Scanning electron micrographs of Stellite 6's microstructure at (a) low magnification and (b) high magnification showing a complex combination of inter-dendritic carbides in a Co-based matrix.

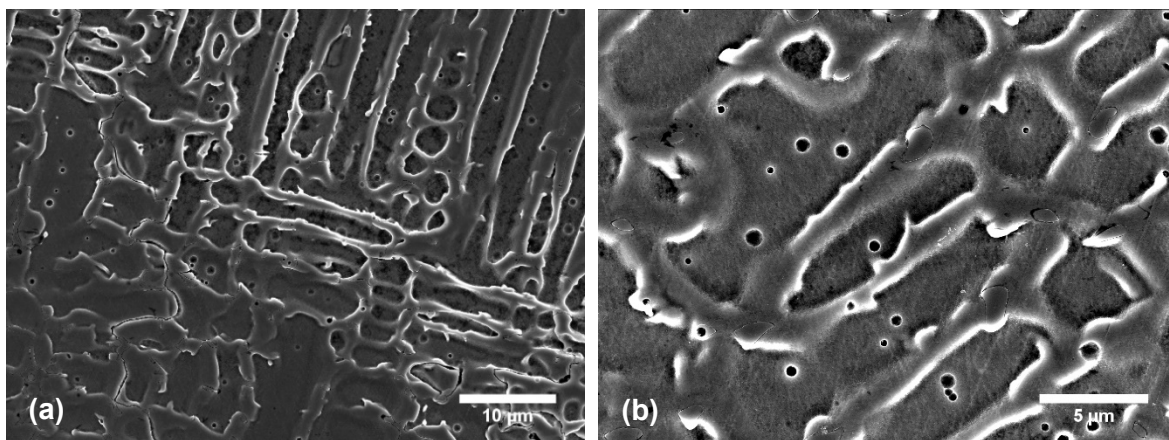


Figure 5-36 Scanning electron micrographs of Stellite 21's microstructure at (a) low magnification and (b) high magnification showing Co-base matrix and inter-dendritic Mo and Cr rich carbides.

An investigation by Davis [118] reported that, in Stellite 21, molybdenum (Mo) is employed for solid-solution strengthening instead of tungsten (W), and carbon contents were kept lower than that of Stellite 6 to improve the corrosion resistance of the cladding material. Therefore, microstructures of Stellite 21 deposits were rather distinct from Stellite 6, as shown in Figure 5-36. Dendritic structure with the typical dendritic morphologies was also discerned for single and double deposition of Stellite 21 deposits, which also suggests the incapability of HTA in avoiding rapid solidification. Generally, the microstructure consists of Co-base matrix and interdendritic Mo and Cr rich carbides. Cracking, as shown in Figure 5-37, was observed for Stellite 21 deposits only at the starting of the second deposition. This might be attributed to the excessive amount of cumulative heat from HTA, the first and second deposition inputting into the deposits. Given that mechanical properties of Stellite 21 are strongly dependent on the dispersed hard carbides in a CoCrMo alloy, any increase in applied heat input might modify the morphology and distribution of the carbides and facilitate the formation of carbides on the dendritic grain boundaries upon solidification. The carbides on the grain boundaries reduce ductility and, therefore, the sites for crack propagation were observed on the grain boundaries.

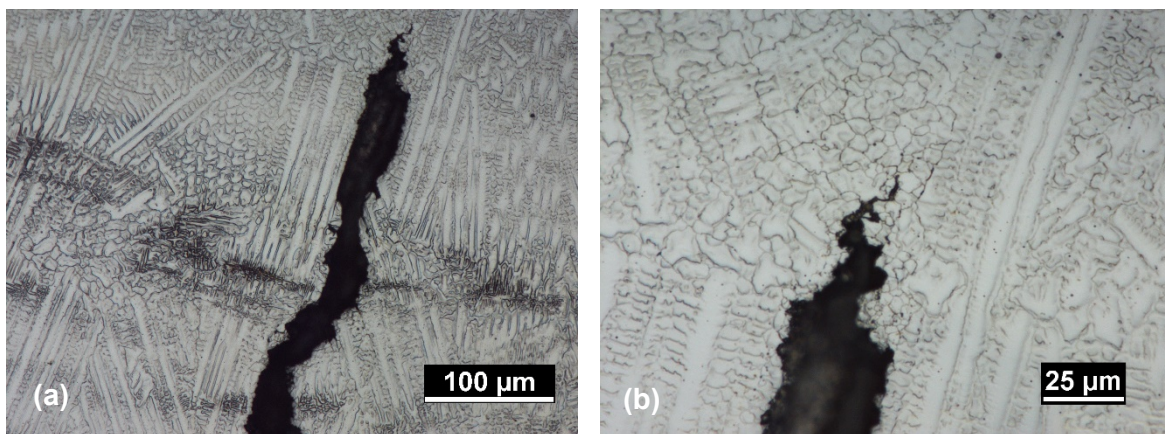


Figure 5-37 Micrographs showing an interdendritic crack for Stellite 21 deposits with HTA at the starting of the second deposition. (a) Low magnification, (b) high magnification.

Regarding the microstructures of HAZ, irrespective of the cladding materials, martensite was detected in the HAZ due to the inadequacy of the applied preheating regime, as shown in Figure 5-25 and Figure 5-27. The formation of martensite was attributed to the rapid heat dissipation even with a preheating temperature of 350 °C, through the sizeable enclosing surface area with significantly lower temperature. Cooling rates were therefore rapid enough for the diffusionless transformation to occur and martensite was formed.

For specimen groups subjected to HTB, PWHT was employed to alleviate residual stresses, control hardness and improve the strength of the deposits across the range of cladding materials. Microstructures of 410L and 420SS were observed with relatively similar characteristics to those with HTA, as shown in Figure 5-4 and Figure 5-5. Nevertheless, severe subsurface cracking occurred for both single and double layers of Stellite 6 and Stellite 21, as shown in Figure 5-6 (c), Figure 5-6 (d), Figure 5-7 (c) and Figure 5-7 (d). The overlapping/remelted regions in the microstructures of claddings were the most susceptible regions to cracking. The cracking was determined to be intergranular with typical characteristics of the reheat cracking phenomenon, which commonly happens for the Cr-Mo alloy steels with PWHT. It might be attributed to the combined influence of dilution effects from the high carbon rail substrate, excessive cumulative heat during the laser deposition, creep deformation caused by the relaxation of residual stresses, etc. The occurrence of cracking is unfavourable for utilisation of the cladding process in railway applications. Further investigations are therefore necessary to confirm the cracking mechanisms of the deposits.

Unlike the HAZ of the deposits subjected to HTA, the tempered martensite was observed as a substitute in the HAZ, particularly at the regions near the unclad surfaces, owing to the influence of PWHT. It suggests that PHWT was effective in tempering the martensite formed in the HAZ, which was able to mitigate the tendency of cracking in the HAZ. Indeed, no severe

cracks were observed, disregarding the variation in cladding materials and cladding layers, as shown in Figure 5-26 and Figure 5-28.

5.4.3 Assessment of structural integrity based on measured mechanical properties

Investigations by Jin et al. [100] and Lewis et al. [50] have shown an inverse relationship between hardness and wear behaviour in wheel-rail contact, i.e. the lower the hardness, the more the wear. Hence, the potential tribological performance of the deposited layers can be estimated using Vickers hardness measurements, provided any microstructural effects are ignored.

When subjected to HTA, 410L deposits showed the lowest average hardness, i.e. 372-375 HV, among the four considered cladding materials due to its lower carbon content. In contrast, 420SS deposits exhibited the highest values of average hardness, i.e. 629-649 HV which was strongly correlated to the microstructure containing a majority of martensitic dendrites.

Therefore, the hardness values of 420SS deposits were inapplicable for the rail-wheel contact due to the high hardness; the 410L deposits might be used for cladding as being close to the hardness requirements of 400-500 HV. However, one would need to be aware of the differences in hardness of the deposits compared to those of the parent hypereutectoid rails. If cladding layers were significantly softer or harder than the hypereutectoid parent rail, such that cumulative wear of the cladding layers would respectively be higher or lower than that of the parental rail. It could result in uneven worn surfaces of the cladded rails, which may, in turn, alter the dynamic interaction between wheels and rails, potentially increasing impact loads, and associated noise and vibration. Generally, one would aim for a cladding hardness around 5–10 % more or less than the parent rail. Nevertheless, for application as a repair option, the parent rail would be work-hardened already, so the 410L deposits may not be appropriate for such application. On the other hand, the average hardness values of the Co-base claddings, i.e. Stellite 6 & Stellite 21, fell within the hardness requirements of 400-500 HV. Stellite 6 & Stellite 21 claddings gave an average

hardness of 441-452 HV and 390-420 HV, respectively. It suggests a more uniform wear rate could be obtained across the profile of the laser cladded rails, a resulting in wheel-rail contact conditions which were closer to those obtained with the undamaged wheel and rail surfaces. However, for Stellite 21 deposits, cracking was observed at the starting of the second deposition.

For the specimen groups subjected to HTB, the application of PWHT resulted in a reduction in hardness of all the deposits, irrespective of cladding materials. 410L deposits were observed to experience the smallest reduction, particularly in the second deposition, as shown in Figure 5-30. It might be due to the microstructure containing a small portion of martensite and a large volume fraction of ferrite, as shown in Figure 5-5. Consequentially, the tempering effects of PWHT on martensitic microstructure were not significant, and a minor reduction in hardness was observed. As the microstructure of 420SS deposits consisted mainly of martensite, the effects of tempering on the microstructure were more discernible. The average hardness of the deposits subjected to HTB reduced nearly 100 HV compared to those subjected to HTA, as shown in Figure 5-31. Lin and Chen [119] reported that high hardness of the Co-base deposits originated from the hardness of intermetallic compounds in Co-rich solid solution and hard carbides. In this current work, with the application of PWHT, the average hardness of Stellite 6 and Stellite 21 decreased to comparable values of the parental rail (400 HV), as shown in Figure 5-30 and Figure 5-31. The reduction in hardness might be due to the stress relieving effects of the PWHT and presence of the reheat cracks so that the residual stresses were significantly released.

An investigation by Magel [75] reported that the development of shear stresses under the contact patch is inevitable in wheel-rail contact conditions, which directly influences the material behaviour, i.e. wear or RCF. Hence, shear punch test data was obtained to assess the relative strength of the rails cladded with the four cladding materials. Only sound and intact deposits were tested. The presented results of the current investigation showed good correlation between

the microstructure and the mechanical properties of the cladded rails. By using the 1% offset definition as defined in Karthik et al.'s work [120], ultimate shear strength (USS) of 937 ± 8 MPa was established for the unprocessed rail substrate as a reference, as shown in Figure 5-34. The USS of 410L was measured to be 84% of that of the untreated rails, which was also the lowest among the four cladding materials. It might be attributed to the large portion of ferrite in the 410L microstructure. With the microstructure containing fully martensitic dendrites, the USS value of 420SS was the highest and approximately 500 MPa greater than that of the substrate. The USS of Stellite 6 and Stellite 21 were rather comparable to that of the uncladded rails, which might be derived from the solid-solution strengthening effects of their metal carbides.

As per the above assessments, cladding material of Stellite 6 which was processed using Group 2's parameters (1200 mm/min; 4 RPM powder and 3200 W) and subjected to HTA was determined to be acceptable. The material was detected with excellent surface and subsurface, it complied with the targeted hardness range between 400 and 500 HV, and the measured ultimate shear strength was comparable to the unprocessed hypereutectoid rail substrate.

5.5 Chapter summary

The present study investigated the influences of applying different laser depositing materials and heat treatment procedures on hypereutectoid rail steels. According to the results and discussion, the following conclusions can be drawn:

- Defect-free surfaces were established on cladded rails utilizing Group 1 (1000 mm/min; 3 RPM powder and 3200W) for 410L and Group 2 (1200 mm/min; 4 RPM powder and 3200 W) for 420SS, Stellite 6 and Stellite 21.

-
- After having all vital aspects, i.e. surface defects, hardness, material strength, taken into account, Stellite 6 was established to be the most acceptable cladding material for wheel-rail applications among the considered materials.
 - The 420SS, Stellite 6 and Stellite 21 specimens showed brittle fracture behaviour in the shear punch test, whereas the 410L specimens behaved in an elastic-plastic manner similar to the virgin rail.
 - Employment of HTA was not able to significantly modify the microstructures of all the four cladding materials, whereas HTB was observed to cause severe reheating cracks for Co-base alloys, i.e. Stellite 6 and Stellite 21. Hence, PWHT might be used with cautions for Co-base alloys.
 - Regardless of the number of deposited layers and depositing materials utilized, application of preheating at the heating length equal to the cladding length (HTA) was insufficient to hinder the martensitic formation in HAZ.
 - Addition of PWHT and slow cooling (HTB) were proven to provide beneficial tempering to the HAZ's microstructure, in particular in those with martensite. Non-cracked and consistent HAZ across the entire rail-longitudinally deposited railhead, therefore, was able to be achieved.
-

- Adding the second layer did not change the thickness of HAZs yet refined the HAZ's microstructure.

 - For HTA, i.e. only preheating, an increase in the number of layers might introduce the greater chance for the development of martensite, since there is sufficient time for the substrate's preheated temperature to drop.
-

6

Elimination of HAZ's Martensitic Transformation and Observation of Carbon Dilution

In this chapter, the impacts of preheating conditions and carbon dilution on the microstructural and mechanical properties of laser cladded rails using single and double cladding layers have been investigated for a hypereutectoid steel grade typically used under heavy haul conditions. Dilution of carbon from the hypereutectoid substrate was observed, and its effect on the microstructures of the 410L ferritic stainless-steel deposits was investigated.

6.1 Introduction

Evaluation of the mechanical performance and metallurgical characteristics of the rail steels after cladding are vital in the development of future rail maintenance strategies. The previous studies [16, 63-65, 79-81] were performed using eutectoid carbon rail steel grades. In the current investigation, the effect of the higher carbon levels associated with premium rail grades such as those used under heavy haul conditions on the characteristics of the cladding layers and the heat-affected zone is studied.

For such an application, information on two fundamental issues, i.e. effects of the higher carbon levels on the characteristics of the cladding layers, and martensitic formation in heat affected zone (HAZ) of the parent rail is scarce in the open literature. The formation of hard and simultaneously brittle phases in the HAZ is expected to increase the susceptibility to cracking under cyclic, dynamic or high impact loading conditions. Also, the effects of carbon dilution from the higher carbon substrate on the mechanical and microstructural characteristics of laser cladded deposits, which has been investigated in this paper, is crucial in controlling the quality and preserving the chemical composition and properties of the laser deposits.

Hence, these fundamental issues are addressed by examining material property data and correlating them to the microstructures of the cladding material and rail substrate. Furthermore, the proposed heat treatment regime in this paper, which hinders the formation of martensite in the HAZ of laser cladded rails, should facilitate the utilisation of laser cladding technology in railway applications.

Therefore, the present study focused on the development of a heat treatment regime to prevent martensite in the HAZ by altering preheating conditions and its effects on the characteristics of

the laser clad rails. The preheating conditions were varied by altering the preheating length of the rail and over which the cladding was then applied. Furthermore, results of the study revealed the influence of diluted carbon from a high carbon rail upon a low carbon laser cladding deposit. In this paper, a functionally graded rail will be established by utilizing a fibre laser to fuse an extra layer of 410L stainless steel onto a 600-mm high-strength hypereutectoid rail piece. Microstructural evolution of the 410L deposits and the resultant HAZ were characterized via optical microscopy (OM), Scanning electron microscopy (SEM) and Electron Backscattered Diffraction (EBSD). By combining with the results of X-ray diffraction (XRD), energy dispersive X-ray spectroscopy (EDS) microanalysis and scanning transmission electron microscopy (STEM), dilution from the substrate to the cladding layers was observed. Mechanical properties were also obtained via Vickers microhardness and shear punching tests. Ultimately, the relationships between microstructural characteristics and mechanical properties of the treated rails were determined.

6.2 Experimental Setup

Two separate specimen groups with different pre-heating lengths and number of deposited layers were prepared as shown in Table 6-1.

To ensure no porosity and cracks on the surface and throughout the laser deposits, specimens were clad in the rail-longitudinal direction using laser power of 3.2kW, traverse speed of 1000 mm/s and powder feed rate of 26.4 g/min. These processing parameters were experimentally achieved and proven by many trials which were reported previously by the authors [107].

Table 6-1 Parameter sets applied for the comparative study of pre-heating length and deposited layer number

Specimens	Pre-heating length	Cladding length	No. of deposited layers
Group 1-1L	400 mm	400 mm	1
Group 1-2L	400 mm	400 mm	2
Group 2-1L	600 mm	400 mm	1
Group 2-2L	600 mm	400 mm	2

6.3 Experimental Results

6.3.1 Microstructural characteristics of 410L deposited layers

Overview micrographs of the representative rail-cross sections for each of the four considered groups of specimens are presented in Figure 6-1 for comparison. Figure 6-1 (i) shows optical images of Group 1-1L which was cladded using one layer and preheating length of 400 mm. The major phases detected are ferrite and martensite with bright and darker etching colours, respectively. The martensitic microstructure is dominant and encloses tiny ferritic grains, particularly near the top surface of the cladded layer. The density of ferritic grains appeared to be significant near the overlapping regions of the laser-tracks and the top surface, as respectively shown in Figure 6-2 (b) & (c), and was minimal as approaching the vicinity of the cladding-substrate interface, as shown in Figure 6-2 (a) & (d).

With two layers, the microstructural characteristics of Group 1-2L were significantly changed, as shown in Figure 6-1 (ii). In the second layer, large elongated ferritic grains are surrounded by a small portion of martensite matrix and originated from the interface between the first and second layers. The ferritic grains extended to the top surface of the second layer due to the high-temperature gradient as the result of the second deposition. Unlike the second layer, dendritic morphology was observed from the first layer-substrate interface to the layers' interface as shown in Figure 6-3 (a) & (c). Typical planar dendritic morphology near both the laser track overlapping regions and the cladding-substrate interface is shown in Figure 6-3 (b) & (d).

Micrographs of a typical rail-cross section of Group 2-1L with one layer and preheating length of 600 mm are shown in Figure 6-1 (iii). Martensite and ferrite are still the two primary phases in the resulting microstructures of Group 2-1L. However, ferritic grains were not as dense and substantial in size as those in the Group 1-1L and martensitic morphology was occupied dominantly throughout the deposited layer as evident in Figure 6-4 (a)-(d). More homogeneous microstructures were seen across Group 2 deposits with one and two layers than Group 1.

For Group 2-2L – Figure 6-1 (iv), the distribution of martensitic morphology was seen to be relatively uniform in the first layer. Like the second deposited layer of Group 1, large dendritic ferrite grains developed from the top surface of the first layer. It was also observed that the dendritic ferrite grains in the second layers tend to remelt and join with the preformed ferritic grains at the overlapping track regions of the first layer and leads to longer elongated ferritic grains in the overlapping regions as shown in Figure 6-1 (iv). Micrographs of the first layer of Group 2-2L, Figure 6-5 (a)-(d), showed similar microstructural characteristics to those of Group 1-2L.

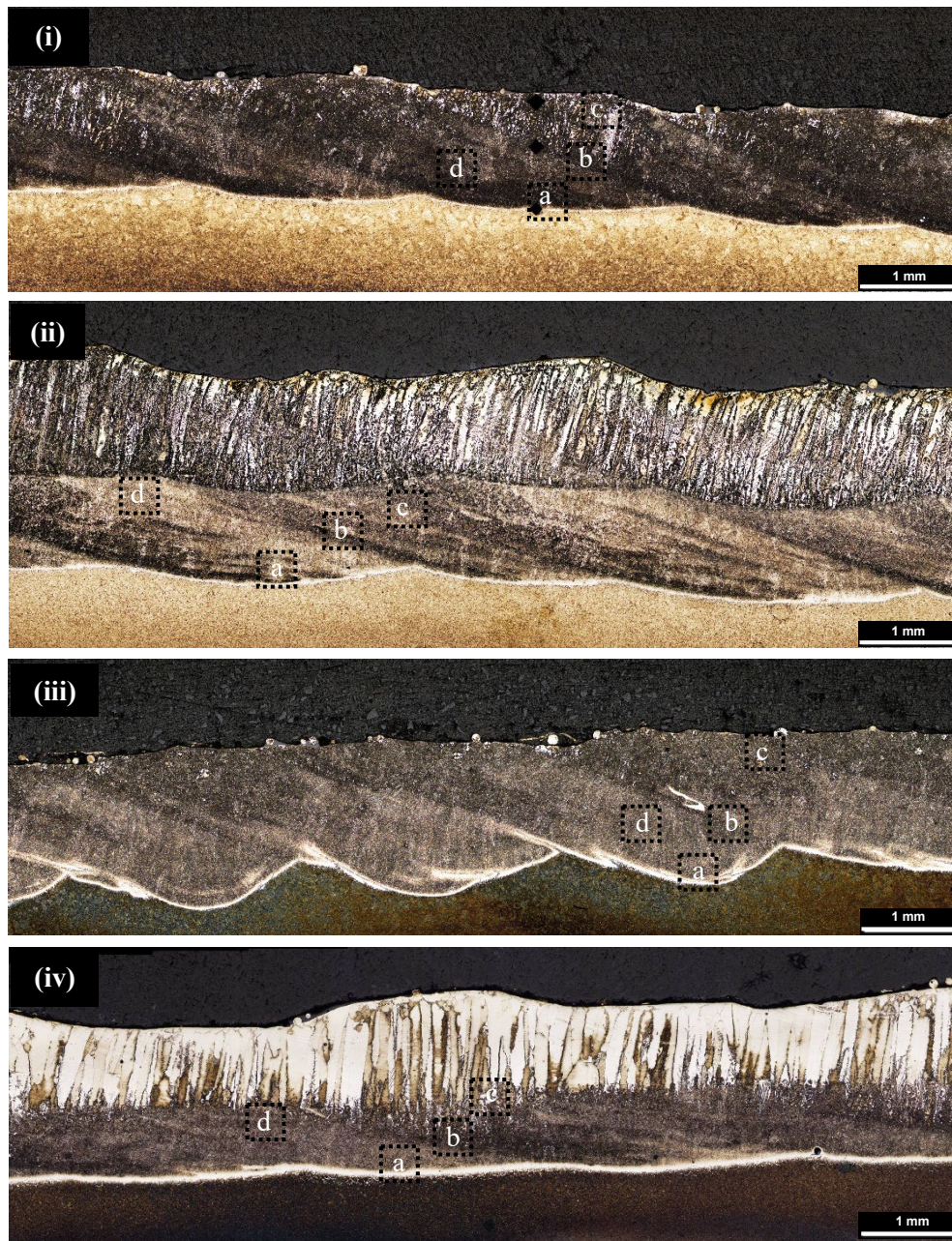


Figure 6-1 Optical micrographs of a representative cross-section of (i) the Group 1 deposits with one layer and preheating length of 400 mm, (ii) Group 1 deposits with two layers and preheating length of 400 mm, (iii) Group 2 deposits with one layer and preheating length of 600 mm, and (iv) Group 2 deposits with two layers and preheating length of 600 mm.

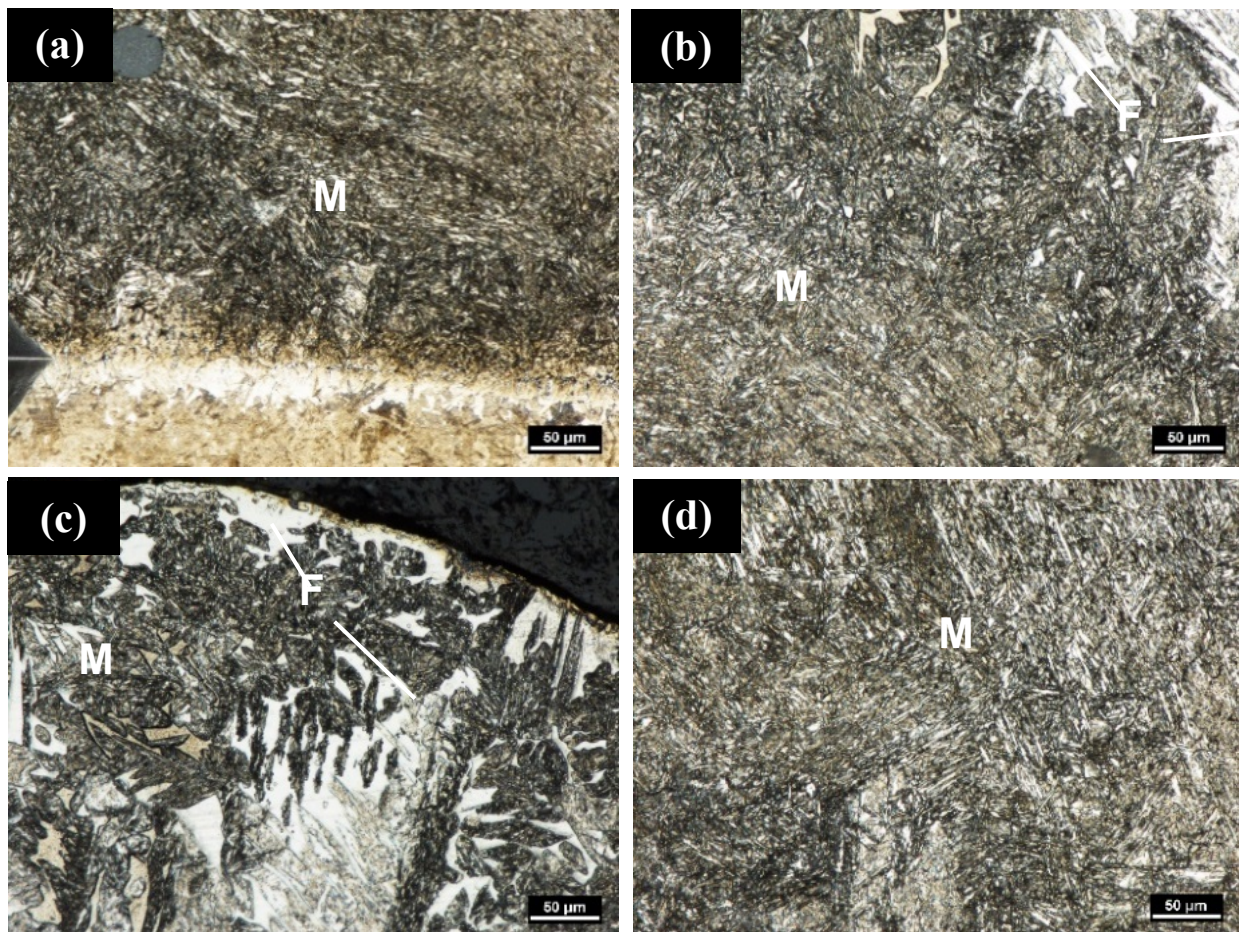


Figure 6-2 Optical micrographs of a representative cross-section of the Group 1-1L deposits with one layer and preheating length of 400 mm. (a) Deposit-substrate interface, (b) laser track overlapping region, (c) typical top portion of an individual track and (d) typical middle portion of an individual track. (M=Martensite, and F=Ferrite)

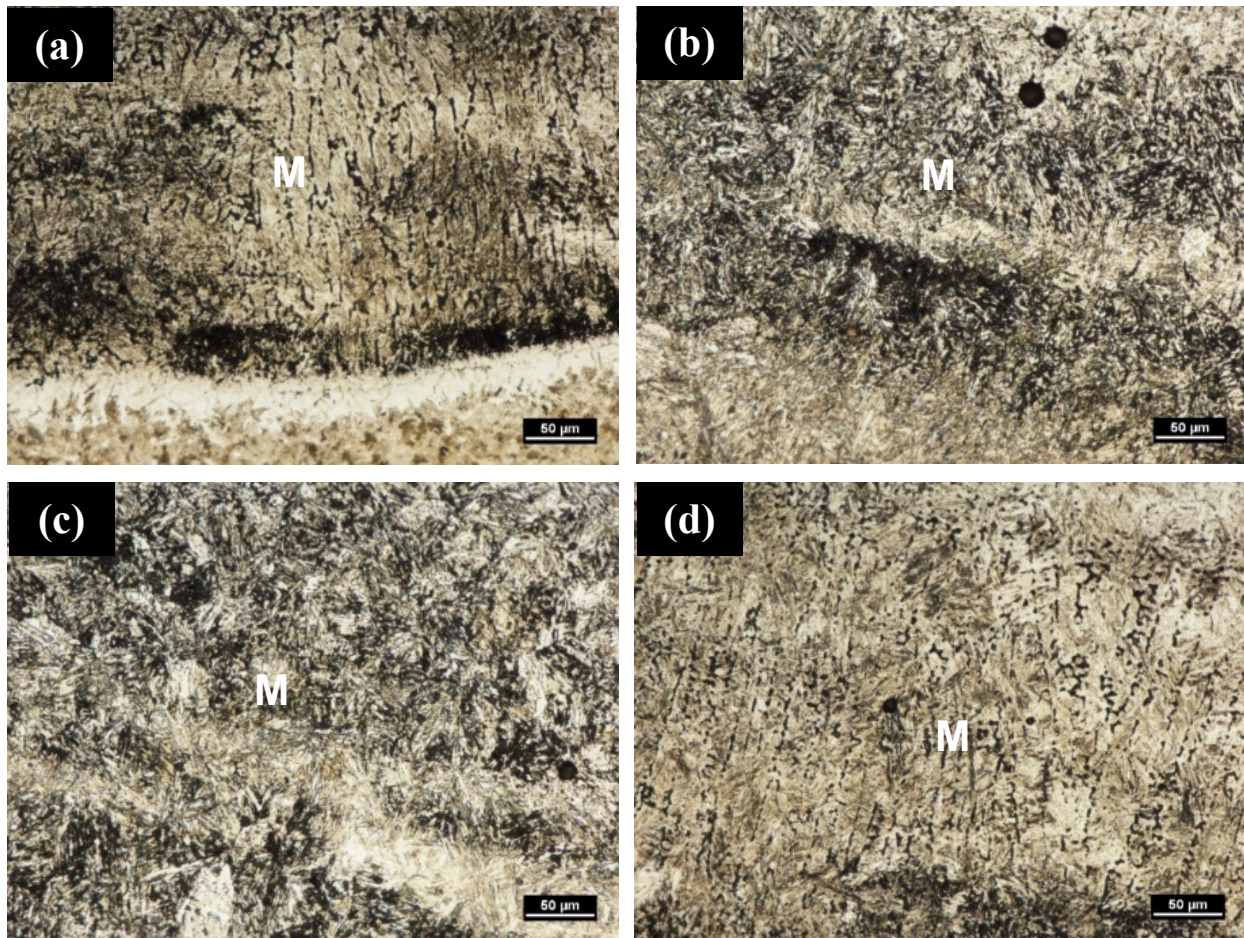


Figure 6-3 Optical micrographs of a representative cross-section of Group 1-2L deposits with two layers and preheating length of 400 mm. For the first layer, (a) deposit-substrate interface, (b) laser track overlapping region, (c) typical top portion of an individual track and (d) typical middle portion of an individual track. (M=Martensite, and F=Ferrite)

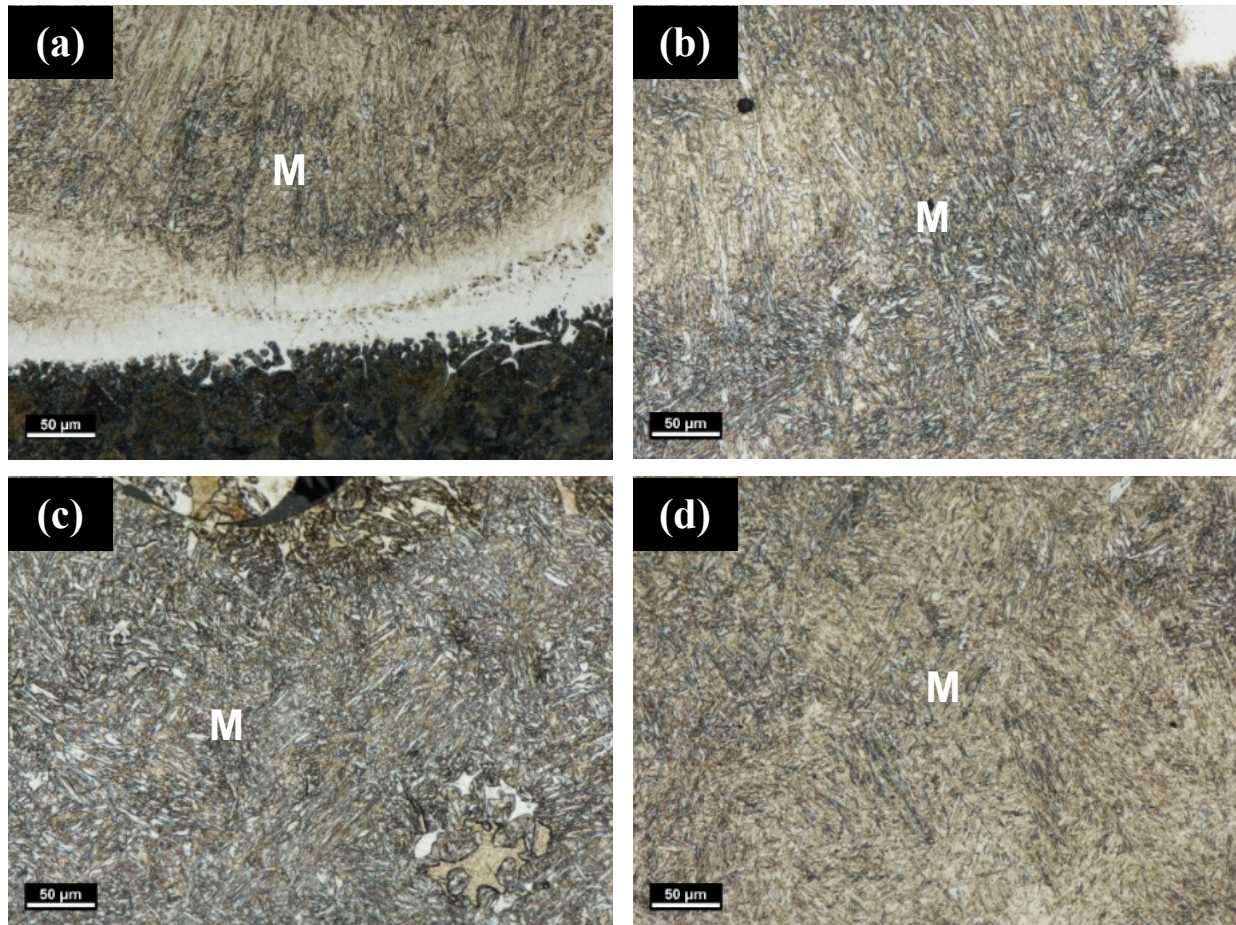


Figure 6-4 Optical micrographs of a representative cross-section of Group 2-1L deposits with two layer and preheating length of 400 mm. (a) Deposit-substrate interface, (b) laser track overlapping region, (c) typical top portion of an individual track and (d) typical middle portion of an individual track. (M=Martensite, and F=Ferrite)

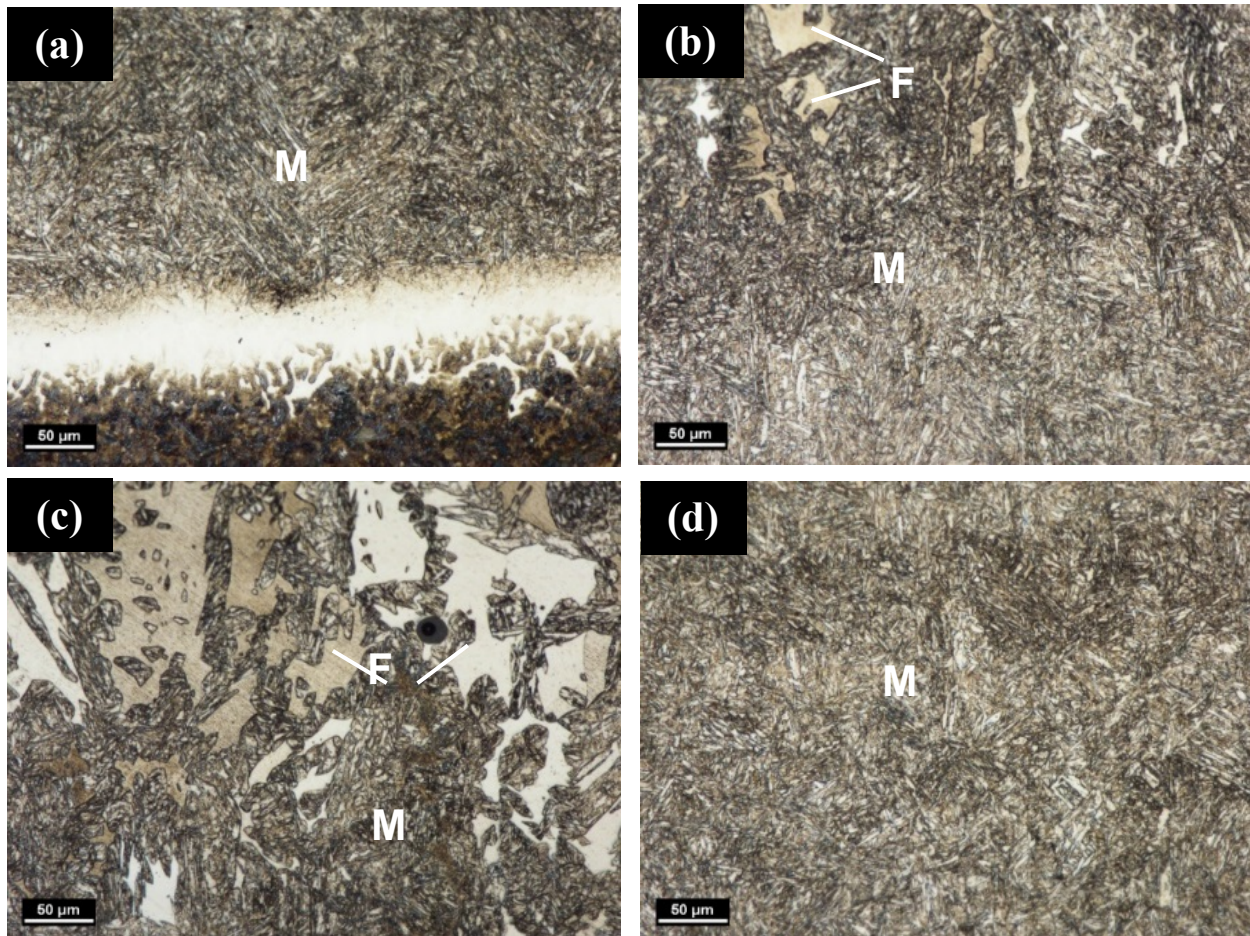


Figure 6-5 Optical micrographs of a representative cross-section of Group 2-2L deposits with two layer and preheating length of 400 mm. (a) Deposit-substrate interface, (b) laser track overlapping region, (c) typical top portion of an individual track and (d) typical middle portion of an individual track. (M=Martensite, and F=Ferrite)

6.3.2 Microstructure of 410L deposits' HAZs

The optical micrographs of the heat affected zones (HAZs) in the representative rail-transverse sections from each of the four cladding groups are shown in Figure 6-6 (i)-(iv). In each group, the four individual micrographs correspond to (a) left gauge corner, (b) right gauge corner, (c) middle section and (d) representative of the longitudinal sections at the starting and finishing ends of the laser tracks, where occurrence of martensite is the most prevalent due to the rapid cooling caused by the low temperature of neighbouring surfaces.

Similar to a previous study conducted by Lai et al.[107], typical microstructures consisting of four sub-regions in the HAZ of laser clad rails, i.e. partially molten zone, coarse-grained HAZ, fine-grained HAZ and spheroidised HAZ were found in the HAZ of the four groups of specimens.

Contiguous to the partially molten zone, the coarse-grained HAZ was established due to the high peak temperature beyond Ac3. An increase in the peak temperature would facilitate the growth of grain size. Depending on the rate of cooling, the formed austenitic grains were subjected to different solid-state transformation. Therefore, the microstructure of the coarse-grained HAZ can be varied, i.e. being pearlite, bainite, martensite or tempered martensite.

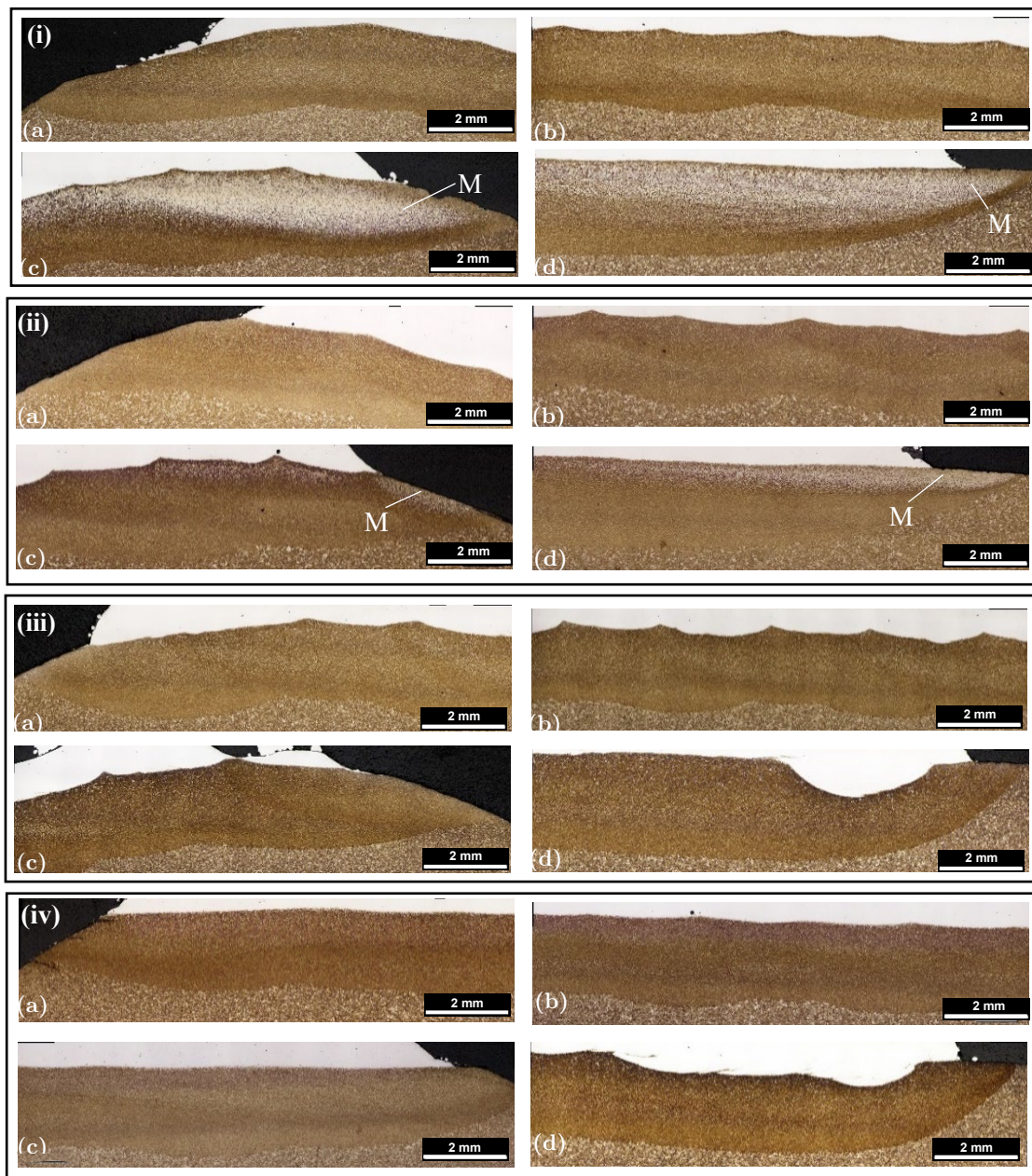


Figure 6-6 Unaffected rail substrate and corresponding HAZ of a typical rail-transverse sections at (a) left gauge corner, (b) middle section, (c) right gauge corner and (d) representative of the longitudinal sections for (i) Group 1-1L, (ii) Group 1-2L, (iii) Group 2-1L & (iv) Group 2-2L. Martensitic morphology (M=martensite) with white etching colour was detected in (c) and (d) of the (i) Group 1-1L and (ii) Group 1-2L.

Martensite was observed to occupy predominantly the coarse-grained HAZ of both Group 1-1L and Group 1-2L, particularly at the right gauge corners of the rail cross sections and the starting and finishing track ends of the rail-longitudinal sections. This might be attributed to the difference in the rate of cooling experienced by Group 1 and Group 2 specimens of clad rails. In other words, the change in the applied pre-heating lengths influenced the morphology of the coarse-grained HAZ. The Group 1 pre-heating length of 400 mm was insufficient to prevent the martensitic transformation. The actual temperature of 350 °C of the preheated substrate was dissipated rapidly owing to the low temperature of the large surrounding surface area, which led to an effect similar to quenching and hence the formation of martensite. The most susceptible regions were at the final laser-tracks (right gauge corners), as shown in Figure 6-6 (i)(c) and Figure 6-6 (ii)(c), and the starting & finishing ends of laser tracks, as shown in Figure 6-6 (i)(d) and Figure 6-6 (ii)(d), where the cooling rate was significantly higher.

Conversely, in the coarse-grained HAZ of Group 2-1L and Group 2-2L, a microstructural combination of bainite and pearlite was observed, as shown in Figure 6-7. By increasing the pre-heating length to 600 mm in Group 2, the time necessary for completing the pearlitic and bainitic transformation was allowed. The reduced rate of cooling hindered the phenomenon of quenching in not only single deposition, but also double deposition as evident in Figure 6-6 (iii) and Figure 6-6 (iv), respectively.

Microstructures of the remaining sub-regions in the four groups of specimens are relatively analogous. Therefore, due to the occurrence of martensite in the HAZ of Group 1-1L & Group 1-2L, with the preheating length of 400 mm, the cracking tendency of these groups was substantially increased.

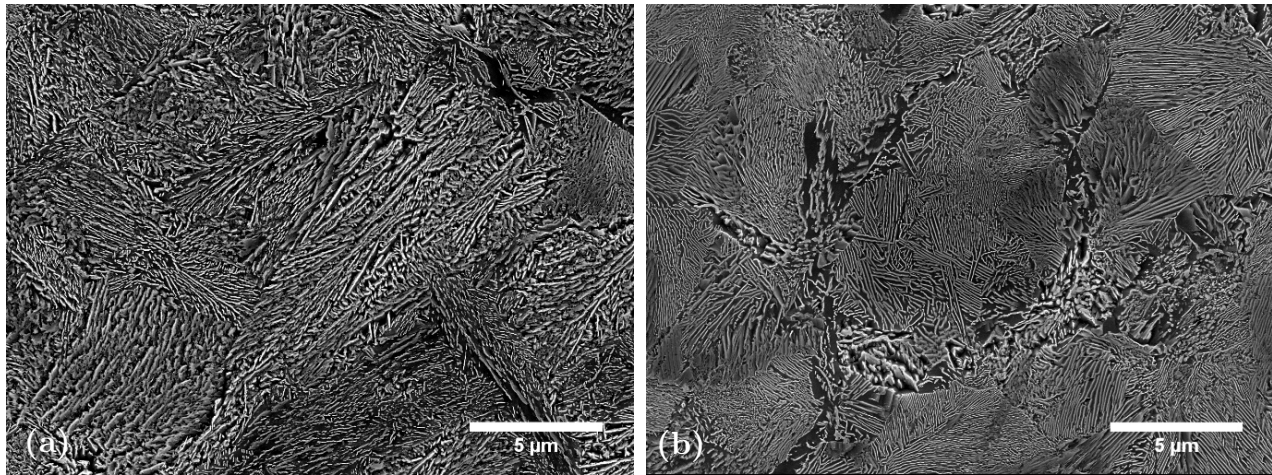
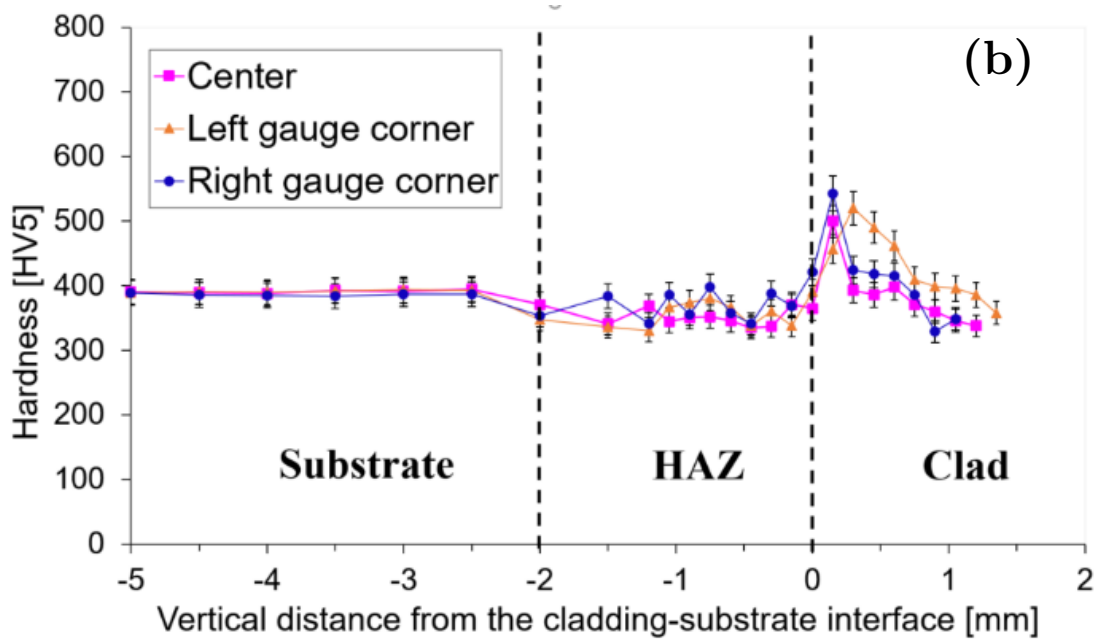
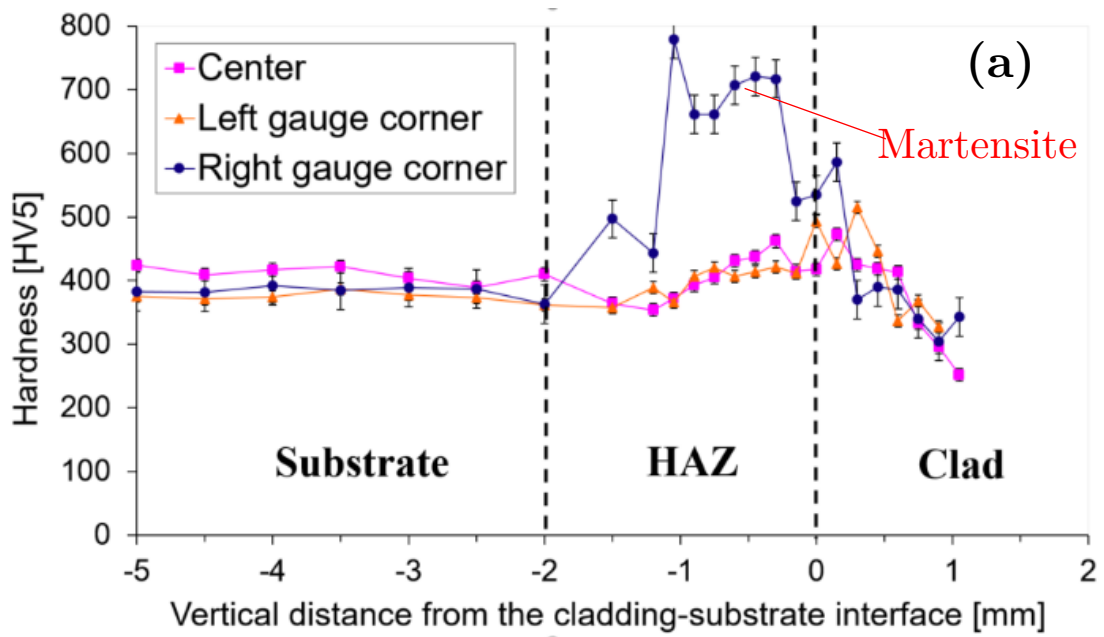


Figure 6-7 SEM micrographs showing typical (a) bainitic and (b) pearlitic morphologies in the sub-regions of the HAZs of Group 2-1L and Group 2-2L.

6.3.3 Microhardness tests

The effects of variation in the applied length of preheating on the surface hardness of the laser clad rails were investigated using five kgf Vickers indentation on the rail cross sections, i.e. middle, right and left gauge corner sections, of the four groups of specimens. Hardness indentations were performed along vertical traversing through the deposited layers, HAZ and unaffected rail substrate.



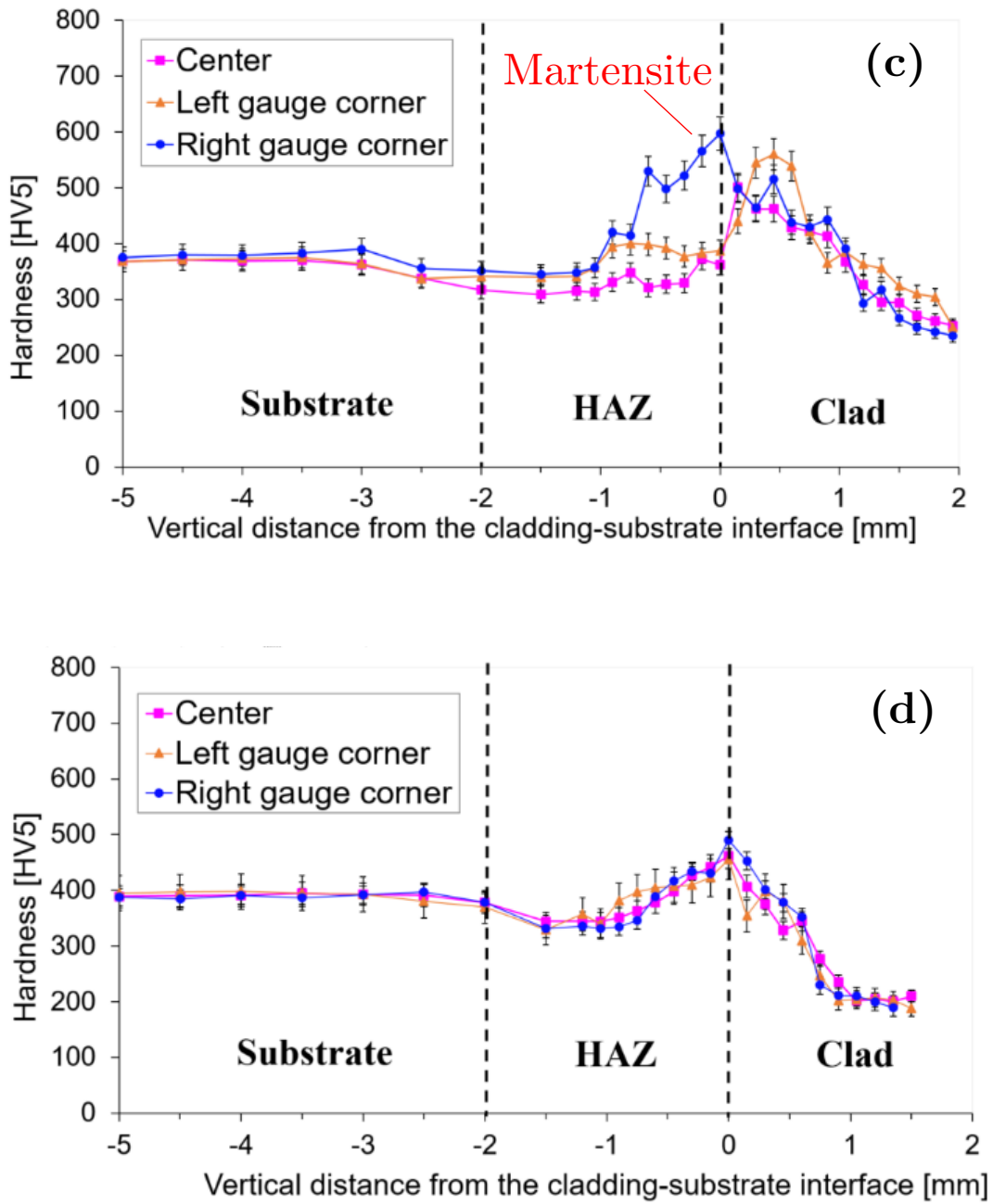


Figure 6-8 Vertical hardness distributions in the laser deposited rails (a) Group 1-1L, (b) Group 1-2L, (c) Group 2-1L and (d) Group 2-2L.

Figure 6-8 (a) shows the vertical microhardness variation of Group 1-1L's cross-sections. In the deposited layer, average hardness values of 373 HV, 403HV and 388 HV were determined for the middle, left and right gauge corner sections respectively. Average hardness values were measured to be 403 HV, 399 HV and 635 HV in the middle section, left gauge corner, and right gauge corner of the HAZ, respectively.

Likewise, the vertical microhardness variation of Group 1-2L's cross sections is illustrated in Figure 6-8 (b). In the deposited layer, average hardness values of 323 HV, 373 HV and 340 HV were determined for the middle, left and right gauge corner sections respectively. The average hardness values of Group 1-2L's HAZ for the middle, left and right gauge corner sections were 352 HV, 360 HV, and 463 HV, respectively.

For Group 2-1L cross sections, the vertical microhardness variation of the cross sections is shown in Figure 6-8 (c). Average hardness values of 387 HV, 431 HV and 409 HV were respectively obtained for the middle, left and right gauge corner sections in the cladding layer. The HAZ's average hardness values of Group 2-1L specimens for the middle, left and right gauge corner sections were 368 HV, 371 HV, and 478 HV, respectively.

For the claddings of Group 2-2L, average hardness values were 279 HV, 269 HV and 292 HV for the middle, left and right gauge corner sections, respectively as illustrated in Figure 6-8 (d). Furthermore, the HAZ's average hardness values of Group 2-2L for the middle, left and right gauge corner sections were determined to be 385 HV, 389 HV, and 384 HV, respectively.

An increase in hardness at the right gauge corners, where the last laser tracks are located, of Group 1-1L and Group 1-2L, was correlated to the formation of martensite in the fine-grained HAZ, as shown in Figure 6-6 (i)(c) and Figure 6-6 (ii)(c). The investigation by Lai et al. [107] also showed higher average hardness values at the last laser tracks when a preheating length of 400 mm was used, regardless of cladding directions. The addition of PWHT provided relatively uniform average hardness across the HAZ, but the HAZ's average hardness values were greater than that of the substrate with the presence of tempered martensite. However, in the current study, the application of a longer preheating length led to HAZ's average hardness, which has a small variation and an average closer to the hardness of the substrate due to the avoidance of martensite formation in the HAZ.

6.3.4 X-ray diffractometric phase analysis of 410L deposits

Phase identification and crystallographic studies were undertaken using X-ray diffractometer (XRD) with Co K_{α} radiation operating at 40kV/25mA. To ensure that the 410L deposits are fully characterized, X-ray diffraction profiles were taken at various discrete depths of the 410L deposits for single and double deposition.

Figure 6-9(a) shows the X-ray diffraction patterns of the untreated 410L powder, and Figure 6-9 (b)-(d) show the resulting patterns of Group 1-1L at the interface, middle and the top surface of the cladding layer. In comparison, only peaks associated with martensite/ferrite (M/F) phase were observed in the patterns of the unprocessed 410L powder, whereas both M/F, as shown in Figures 6-9 (a) - 6-12 (a), and austenite (A) FCC peaks were recorded for Group 1-1L. In the cladding layer, the volume fraction of the austenitic phase was determined to be small, at approximately less than five percent, but increased significantly close to the interface. Comparing to the peak intensities at the interface, as shown in Figure 6-9 (b), and the middle of the deposited layer, as

shown in Figure 6-9(c), the peak intensities at the top surface was marginal in magnitude, which corresponds to more equiaxed M/F microstructure at the top surface.

For Group 1-2L, the X-ray diffraction patterns are shown at the cladding-substrate interface – Figure 6-10 (b), first layer midway surface – Figure 6-10 (c), first-second layer interface – Figure 6-12 (d), the middle of the second layer – Figure 6-10 (e) and second layer's top surface - Figure 6-10 (f). M/F and A peaks are prominently observed in the first layer. Whereas, in the second layer, only the peaks of M/F phase were identified. It was also noticed that there is a shift in intensities of the M/F peaks from the plane of (110) to the plane of (200) as one is approaching from the interface of the first and second layer to the top surface of the second layer, which suggests a development of preferred crystallographic orientation in the second layer of Group 1-2L.

The X-ray diffraction patterns of Group 2-1L with longer pre-heating length are shown in Figure 6-11 at (b) at the interface, (c) middle and (d) top surfaces of the cladding layer, respectively. Figure 6-12 shows the X-ray diffraction patterns of Group 2-2L at (b) the first layer-substrate interface, (c) middle of the first cladding layer, (d) first-second layer interface, (e) the middle of the second cladding layer and (f) second layer's top surface. For Group 2, the characteristics of X-ray diffraction peaks of both single and double cladding layers are generally similar to those of Group 1.

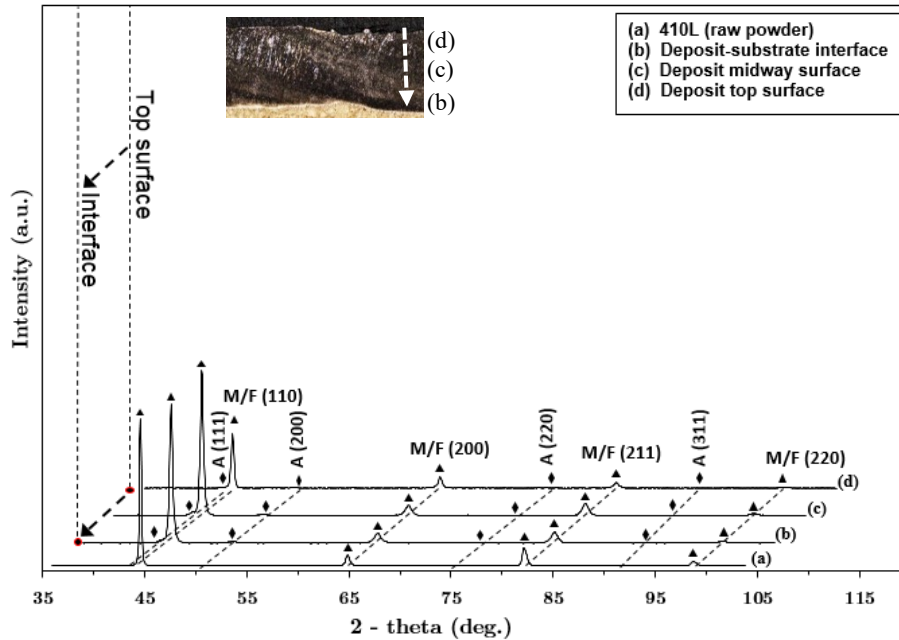


Figure 6-9 X-ray diffraction patterns of (a) the raw 410L powder and the 410L deposit with single layer and preheating length of 400m (Group 1-1L) at (b) the deposit-substrate interface, (c) the deposit halfway surface and (d) deposit top surface, respectively.

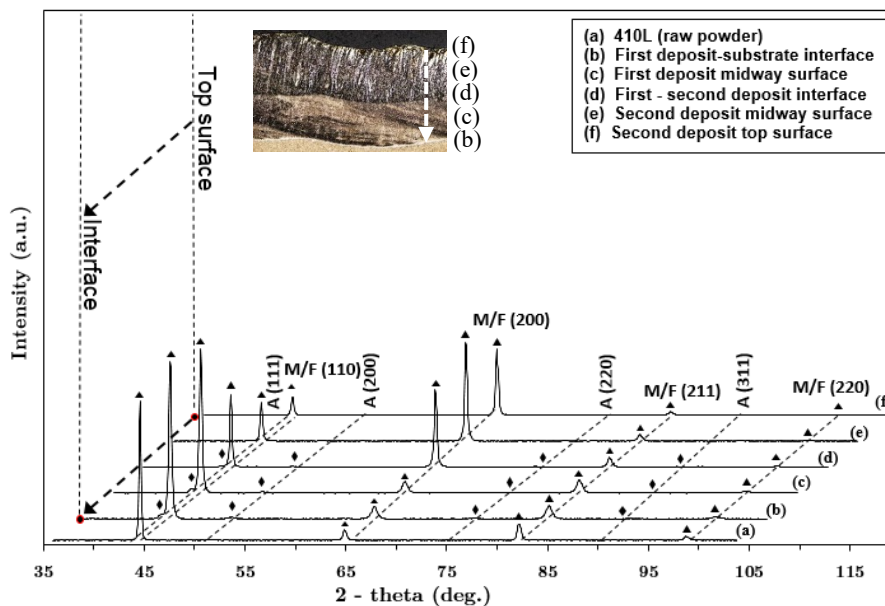


Figure 6-10 X-ray diffraction patterns of (a) the raw 410L powder and the 410L deposit with double layer and preheating length of 400m (Group 1-2L) at (b) the deposit-substrate interface, (c) the deposit halfway surface and (d) deposit top surface, respectively.

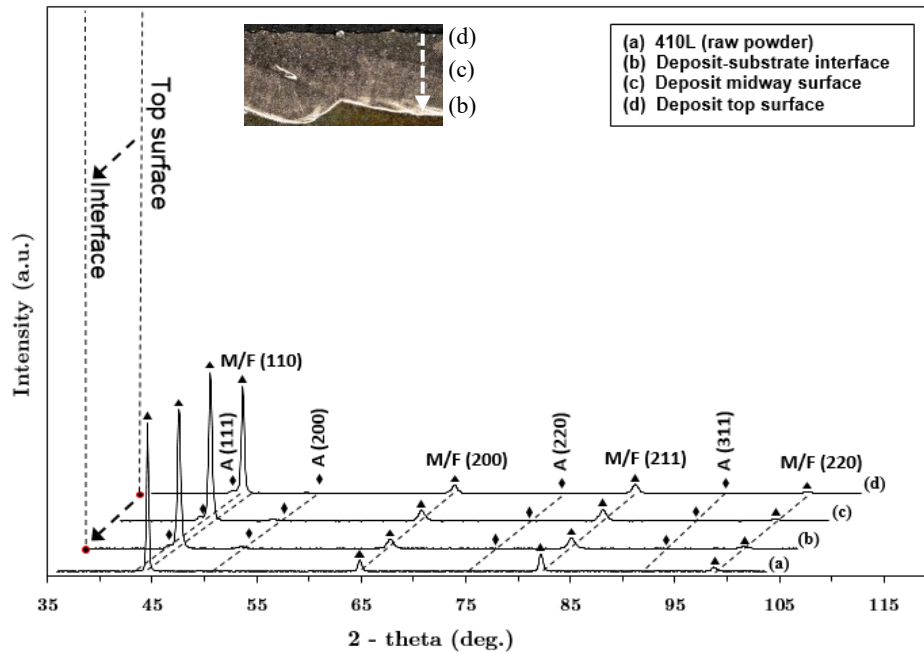


Figure 6-11 X-ray diffraction patterns of (a) the raw 410L powder and the 410L deposit with a single layer and preheating length of 600m (Group 2-1L) at (b) the deposit-substrate interface, (c) the deposit halfway surface and (d) deposit top surface, respectively.

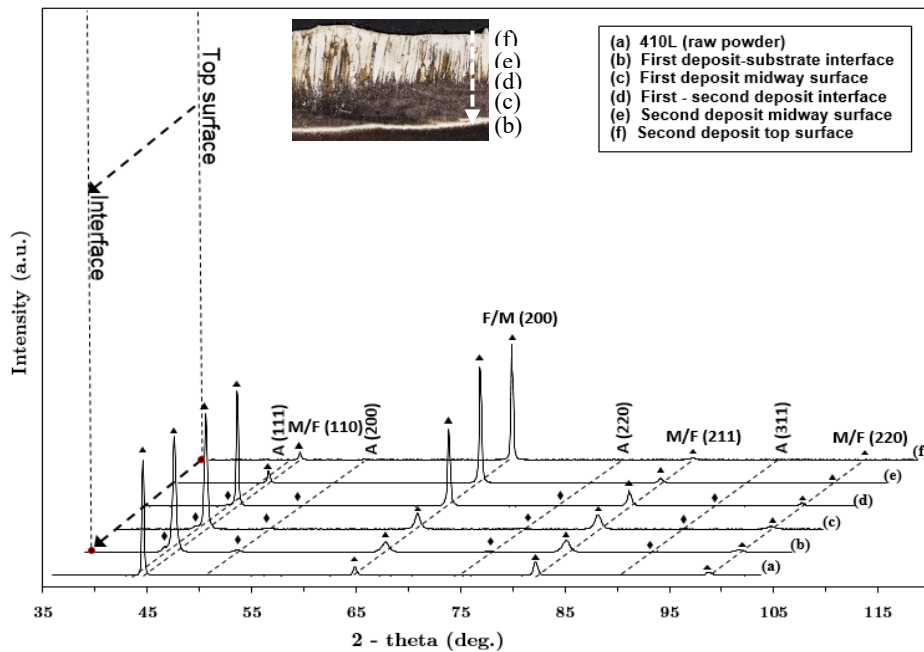


Figure 6-12 X-ray diffraction patterns of (a) the raw 410L powder and the 410L deposit with double layer and preheating length of 600m (Group 2-2L) at (b) the deposit-substrate interface, (c) the deposit halfway surface and (d) deposit top surface, respectively.

In Figures 6-9 – 6-12, the difference in the intensity of the peaks might be related to variation in cooling rates through the thickness of the deposits and preferential orientation of the grains towards the centre of the molten pool. In powder form, the 410L polycrystalline material with random orientation was not subjected to any treatment. Hence this led to typical peak distribution and diffraction patterns [106, 121], as shown in Figures 6-9 – 6-12 line (a). Due to the rapid melting and cooling during cladding process, particularly in the vicinity of the top surface, the M/F (211) peak becomes broader and lower in the peak intensity towards the top surface of the deposit. The lower peak intensities in the vicinity of the top surface of the deposits were also observed in Figures 6-9 – 6-12 line (d), which may be attributed to the difference in the graininess of the top surface regions. Investigations by Farnia et al. [122] reported a significant difference in grain shape orientation between regions of the top surface and the remaining regions of the deposits. In the current work, such difference in grain shape orientation was also discerned, as shown in Figures 6-15 - 6-18 (a). However, the variation in preheating and number of layers might have influenced the change in grain shape orientation through the thickness of the deposits.

In the first layer of the clad, phase A was determined to have a small volume fraction, as shown by small peaks related to planes: A (111), A (200) and A (220) close to the interface. This is due to the carbon dilution from the pearlitic substrate. The carbon acted as an austenitic stabiliser. Hence, a small amount of retained austenite was formed in the first layer, as shown by line (b), (c) and (d) in Figures. 6-9 – 6-12. For double layers, shown in Figs. 11 & 13 lines (d)-(f), the first layer was considered as the low carbon substrate for the second deposition. Therefore, the A (220) is only present up to the interface of the two layers. The lack of carbon led to the absence of A (220) peaks in the second deposit Figure 6-10 (e)-(f).

6.3.5 STEM microstructural analyses of 410L deposits

Ferritic grains were observed to be near the top surface of the single layer deposits and were surrounded by a martensitic matrix. In other words, ferritic and martensitic morphologies were developed at an equal distance from the cladding-substrate interface and under a similar cooling conditions. In this investigation, the formation of the ferritic grains in the vicinity of the top surface of the 410L cladding layers was studied. By means of STEM and EDS, typical results of the comprehensive observation of the ferritic grains were presented in Figure 6-13.

Song et al. [123] were able to detect fine carbide (<200 nm) in low carbon martensitic stainless steels in high-angle annular dark-field (HAADF) images. However, in the current investigations, the entire grain boundary was observed to be free from carbides, as evident in Figure 6-13(a). Additionally, a corresponding Dark-field TEM micrograph shown in Figure 6-13 (b) also confirms that there is no conspicuous contrast in colour discerned along the grain boundary. An EDS qualitative chemical microanalysis was performed in the proximity of the ferritic grain boundary for detecting the diffusion behaviour of carbon. Figure 6-13 (c) and Figure 6-13 (d) shows the high magnification TEM image of the EDS scan line (1) started from the ferritic side and the corresponding EDS results.

The EDS profile of carbon shows an increasing trend in peak intensities across the grain boundary from the ferritic grain to the martensitic matrix. Since the ferritic microstructure is renowned for containing virtually zero carbon, a significant difference in carbon content between ferritic and martensitic sides was noticed. The EDS line scan results also show that no obvious carbon segregation on the grain boundary.

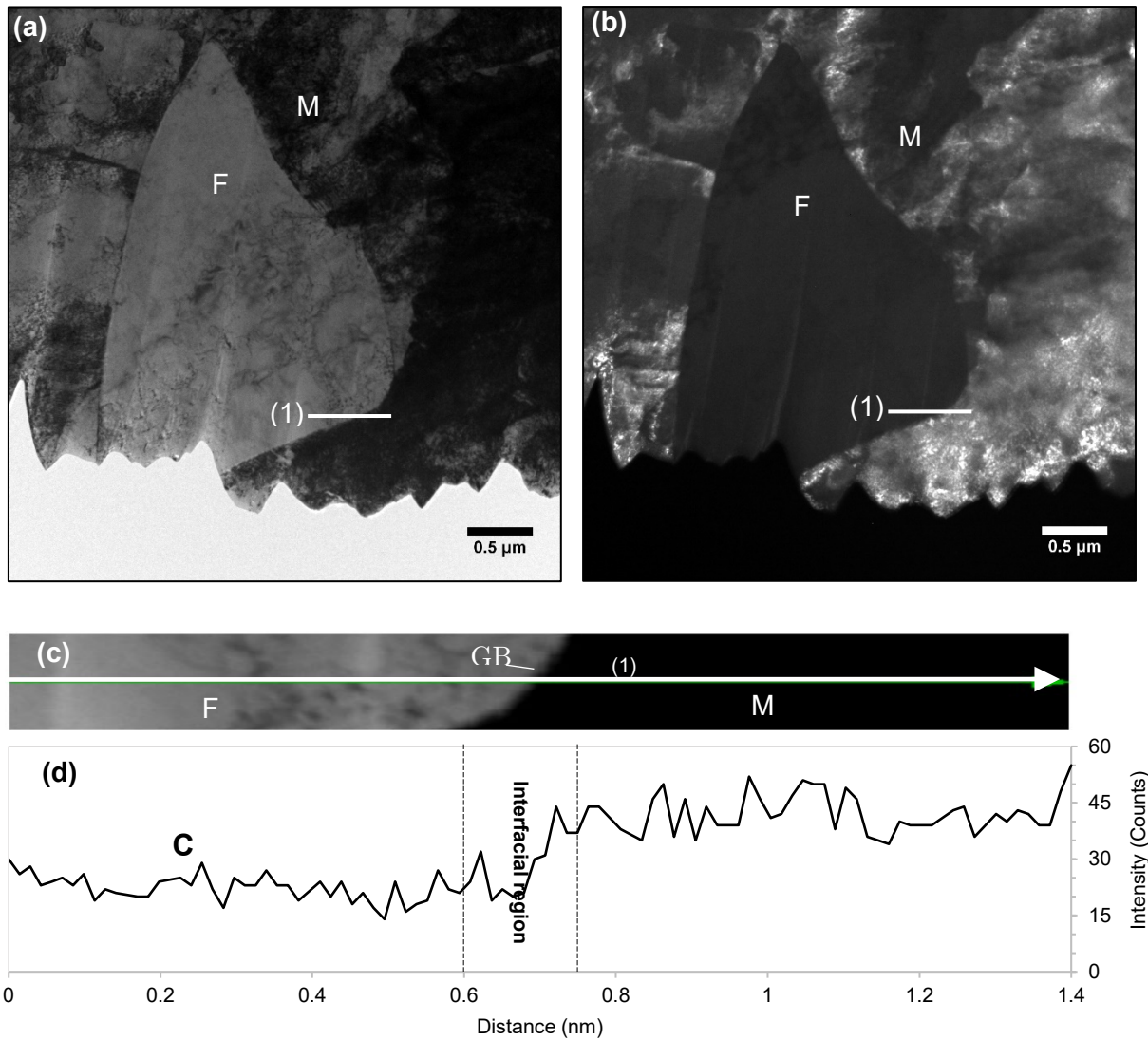


Figure 6-13 (a) Bright field TEM and (b) Dark-field TEM images of a representative ferritic grain in the vicinity of the deposit's top surface, showing no precipitation on the grain boundary. (c) High magnification TEM image of the EDS scan line (1) with the length of 1.4 nm and its resulting EDS profiles. (d) The range from 0 to 60 counts of the EDS profiles.

6.3.6 Shear strength of laser clad rails

Wheel-rail contact conditions resulted in the development of shear stresses below the contact patch, the distribution of which is influenced by the level of traction or creepage forces at the contact patch [74]. For low creepage conditions, i.e. $T/N < 0.3$, where N and T are the normal and tangential forces, respectively, at the contact patch, the maximum shear stress occurs below the surface, whereas for $T/N > 0.3$, the maximum shear stress occurs at the surface. The magnitude of these stresses and the positions at which they occur will influence the material behaviour, in particular, the propensity for wear or rolling contact fatigue damage [75]. The evaluation of the shear strength of the laser treated rails is therefore indispensable. By means of shear punch testing (SPT), the shear strength of the laser treated samples can be acquired even with limited material availability, i.e. the maximum cladding thickness of 2 mm. Given the small thicknesses of the specimens, the comparison of shear punch test data would provide a useful indication of the relative strength of the clad rails that none of the standard tests could achieve.

To establish a baseline, samples from the unclad parent rails with a thickness of 5 mm were tested and then compared to the aforementioned specimen groups. A shear yield strength (YS) of 764.35 ± 6.37 MPa using the 1% offset definition [120] and ultimate shear strength (USS) of 806.61 ± 8.28 MPa were required by the parent rail to fail in an elastic-plastic fashion as shown in Figure 6-14.

Similarly, measurements on the four specimen groups also exhibited an elastic-plastic failure behaviour during failure. Shear YS values of 709.58 ± 3.86 MPa, 718.3 ± 2.96 MPa, 665.45 ± 7.84 MPa and 650.52 ± 4.83 MPa using the 1% offset definition and USS values of 723.02 ± 2.97 MPa, 725.12 ± 6.74 MPa, 671.66 ± 11.97 MPa and 663.54 ± 9.85 MPa were recorded by using the SPT for

Group 1-1L, Group 2-1L, Group 1-2L and Group 2-2L, respectively. The variation in USS of such specimen groups is attributed to the dilution level extracted from the hypereutectoid rail substrate, a number of cladding layers and the applied heat treatment, however, is not significant due to the cladding materials of 410L.

A change in slopes of the stress curves was also noticed, although the USS values are virtually similar for the groups with the same number of cladding layers. This change was attributed to the effects of bending or compression of the thin specimens used in the SPT [76, 120].

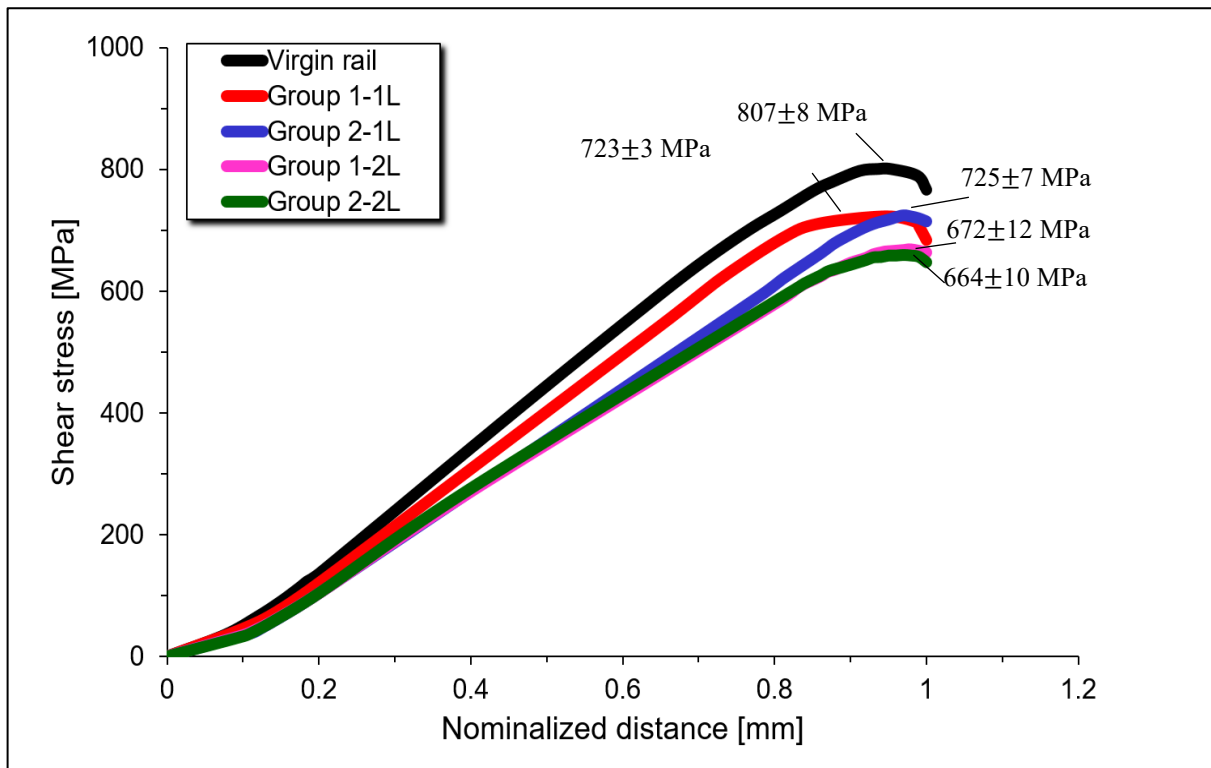


Figure 6-14 Shear-punch test curves with the corresponding USS procured for the virgin rail, Group 1-1L, Group 1-2L, Group 2-1L and Group 2-2L.

As the number of cladding layers increases; there is a greater volume fraction of ferrite added due to the lack of inherent carbon in the raw powder. In contrast, the volume fraction of martensite remains constant as carbon was diluted from the substrate as observed in Figure 6-1. It might explain the fall in shear strength of the double layers, which is a consequence of having more ferrite in the microstructures.

A previous work conducted by Pun et al. [116] demonstrated that the tensile YS were 905 MPa and 850 MPa and the corresponding ultimate tensile strengths (UTS) were 1384 MPa and 1429 MPa for the comparable hypereutectoid rail grades in the Pun et al.'s study. By applying the previously established correlation between shear and tensile strengths [76, 120], estimation of the tensile YS of 1055 ± 9 MPa and the UTS of 1452 ± 15 MPa were obtained for the parent material, which is comparable to the unprocessed rails and validates the applicability of the SPT.

Estimations of the tensile YS of 978 ± 5 MPa, 991 ± 4 MPa, 918 ± 11 MPa and 898 ± 6 MPa and the corresponding UTS of 1301 ± 5 MPa, 1305 ± 12 MPa, 1209 ± 22 MPa and 1194 ± 18 MPa were obtained for the Group 1-1L, Group 2-1L, Group 1-2L and Group 2-2L respectively, which are at least 80% of the unprocessed rails. However, a rigorous assessment in field test conditions may be necessary to relate the test results to the actual performance in wheel-rail contact with confidence.

6.3.7 Crystallographic texture of laser cladded rails

The morphology, distribution of grain size, quantitative phase identification and crystallographic orientation of the four groups of specimens were investigated using EBSD. Results from the EBSD analysis encompassing the top surface of the cladding-substrate interface are presented. It should be noted that all specimens share a common cladding direction and the analysis was conducted at cross-sections perpendicular to the cladding direction (i.e. transverse cross-sections).

Figures 6-15 – 6-18 show the orientation maps, pole figures, grain size distribution and grain misorientation profiles for Group 1-1L, Group 1-2L, Group 2-1L and Group 2-2L after the laser deposition. Figure 6-15 – 6-18 (a) show the morphological texture results of EBSD large area mapping, being used in conjunction with inverse pole figure legends as shown in Figures 6-15 – 6-18 (b).

It can be seen from the orientation maps and pole figures in Figure 6-15 and Figure 6-16 that the specimen groups with single deposition show random texture. The maximum intensity in pole figure for those two groups is only three. Some of the martensitic blocks (as highlighted in white dotted lines) in Group 1-1L, as shown in Figure 6-15 (a), were elongated at an angle of approximately $65 \pm 5^\circ$ towards the cladding direction, which was attributed to the greater temperature gradient caused by the shorter preheating length of 400 mm. At first, grain nucleation was almost heterogeneous at the cladding-substrate interface. During laser deposition, the presence of greater temperature gradient promoted the grains to grow faster and nearly parallel to the heat-flow direction which is almost vertical initially. Due to the motion of the laser source, the heat-flow direction is tilted and, thus, most of the grains were observed at an angle of approximately $65 \pm 5^\circ$ towards the cladding direction. Within the martensitic blocks, misorientation of neighbouring laths was detected to be typically 2° .

Specimen groups with double depositions, as shown in Figure 6-17 and Figure 6-18, showed a finer and random crystallographic orientation in the first cladding layer owing to the effect of the annealing caused by the heat input of the second layer. However, the (001) texture in the second cladding layer (the top layer) was strongly preferred. The strong solidification fibre texture was developed prominently in the (100) pole figures in the second deposit layer, as shown in Figure 6-17 (c) and Figure 6-18 (c).

The sudden increase in grain size and a change in crystallographic orientation were observed in the central part of the second cladding layer. The formation of large tilted ferritic cellular dendrites in the central part of the second cladding layers may be attributed to the combined effects of the reduction in preheating temperature via air convection, insufficient dilution level of carbon from the hypereutectoid rail substrate, the motion of laser nozzle, etc. The interdendritic regions were detected with martensitic morphology. At the very top of the cladding layer, a thin layer containing horizontally elongated grains was found for the two groups of specimens. It is to be noticed that Farnia et al.[122] have reported similar microstructural characteristics due to the absence of preheating prior to a laser cladding process.

Figures 6-15 – 6-18 (d) show the distribution of grain size of the four specimen groups. For single deposition, the majority of the grains are found to be fine and below $40\ \mu\text{m}$ owing to the presence of the dense martensitic laths from the interface up to the central part of the cladding layer, as shown in Figure 6-15 (a) and Figure 6-16 (a). These granular characteristics were shared by both Group 1-1L and Group 2-1L, as shown in Figure 6-15 (d) and Figure 6-16 (d).

Therefore, the bar charts of the distribution of the grain size for the single deposition show maxima values of $10\ \mu\text{m}$ approximately and reduce significantly onwards. A sudden increase in grain size was noticed as approaching the top of the cladding layers, because of the formation of ferrite with a maximum grain size of $100\ \mu\text{m}$ approximately. Such grains were observed to be in low density and scattered. Additionally, it can be seen from Figure 6-15 (d) and Figure 6-16 (d) that there is a lower percentage of grains with $100\ \mu\text{m}$ in size in Group 1-1L than that of Group 2-1L, which suggests that having longer preheating length reduces the cooling rate and promotes carbon dilution from the substrate.

Generally, for double deposition, grains under 100 μm in size have the major portion with 87% and 79% respectively for Group 1-2L and Group 2-2L, as shown in Figure 6-17 (d) and Figure 6-18 (d) and are primarily located in the first cladding layers. The detailed grain size distributions for grains below 100 μm show similar features to the single deposition and further emphasize the effect of dilution from the rail substrate. By adding the second layer, upsurges of grain size up to 1100 μm can be observed in Figure 6-17 (d) and Figure 6-18 (d), owing to the formation of ferritic cellular dendrites in the second layers.

The results of misorientation angle distribution are presented in Figures 6-17 - 6-18 (e), which collectively suggest that approximately 75% of grain boundary are 10-15° low-angle grain boundary (LAGBs) and the remaining 25% are high-angle grain boundary (HAGBs) with the majority ranging from 50° to 60°. Figures 6-15 – 6-18 (d) show a similar trend for grain size distribution for all groups.

6.4 Discussion

6.4.1 Impact of preheating condition on Microstructural characteristics of HAZs of cladded rails

Four sub-regions in the HAZ (e.g. Partially molten zone, coarse-grained HAZ, fine-grained HAZ and spheroidised/partially spheroidised HAZ) were identified as the results of the laser heat input after the deposition of 410L layers on hypereutectoid rails. The resulting microstructures and properties of such sub-regions differ from the substrate and commonly serve as the weakest part of cladded rails [124].

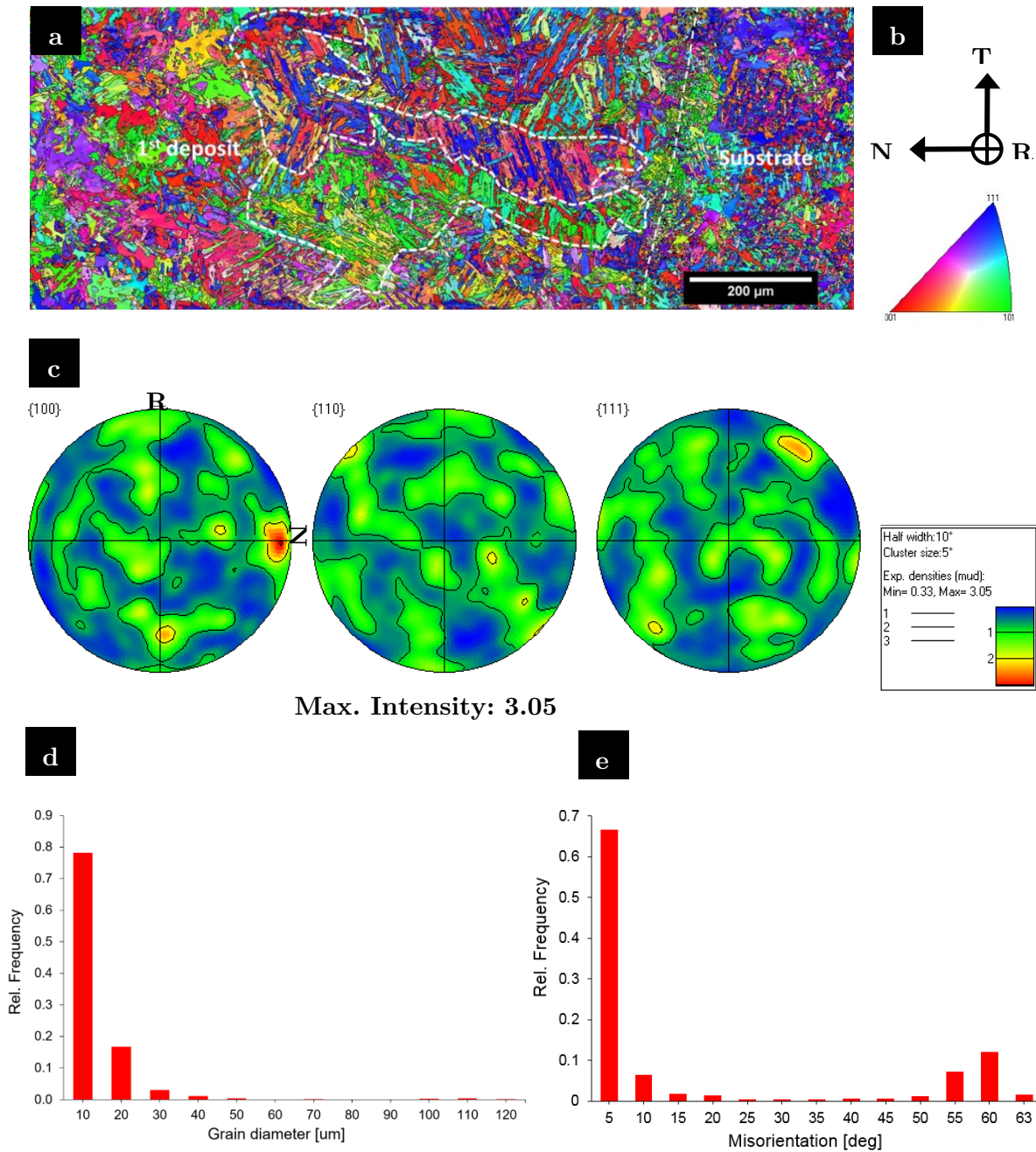


Figure 6-15 Results of EBSD large area mapping of Group 1-1L. (a) Orientation map being used in conjunction with (b) Inverse Pole Figure (IPF) legends. (c) (100), (110) and (111) pole figures attached with an intensity legend. (d) Distribution of grain size. (e) Distribution of misorientation angle.

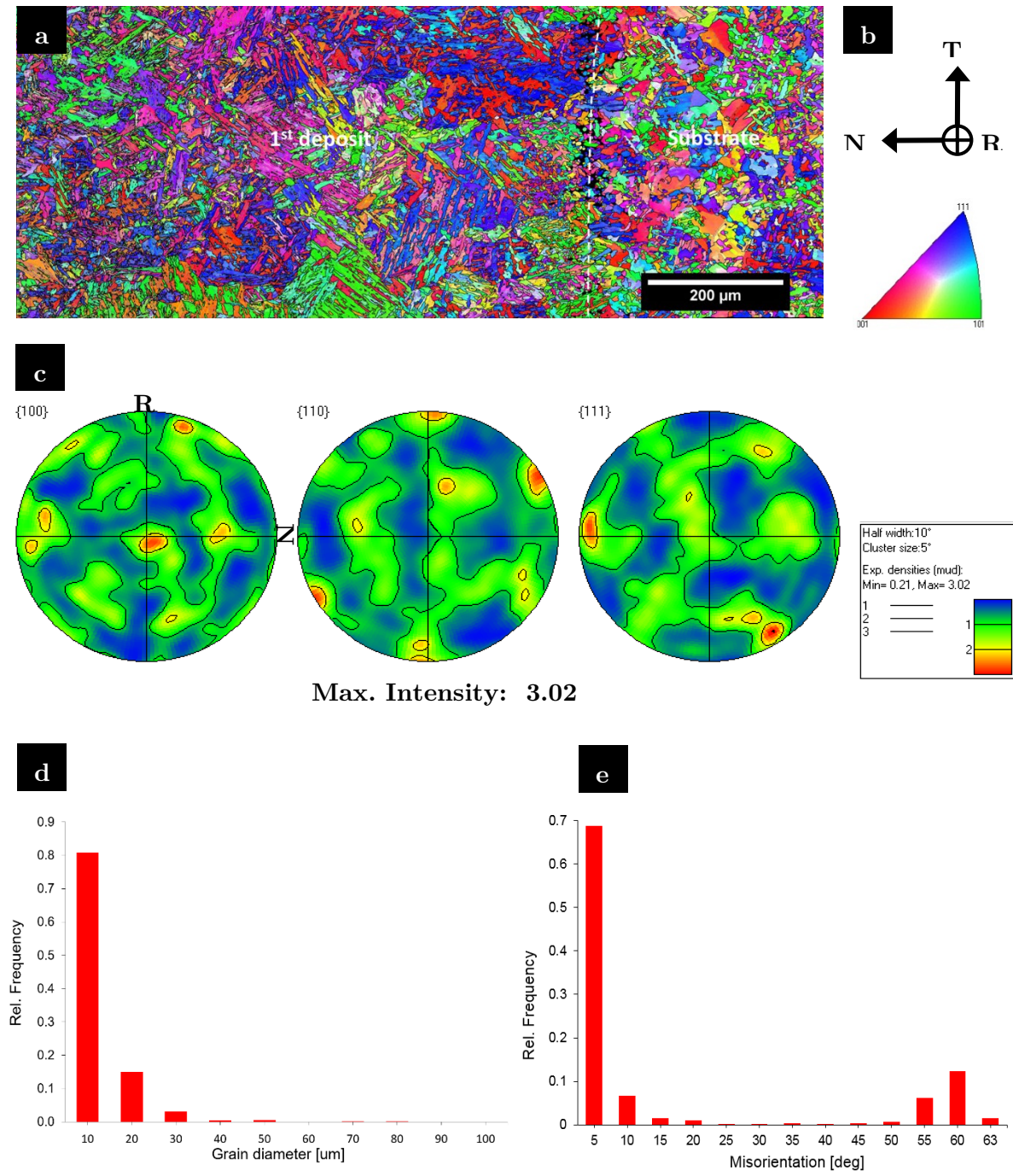


Figure 6-16 Results of EBSD large area mapping of Group 2-1L. (a) Orientation map being used in conjunction with (b) Inverse Pole Figure (IPF) legends. (c) (100), (110) and (111) pole figures attached with an intensity legend. (d) Distribution of grain size. (e) Distribution of misorientation angle.

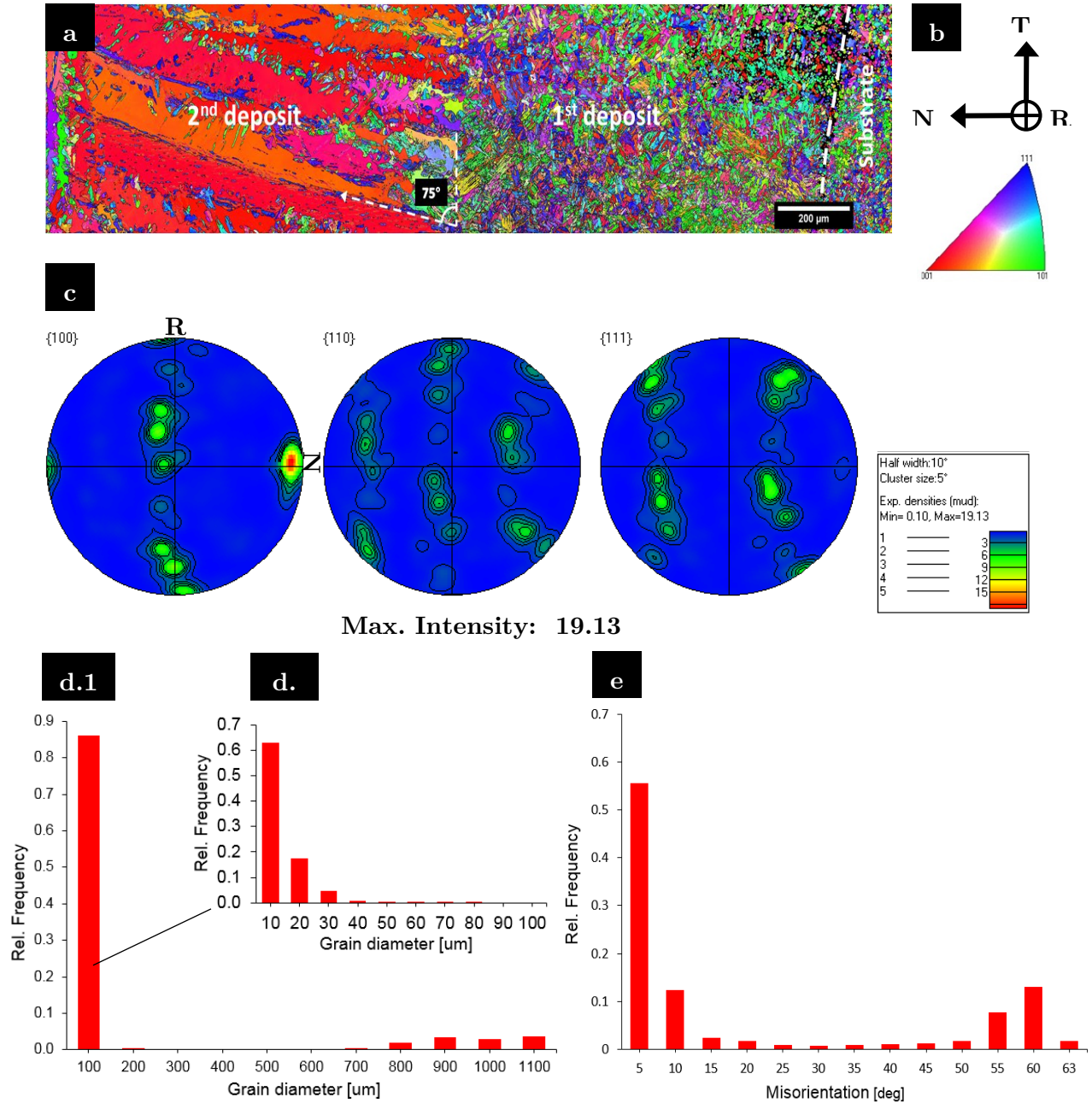


Figure 6-17 Results of EBSD large area mapping of Group 1-2L. (a) Orientation map being used in conjunction with (b) Inverse Pole Figure (IPF) legends. (c) (100), (110) and (111) pole figures from the second cladding layer. (d.1) Distribution of grain size. (d.2) The detailed distribution of grain size less than 100 μm. (e) Distribution of misorientation angle.

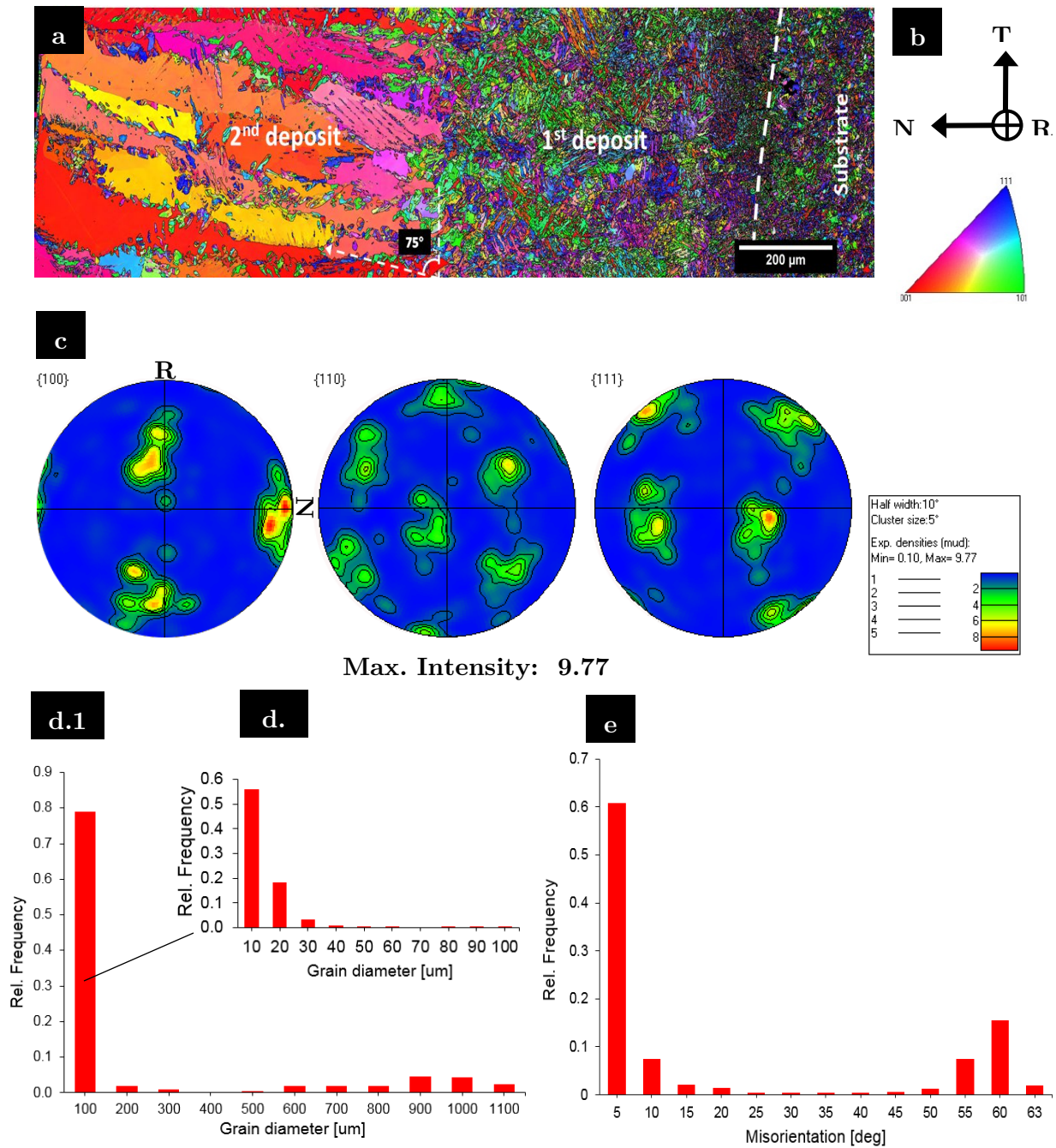


Figure 6-18 Results of EBSD large area mapping of Group 2-2L. (a) Orientation map being used in conjunction with (b) Inverse Pole Figure (IPF) legends. (c) (100), (110) and (111) pole figures from the second cladding layer. (d.1) Distribution of grain size. (d.2) The detailed distribution of grain size less than 100 μm. (e) Distribution of misorientation angle.

For both single and double deposition, preheating at 350 °C with the length of 400 mm (Group 1) was incapable of inhibiting the formation of martensite in the HAZ. Despite having a greater hardness than the pearlitic substrate, the presence of martensite in the HAZ has adverse impacts on the overall performance of the laser cladded rails, e.g. increasing internal residual stresses during the martensitic phase transformation, upsurge in brittleness, reducing strength and crack resistance. Thus, catastrophic failures might be originated from the HAZ.

Proper application of preheating heat treatment was established to exert a salient impact on the prevention of martensitic formation by cladding in the rail-longitudinal direction, constant laser power, and traverse speed. As evidenced by the similarities of Figure 6-6 (i) and Figure 6-6 (ii); formation of martensite occurred at the final laser tracks and the ends of laser tracks, where the rate of cooling was firstly increased by convection and conduction to a sufficiently high rate to form martensite. An investigation by Lai et al. [107] reported a similar mechanism of martensitic formation in the HAZ of cladded rails when preheating, or preheating followed by post-heating (PWHT) were applied. The PHWT was found to temper the martensite previously formed in the HAZ.

Extending the length of the applied preheating decreases the rate of cooling and impedes the phenomenon of quenching as the laser source traverses along the rails. As a result, a martensite-free microstructure is able to be engendered in the HAZ. Accordingly, regardless of the number of deposited layers, the preheating at 350 °C of 600 mm long (Group 2) resulted in no formation of martensite in the HAZ for single and double deposition, as shown in Figure 6-6 (iii) and Figure 6-6 (iv), respectively.

Changing preheating lengths resulted in marked differences in the HAZs' hardness between Group 1 and Group 2. Peak hardness values above 600 HV, which correspond to those of martensitic

microstructure, were detected for Group 1 specimens with both single and double deposition, as shown in Figure 6-8 (a) and Figure 6-8 (c). By successfully removing the martensite in the HAZs, hardness values of Group 2 specimens consistently fall within the range of 400-500 HV and were relatively comparable to the substrate's average hardness of 400 HV, as shown in Figure 6-8 (b) and Figure 6-8 (d). This suggests that the microstructural and resultant mechanical characteristics of the HAZ are substantially influenced by the preheating. The application of preheating length extending at least 100 mm from each side of cladding region is recommended to avoid the formation of martensite in the HAZ.

Therefore, the optimum samples were achieved using a preheating length of 600 mm at 350 °C and processing parameters of Group 2, when HAZs were free of martensite and had a hardness within the required specifications between 400 and 500 HV.

6.4.2 Impact of preheating condition on Microstructural characteristics of 410L laser deposits

Previous works [83, 84] have established the correlations of microstructural characteristics of laser cladding and local G/R ratio, where G is a temperature gradient, and R is solid-liquid interface growth rate. Depending on the local G/R ratio, different dendritic grain morphologies were seen.

Application of the preheating may reduce the magnitude of G during laser cladding. As a result, dendritic morphology did not dominate the microstructures of the 410L laser deposits. The longer the preheating length, the lower the magnitude of G. As can be seen from the comparison of Figure 6-15 (a)-(b) and Figure 6-16 (a)-(b), for single deposition, martensitic dendrites (dotted lines) were scattered in the central part of Group 1-1L with 400 mm preheating length, but there was none found in Group 2-1L with 600 mm preheating length. Additionally, the distribution of

maxima intensity in (100) pole figures for single deposition also indicates that Group 1-1L have a stronger tendency for having a preferred orientation than Group 2-1L as shown in Figure 6-15 (c) and Figure 6-16 (c). This established the significance of applying a proper and sufficient preheating to optimise the homogeneity of microstructural characteristics and corresponding mechanical properties of clad rails.

Comparison of double layer deposition, as shown in Figure 6-17 (c) and Figure 6-18 (c), further consolidates the importance of preheating during the cladding of rail steels. In the deposition of the second layer, the effect of preheating was eliminated as a result of the heat loss mechanisms due to conduction (neighbouring rail unclad surfaces acting as a highly effective heat sink) and air convection (ambient temperature). Consequentially, dendritic grains were found to develop with similar characteristics for both Group 1-2L and Group 2-2L with preheating length of 400 mm and 600 mm, respectively. Randomly distributed grain morphologies were seen starting from the first cladding-substrate interface to the interface of the two layers. The central and top parts of the second layer were detected with cellular dendritic morphology and horizontally elongated grains. Furthermore, for double deposition, the strong solidification fibre texture was collectively observed in (100) pole figures for Group 1-2L and Group 2-2L, as shown in Figure 6-17 (c) and Figure 6-18 (c), respectively. This is attributed to the absence of preheating during the deposition of the second layer. Therefore, it is crucial to maintaining the constant preheating temperature of 350 °C for multilayer laser deposition to ensure the homogeneous properties across the cladding layers.

Depending on the level of carbon dilution from the hypereutectoid rail substrate, the microstructural characteristics of ferritic morphology differed between single and double deposition. For the single deposition, ferritic morphology, as shown in Figure 6-1, was found with mostly equiaxed dendritic grains due to the low ratio of local temperature gradient (G) and solid-

liquid interface growth rate (R). However, microstructural characteristics of ferrite in the second deposition were substantially different because of the low dilution level and the elimination of preheating.

6.4.3 Observations of carbon dilution

Preliminary TEM investigations revealed that the formation of ferrite in the 410L cladding layers was merely attributed to the lack of localized carbon content, and no carbide formation was observed, as shown in Figure 6-13. The microstructural characterization of the 410L deposit agreed with the TEM results, as it can be seen in Figure 6-1, and also revealed the extent and complex mechanism of dilution from the substrate of hypereutectoid rail to the laser deposits.

In the single deposition, ferritic grains were found near the top surface of the cladding layer, as shown in Figure 6-1 (i)(c) & Figure 6-1 (iii)(c). Also, they were seen in the overlapping regions of the laser tracks, since the carbon content in laser track is insufficient to dilute, as shown in Figure 6-1 (i)(b) & Figure 6-1 (iii)(b).

The ferritic morphology near the top surface might be developed by the reasons of being distant from the high carbon rail substrate and having a non-homogenous distribution of the diluted carbon and other alloying elements. Such non-homogeneous distribution was generated by cladding upon two substrates with different content of alloying elements. The first was the rail substrate and the second was preceding laser tracks owing to overlapping of the deposited beads. As a result of being close to the top surface of the cladding layer, the cooling rate was significant, which led to the insufficient time to homogenize the distribution of the alloying elements, particularly carbon, before solidification. Therefore, for single deposition, the formation of ferritic

and martensitic morphologies occurred at an equal distance from the cladding-substrate interface and under a similar cooling condition.

In the double depositions – Figure 6-1 (ii) and Figure 6-1 (iv), the development of ferrite was detected steadily throughout the second layer, but none was found in its first layer where the carbon dilution was effective. This may be because the first deposited layer was acting as a barrier against the dilution of carbon from the substrate.

Also, during the second deposition, carbon atoms might be redistributed due to the influence of the heat input from the second deposition, and ferrite grains located at the top of the first deposition were able to merge into the newly-formed dendritic ferrite grains.

Hardness distributions, as shown in Figure 6-8, established a direct correlation with the corresponding morphology of the cladding layers and showed that the fine morphology of martensite in the diluted regions affects the hardness distributions and gave high hardness at the cladding-substrate interface and extended until the interface of the two layers.

For single deposition, the sudden drop in hardness as approaching the top surface of cladding layer indicated the impact of being outside the dilution range on the mechanical properties of laser cladding layers. The reduction in hardness, as shown in Figure 6-8 (a) and Figure 6-8 (b), became more severe after adding the second layer, as shown in Figure 6-8 (c) and Figure 6-8 (d).

Additionally, the corresponding microstructures showed ferritic morphology at the locations where the hardness was reduced. Effectively, a conservative estimation of the thickness of dilution band

for hypereutectoid rails, as described in Table 3-2, could be made by selecting the low carbon content of the 410L cladding material, as described in Table 3-1. The thickness of the dilution band was estimated to be virtually equal to the thickness of the first layer. With the aid of an image analysing software, the thicknesses of the dilution bands were determined to be 900 ± 200 mm for single deposition and 750 ± 250 mm for double deposition.

Additionally, correlations of shear punch results, as shown in Figure 6-14, with the corresponding hardness and microstructures, indicated the intense dilution effects of hypereutectoid rail substrates on the properties of the first cladding-substrate interface and its proximity. The increase in carbon content due to dilution, as shown in Figure 6-13 (d), might increase brittleness and reduce weldability of the affected regions.

6.5 Chapter Summary

The presented investigations established the importance and significance of applying an appropriate preheating to multi-layer laser deposition on hypereutectoid rails. According to the study, the following can be concluded:

- Formation of martensite in the HAZs of laser clad hypereutectoid rails, which is known for its adverse impacts, was eliminated for both single and double deposition by increasing the length of preheating from 400 mm to 600 mm. The increase in preheating length retards the rate of cooling and, therefore, hinders the phenomenon of quenching as the laser source traverses along the clad rail.

-
- For the clad layers undergone either single or double-layer laser deposition, application of a longer preheating length of 600 mm resulted in a more homogeneous microstructure in the clad layers. In the absence of preheating, dendritic morphology was found to dominantly occupy the deposits' microstructure.
 - Dilution of carbon in the laser deposition of the 410L stainless steel on hypereutectoid rails was substantial. Dilution band was estimated to be approximately equal to the thickness of the first deposited layers. Martensitic morphology was found in the dilution band as a result of the increase in carbon content.
 - Despite the low carbon content of the 410L ferritic stainless-steel deposits, the UTS and USS were estimated to be at least 80% compared to those of the unclad rails. This may be due to the effects of carbon dilution from the hypereutectoid substrate. One needs to be aware of such effects in the cladding of hypereutectoid rails.
-

7

Finite Element Analysis of thermal cycle in laser cladding of rail steels

This chapter reports the influence of laser cladding directions on thermal cycle and the corresponding microstructures and service performance of laser clad premium hypereutectoid rails. For two separate cladding directions, thermal information of pre-, during and post-laser treatment on three-dimensional 68 kg rail models was simulated via ANSYS platform. Furthermore, microstructural characteristics of the actual rails under the analogous processing conditions were assessed via optical microscopy. Potential mechanical and tribological properties were characterized by Vickers indentation. The unified correlations between the measured properties and observed microstructural features were acquired. The reasons for the formation of

martensite renowned for great cracking tendency at certain regions in HAZ were unveiled. Thus future prevention of forming martensite can be achieved.

7.1 Introduction

This chapter reports the influence of laser cladding directions on thermal cycle via numerical results and the corresponding microstructures and service performance of laser clad premium hypereutectoid rails. For two separate cladding directions, thermal information of pre-, during and post-laser treatment on three-dimensional 68 kg rail models was simulated via ANSYS platform. Furthermore, microstructural characteristics of the actual rails under the analogous processing conditions were assessed via optical microscopy. Potential mechanical and tribological properties were characterized by Vickers indentation. The unified correlations between the measured properties and observed microstructural features were acquired. The reasons for the formation of martensite renowned for great cracking tendency at certain regions in HAZ were unveiled. Thus future prevention of forming martensite can be achieved.

In order to obtain detailed information regarding temperature profiles, mechanisms of heat loss, characteristics of molten pool and the influences of processing parameters on thermal and mechanical properties of the treated components, numerical simulations of the laser cladding process are ordinarily preferred owing to their lower cost and risks involved as compared to experimental studies or field tests. However, numerous challenging aspects including the appropriate geometrical constraints, the material nonlinearities, the combined effects of thermal, mechanical and metallurgical phenomena, etc. must be considered while simulating the process of laser cladding. Therefore, a multitude of research studies have been proposed to understand the thermal cycle of laser cladding process by means of modelling and simulation; such information

plays a salient role in analyzing the microstructural characteristics and mechanical properties and controlling the quality of the laser deposits.

Hoadley et al. [125] utilized a two-dimensional finite element model (FEM) to simulate the quasi-steady temperature field for the longitudinal section of a clad track. A linear relationship between the laser power, the processing velocity and the thickness of the deposited layer was reported. Qi et al. [126] developed a three-dimensional transient model for a coaxial powder injection laser cladding process in which AISI H13 tool steel powder was deposited on a carbon steel substrate. The model simulated heat transfer, phase changes and fluid flow in the molten pool and revealed 7%-20% laser power attenuation with a powder feed rate of 6-12 g/min and 7-10 mm of interaction distance. Toyserkani et al. [127] introduced a three-dimensional FEM of laser cladding of mild steel by 98 wt% iron powder injection to predict the clad geometry as a function of time and process parameters including laser pulse shaping, travel velocity, laser pulse energy, powder jet geometry and material properties. Similarly, Zhao et al. [128] investigated the contamination level of the clad layer's properties by substrate metals using a code of FEM with Lagrangian viewpoint. Three specimen groups were examined, AISI 304 wire on Inconel 600 plate, AISI 304 wire on AISI 316 plate, and Inconel 600 wire on Inconel 600 plate. It was found that to keep a constant dilution in the multi-path cladding, the incident energy must be diminished with increasing numbers of the clad track. Cho et al. [129] investigated the effects of latent heat on laser cladding process using ABAQUS codes, then compared to present experimental publications elsewhere. Alimardani et al. [130] studied temperature and thermal stress distributions during a laser deposition process of a four-layer thin wall of AISI 304L stainless steel on a workpiece with the similar material using a 3D dynamic numerical approach. Fang et al. [131] simulated the laser deposition of H13 powder on P20 steel and demonstrated the average errors of width and depth are 15% and 4.5%, respectively. Lei et al. performed a 3D simulation of high-power laser clad TiC/NiCrBSiC composite coatings on Ti6Al4V alloys and verified the proposed model by comparing with the microstructure of the coatings. Heigel et al. [132] conducted simulations of a

multi-layer deposition on Inconel 625 plates showed that a single Inconel 625 wire layer generated lower temperature and less deformation than a single Inconel 625 powder layer. Santanu Paul et al. [133] focused on the development of a 3D finite element thermal model for laser cladding of CPM 9 V powder on H13 tool steel. However, the wire clad will produce greater total deformation because two layers are required to achieve the same thickness as the powder clad.

Simulating a laser cladding process is taxing due to the involvement of multiple sophisticated aspects, i.e. laser-powder interaction, liquid metal flow, melting, metal evaporation, solidification, absorption mechanism, heat transfer, multicomponent mass transfer, etc. A number of numerical models for the laser cladding processes have been, therefore, proposed and studied by many research groups. However, little insight and work were focusing on the effects of altering the processing parameters and heat treatments on the temperature distribution and thus the resulting deposit properties during laser deposition on rail steels.

The present work aims firstly to characterize the temperature fields as varying cladding directions, and secondly to analyze and interpret the evolution of cladding microstructure and the thermally induced mechanical properties. Three-dimensional finite element models of 68kg hypereutectoid rails complied with the AS1085.1 - 2002 specifications were developed based on ANSYS platform. To replicate the forward motion of the laser beam and the additive nature of the cladding process, the element birth and death feature built-in ANSYS was applied. The numerical results obtained was then experimentally verified.

7.2 Experimental procedure

Similar to the previous studies, a premium hypereutectoid rail grade complied with the EN 13674 requirements for the R400HT grade for heavy-haul railroad service was selected as a substrate material for experiments. The compositions of actual samples and R400HT requirements are listed in Table 3-2. Powder of 410L grade stainless with 150 μm average particle diameter was selected as a depositing material due to its strength, toughness, abrasive and corrosive resistance. The chemical composition of the 410L powder is listed in Table 3-1. Prior to applying the laser treatment, the rail portions were ground, polished and cleaned.

The rail substrate was laser clad by a laser coaxial head comprising 4 kW IPG fibre laser gun and a Sultzer-Metco twin-10 powder feeder. The laser beam was optically modified to deliver a concentrated circular laser spot with a spot size of 5 mm on the surface of the substrate. Shielding gas of 50% Argon and 50% Helium around the laser beam was used to avoid undue oxidation during the process. The system was air-cooled. Two groups of specimens were produced by altering cladding direction as shown in Table 7-1. The microstructural evolutions of the 410L depositing layer and the heat affected zone (HAZ) of the rail substrate were analyzed via optical microscopy (OM).

Metallographic specimens were undergone a two-stage etching procedure. A 2% Nital etching solution was used to visualize rail steel substrate microstructure. A Kalling's no. 2 (5g CuCl_2 , 100 ml HCl and 100ml ethanol) was used to reveal the microstructure of the laser deposited layer. Comparison of mechanical properties between different depositing materials was obtained by utilizing shear punch testing. Indications of wear resistance of cladding layer were obtained via Vickers indentation, thereby, the correlation between the microstructural characteristics and the wear performance was also established.

Table 7-1 Parameter sets applied for the comparative study of heat treatment.

Specimens	Heat treatment procedure	Cladding direction
Group 1	Preheating to 350 °C	Transverse
Group 2	Preheating to 350 °C	Longitudinal

7.3 Finite element analysis

7.3.1 Thermal model

Thermal history of a 68kg rail model undergone a laser treatment is investigated by using a three-dimensional dynamic thermal analysis, as shown in Figure 7-1. The following assumptions have been considered to mitigate computational efforts and time: The substrate material undergoes no phase transformation during the cladding procedure. Conduction, radiation and convection influence the HAZ's thermal cycle. A constant convection coefficient between the ambience and the rail workpiece is assumed. The effect of fluid flow within the melt pool is not included either. Moreover, no keyhole phenomenon, i.e. laser beam intensity is comparatively high, the welded material can be heated to the extent that there is intensive vaporization from the weld pool surface, leading to the formation of a keyhole, in the process is considered. The thermal analysis is substantially governed by factors such as the density, specific heat and thermal conductivity of the material. The equation of heat transfer energy balance is:

$$\rho C_p \frac{dT}{dt} = -\nabla \cdot q(\mathbf{r}, t) + Q(\mathbf{r}, t) \quad (7.1)$$

Where Q , t , T , r , ρ , C_p and q are the heat source, time, temperature, relative reference coordinate, density, specific heat and heat flux vector. The equation for heat flux vector is listed as below:

$$q = -k\nabla T \quad (7.2)$$

Where q and k are heat flux and thermal conductivity. The occurrence of heat loss on all surfaces of the rail model via mechanisms of radiation and convection is replicated. By using the Stefan–Boltzman’s law, radiation is quantified as:

$$q_{rad} = \varepsilon\beta(T_s^4 - T_\infty^4) \quad (7.3)$$

where q_{rad} , ε , β , T_s and T_∞ are the radiation heat transfer, the emissivity of the material, the Stefan–Boltzman constant, the surface temperature and the measured ambient temperature. Heat loss contributed by convection mechanism is governed by:

$$q_{conv} = h(T_s - T_\infty) \quad (7.4)$$

where q_{conv} and h are the convection heat transfer and the coefficient of convection.

7.3.2 Numerical implementation

The 3D mesh used for the thermal analysis of the rail workpiece is shown in Figure 7-2. The mesh facilitates the simulation of overlapping laser tracks using hex dominant method and consists of 900,000 nodes and 550,000 hex elements. Element size was chosen to be one-fifth of the laser spot size (5 mm).

Thermal constraints are applied to the substrate to simulate the thermal conditions in the laser deposition. Forced convection was created due to the emission of a shielding gas consisting of 50% Argon and 50% Helium using a coaxial nozzle. The surface of the deposited clad is considered to be relatively rough. Therefore the applied convection [132], h_{rough} , can be calculated as followed:

$$h_{rough} = 69e^{-0.07r} + 21.7 \quad (7.5)$$

Where the radial distance measured in mm and from the central point of the laser spot.

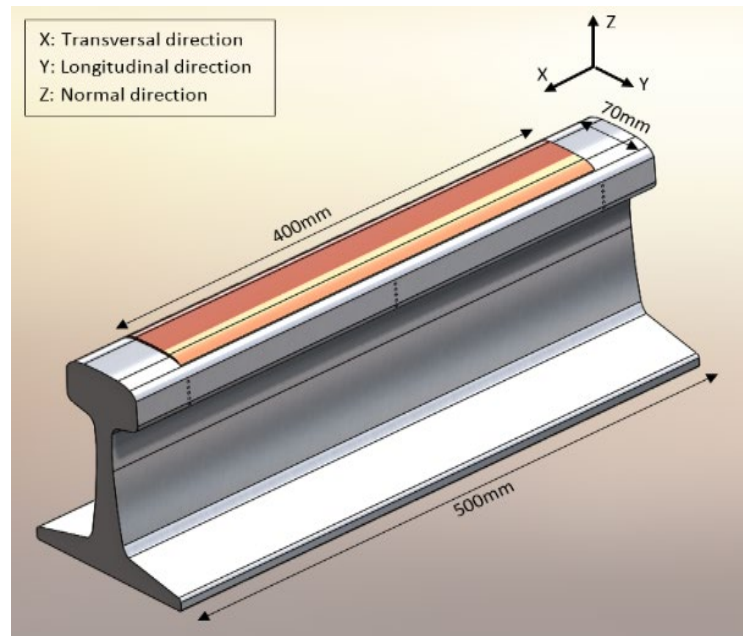


Figure 7-1 Schematic of the laser cladded rail sample with detailed dimensions used for the preliminary study.

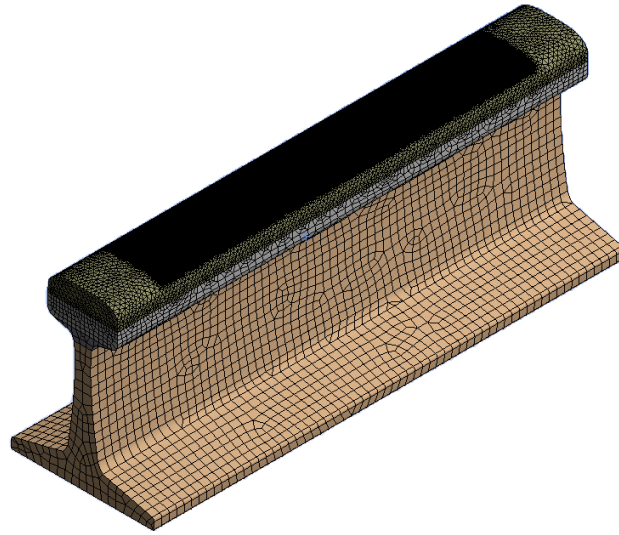


Figure 7-2 Schematic of finite element mesh model of the 68kg hypereutectoid rail substrate.

7.4 Results and Discussion

Experimental results from chapter 4 were used to verify the obtained numerical results. The optical images of the HAZs of cladded rails of Group 1 specimens, as described in Table 7-1, are shown in Figure 7-3 (a)-(c) at different locations in the HAZs using transverse sections. Likewise, Figure 7-3 (d) shows microstructures of the HAZs using longitudinal sections.

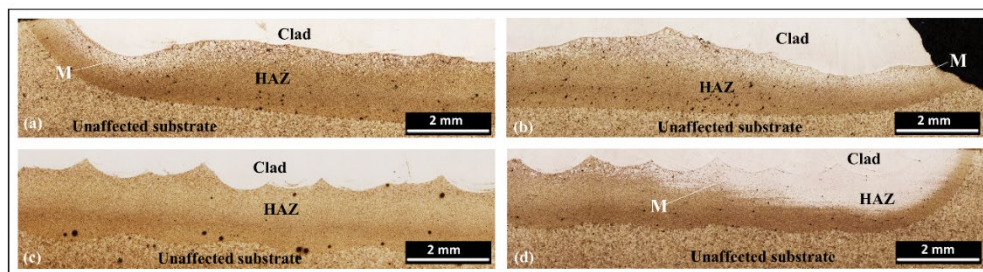


Figure 7-3 Micrograph showing the HAZ and rail substrate of the rail-cross sections at (a) left gauge corner, (b) right gauge corner, (c) middle section and (d) a representative of the longitudinal sections under the 410L rail-transversely deposited cladding layer (Group 1). The light etching microconstituent in the HAZ of (a), (b) and (d) is martensite. (M=martensite)

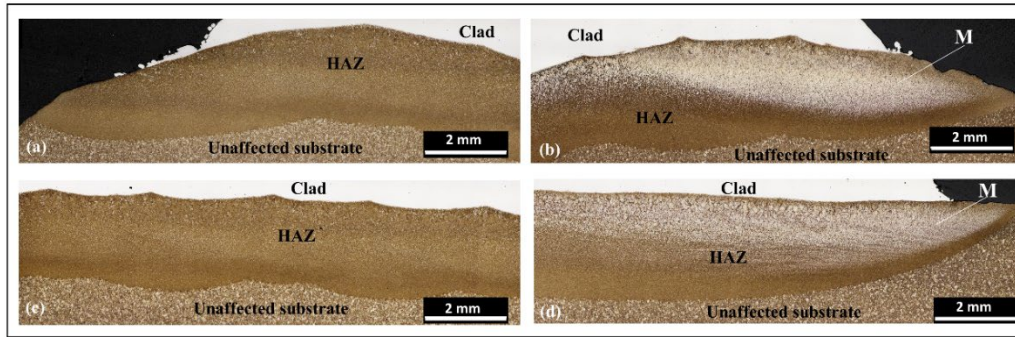


Figure 7-4 Micrograph showing the HAZ and rail substrate of the rail-cross sections at (a) left gauge corner, (b) right gauge corner, (c) middle section and (d) a representative of the longitudinal sections under the 410L rail-transversely deposited cladding layer (Group 2). The light etching microconstituent in the HAZ of (b) and (d) is martensite. (M=martensite)

As discussed in the previous chapters, four sub-regions were detected inside Group 1's HAZs using the transverse sections. (i) Partially molten zone featuring a metallurgical bond between the deposited layer and substrate. (ii) Coarse-grained HAZ, in rail-transverse sections, characterized by full pearlite microstructure in the middle of the HAZ. However, at the gauge corners of the railhead, martensite microstructure was observed as shown in Figure 7-3 (a) and (b). Whereas in the rail-longitudinal sections, martensite microstructure was detected in the Coarse-grained HAZ as shown in Figure 7-3 (d). (iii) Fine-grained HAZ with partially and fully pearlitic microstructure. (iv) Spheroidised or partial spheroidised microstructure is located adjacent to the unaffected substrate and furthest from the interface. Each of these sub-regions is completely influenced by their local thermal history.

Micrographs of the HAZ of cladded rails of Group 2 specimens, as described in Table 7-1, are shown in Figure 7-4 (a)-(c) at different locations using transverse sections and Figure 7-4 (d) using the longitudinal sections. Similar to Group 1, the aforementioned four sub-regions were also detected in the HAZ of Group 2 specimens. However, the micrographs of Group 2 specimens showed bainitic microstructure instead of pearlitic microstructure, which was observed in coarse-

grained HAZ and fine-grained HAZ of the Group 1's specimen. Martensite was detected at the right gauge corner where the finishing laser runs are located as shown in Figure 7-4 (b), and the at the starting and ending of the laser tracks, particularly near the interface, as shown in Figure 7-4 (d).

The numerical modelling of thermal cycles was conducted to explain the evolution of microstructure. Figures 7-5 and 7-6 show the simulated thermal history for Group 1 and Group 2's specimens, respectively. It can be seen from Figure 7-5, the shorter cladding length of laser tracks used in the rail transversely deposited claddings (Group 1) was found to increase the duration of temperature peak at the heated laser area. This suggests that the variation in temperature between the laser heated area (melting pool), shown in black, and the temperature of the preheated rail substrate, shown in red, is elevating as the temperature of the preheated rail substrate is cooling down, which leads to a greater probability and severity of the martensitic formation. Additionally, the effective preheating temperature was observed to be being beneath 100 °C at the last laser tracks for both Group 1 and Group 2 specimens. As a result, martensitic morphology was detected respectively at the entirety of the finishing rail end for Group 1 and at the right or finishing gauge corner for Group 2 where the last tracks are.

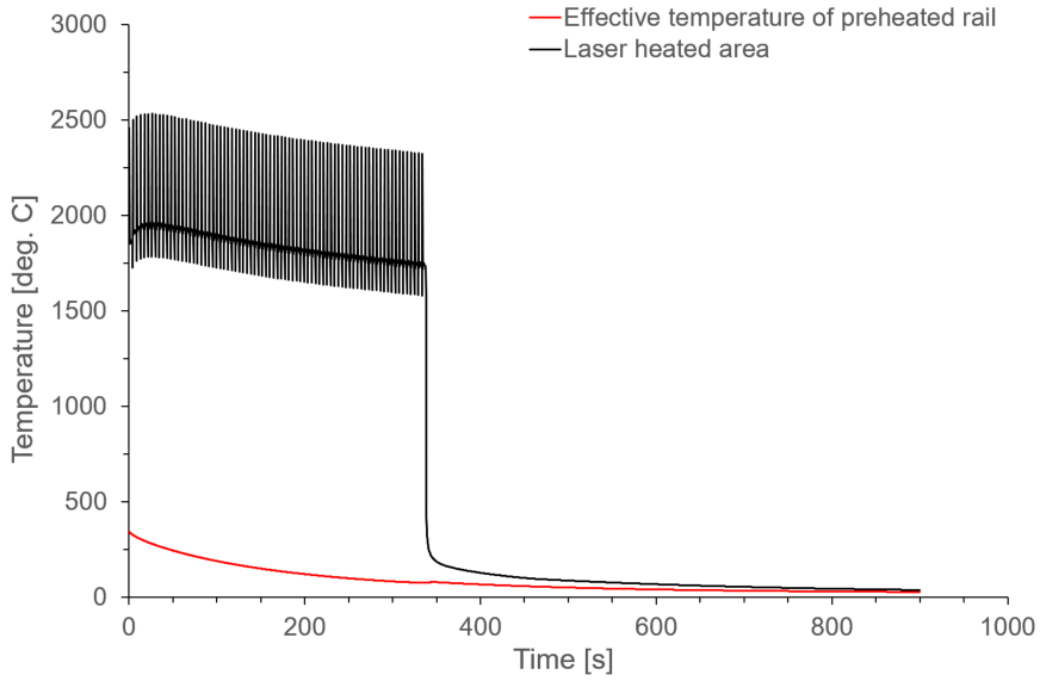


Figure 7-5 Numerical simulations of the thermal profile during laser deposition of Group 1 specimens.

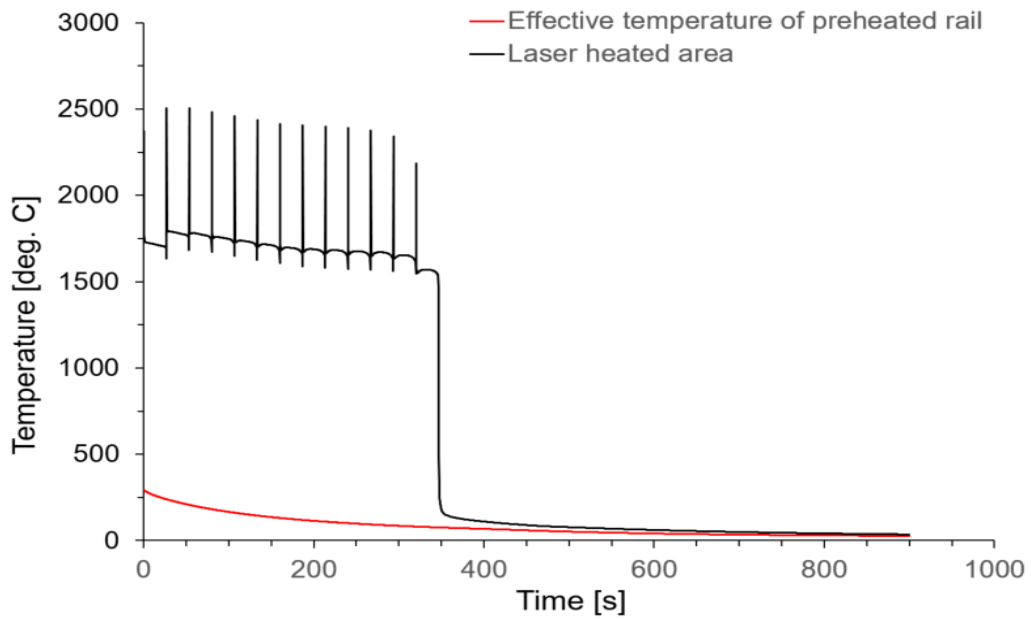


Figure 7-6 Numerical simulations of the thermal profile during laser deposition of Group 2 specimens.

By using the achieved measurement of microhardness on the cross-sections of the samples, the results of the numerical models were further verified. Figure 4-17 shows the microhardness distributions of Group 1 in rail-transverse direction. For the HAZ, the hardness of 497 HV, 586 HV and 654 HV were measured in the Coarse-grained HAZ for the middle section, left gauge corner, and right gauge corner, respectively. These hardness values can be related to that of martensite, which ranges between 500 - 700 HV. The vertical microhardness distribution at rail-transverse sections of the Group 2 deposited layer is shown in Figure 4-18. Moreover, the greatest hardness values in the Group 2 HAZ were determined to be at the finishing gauge corner where the last tracks are. Average hardness values were found to be 403 HV, 399 HV, and 635 HV at the middle section, left gauge corner, and right gauge corner, respectively, which demonstrated great correlation with the microstructures observed and numerical results obtained.

In summary, the formation of martensite was detected for both Group 1 and 2's HAZs. This is attributed to the pre-heating temperature applied was insufficient to prevent the martensitic transformation. In other words, the resulting temperature of the preheated substrate was under the martensitic transformation temperature, which led to a similar effect to quenching. Therefore, the larger surrounding surface area, the larger extent of martensite formed.

During the process, the heat was accumulated above the martensitic transformation temperature and induced the pearlitic coarse-grained HAZ at the middle sections of the laser cladding pad of Group 1 and 2. Nevertheless, the accumulated heat was dissipated more rapidly at the gauge corners due to the large neighbouring surface area of the substrate. Thus, the martensite was formed. At the beginning and end of the laser tracks, the neighbouring substrate's surface area was even larger. Consequently, a great amount of martensite was found.

7.5 Chapter summary

The presented findings emphasized the influence of laser depositing directions and heat treatment regimes on the microstructure of the HAZ of the cladded rails via the means of ANSYS platform. The findings also conformed the corresponding hardness of the laser deposited layers and the HAZ, which are the key indications of wear and mechanical performance of the cladded rail repairs in the premium hypereutectoid rail grade. Although FE analyses might not provide all the details, especially on the details of microstructures, they could provide rather good information on temperature profile (including temperature profile as a function of time). This information could shed light on what to expect on microstructures and mechanical strengths to be expected. As such, once a properly validated FE model has been established, it can be used as a predictive tool to guide what further experiments to be conducted. The specific conclusions made from the investigation regarding influence of clad are summarized as follows:

- For HAZ, the application of preheating at 350 °C at a heating length equal to the cladding length was found to be insufficient in preventing the formation of martensite regardless of cladding directions.
 - Applying preheating heat treatment properly may be the key factor to prevent the formation of martensite in the HAZ.
 - Microstructural characteristics of the HAZ was dependent on the cladding direction and showed a similar correlation with hardness distribution. Rail-transverse cladding direction showed less significant martensitic formation than rail-longitudinal cladding direction.
-

8

Conclusions and Summary

The ultimate objective of this dissertation was to develop a novel commercially-viable rail-wheel maintenance technology by using laser cladding technology, which can be applied to extend component lives of rails and to address other undesirable consequences of wheel-rail contact such as wheel squeal and flanging noise. Consequentially, the study was divided into two main tasks, i.e. Task 1 was to determine the most suitable cladding materials for rail steel deposition under the different processing condition, and Task 2 was to determine the effects of processing parameters on the microhardness, metallurgical microstructure of the steel and the mechanical properties of these microstructure introduced by the cladding process.

A review of literature had disclosed the importance and significance of utilising laser cladding in improving the current railway maintenance strategies and developing the innovative rail-wheel maintenance technology. Consequentially, accurate prediction and comprehension of the mechanical performance and metallurgical characteristics of laser clad rails are crucial. However, previous studies have been targeted merely either hypoeutectoid or eutectoid rail grades. Applications of laser cladding to premium hypereutectoid rail grade, commonly used in heavy-haul rail systems, remained limited in the open literature.

The Australasian Railway Association (2009) predicted that 95% of bulk commodities by land and gross tonne kilometres would be transported by rail by 2017. From the current annual haulage rates of 200 million gross tonnes (MGT) per annum for individual iron ore or coal haulage systems, the projected annual haulage rates in mineral haulage systems will be ~300 MGT per annum.

To expand the national economy, development of railway infrastructure has been considered as a national priority for investment owing to the increase in demand for freight transportation. Novelty in technology must be developed and implemented in railway industry to cope and withstand such high demand. This study falls directly within the crucial segment of the national development.

To meet the ever-growing demands for the increased axle loads, which lead to increasing rates of rail degradation, and high frequency of train operations, which limit the extent to which rail track is available for maintenance activities such as rail replacement, the development of effective and time-efficient strategies for rail-wheel maintenance and implementation of high strength rail grade, i.e. hypereutectoid rails, are necessary to ensure the structural integrity of rail infrastructure. An

investigation into examining the feasibility and employability of laser cladding to the premium rails was an integral part of this current research.

8.1 Major findings and contributions

In developing and establishing the proposed rail-wheel maintenance technology using laser cladding, numerous additional aspects were studied and investigated. Their corresponding outcomes and findings obtained from the investigations are detailed. The results achieved from the current studies and the major conclusions drawn from the investigation are presented and discussed in the following sections.

8.1.1 Selection of the suitable cladding direction

At this stage of the research, the development of effective rail maintenance for hypereutectoid rails was proceeded by applying surface engineering techniques, particularly laser cladding. Laser cladding is extensively used in many industrial applications. However, its industrial implementation for heavy haul railway transportation has not been optimized, which has contributed to the lack of publications for the application of laser cladding on the hypereutectoid rails. In this thesis, appropriate cladding direction for the laser deposition on hypereutectoid rails was determined, which could be considered as a benchmark for latter investigations. The following findings were summarized from the conducted experiments:

- Cladding direction has a significant impact on the microstructural characteristics of the deposits. This is attributed to the combined effect of cooling rate and dilution of the substrate. Employment of post-heating and slow cooling leads to a detrimental softening
-

effect with relatively low hardness. Solid solution strengthening may increase the hardness of the deposit.

- The strength and fracture mechanism of the 410L laser deposited layers are considerably dependent on cladding directions. Rail-longitudinal cladding direction resulted in more favourable mechanical properties in the laser deposited layers. The UTS of the 410L deposits is comparable to the virgin rails concerning strength.
- Distribution of the micro-constituents in the deposited layers was strongly influenced by the micro-segregation of alloying elements within the deposits during solidification and at the interface owing to dilution from the parent material.
- Microstructural characteristics of the deposited layer's remelted regions was dependent on the cladding directions and heat treatments and showed a similar correlation with hardness distribution.

The work discussed in this section was published, and the related journal paper is shown below:

- ❖ *Lai, Q., Abrahams, R., Yan, W., Qiu, C., Mutton, P., Paradowska, X., Soodi, M., and Wu, X., 2018. Investigation of a novel functionally graded material for the repair of premium hypereutectoid rails using laser cladding technology, Composites Part B: Engineering 130, 174-191.*

8.1.2 Correlation between elimination of martensitic formation in HAZ of hypereutectoid rails and selection of an appropriate applied heat treatment

Successful removal of martensitic formation in the HAZ of laser clad hypereutectoid rails was achieved. Owing to the absence of martensite, the clad specimens might be able to overcome the susceptibility to cracking at the HAZs under cyclic, dynamic or high impact loading conditions. Microstructural observations revealed a microstructure with the majority containing a microstructural combination of bainite and pearlite. As a result, hardness values of the clad specimens consistently fall within the targeted range of 400-500 HV and were relatively comparable to the substrate's average hardness of 400 HV. In contrast, the peak hardness values above 600 HV were detected for those with martensitic microstructure. This fundamental issue was addressed by modifying the applied heat treatment regime. Numerous heat treatment regimes were proposed and tested. The following covers the main results:

- The application of preheating at 350 °C at a heating length equal to the cladding length was found to be insufficient in preventing the formation of martensite regardless of cladding directions. In contrast, the combination of pre-heating, post-heating and slow cooling was proven to provide beneficial tempering to the HAZ microstructure, particularly in those with martensite, and excellent microstructural consistency.
 - Formation of martensite in the HAZs of laser clad hypereutectoid rails, which is known for its adverse impacts, was eliminated for both single and double deposition by increasing the length of preheating from 400 mm to 600 mm. The increase in preheating length retards the rate of cooling and, therefore, hinders the phenomenon of quenching as the laser source traverses along the clad rail.
-

- For the clad layers undergone either single or double-layer laser deposition, application of a longer preheating length of 600 mm resulted in a more homogeneous microstructure in the clad layers. In the absence of preheating, dendritic morphology was found to dominantly occupy the deposits' microstructure.

The work discussed in this section was published, and the related journal paper is shown below:

- ❖ *Lai, Q., Abrahams, R., Yan, W., Qiu, C., Mutton, P., Paradowska, A., Fang, X., Soodi, M., Wu, X., 2018. Effects of preheating and carbon dilution on material characteristics of laser-clad hypereutectoid rail steels. Materials Science and Engineering: A 712, 548-563.*

8.1.3 Observations of carbon dilution from the hypereutectoid rail substrate

Dilution is one of the important factors in determining the performance of any forms of welding. In laser cladding, it is desirable to know the extent of dilution from the rail substrate. In other words, how much the properties of the cladding are influenced by that of the high carbon rail so that the appropriate measure can be undertaken. A conservative estimation of dilution band thickness could be made by selecting the ferritic stainless-steel cladding material with low carbon content. Ferrite was always observed to be near the top surface of the deposits and was surrounded by a martensitic matrix for the single and double layer. Many reasons can be utilised to explain the above observations, i.e. carbon diluted from the substrate could not reach the regions where ferrite formed, or it might be because of formation of carbide, so that carbon is segregating on the grain boundary, and carbon deficient regions were formed. TEM investigation was conducted.

Song et al. [123] were able to detect fine carbides in also low carbon stainless steels using TEM dark-field images. Using similar techniques, the entire grain boundary was observed to be free from carbides. There is no noticeable colour contrast along the grain boundary. The following conclusions were made from the obtained results:

- Martensitic morphology was found in the dilution band as a result of the increase in Carbon content due to dilution
- Dilution band was estimated to be approximately equal to the thickness of the first cladding layer.

The work discussed in this section was published, and the related journal paper is shown below:

- ❖ *Lai, Q., Abrahams, R., Yan, W., Qiu, C., Mutton, P., Paradowska, A., Fang, X., Soodi, M., Wu, X., 2018. Effects of preheating and carbon dilution on material characteristics of laser-cladded hypereutectoid rail steels. Materials Science and Engineering: A 712, 548-563.*

8.1.4 Selection of suitable cladding materials and processing parameters

Optimization of the application of laser cladding on hypereutectoid rails was further pursued by studying the influence of different cladding materials, and processing parameters on microstructural and mechanical characteristics of hypereutectoid rails after cladding. Cladding materials of 410L, 420SS, Stellite 6 and Stellite 21 with single and double depositions were considered for the comparative study of different cladding materials and processing parameters.

To ensure the constant thickness of the claddings for comparison purposes, transverse speed and powder feed rate were modified concurrently in the ranges of 1000 - 1200 mm/min and 3 - 4 RPM, respectively. Process parameters for each considered cladding material were determined to achieve no surface defects. The most suitable cladding material for rail-wheel contact was established by assessing all crucial aspects, i.e. surface defects, hardness, microstructural and mechanical properties. According to the results and discussion, the following conclusions can be drawn:

- Defect-free surfaces were established on cladded rails utilizing (1000 mm/min; 3 RPM powder and 3200 W) for 410L and (1200 mm/min; 4 RPM powder and 3200 W) for 420SS, Stellite 6 and Stellite 21.
 - After all critical aspects, i.e. surface defects, hardness, material strength, were taken into account, Stellite 6 was determined to be the most acceptable cladding material for wheel-rail applications of the considered cladding materials.
 - The 420SS, Stellite 6 and Stellite 21 specimens showed brittle fracture behaviour in the shear punch test, whereas the 410L specimens behaved in an elastic-plastic manner similar to the virgin rail.
 - Application of preheating was not able to significantly modify the microstructures of all the four cladding materials, whereas a combination of preheating and PWHT was observed to cause severe reheating cracks for Co-base alloys, i.e. Stellite 6 and Stellite 21. Hence, PWHT may be used with caution for Co-base alloys.
-

- Irrespective of the number of deposited layers and depositing materials, application of 400-mm long preheating (HTA) was inadequate to halt the formation of martensite in the HAZ of the cladded rails.
- Adding a second cladding layer did not change the thickness of HAZs, yet refined the HAZ's microstructure.
- The application of preheating only and increasing the number of cladding layers may introduce the greater probability of martensite development as a result of the higher rate of cooling.

The work discussed in this section was submitted and currently under review in the Journal of Materials Processing Technology as shown below:

Lai, Q., Abrahams, R., Yan, W., Qiu, C., Mutton, P., Paradowska, X., Soodi, M., Wu, X., 2019. Influences of depositing materials, processing parameters and heating conditions on material characteristics of laser-cladded hypereutectoid rails, Materials Processing Technology 263, 1-20.

8.1.5 Numerical study of the thermal cycle in HAZ during laser cladding and its validations

Information on thermal cycle is vital in understanding the evolution of microstructures in the HAZ of cladded hypereutectoid rails. In this study, thermal information throughout the laser treatment on three-dimensional 68 kg rail models was simulated via ANSYS platform. Two separate cladding directions were numerically simulated. Microstructural characteristics of the actual rails under the analogous processing conditions were conducted, and Vickers indentation was performed on the obtained specimens for validation. Numerical results demonstrated that, for HAZ, the application of preheating at 350 °C at a heating length equal to the cladding length was found to be insufficient in preventing the formation of martensite regardless of cladding directions. Microstructural characteristics of the HAZ was dependent on the cladding and showed a similar correlation with hardness distribution. The FE analyses could well be used to guide future experimental investigations since a validated FE model has already been established.

The achievements from the numerical investigation were presented in the CORE conference as follows:

Lai, Q., Abrahams, R., Yan, W., Qiu, C., Mutton, P., Paradowska, A., Fang, X., Soodi, M., Wu, X, Material characteristics of laser-cladded hypereutectoid rail steels, CORE 2018 Conference on Railway Excellence, Sydney.

8.2 Recommendations for Future Work

The current studies were performed on 600-mm long rail sections in a high strength, hypereutectoid steel grade. Achievements of the initial aims have greatly advanced our understanding of laser cladding on high carbon rails [107]. The orientation (i.e. direction) that the cladding was applied relative to the longitudinal direction of the rail section was determined to have a significant impact on the microstructural characteristics and mechanical properties, i.e. strength and fracture behaviour, of the deposits. A longitudinal cladding direction resulted in more favourable mechanical properties in the laser deposited layers. By applying the appropriate length of preheating, without the involvement of post weld heat treatment (PWHT), formation of martensite in the HAZs of laser clad hypereutectoid rails, which is known to detrimentally affect toughness and impact resistance, was eliminated for both single and double deposition, and hardness values of the HAZs were ensured to be comparable to those of the unaffected rail substrate. The removal of PHWT as a requirement to control the microstructures and mechanical properties of the HAZ will shorten the network downtime necessary for the repairs, hence fewer disruptions to freight transport and commuters. Effects of carbon dilution from the hypereutectoid rail substrate on microstructures and mechanical performance of clad rails were investigated. The unfavorable increase in carbon content due to dilution may increase brittleness and reduce weldability of the affected regions. Dilution bands were estimated to be approximately equal to the thickness of the first deposited layers. By knowing the thicknesses of such dilution bands, one needs to take into account such effects in the cladding of hypereutectoid rails. A suitable cladding material was also selected from a range of candidates, which provides better wear resistance and mechanical performance. After considering all the findings and outcomes achieved from this study, the following recommendations for future work should be considered to further improve the in-situ employability of laser cladding technique:

- Length of the rail pieces subjected to the treatment of laser cladding was kept constant for all the investigations performed in this study. Research on the impacts of extending the length of the subjected rail substrate on the quality and characteristics of the laser deposits would be a crucial topic to further enhance the employability of the technique in in-situ conditions.
- The current research considered only a premium hypereutectoid rail grade from NSP for the laser treatment. A useful comparison will be provided by performing laser cladding on the premium rails from other rail manufacturers to ensure a generic railway maintenance strategy being developed.
- Studies on effective repairs of railways in heavy haul transportation are innovative which are sparse in the open literature. The future research can be extended to repair damaged or worn railway wheels by utilizing the developed railway strategy for rail tracks.

References

- [1] M. Kerr, A. Wilson, Engineering Manual Track, TMC 226, Rail Defects Handbook, Version 1.2, Transport Rail Corps Engineering Standards and Procedure Publications (2012).
- [2] H. Soleimani, M. Moavenian, Tribological Aspects of Wheel–Rail Contact: A Review of Wear Mechanisms and Effective Factors on Rolling Contact Fatigue, Urban Rail Transit 3(4) (2017) 227-237.
- [3] ABARE, Australian commodities, March quarter 2010.
http://www.agriculture.gov.au/abares/publications/display?url=http://143.188.17.20/anrdl/DAFFService/display.php?fid=pe_abare99014401_11b.xml.

-
- [4] P. Mutton, Fatigue damage in rails and rails welds under high axle load conditions, Institute of Rail Technology, 2014.
- [5] T.W. Australian, Rio announces \$226m expansion at Cape Lambert, 2010.
<https://au.news.yahoo.com/thewest/business/wa/a/7581935/rio-announces-226m-expansion-at-cape-lambert/>.
- [6] O.O. Adam Clare, Janet Folkes and Peter Farayibi, Laser cladding for railway repair and preventative maintenance, *Journal of Laser Applications* 24(032004) (2012).
- [7] M. Wiest, W. Daves, F. Fischer, H. Ossberger, Deformation and damage of a crossing nose due to wheel passages, *Wear* 265(9) (2008) 1431-1438.
- [8] D.T. Eadie, M. Santoro, K. Oldknow, Y. Oka, Field studies of the effect of friction modifiers on short pitch corrugation generation in curves, *Wear* 265(9-10) (2008) 1212-1221.
- [9] U. Olofsson, Y. Zhu, S. Abbasi, R. Lewis, S. Lewis, Tribology of the wheel-rail contact-aspects of wear, particle emission and adhesion, *Vehicle System Dynamics* 51(7) (2013) 1091-1120.
- [10] H. Kanehara, T. Fujioka, Measuring rail/wheel contact points of running railway vehicles, *Wear* 253(1-2) (2002) 275-283.
- [11] X. Jin, J. Zhang, A complementary principle of elastic bodies of arbitrary geometry in rolling contact, *Computers & Structures* 79(29-30) (2001) 2635-2644.
- [12] L. Chevalier, S. Cloupet, M. Quillien, Friction and wear during twin-disc experiments under ambient and cryogenic conditions, *Tribology international* 39(11) (2006) 1376-1387.
- [13] J. Archard, Contact and rubbing of flat surfaces, *Journal of applied physics* 24(8) (1953) 981-988.
-

-
- [14] J. Zheng, J. Luo, J. Mo, J. Peng, X. Jin, M. Zhu, Fretting wear behaviors of a railway axle steel, *Tribology International* 43(5-6) (2010) 906-911.
- [15] R. Waterhouse, Fretting wear, *Wear* 100(1-3) (1984) 107-118.
- [16] D. Housed, Welding of Railroad Rails—A Literature and Industry Survey', *Rail Steels: Developments, processing, and use* 644 (1978) 118.
- [17] R. Lahnsteiner, J. Ehrlich, Weld joint between two rails arranged behind each other along a rail track, Google Patents, 1997.
- [18] M. Andrews, When, where and why to use MIG welding, 2008. <http://source.theengineer.co.uk/production-and-automation/welding/joining/arc-welding/when-where-and-why-to-use-mig-welding/315823.article>.
- [19] J.C. Ion, *Laser Processing of Engineering Materials*, Elsevier Butterworth-Heineman 2005.
- [20] E. Toyserkani, A. Khajepour, S.F. Corbin, *Laser cladding*, CRC press 2010.
- [21] T.H. Maiman, *Stimulated optical radiation in ruby*, (1960).
- [22] D. Gnanamuthu, Laser surface treatment, *Optical Engineering* 19(5) (1980) 195783-195783-.
- [23] W. Steen, C. Courtney, Surface heat treatment of EnS steel using a 2kW continuous-wave CO2 laser, *Metals Technology* 6(1) (1979) 456-462.
- [24] W. Steen, C. Courtney, Hardfacing of Nimonic 75 using 2 kW continuouswave CO2 laser, *Metals technology* 7(1) (1980) 232-237.
- [25] V. Weerasinghe, W. Steen, Laser cladding by powder injection, *Proceedings of the 1st International Conference on Lasers in Manufacturing*, 1983, pp. 125-132.
-

-
- [26] V. Weerasinghe, W. Steen, Laser cladding with pneumatic powder delivery, *Applied Laser Tooling*, Springer1987, pp. 183-211.
- [27] V. Weerasinghe, W. Steen, Computer simulation model for laser cladding, *ASME HTD* 29 (1983) 15-23.
- [28] L. Li, J. Mazumder, A study of the mechanism of laser cladding processes, *Laser Processing of Materials* (1984) 35-50.
- [29] A. Kar, J. Mazumder, One-dimensional finite-medium diffusion model for extended solid solution in laser cladding of Hf on nickel, *Acta Metallurgica* 36(3) (1988) 701-712.
- [30] J. Mazumder, J. Singh, Laser surface alloying and cladding for corrosion and wear, *High Temperature Materials and Processes* 7(2-3) (1986) 101-106.
- [31] J. Mazumder, A. Kar, Solid solubility in laser cladding, *JOM* 39(2) (1987) 18-23.
- [32] A. Kar, J. Mazumder, Effect of cooling rate on solid solubility in laser cladding, *Proc. ASME/JSME* 3 (1987) 237-249.
- [33] G. Eboo, A. Lindemanis, *Advances in laser cladding process technology*, 1985 Los Angeles Technical Symposium, International Society for Optics and Photonics, 1985, pp. 86-94.
- [34] P. Koshy, *Laser cladding techniques for application to wear and corrosion resistant coatings*, 1985 Los Angeles Technical Symposium, International Society for Optics and Photonics, 1985, pp. 80-85.
- [35] T. Tucker, A. Clauer, I. Wright, J. Stropki, Laser-processed composite metal cladding for slurry erosion resistance, *Thin Solid Films* 118(1) (1984) 73-84.
- [36] S. Doran, The laser where flexibility ultimately means economy, *Production Magazine*, 13p (1987).
-

-
- [37] J.A. Hopkins, M.H. McCay, N. Dahotre, M. Martin, Laser Processed Aluminum Surfaces in Automotive Applications: Performance Requirements for Cylinder Bores and Valve Seats, SAE Technical Paper, 1998.
- [38] K. Tanaka, T. Saito, Y. Shimura, K. Mori, M. Kawasaki, M. Koyama, H. Murase, New Copper Based Composite for Engine Valve Seat Directly Deposited onto Aluminium Alloy by Laser Cladding Process.(In Japanese.), *J Jpn Inst Met* 57(10) (1993) 1114-1122.
- [39] A. Conde, F. Zubiri, Cladding of Ni-Cr-B-Si coatings with a high power diode laser, *Materials Science and Engineering: A* 334(1) (2002) 233-238.
- [40] T. Tanaka, J. Chen, S. Takezono, G. Li, Effect of laser cladding on fatigue strength of an alloy steel, *J. Soc. Mater. Sci., Jpn.(Japan)* 44(498) (1995) 343-347.
- [41] I. Manna, J.D. Majumdar, B.R. Chandra, S. Nayak, N.B. Dahotre, Laser surface cladding of Fe-B-C, Fe-B-Si and Fe-BC-Si-Al-C on plain carbon steel, *Surface and Coatings Technology* 201(1) (2006) 434-440.
- [42] S. Sun, Y. Durandet, M. Brandt, Parametric investigation of pulsed Nd: YAG laser cladding of stellite 6 on stainless steel, *Surface and Coatings Technology* 194(2) (2005) 225-231.
- [43] T. Webber, Application of a Hardface Coating with CO₂ and CW Nd: YAG Lasers, *Proceedings-Spie The International Society For Optical Engineering*, Spie The International Society For Optical, 1992, pp. 380-380.
- [44] M. Capp, J. Rigsbee, Laser processing of plasma-sprayed coatings, *Materials Science and Engineering* 62(1) (1984) 49-56.
- [45] M. Zhong, W. Liu, K. Yao, J.-C. Goussain, C. Mayer, A. Becker, Microstructural evolution in high power laser cladding of Stellite 6+ WC layers, *Surface and Coatings Technology* 157(2) (2002) 128-137.
-

-
- [46] A. Clare, O. Oyelola, T. Abioye, P. Farayibi, Laser cladding of rail steel with Co-Cr, *Surface Engineering* 29(10) (2013) 731-736.
- [47] H.-m. Guo, Q. Wang, W.-j. Wang, J. Guo, Q.-y. Liu, M.-h. Zhu, Investigation on wear and damage performance of laser cladding Co-based alloy on single wheel or rail material, *Wear* 328 (2015) 329-337.
- [48] W. Wang, J. Hu, J. Guo, Q. Liu, M. Zhu, Effect of laser cladding on wear and damage behaviors of heavy-haul wheel/rail materials, *Wear* 311(1-2) (2014) 130-136.
- [49] S. Lewis, S. Fretwell-Smith, P. Goodwin, L. Smith, R. Lewis, M. Aslam, D. Fletcher, K. Murray, R. Lambert, Improving rail wear and RCF performance using laser cladding, *Wear* 366 (2016) 268-278.
- [50] S. Lewis, R. Lewis, D. Fletcher, Assessment of laser cladding as an option for repairing/enhancing rails, *Wear* 330 (2015) 581-591.
- [51] S. Lewis, R. Lewis, P. Goodwin, S. Fretwell-Smith, D. Fletcher, K. Murray, J. Jaiswal, Full-scale testing of laser clad railway track; Case study—Testing for wear, bend fatigue and insulated block joint lipping integrity, *Wear* 376 (2017) 1930-1937.
- [52] S. Niederhauser, Laser clad steel: Microstructures and mechanical properties of relevance for railway applications, (2006).
- [53] W.-J. Wang, Z.-K. Fu, J. Guo, Y.-Q. Zhang, Q.-Y. Liu, M.-H. Zhu, Investigation on Wear Resistance and Fatigue Damage of Laser Cladding Coating on Wheel and Rail Materials under the Oil Lubrication Condition, *Tribology Transactions* 59(5) (2016) 810-817.
- [54] J. Tuominen, P. Vuoristo, T. Mäntylä, S. Ahmaniemi, J. Vihinen, P. Andersson, Corrosion behavior of HVOF-sprayed and Nd-YAG laser-remelted high-chromium, nickel-chromium coatings, *Journal of thermal spray technology* 11(2) (2002) 233-243.
-

-
- [55] J. Singh, J. Mazumder, Effect of extended solid solution of Hf on the microstructure of the laser clad Ni-Fe-Cr-Al-Hf alloys, *Acta Metallurgica* 35(8) (1987) 1995-2003.
- [56] A. Wetzig, B. Brenner, V. Fux, E. Beyer, Induction assisted laser-cladding: a new and effective method for producing high wear resistant coatings on steel components, *ICALEO'98*, 1998.
- [57] M. Pilloz, J. Pelletier, A. Vannes, Residual stresses induced by laser coatings: phenomenological analysis and predictions, *Journal of materials science* 27(5) (1992) 1240-1244.
- [58] E. Eiholzer, C. Cusano, J. Mazumder, Wear properties of laser alloyed and clad Fe-Cr-Mn-C alloys, *Proc. ICALEO*, 1985, pp. 159-167.
- [59] J. Singh, J. Mazumder, Microstructure and wear properties of laser clad Fe- Cr- Mn- C alloys, *Metallurgical Transactions A* 18(2) (1987) 313-322.
- [60] J. Choi, J. Mazumder, Non-equilibrium synthesis of Fe-Cr-CW alloy by laser cladding, *Journal of materials science* 29(17) (1994) 4460-4476.
- [61] J. Choi, S. Choudhuri, J. Mazumder, Role of preheating and specific energy input on the evolution of microstructure and wear properties of laser clad Fe-Cr-CW alloys, *Journal of materials science* 35(13) (2000) 3213-3219.
- [62] F.R. Hernández, A. Okonkwo, V. Kadekar, T. Metz, N. Badi, Laser cladding: The alternative for field thermite welds life extension, *Materials & Design* 111 (2016) 165-173.
- [63] S. Niederhauser, B. Karlsson, Fatigue behaviour of Co-Cr laser clad steel plates for railway applications, *Wear* 258(7) (2005) 1156-1164.
- [64] J.W. Ringsberg, A. Skyttebol, B.L. Josefson, Investigation of the rolling contact fatigue resistance of laser clad twin-disc specimens: FE simulation of laser cladding, grinding and a twin-disc test, *International Journal of Fatigue* 27(6) (2005) 702-714.
-

-
- [65] F. Franklin, G.-J. Weeda, A. Kapoor, E. Hiensch, Rolling contact fatigue and wear behaviour of the Infrastar two-material rail, *Wear* 258(7) (2005) 1048-1054.
- [66] M. Hiensch, P.-O. Larsson, O. Nilsson, D. Levy, A. Kapoor, F. Franklin, J. Nielsen, J.W. Ringsberg, B.L. Josefson, Two-material rail development: field test results regarding rolling contact fatigue and squeal noise behaviour, *Wear* 258(7) (2005) 964-972.
- [67] H. Berns, Manufacture and application of high nitrogen steels, *ISIJ international* 36(7) (1996) 909-914.
- [68] P.T. Lovejoy, Structure and constitution of wrought martensitic stainless steels, *Handbook of Stainless Steels*, McGraw-Hill, New York (1977) 800.
- [69] B.W. Madsen, Measurement of erosion-corrosion synergism with a slurry wear test apparatus, *Wear* 123(2) (1988) 127-142.
- [70] R.A. Jeshvaghani, M. Shamanian, M. Jaberzadeh, Enhancement of wear resistance of ductile iron surface alloyed by stellite 6, *Materials & Design* 32(4) (2011) 2028-2033.
- [71] G. Rajeev, M. Kamaraj, S.R. Bakshi, Hardfacing of AISI H13 tool steel with Stellite 21 alloy using cold metal transfer welding process, *Surface and Coatings Technology* 326 (2017) 63-71.
- [72] A. Gholipour, M. Shamanian, F. Ashrafizadeh, Microstructure and wear behavior of stellite 6 cladding on 17-4 PH stainless steel, *Journal of Alloys and Compounds* 509(14) (2011) 4905-4909.
- [73] R. Ahmed, H. de Villiers Lovelock, S. Davies, N. Faisal, Influence of Re-HIPing on the structure-property relationships of cobalt-based alloys, *Tribology International* 57 (2013) 8-21.
- [74] K.L. Johnson, *Contact mechanics*, Cambridge university press 1987.
- [75] E.E. Magel, *Rolling contact fatigue: a comprehensive review*, 2011.
-

-
- [76] R. Guduru, K. Darling, R. Kishore, R. Scattergood, C. Koch, K. Murty, Evaluation of mechanical properties using shear-punch testing, *Materials Science and Engineering: A* 395(1) (2005) 307-314.
- [77] G. Hankin, M. Toloczko, K. Johnson, M. Khaleel, M. Hamilton, F. Garner, R. Davies, R. Faulkner, An investigation into the origin and nature of the slope and X-axis intercept of the shear punch-tensile yield strength correlation using finite element analysis, *Effects of Radiation on Materials: 19th International Symposium*, ASTM International, 2000.
- [78] G. Hankin, M. Toloczko, M. Hamilton, F. Garner, R. Faulkner, Shear punch testing of 59 Ni isotopically-doped model austenitic alloys after irradiation in FFTF at different He/dpa ratios, *Journal of Nuclear Materials* 258 (1998) 1657-1663.
- [79] S. Aldajah, O.O. Ajayi, G.R. Fenske, S. Kumar, Investigation of top of rail lubrication and laser glazing for improved railroad energy efficiency, *Journal of Tribology* 125(3) (2003) 643-648.
- [80] R. DiMelfi, P. Sanders, B. Hunter, J. Eastman, K. Sawley, K. Leong, J. Kramer, Mitigation of subsurface crack propagation in railroad rails by laser surface modification, *Surface and Coatings Technology* 106(1) (1998) 30-43.
- [81] S. Shariff, T. Pal, G. Padmanabham, S. Joshi, Sliding wear behaviour of laser surface modified pearlitic rail steel, *Surface Engineering* 26(3) (2010) 199-208.
- [82] M. Salehi, K. Dehghani, Structure and properties of nanostructured aluminum A413. 1 produced by melt spinning compared with ingot microstructure, *Journal of Alloys and Compounds* 457(1) (2008) 357-361.
- [83] I. Hemmati, V. Ocelik, J.T.M. De Hosson, Microstructural characterization of AISI 431 martensitic stainless steel laser-deposited coatings, *Journal of materials science* 46(10) (2011) 3405-3414.
-

-
- [84] S. Kou 2nd, *Welding metallurgy* 2nd edn, John Wiley & Sons, New Jersey, 2003.
- [85] V.K. Balla, S. Bose, A. Bandyopadhyay, Microstructure and wear properties of laser deposited WC-12% Co composites, *Materials Science and Engineering: A* 527(24) (2010) 6677-6682.
- [86] M. Toloczko, M. Hamilton, G. Lucas, Ductility correlations between shear punch and uniaxial tensile test data, *Journal of nuclear materials* 283 (2000) 987-991.
- [87] C. Zhenda, L.L. Chew, Q. Ming, Laser cladding of WC \boxtimes Ni composite, *Journal of materials processing technology* 62(4) (1996) 321-323.
- [88] R. Colaço, R. Vilar, Stabilisation of retained austenite in laser surface melted tool steels, *Materials Science and Engineering: A* 385(1) (2004) 123-127.
- [89] P. Krakhmalev, I. Yadroitsava, G. Fredriksson, I. Yadroitsev, In situ heat treatment in selective laser melted martensitic AISI 420 stainless steels, *Materials & Design* 87 (2015) 380-385.
- [90] M. Gagné, *The Sorelmetal book of ductile iron*, Rio Tinto Iron & Titanium Inc (2004) 23-45.
- [91] G.E. Totten, M.A. Howes, *Steel heat treatment handbook*, CRC Press 1997.
- [92] C. Lee, H. Park, J. Yoo, C. Lee, W. Woo, S. Park, Residual stress and crack initiation in laser clad composite layer with Co-based alloy and WC+ NiCr, *Applied Surface Science* 345 (2015) 286-294.
- [93] Z. Zhang, P. Farahmand, R. Kovacevic, Laser cladding of 420 stainless steel with molybdenum on mild steel A36 by a high power direct diode laser, *Materials & Design* 109 (2016) 686-699.
- [94] K. Li, D. Li, D. Liu, G. Pei, L. Sun, Microstructure evolution and mechanical properties of multiple-layer laser cladding coating of 308L stainless steel, *Applied Surface Science* 340 (2015) 143-150.
-

-
- [95] G.G. Tibbetts, Diffusivity of carbon in iron and steels at high temperatures, *Journal of Applied Physics* 51(9) (1980) 4813-4816.
- [96] W.F. Gale, T.C. Totemeier, *Smithells metals reference book*, Butterworth-Heinemann 2003.
- [97] H. Bhadeshia, R. Honeycombe, *Steels: microstructure and properties: microstructure and properties*, Butterworth-Heinemann 2011.
- [98] H. Kerr, A review of factors affecting toughness in welded steels, *International Journal of Pressure Vessels and Piping* 4(2) (1976) 119-141.
- [99] S. Lewis, S. Fretwell-Smith, P. Goodwin, L. Smith, R. Lewis, M. Aslam, D. Fletcher, K. Murray, R. Lambert, Improving Rail Wear and RCF Performance using Laser Cladding, *Wear* 336-367 (2016) 268-278.
- [100] Y. Jin, M. Ishida, A. Namura, Experimental simulation and prediction of wear of wheel flange and rail gauge corner, *Wear* 271(1) (2011) 259-267.
- [101] B.V. Krishna, A. Bandyopadhyay, Surface modification of AISI 410 stainless steel using laser engineered net shaping (LENS TM), *Materials & Design* 30(5) (2009) 1490-1496.
- [102] W.D. Callister, D.G. Rethwisch, *Materials science and engineering: an introduction*, Wiley New York 2007.
- [103] G. Lacroix, T. Pardoën, P. Jacques, The fracture toughness of TRIP-assisted multiphase steels, *Acta Materialia* 56(15) (2008) 3900-3913.
- [104] Z. Fu, H. Ding, W. Wang, Q. Liu, J. Guo, M. Zhu, Investigation on microstructure and wear characteristic of laser cladding Fe-based alloy on wheel/rail materials, *Wear* 330 (2015) 592-599.
-

-
- [105] W. Wang, Z. Fu, X. Cao, J. Guo, Q. Liu, M. Zhu, The role of lanthanum oxide on wear and contact fatigue damage resistance of laser cladding Fe-based alloy coating under oil lubrication condition, *Tribology International* 94 (2016) 470-478.
- [106] S.-H. Wang, J.-Y. Chen, L. Xue, A study of the abrasive wear behaviour of laser-clad tool steel coatings, *Surface and Coatings Technology* 200(11) (2006) 3446-3458.
- [107] Q. Lai, R. Abrahams, W. Yan, C. Qiu, P. Mutton, A. Paradowska, M. Soodi, Investigation of a novel functionally graded material for the repair of premium hypereutectoid rails using laser cladding technology, *Composites Part B: Engineering* 130 (2017) 174-191.
- [108] S. Kou, *Welding metallurgy*, John Wiley & Sons 2003.
- [109] A. Farnia, F.M. Ghaini, J. Rao, V. Ocelík, J.T.M. De Hosson, Effect of Ta on the microstructure and hardness of Stellite 6 coating deposited by low power pulse laser treatments, *Surface and Coatings Technology* 213 (2012) 278-284.
- [110] M. Brandt, S. Sun, N. Alam, P. Bendeich, A. Bishop, Laser cladding repair of turbine blades in power plants: from research to commercialisation, *International Heat Treatment and Surface Engineering* 3(3) (2009) 105-114.
- [111] E. Harati, F. Malek Ghaini, M.J. Torkamany, Microstructural Analysis of Laser Cladding of Stellite 6 on Ductile Iron, *The 6th Swedish Production Symposium 2014*, 2014, pp. 1-8.
- [112] G. Xu, M. Kutsuna, Z. Liu, K. Yamada, Comparison between diode laser and TIG cladding of Co-based alloys on the SUS403 stainless steel, *Surface and Coatings Technology* 201(3) (2006) 1138-1144.
- [113] P. Ganesh, A. Moitra, P. Tiwari, S. Sathyanarayanan, H. Kumar, S. Rai, R. Kaul, C. Paul, R. Prasad, L. Kukreja, Fracture behavior of laser-clad joint of Stellite 21 on AISI 316L stainless steel, *Materials Science and Engineering: A* 527(16) (2010) 3748-3756.
-

-
- [114] T. EN 13674-1, 13674-1: Railway applications–track–rail–part 1: Vignole railway rails 46 kg/m and above, Brussels, 2011.
- [115] P. Sellamuthu, P. Collins, P. Hodgson, N. Stanford, Correlation of tensile test properties with those predicted by the shear punch test, *Materials & Design* 47 (2013) 258-266.
- [116] C.L. Pun, Q. Kan, P.J. Mutton, G. Kang, W. Yan, Ratcheting behaviour of high strength rail steels under bi-axial compression–torsion loadings: Experiment and simulation, *International Journal of Fatigue* 66 (2014) 138-154.
- [117] Q. Lai, R. Abrahams, W. Yan, C. Qiu, P. Mutton, A. Paradowska, X. Fang, M. Soodi, X. Wu, Effects of preheating and carbon dilution on material characteristics of laser-cladded hypereutectoid rail steels, *Materials Science and Engineering: A* 712 (2018) 548-563.
- [118] J.R. Davis, Nickel, cobalt, and their alloys, ASM international 2000.
- [119] W. Lin, C. Chen, Characteristics of thin surface layers of cobalt-based alloys deposited by laser cladding, *Surface and Coatings Technology* 200(14) (2006) 4557-4563.
- [120] V. Karthik, P. Visweswaran, A. Vijayraghavan, K. Kasiviswanathan, B. Raj, Tensile–shear correlations obtained from shear punch test technique using a modified experimental approach, *Journal of nuclear materials* 393(3) (2009) 425-432.
- [121] G. Sun, R. Zhou, J. Lu, J. Mazumder, Evaluation of defect density, microstructure, residual stress, elastic modulus, hardness and strength of laser-deposited AISI 4340 steel, *Acta Materialia* 84 (2015) 172-189.
- [122] A. Farnia, F.M. Ghaini, V. Ocelík, J.T.M. De Hosson, Microstructural characterization of Co-based coating deposited by low power pulse laser cladding, *Journal of Materials Science* 48(6) (2013) 2714-2723.
-

-
- [123] Y. Song, D. Ping, F. Yin, X. Li, Y. Li, Microstructural evolution and low temperature impact toughness of a Fe-13% Cr-4% Ni-Mo martensitic stainless steel, *Materials Science and Engineering: A* 527(3) (2010) 614-618.
- [124] K. Ohya, J. Kim, K.i. Yokoyama, M. Nagumo, Microstructures relevant to brittle fracture initiation at the heat-affected zone of weldment of a low carbon steel, *Metallurgical and Materials Transactions A* 27(9) (1996) 2574-2582.
- [125] A. Hoadley, M. Rappaz, A thermal model of laser cladding by powder injection, *Metallurgical transactions B* 23(5) (1992) 631-642.
- [126] H. Qi, J. Mazumder, H. Ki, Numerical simulation of heat transfer and fluid flow in coaxial laser cladding process for direct metal deposition, *Journal of applied physics* 100(2) (2006) 024903.
- [127] E. Toyserkani, A. Khajepour, S. Corbin, 3-D finite element modeling of laser cladding by powder injection: effects of laser pulse shaping on the process, *Optics and Lasers in Engineering* 41(6) (2004) 849-867.
- [128] G. Zhao, C. Cho, J.-D. Kim, Application of 3-D finite element method using Lagrangian formulation to dilution control in laser cladding process, *International Journal of Mechanical Sciences* 45(5) (2003) 777-796.
- [129] C. Cho, G. Zhao, S.-Y. Kwak, C.B. Kim, Computational mechanics of laser cladding process, *Journal of materials processing technology* 153 (2004) 494-500.
- [130] M. Alimardani, E. Toyserkani, J.P. Huissoon, A 3D dynamic numerical approach for temperature and thermal stress distributions in multilayer laser solid freeform fabrication process, *Optics and Lasers in Engineering* 45(12) (2007) 1115-1130.
-

[131] L. Fang, J.-h. Yao, X.-x. Hu, G.-Z. Chai, Effect of laser power on the cladding temperature field and the heat affected zone, *Journal of Iron and Steel Research, International* 18(1) (2011) 73-78.

[132] J. Heigel, M. Gouge, P. Michaleris, T. Palmer, Selection of powder or wire feedstock material for the laser cladding of Inconel® 625, *Journal of Materials Processing Technology* 231 (2016) 357-365.

[133] S. Paul, R. Singh, W. Yan, Thermal model for additive restoration of mold steels using crucible steel, *Journal of Manufacturing Processes* 24 (2016) 346-354.
